Control of a Variable-Speed Wind Turbine

John Licari
Institute of Energy
Cardiff University

A thesis submitted for the degree of

Doctor of Philosophy

February, 2013

To my family

Acknowledgements

This research would not have been possible without the help of many people. First and foremost, I would like to express my gratitude for the support, guidance and assistance of my supervisors Prof. Nick Jenkins and Dr. Jun Liang over the course of this research.

My sincere appreciation to Dr. Janaka Ekanayake and Dr. Carlos Ugalde-Loo for the time, advice and encouragement received. My thanks also to Dr. Ervin Bossanyi from Garrad Hassan for the helpful discussions we had and his interest in this work.

Very special thanks to my family and my dearest wife for their support, patience, encouragement and understanding over the past two and a half years.

This research was funded by Nordic WindPower and Cardiff University through the President's Scholarship scheme. I gratefully acknowledge the financial support provided by them.

Declaration

This work has not previously been accepted in substance for any degree and is not concurrently submitted in candidature for any degree.

Signed …………………….……….. (candidate) Date ……………………….

This thesis is being submitted in partial fulfilment of the requirements for the degree of PhD.

Signed …………………….……….. (candidate) Date ……………………….

This thesis is the result of my own independent work/investigation, except where otherwise stated. Other sources are acknowledged by explicit references.

Signed …………………….……….. (candidate) Date ……………………….

I hereby give consent for my thesis, if accepted, to be available for photocopying and for inter-library loan, and for the title and summary to be made available to outside organisations.

Signed …………………….……….. (candidate) Date ……………………….

Abstract

The requirement for achieving better cost-effectiveness of wind turbines (in this case by alleviation of fatigue loads on the drive-train and tower) and the impact of large wind penetration on the inertia of the power system are addressed. In order to implement and test the proposals addressing these aspects, a 2 MW wind turbine model is developed in Simulink®. A 1.2 kW experimental test rig that emulates the drive-train of a variable-speed wind turbine is then used to validate the simulations performed in Simulink®.

Two torsional vibration dampers based on different design approaches are designed to reduce excess fatigue in the drive-train. One is based on a conventional band-pass filter approach and the other on a model-based approach. Stability and performance analyses are performed on the system for the two dampers for cases with and without model uncertainties. The analyses are verified using simulations and validated using the test rig. Results show that the performance of the model-based damper to damp torsional vibrations is superior to the conventional damper in both cases. The conventional damper needs re-tuning to recover its original performance when model uncertainties are present.

An algorithm to prevent the rotor rotational frequency from exciting the side-side tower mode is designed. It defines a range of generator speeds around this tower mode where sustained operation is restricted. The effectiveness of the algorithm is observed through simulations and experiments. Different restricted operation range widths are tested to assess how the turbine performance is affected. Results show that with a wider range restriction, the tower mode is excited less at the expense of some power loss.

The provision of inertial response from a variable-speed wind turbine using an auxiliary control loop is tested. Simulation and experimental results show the inadequacy of such turbines for providing inertia response in compliance with the primary response requirements. To improve this, a number of wind turbine models are connected in parallel (operating under different wind speeds) to model a wind farm. Simulation results show a significant improvement when the inertial response of individual turbines is coordinated.

Table of Contents

List of Figures

List of Tables

Abbreviations

1P	Rotor frequency
3P	Blade passing frequency
BPF	Band-pass filter
DC	Direct current
DFIG	Doubly-fed induction generator
DSP	Digital signal processor
EESG	Electrically-excited synchronous generator
FRC	Full-rated converter
GM	Gain margin
HSS	High-speed shaft
IG	Induction generator
KF	Kalman filter
LSS	Low-speed shaft
PM	Phase margin
PMSG	Permanent magnet synchronous generator
PRC	Partially-rated converter
pu	Per unit
PWM	Pulse width modulation
SCADA	Supervisory control and data acquisition
SG	Synchronous generator
VSC	Voltage source converter
VSWT	Variable-speed wind turbine
WT	Wind turbine

Chapter 1

Introduction

Summary:

This chapter starts with a discussion on the status of the installed capacity of renewable energy sources in Europe, with particular focus on wind energy. The evolution of WTs during the last two decades is then briefly outlined. The research objectives based on two of the challenges brought up with this development are outlined. The chapter ends with the structure of the thesis listing the highlights of each chapter.

1.1. Background

In recent years, reliance upon fossil fuels has given rise to concerns over climate change due to emissions of greenhouse gases. The electricity and heat production sector accounts for nearly 30% of all greenhouse gases emissions in Europe, of which carbon dioxide (CO_2) is the predominant pollutant [1]. In response, the European Union (EU) issued a directive (2001/77/EC) on the promotion of electricity produced by renewable energy sources in 2001. In 2009, this directive was repealed by another stringent Renewable Energy Sources Directive (2009/28/EC), which requires that by 2020, 20% of the gross final consumption of energy is generated from renewable energy sources, with varying legally binding national targets for each member state [2].

The share of renewable power installations has grown (almost tenfold) over the past 11 years in the EU countries. A history of the power installed capacity per year indicating the share of renewable energy sources between 1995 and 2011 is shown in Figure 1.1. In 2000, the total installed capacity of renewable energy sources was 3.5 GW (20.7%). In 2011, it reached 32 GW (71.3%) of which 9.6 GW (21.4%) was wind power [3], implying that the total installed wind power in the EU has now reached 84.3 GW. Further growth is predicted and by 2015 the total wind power capacity installed is expected to reach 144 GW [4].

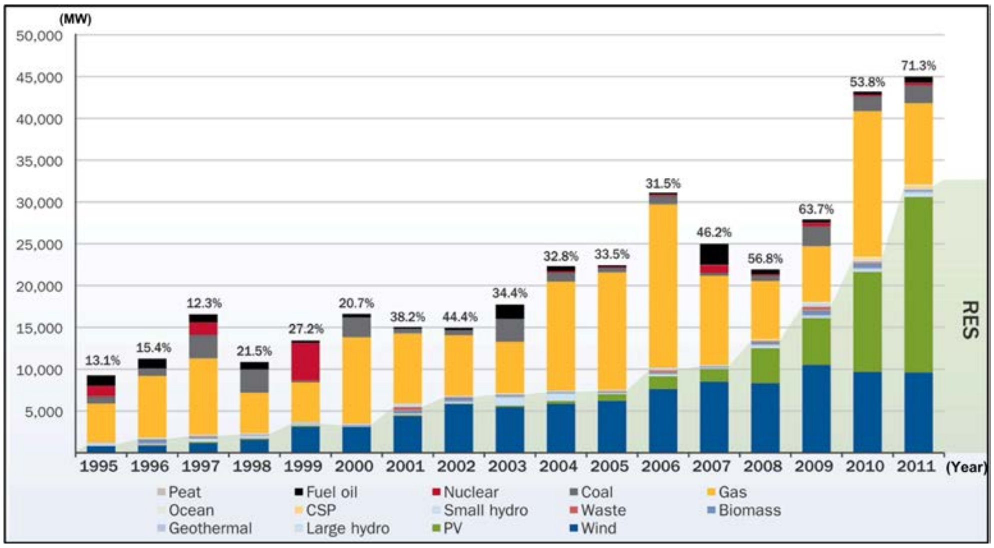

Figure 1.1: EU power generating capacity added per year in MW showing the renewable energy sources share in percentage [3]

1.2. Advancements in Wind Turbines

During the last two decades, the wind industry has made large technological advancements on WTs. Initially, WT technology started with fixed-speed generators. Subsequently, it moved to variable-speed operation which enabled the possibility of increasing the extracted power during below rated wind speeds and reducing the loads [5]. At the same time, WTs have increased both in diameter and hub heights to allow higher power extraction from wind. Figure 1.2 shows how WT technology and size have evolved over the last 25 years [6].

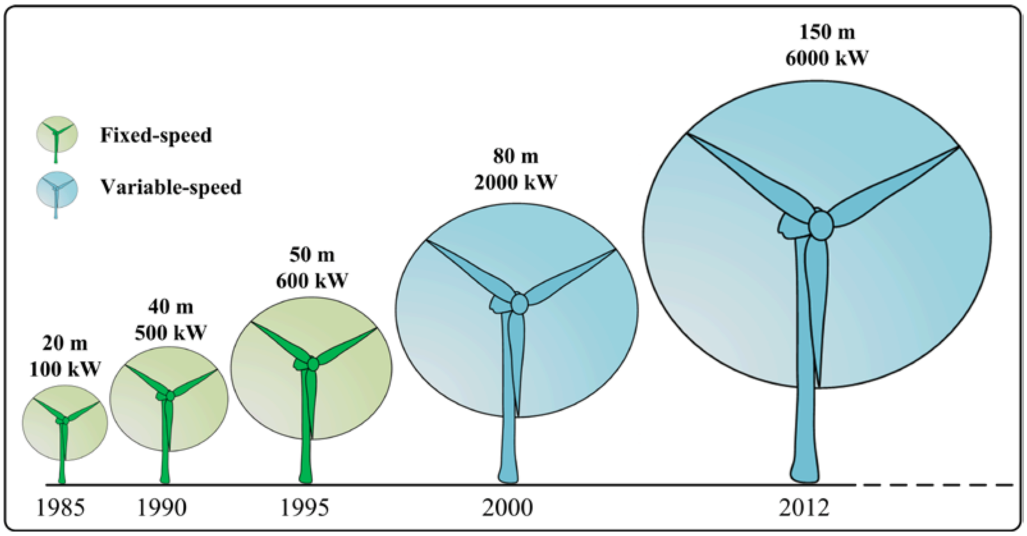

Figure 1.2: Technology and size evolution of WTs

This technological development can be attributed to attempts made for reducing the cost of energy. The energy generated from a WT is proportional to the area swept by the rotor and therefore to the square of the rotor diameter. On the other hand, the cost related to the mass of material needed is proportional to the volume and thus to the rotor diameter cubed. This relationship is referred to as the squared-cubed law [7]. Hence, as turbine sizes increase, manufacturers are faced with challenges for achieving better cost effectiveness. This is currently being addressed through optimisation of components with respect to material usage, where component strength is provided only if necessary. The reduction of component masses leads to turbines becoming less tolerant to fatigue loads [8]. Hence, the reliability of turbine components becomes an important issue.

According to [6], the drive-train is considered among the most critical components in a WT in terms of reliability. A premature failure in the drive-train leads to an increase in the cost of energy due to component replacement and turbine downtime. Typical replacement costs for a 1.5 MW VSWT in 2005 were about €150,000 for a gearbox, €98,000 for a generator and €25,000 for a main bearing [9]. Additionally, there is the cost associated with the loss of production during the WT downtime. Figure 1.3 shows an aggregated downtime per turbine subsystems. This data represents about 27,000 WTs ranging from 500 kW to 5 MW for the period 2003 – 2009 reported by Wind Stats [10]. It can be clearly noted that two of the drive-train components (gearbox and generator shown in red) are among the highest contributors to WT downtime.

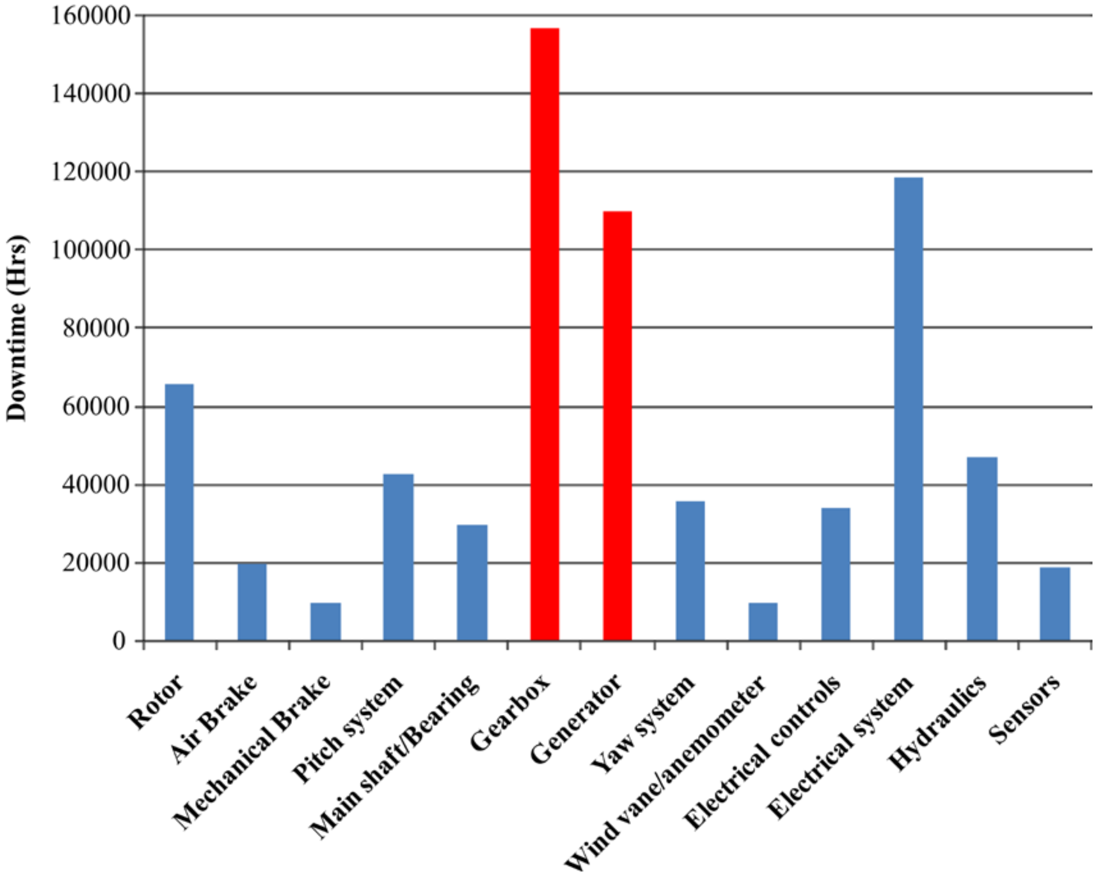

Figure 1.3: Wind Stats (2003 − 2009) − Aggregated downtime per turbine subsystem [10]

1.3. Research Objectives

The objectives of this research work are motivated by the requirements of achieving more cost effective WTs and the large scale penetration of wind energy into the power system.

As outlined in Section 1.2, the cost of energy is partly dependent on the reliability of WT components. The reliability of a WT can be significantly improved if the loads are minimised. The first objective is the mitigation of loads in the drive-train. Turbulent winds and gusts can excite modes that can lead to torsional vibrations in the drive-train, which in turn produce large stresses on components. Ultimately this may reduce the lifetime of components, such as the gearbox [11, 12]. To address the first objective, an investigation of an effective controller that damps torsional vibrations in the drive-train and reduces re-tuning procedures during WT commissioning is carried out.

Similarly, the tower of a WT can be excited when the side-side bending mode is made close or within the rotor or the blade passing frequency regions. This would trigger tower vibrations that lead to an increase in fatigue loads, which in turn can cause the tower to fail prematurely. As a secondary effect, these vibrations can couple with the drive-train torsional mode and trigger torsional vibrations [13]. The second objective of this work is to develop an algorithm to avoid large tower vibrations when its side-side bending mode is designed within the rotor rotational frequency region.

By 2020, a large amount of wind energy is expected to be installed in the EU (230 GW), both onshore and offshore [4]. This high penetration of WTs will eventually replace conventional generating plants. Due to the lack of inertial coupling of VSWT, the overall inertia of the power system will reduce, leading to unacceptable excursions of grid frequency. This is one of the challenges faced by the power system. The last objective of this work addresses this issue by investigating the possibility of providing a coordinated inertial response from wind farms in order to support the power system during a frequency event.

1.4. Thesis Structure

The structure of the thesis is as follows:

Chapter 2 reviews different aspects of wind energy conversion system technologies, types of loads in WTs, mitigation techniques for torsional vibrations and frequency support options for augmenting the frequency response of VSWTs.

Chapter 3 gives a detailed description of the models used and the controllers designed to build a FRC-PMSG based VSWT model in Simulink®. It also includes simulation results for below and above rated wind speeds operating conditions to verify that the operation of the WT model is sound.

Chapter 4 introduces the experimental test rig and describes the hardware-in-the-loop experimental sequence used to validate the simulations results presented in Chapter 5−7.

Chapter 5 presents the design of a model-based and a BPF-based torsional vibration damper. It also includes a performance and stability analysis of both dampers when subjected to model uncertainties. The chapter finishes by presenting simulation and experimental results comparing the performance of both dampers.

Chapter 6 introduces a speed exclusion zone algorithm to prevent the rotor from exciting the tower side-side bending mode. Simulation and experimental results for various turbulent wind speeds conditions showing the effectiveness of the algorithm are then presented. The chapter ends with a comparison on the effect that different speed exclusion zone widths have on tower vibrations and annual energy yield.

Chapter 7 details a controller that can provide inertial response from a FRC-PMSG based WT. It also shows the possible application of this controller to a wind farm to provide a coordinated inertial response through a SCADA system. Simulation and experimental results are presented.

Chapter 8 draws a final conclusion of the thesis, lists the contributions and publications and proposes suggestions for future work.

Chapter 2

State of Art of Wind Energy Conversion

Summary:

This chapter reviews different aspects of wind energy conversion systems. Aerodynamic energy conversion is considered first where the operating regions and different aerodynamic power control techniques are discussed. This is followed by an overview of the types of VSWTs architectures, generators and drive-trains. The salient features of the turbine architectures are also discussed. The types of loads in a VSWT are considered next with particular focus on fatigue loads. The sources of torsional vibrations in the drive-train of a WT are then discussed and a review of possible torsional vibrations mitigation techniques is presented. In the final part of the chapter, a review of inertial frequency response is carried out. This includes a brief overview of the frequency response requirements from different grid codes and an analysis of the frequency response from different VSWTs architectures. Finally, a review of the frequency support options for augmenting the frequency response of VSWTs is presented.

2.1. Wind Energy Conversion Systems

A typical modern wind energy conversion system consists of a three bladed rotor that captures energy from the wind and converts it into mechanical energy. This energy is then transmitted to a generator which converts it into electrical energy.

2.1.1. Aerodynamic Energy Conversion

The power available from the wind is given by [13, 14]

$$P_{air} = \frac{1}{2}\rho A V_w^3 \tag{2.1}$$

where P_{air} is the power available from the wind [W], ρ is the air density [kg/m^3], A is the cross-sectional area [m^2] and V_w is the free wind velocity [m/s].

The power available from the wind cannot be completely extracted and is dependent on the power coefficient C_P defined by [15]

$$C_P = \frac{P_w}{P_{air}} \tag{2.2}$$

which is the ratio between the extracted power P_w and the available power P_{air}. This can have a maximum of 0.593, known as the Betz limit. The power coefficient is a function of two variables: the blade pitch angle β and the tip speed ratio λ which is defined by [13]

$$\lambda = \frac{\omega_{rot} R}{V_w} \tag{2.3}$$

where R is the radius of the rotor [m] and ω_{rot} is the speed of the rotor [rad/s]. Hence, the power extracted by the rotor of a WT is given by [13]

$$P_w = \frac{1}{2}\rho A V_w^3 C_P\left(\beta, \lambda\right) \tag{2.4}$$

A typical variation of C_P as a function of the tip speed ratio for different pitch angles is shown in Figure 2.1. It can be observed that there is only one tip speed ratio value at each pitch angle that gives a maximum C_P. Therefore, by controlling the speed of the rotor (generator) to follow the tip speed ratio that maximises C_P, maximum power extraction can be achieved at different wind speeds [16]. This is one of the motivations for using variable-speed operation.

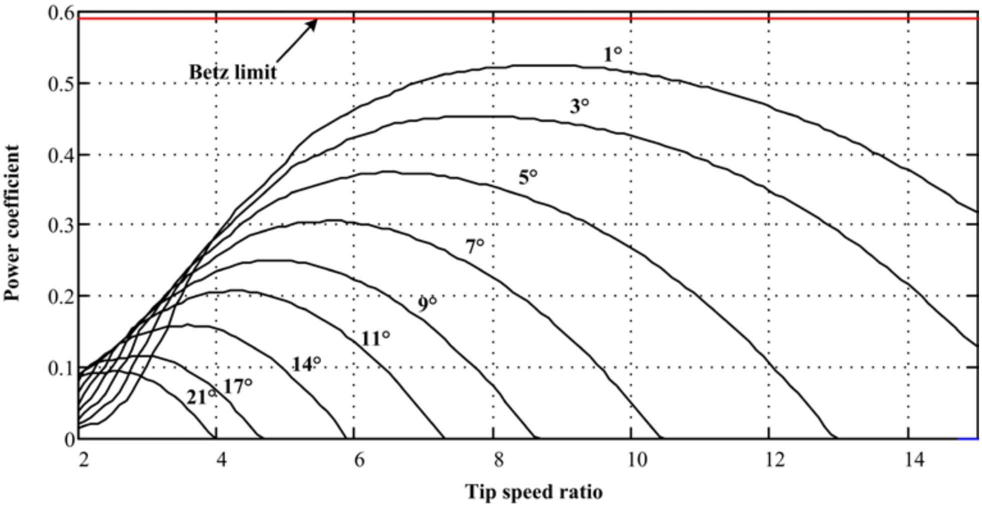

Figure 2.1: Variation of C_P as a function of the blade pitch angle β and tip speed ratio λ

2.1.1.1. Operating regions of a variable-speed wind turbine

A typical power *vs*. speed characteristic of a VSWT is shown in Figure 2.2, where the optimal rotor speeds for maximum power extraction at different wind speeds are highlighted. Moreover, the three different operating regions of a VSWT are illustrated.

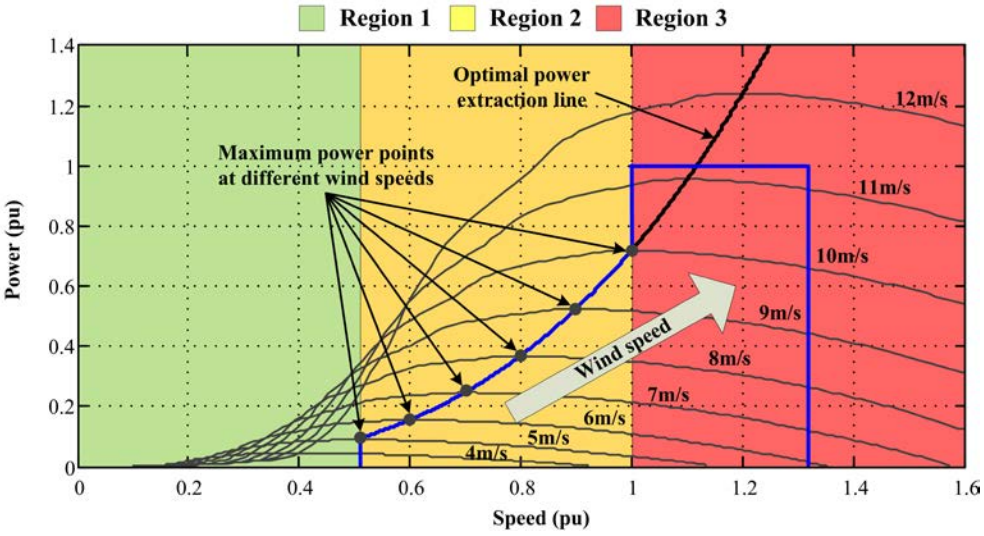

Figure 2.2: Power *vs*. speed characteristic of a VSWT

The operating regions of a WT can be divided into three regions and are shown in Figure 2.2. The amount of wind power available in Region 1 is not enough to overcome the WT losses and therefore it is unproductive. In this region, the WT rotor is held stationary and the generator is disconnected from the utility grid until the cut-in wind speed is reached. Typical cut-in wind speeds vary between 3 to 5 m/s depending on the turbine design [17-19]. In Region 2, the turbine operates at variable speed to maximise the extracted power from the wind. This region ranges from the cut-in to the rated wind speed at which maximum power is produced. Region 3 is the constant speed region which ranges from rated to the cut-out wind speed, which for most turbines is 25 m/s. In this region, the aerodynamic power is limited in order not to overload the turbine component design ratings. There are mainly three ways of controlling aerodynamic power: by stall regulation, pitch angle control or yaw control [13].

2.1.1.2. Aerodynamic power control

The most common method used for controlling power above rated wind speed is achieved using pitch angle control. There are two variances of pitch angle control, namely the active and passive pitch control. In the active pitch control, the pitch actuator rotates the blades about their axis (increase of β) in such a way that the leading edge of the blade is moved into the wind. This results in a reduction of the angle of attack and hence a reduction in the aerodynamic lift developed [14]. On the other hand, the idea behind passive pitch control is to have a blade designed to twist when the loads on the blades exceeds a certain level. The blade twisting effectively alters the pitch angle which results in a reduction of the lift force. Therefore, the higher the wind speed, the higher are the loads on the blades and the larger is the pitch angle [13]. Another option for limiting the aerodynamic power is stall control. Similarly, there are two types of stall control: passive stall and active stall. In passive stall control the blades are designed to naturally stall in high wind speeds, hence reducing the aerodynamic lift [13]. In active stall control a pitch actuator is employed to drive the blades into stall, thereby reducing the lift force. A third option to control the aerodynamic power is by yaw control, where the turbine is rotated away from the incoming wind direction. This method requires a robust yaw system [14].

2.1.2. Variable-Speed Wind Turbine Architectures

The present techniques for converting mechanical to electrical energy in a VSWT are shown in Figure 2.3. It shows different possible technological options such as with or without gearbox, with synchronous or asynchronous machines and different power converter topologies. These concepts can be split into two groups according to their power converter rating: PRC and the FRC.

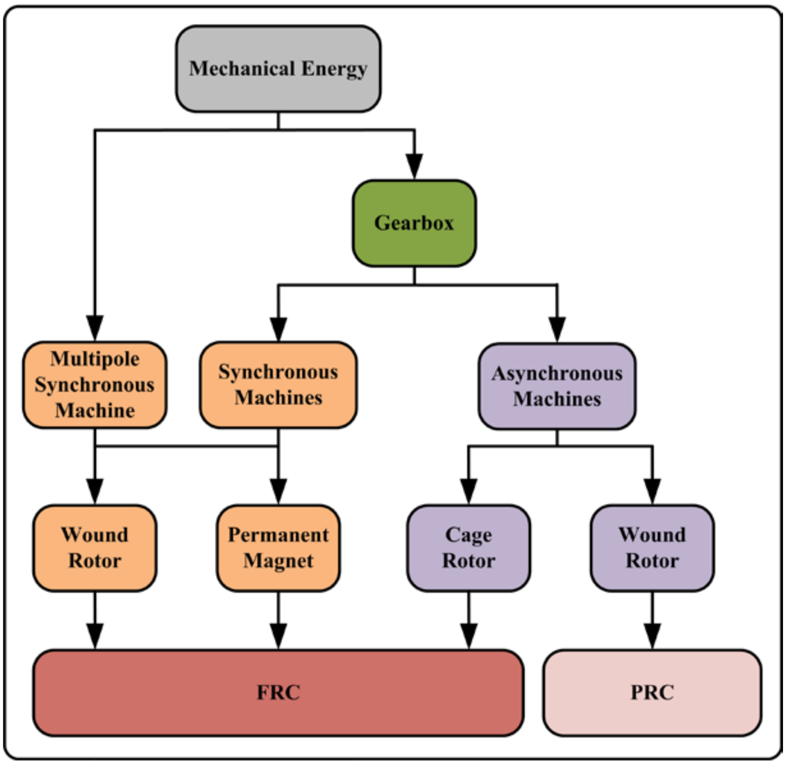

Figure 2.3 Wind energy conversion technology routes [20]

2.1.2.1. Wind turbines with partially rated converter

A WT equipped with a wound rotor asynchronous machine with a PRC has been a very popular approach for achieving variable-speed operation. The advantages of this architecture are lower converter costs and losses, since the power converter handles only a fraction (20–30%) of the total power [21]. The disadvantages of such system is a limited variable-speed operation range and higher maintenance costs due to the slip rings needed to access the rotor windings [22]. There are two variants of this approach: the variable-slip operation and the DFIG [20, 23].

Figure 2.4 shows a block diagram of a WT with a wound rotor IG configured for variable-slip operation. In this case the rotor windings are connected to external resistors through a power converter. Any variation in the rotor resistance will result in a variation of the slip, which ultimately affects the generator speed [22]. The typical speed variation with the variable-slip operation is less than 10% [13, 20, 21]. In this configuration the generator draws reactive power from the grid to build up the magnetic field. Therefore, capacitor banks are usually installed to compensate for the reactive power absorbed [22]. Moreover, a soft-starter is needed to limit the inrush current during start-up [23].

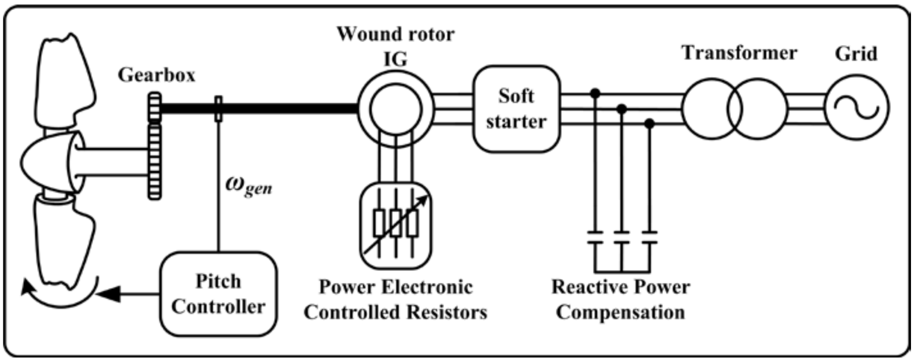

Figure 2.4: Wound rotor IG with variable-slip configuration

A typical configuration of a DFIG based WT is shown in Figure 2.5. It consists of wound rotor IG which has its rotor connected to the grid through a PRC. The converter is typically a back-to-back VSC with a typical rating of 30% of the full power [20]. This converter decouples the rotor frequency from the grid frequency, hence enabling variable-speed operation [15]. This operation is achieved by injecting a controllable voltage into the rotor at the slip frequency [23]. The speed variation is directly related to the power of the rotor side converter and is typically ±30% of the synchronous speed [20, 22]. In this configuration, electrical power can be delivered to the grid through both the stator and the rotor depending on the generator speed. In the case of super-synchronous speed operation, electrical power is delivered to the grid through both the stator and rotor. On the other hand, when the generator is operating in sub-synchronous speed, electrical power is delivered to the grid through the stator only whilst the rotor side absorbs active power [15]. As a safety measure to protect the VSC and the generator from over-current during faults on the network, a crowbar circuit is employed on the rotor side.

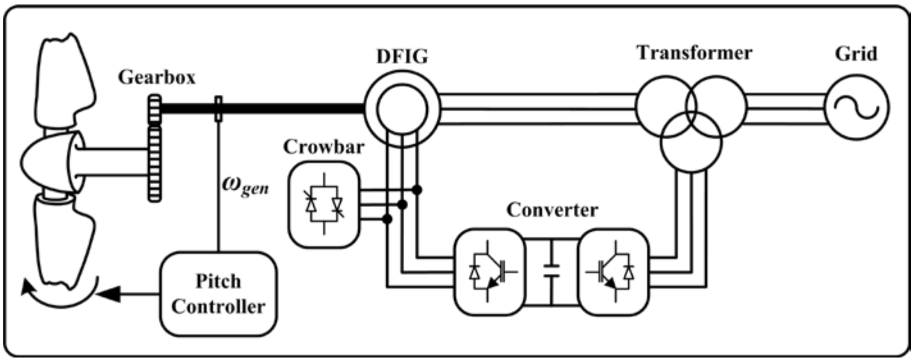

Figure 2.5: DFIG configuration

2.1.2.2. Wind turbines with full-rated converter

A typical configuration of a FRC based WT is shown in Figure 2.6. The FRC configuration is characterised by a broad variable-speed operation ranging from stand-still to the full rated speed [13]. This is one of the advantages of a FRC over the PRC based WTs. However, in this case the converter cost and losses are higher because of the full power rating [21].

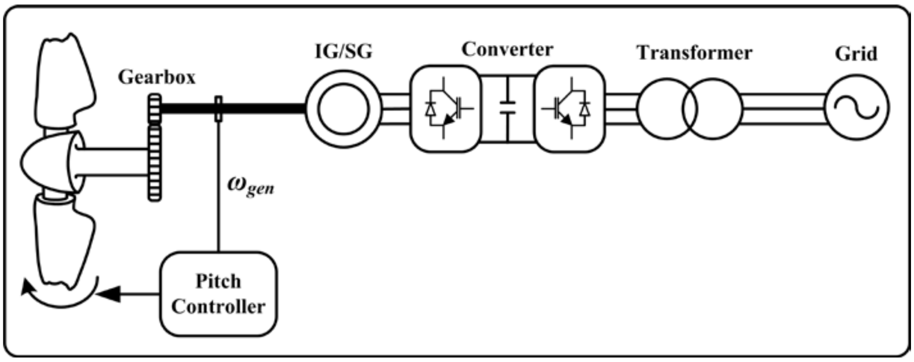

Figure 2.6: FRC configuration

In this configuration, the generator (either an IG or a SG) is connected to the grid through a back-to-back VSC. Therefore, it offers complete decoupling of the generator from the grid frequency, thereby enabling variable-speed operation. Moreover, full control of the active and reactive powers is possible with this type of converter [22]. This is highly desirable in order to fulfil the present Grid-Code requirements [23].

A SG has the ability to provide its own excitation on the rotor, either by having a wound rotor or by permanent magnets. The two generator variants are termed as the EESG and the PMSG, respectively. In the case of a SG, the VSC on the generator-side can be replaced by a diode rectifier as shown in Figure 2.7.

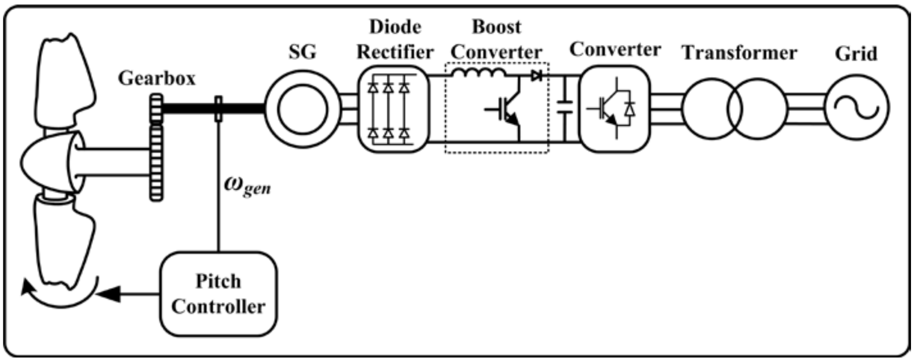

Figure 2.7: FRC with diode rectifier configuration

This makes the converter cheaper; however, the control of the whole system becomes more difficult. A boost converter is normally used to control the DC link voltage and the grid-side converter controls the operation of the generator [24].

The EESG based WT configuration is shown in Figure 2.8. It can be observed that in addition to the FRC there is a diode rectifier to provide the DC excitation current to the rotor. The rotor of an EESG can be either cylindrical or salient pole type. The latter configuration is attractive for direct-drive applications [21].

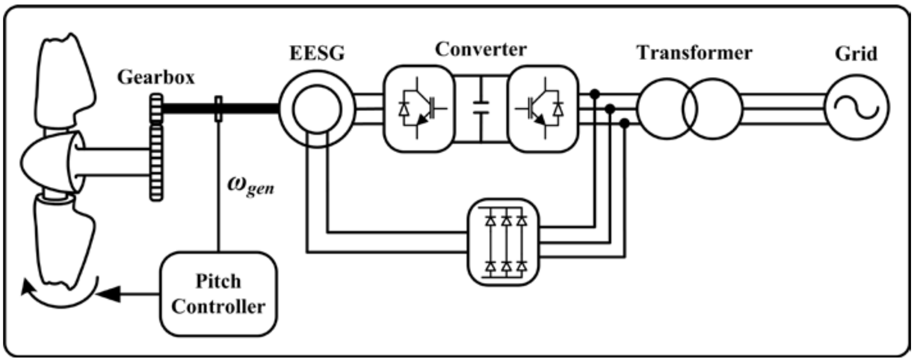

Figure 2.8: EESG configuration

Apart from the conventional types of generators there are other types of generators that were or are being investigated. These include the switched reluctance generator, the high voltage generator and the superconducting generator.

The switched reluctance generator is robust and is appropriate for harsh environments due to the absence of windings and permanent magnets on the rotor [25, 26]. Despite having such features, the switched reluctance generator is considered inferior to the PMSG in terms of the power density and the requirement for sophisticated converter control [24].

The main motivation behind the high voltage generator was to reduce the current in the system, thereby reducing the copper losses. An additional benefit for WT applications is the elimination of the transformer [27]. On the hand, the drawback of such generators is the necessity for a high voltage converter, which is more expensive [24].

The concept of using a superconducting generator in a WT is relatively new. The advantages of such generator are a high torque with compact and light weight design and a slow rotational speed (direct-drive) when compared to PMSGs [28, 29]. The mechanical simplification is possible due to high magnetic field strength that can be produced by the superconductive coils with very little loss. Although this generator technology is quite promising, it is not yet feasible due to the high cost of the superconducting cables and the need for cooling to cryogenic temperatures [30].

2.1.3. Drive-trains

A drive-train consists of the components responsible for transmitting power between the rotor of the WT and the electrical terminals of the generator. There are three main types of drive-trains [31]: the three-stage gearbox with a high-speed generator (Figure 2.9), the one/two-stage gearbox with medium speed generator (Figure 2.10) and the direct-drive generator (no gearbox) (Figure 2.11).

During the last decade the three-stage gearbox with a high-speed generator has been the most popular drive-train. This accounted for 75–80% of the market share [32, 33]. In this arrangement, the generator is typically a 4-pole machine with a rated speed of 1500 rpm (50 Hz supply) and the gearbox ratio is typically between 75:1 and 100:1. The type of generator used with this drive-train is predominantly the DFIG; however, the PMSG is gaining popularity due to higher part load efficiencies [34].

Due to its reliability, the gearbox has been a subject for controversy for some time in the wind industry. Statistical data collected by industrial surveys (Wind Stats and Landwirtschaftskammer) have suggested that the drive-train components are not responsible for the most frequent system failures [35]. However, the downtime associated with a gearbox or generator failure is among the highest. The downtime issue together with the attempt to minimise failures by having a simpler drive-train with fewer components have stimulated interest in direct-drive technology [7, 36]. In a direct-drive arrangement, the generator is designed for low-speed operation (large number of poles) to eliminate the gearbox. This requires that the generator has a very high rated torque in order to match the turbine rotor torque [31]. Therefore, such generator tends to be diametrically large. The two types of generators used for direct-drive WTs are the EESG and the PMSG; with the former being the most widely used generator so far. However, the PMSG technology is gaining popularity due to higher annual energy yield and lower weight [21, 33, 37].

Figure 2.9: High-speed drive-train arrangement [38]

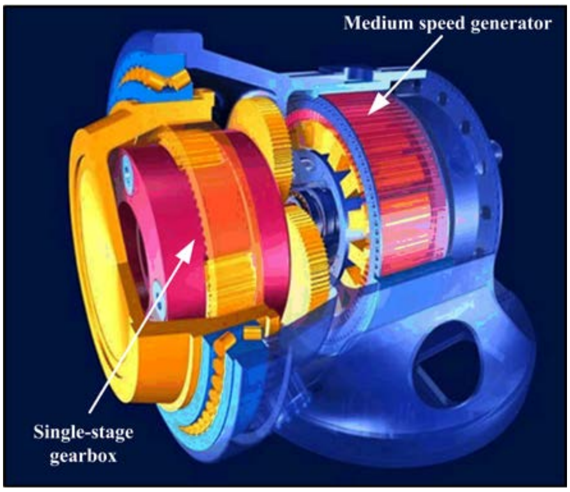

Figure 2.10: Medium-speed drive-train arrangement [39]

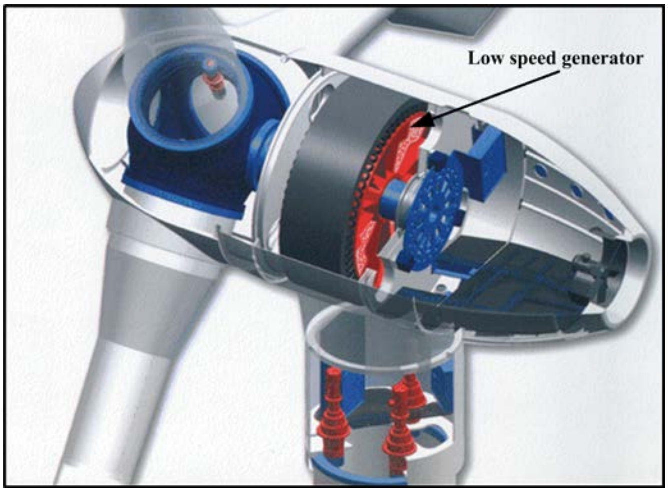

Figure 2.11: Direct-drive arrangement [40]

A relatively new drive-train concept is the medium-speed generator with one/two stage gearbox. Typically in this arrangement the generator speed is designed to be around 150 rpm with a gearbox ratio of 10:1 [31]. This leads to a system with a smaller generator size than a direct-drive and a lighter gearbox than a three-stage gearbox. The size and weight savings opens the possibility of integrating the generator and the gearbox as a single unit. This option gives the added advantage of reducing the nacelle weight and thus simplifying the structural design [41].

2.2. Wind Turbine Loads

WT loads are the forces or moments that are experienced by a turbine, both during operational and non-operational cases. The correct identification of the various loads a turbine experiences during its lifetime is very important and is part of the design process of a WT [42]. The sources of loads can be broadly categorised as external and local loads.

External loads refer to forces acting on the turbine and determined by the components' surroundings. These include environmental loads such as inertial and gravitational, aerodynamic and operational loads [43]. The inertial and gravitational loads are static and dynamic loads acting on WTs as a consequence of vibration, gravity, rotation and seismic effects [14]. The primary load source during stationary operation at high winds is the drag force, whereas the lift force is the primary source during the turbine operation. Hence, the aerodynamic loads are mainly dependent on the rotational speed of the rotor, the average wind speed across the rotor plane and the turbulence intensity [44]. Other loads that can occur on WTs include wake, impact and ice loads [45]. During operation of a turbine, the dynamic interaction between turbine components, either provoked by the turbine structure or induced by the control system, may be a source of significant loads [43]. For instance, starting, stopping, braking, yawing and pitch control can generate substantial loads on the WT structure [13, 45].

Local loads are loads due to stresses and deformations on turbine components caused by external loads. There are two types of local loads: extreme and fatigue. The extreme loads are characterised by extremely high magnitude which can cause a component to fail the first time it experiences the load. On the other hand, fatigue loads are characterised by relatively low amplitude repetitive cycles which can cause fatigue fractures in materials [46, 47].

The main sources of fatigue loads are component vibrations which can be generally divided into forced and natural vibrations [46]. Forced vibrations occur when a component is made to vibrate at the frequency of the external load. For instance, the load frequency that is experienced by some components in a turbine is the blade passing frequency which equates to triple the rotor frequency for a three bladed WT. On the other hand, natural vibration occurs when a mode of a component is excited. In this case the component vibrates according to its eigen-frequency and mode shape.

Impulse and step loads on a turbine can excite different components' modes simultaneously. This happens because such loads contain all frequencies [46, 48]. Hence, a component can vibrate with its own natural frequency (natural vibrations) and with other load frequencies (forced vibrations) simultaneously. The sources of forced vibrations depend on the coupling of the component under consideration to other external component modes. Torsional vibrations in the drive-train are a good example of natural and forced vibrations occurring at the same time.

The life expectancy of a WT is typically 20 years. Hence, each turbine component has to be designed to withstand both extreme and fatigue loads throughout the turbine lifetime. It is often the case that the design of many WT components is driven by fatigue rather than extreme loads [13]; however, the designer needs to verify this through a number of relevant load cases [42]. The standard IEC 61400-1 'Wind turbines – Part 1: Design Requirements' identifies a total of 22 different load cases (17 extreme, 5 fatigue), which are considered as a minimum for WT design [44]. These load cases are constructed from a combination of different situations of wind conditions and WT operation states [13]. A larger number of load cases are given in the Germanischer Lloyd's 'Guidelines for the Certification of Wind turbines' [45].

2.3. Torsional Vibrations

Torsional vibrations can be defined as unwanted torque oscillations in the drive-train of a WT that occur whenever the system gets excited by either mechanical or electrical load changes [49]. Assuming a high-speed drive-train arrangement (Figure 2.9), the drive-train consists of a LSS, gearbox, HSS and a generator.

A drive-train can be modelled through a system of rotating masses connected by shafts. These masses are assumed to have inertia but no stiffness, whereas the shafts possess stiffness but not inertia [14]. The complexity of the drive-train model to be used depends on the type of analysis being performed and the level of accuracy needed. In the literature, a two-mass model is typically used to model the drive-train dynamics [49-51]. However, this model is limited because it considers only the torsional mode of the drive-train (natural vibrations). In the study of torsional vibrations in the drive-train of a WT, it is important to consider not only the torsional mode but also other component modes responsible for forced vibrations in the drive-train. The components that can possibly lead to forced vibrations are the blade (can couple with the drive-train through the hub and the shaft) and the tower (can contain rotational movement at the tower top) [16, 52].

A blade bends about its weak and strong principal axis, which are known as the flapwise and edgewise bending, respectively. Due to the twist in the blades, the axis directions change along the blade span. Hence, an alternative system of directions can be defined. This is based on the rotor plane, where the bending modes of a blade are referred to as out-of-plane and in-plane modes [43]. The out-of-plane modes account for the perpendicular motion of the blade to the rotor plane and are governed mainly by thrust forces on the rotor [53]. Since these modes are orthogonal to the rotational direction of the rotor, they do not couple to the drive-train. Conversely, the in-plane modes can couple to the drive-train because they are responsible for the motion of the blade in the rotational direction [23].

The in-plane modes consist of symmetrical and asymmetrical vibration modes. In the symmetrical modes, all the blades vibrate collectively in one direction with respect to the rotation axis as shown in Figure 2.12(a). Hence, these modes affect the torque and therefore blade vibrations can couple with the drive-train through the hub and the main shaft. On the other hand, in the asymmetrical modes the blades vibrate against each others' direction and each blade tends to cancel each others' effect. This is shown in Figure 2.12(b). Due to this, the rotor does not experience any rotational effects and thus no torque vibrations are transmitted to the main shaft [54]. Hence, the asymmetrical blade modes do not couple with the drive-train and can be neglected.

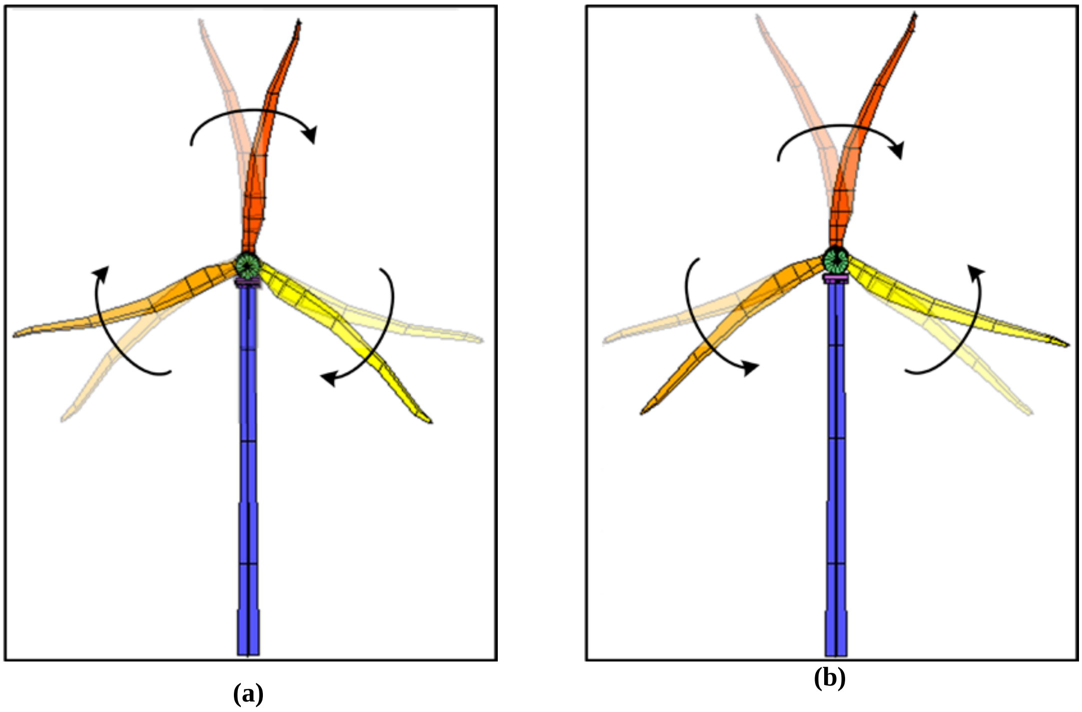
(a) **(b)**

Figure 2.12: First blade in-plane modes (a) symmetrical mode (b) asymmetrical mode

The tower bending modes consist of fore-aft and side-side modes. The fore-aft modes are characterised by the displacement of the nacelle normal to the rotor plane and hence do not couple with the drive-train mode. On the other hand, the side-side modes are characterised by displacements of the nacelle in the rotor plane [13]. These modes can couple with the drive-train mode when they have significant rotation at the tower top [13, 16, 52]. This mode is shown in Figure 2.13.

The level of coupling between different components modes varies for every turbine. Hence, the complexity of the model used for torsional vibration studies depends on the level of coupling of the symmetrical blade in-plane and the tower side-side modes to the drive-train mode. In the case where only strong coupling exists between the drive-train mode and the blade in-plane mode, a three-mass model is sufficient [16, 52]. On the other hand, if strong coupling exists between all the three modes a higher order model should be used, as outlined in [55].

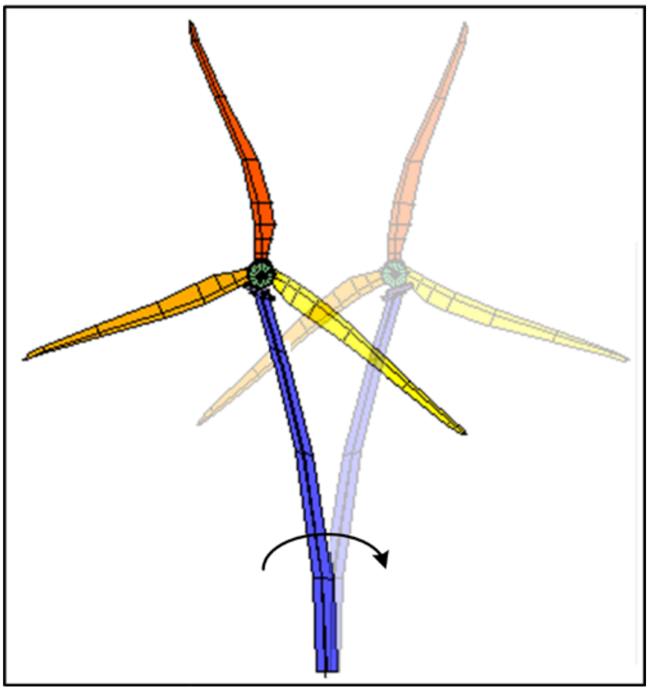

Figure 2.13: Tower side-side mode

2.3.1. Mitigation of torsional vibrations

A WT operating below rated wind speed has inherent damping of torsional vibrations. This is because any torque vibrations in the drive-train are reflected on the generator speed. The torque controller uses the generator speed to derive a reference torque for the generator that maximises the power extracted from the turbine. At the same time, when there is a positive peak on the speed oscillations due to torque vibrations, the torque controller demands more torque from the generator whereas when there is a negative peak it demands less torque. This provides a counteracting torque that damps torsional vibrations. This in-built damping capability is present only during variable-speed operation where the generator torque is varied to optimise the extracted power.

At above rated wind speed, the torque of the generator is held constant and no inherent damping torque is offered, hence torsional vibrations persist [13, 56]. These vibrations cause high mechanical stresses in the drive-train and have harmful effects on the fatigue life of the drive-train components [57]. It is therefore crucial to damp these vibrations to reduce fatigue loading.

2.3.1.1. Mechanical damping

The extenuation of torsional vibrations is possible through additional mechanical damping by means of appropriately designed rubber mounts or couplings [58]. However, there is a cost associated with this approach which makes it unattractive [52]. An alternative approach to damp these vibrations is to use blade pitching [59-61]. The idea is to use the blades to produce a torque component that opposes the change in rotor speed. Some drawbacks have been reported with this damping approach: it reduces slightly the energy output as the turbine is no longer operating at optimum pitch and it makes the pitch system more active with demands for faster pitching rates [60, 61]. Moreover, it has been observed that this damping method was not particularly effective [59, 62].

An alternative way of damping these vibrations is to use the generator to produce an auxiliary damping torque [49, 56]. Depending on which control scheme is adopted for the generator-side converter, the auxiliary damping can be achieved using either the torque controller or the DC link voltage controller.

2.3.1.2. Auxiliary damping with the generator torque controller

In the traditional VSC control strategy, the generator-side converter is used to control the power or torque of the generator, whilst the grid-side converter is used to control the DC link voltage and the power factor. A very effective way to damp torsional vibrations is to use the generator to provide a counteracting damping torque [13]. This can be achieved by adding a small ripple containing the vibration information to the generator torque control loop [52]. Typically this ripple is derived from a filtered version of the generator speed by a vibration damper which usually consists of a BPF, a notch filter and a phase compensator [49, 56, 63]. In such approach, the performance of the vibration damper relies on the correct identification of the vibration frequencies and their phases from the speed information.

An alternative way for deriving the vibration information without using any filtering of the generator speed was proposed in [51]. The basis of this method relies on the fact that speed information is contained in the electrical power flow. Hence, if the DC link voltage is held constant, the speed is then proportional to the DC link current. The vibration information can then be extracted from the DC link current. Similarly, this information is then used to add an additional damping term to the generator torque control loop. Although this approach was shown to be functional, no indication of an improved performance of the torsional vibration damper was presented.

2.3.1.3. Auxiliary damping with the DC link voltage controller

The use of the generator torque or power controller to damp torsional vibrations proved to be very effective and has been successfully adopted on several WTs [16, 52, 64]. However, in [56, 65] it was reported that with this damping approach, the energy used to damp torsional vibrations tend to be reflected as electrical power fluctuations if the constant power control scheme is used. This is undesirable because such oscillations can cause instabilities (possible interaction with power system modes) and power quality issues (flicker) [51, 66, 67]. Such a drawback can be avoided by using an alternative control strategy in which the control function of each converter is reversed [49], namely the generator-side converter controls the DC link voltage whilst the grid-side converter controls the active and reactive power flows into the grid independently. In this scheme, the damper derives the vibration information from the generator speed and is added to the DC link voltage reference. Ultimately, the DC link voltage controller influences the generator torque which counteracts the torsional vibrations. With this control scheme, the output of the WT exhibits lower power fluctuations and therefore can be used when large wind power is injected to the power system [67].

2.3.1.4. Torsional vibrations damping with specialised controllers

Other alternatives for damping torsional vibrations using modern control design techniques have been reported in the literature. In [61, 68], a generator torque controller that enhances the system damping was designed using pole placement with state-feedback. The enhancement of the lightly damped modes was achieved by increasing the negative real part of their eigenvalues. In order to optimally place the eigenvalues of the system, the linear quadratic regulator method was used. Moreover, a Luenberger state estimator was used to estimate the state variables. Although the performance of such damping scheme is good, it relies heavily on the level of accuracy of the model used in the state estimator. Hence, in absence of an accurate system model the robustness of the system with such damping approach is lost. An improvement to this approach that ensures robustness was suggested for rolling mill applications in [69]. In this case, the damper design was again based on pole placement with state-feedback approach; however, the state estimator used in this case was a KF.

Another vibration damping approach based on a sliding mode control was suggested in [57]. This controller was designed to address the issue of robustness. The results presented showed that this controller provides complete robustness to grid disturbances and uncertainties in the electrical parameters of the generator. However, it failed to show how such damper performs when subjected to plant model uncertainty.

2.4. Inertial Frequency Response

A utility scale electrical power system consists of a number of large generators and a multitude of loads. In order to maintain the system frequency within limits (*e.g.*, UK: 49.5 – 50.5 Hz [70]) and ensure secure operation of the power system, the generation and demand should be balanced in real time. Nevertheless, in the event of a sudden failure of a generator or a connection of a large load, the system frequency starts dropping at a rate mainly determined by the summation of the angular momentum of all generators and the rotating loads. In order to arrest this frequency change and to bring the system back to its normal operation, the TSO[†] asks for frequency response services.

In the UK, the frequency response services are classified into continuous and occasional, as shown in Figure 2.14. The continuous service is provided by the generation plant while the occasional service can be provided by the generation plant and by load reduction from customers [72].

[†] *Transmission System Operator (TSO) - "a natural or legal person responsible for operating, ensuring the maintenance of and, if necessary, developing the transmission system in a given area and, where applicable, its interconnections with other systems, and for ensuring the long-term ability of the system to meet reasonable demands for the transmission of electricity" [71]*

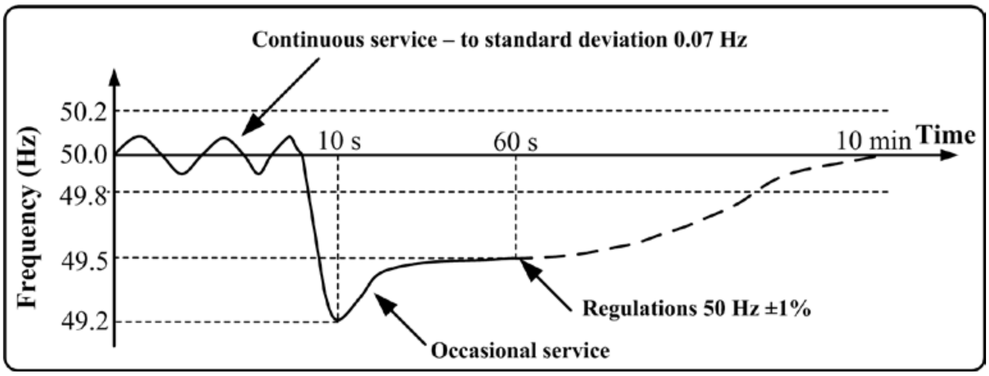

Figure 2.14: Frequency services in the UK [72]

The occasional service consists of three parts: primary, secondary and high frequency response. Primary frequency response can be defined as the minimum increase in power that can be delivered increasingly with time over a period of 10 s from a generating unit that is available within 10 and 30 s after a frequency event. Secondary response is the minimum increase in active power output which can be sustained between 30 s and 30 min after a frequency event. The high frequency response is defined as the capability of a generating unit to reduce its active power within 10 s following a frequency event [73].

With the increase in renewable power generation, part of the conventional power generation plants are being replaced by electronically controlled and/or connected power plants. It is recognised that most of the wind power plants will fall into the latter category. Wind farms equipped with VSWT does not provide the same natural response to frequency changes as the synchronous and the fixed-speed induction generators. Therefore, the addition of wind farms will result in a reduction of the overall inertia of the power system, thus leading to unacceptable excursions of the grid frequency.

Recognising the operating difficulties arising from a large penetration of wind, many power system operators are considering making synthetic inertia response mandatory. For instance, the European draft code (ENTSO-E) requires an inertia response from a plant above an agreed size. It specifies that [71],

> *"The relevant TSO shall have the right, determined in co-operation with other TSOs in the relevant synchronous area, to require each Power Park*

> *Module*[‡]*, which does not inherently have a capability to supply additional active power to the network by its inertia and which is greater than a MW size to be specified by the relevant TSO, to install a feature in the control system which operates the Power Park Module so as to supply additional active power to the network in order to limit the rate of change of frequency following a sudden generation loss."*

Furthermore, in the Hydro-Quebec grid codes an 'inertial response' from WTs is required to act during 'major frequency deviations' in order to help restore the system frequency [74]. To achieve this, wind power plants with rated capacity greater than 10 MW should be equipped with a frequency control system that acts during frequency events.

> *"The system must reduce large, short-duration frequency deviations at least as much as does the inertia response from a conventional synchronous generator whose inertia (H) equals 3.5s. This target performance is met, for instance, when the system varies the real power dynamically and rapidly by at least 5% for about 10s when a large, short-duration frequency deviation occurs on the power system."*

In the UK, the National Grid frequency response working group considered the inertia response capability of WTs and proposed a synthetic inertia response [75]. However, they decided not to include this requirement in the GB Grid Codes.

2.4.1. Inertial coupling capabilities of different wind turbine types

The types of WTs can be broadly classified in two categories: the fixed-speed and the variable-speed. In fixed-speed WT applications, a squirrel-cage IG is typically used whereas for VSWT applications, different generator (IG, DFIG and SG) options are possible as outlined in Section 2.1.2.

[‡] *Power Park Module (PPM) - "any unit or ensemble of units generating electricity which is not synchronously connected to the network. This includes any connection through power electronics and any ensemble of units having a single Connection Point to the network" [71]*

2.4.1.1. *Inertia coupling properties of fixed-speed wind turbines*

As in the case of a conventional SG in a generating plant, a squirrel-cage IG based WT possesses a strong coupling between the generator and the grid because the stator of the generator and the grid are directly connected. Hence, the stator field is rotating at the system frequency. The per unit difference between the synchronous speed and the rotor rotational speed is known as the slip, and is given by

$$s = \frac{\omega_{syn} - \omega_{rot}}{\omega_{syn}} \tag{2.5}$$

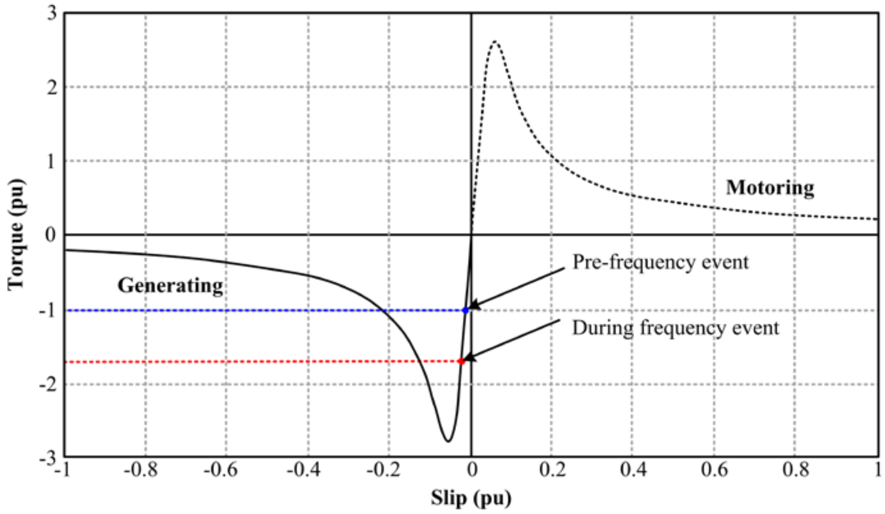

Figure 2.15: Torque *vs.* slip characteristic of an induction machine

When the system frequency (ω_{syn}) drops, the rotor speed does not change instantaneously due to high inertia of the WT rotor. However, the slip increases (negatively) and the electromagnetic torque of the generator increases proportionally for small s [23]. This is shown in Figure 2.15. Due to this increase, the output power increases and the extracted power from the turbine becomes higher than the available aerodynamic power ($P_{gen} > P_{aero}$). The deficit power is extracted from the kinetic energy of the rotor. As a consequence, the rotor slows down until a new operation point is reached ($P_{gen} = P_{aero}$).

The relation between the system frequency and the rotor speed shows that the squirrel-cage IG based WTs possess inertial coupling and give rise to an inertial response whenever there is a frequency event.

2.4.1.2. Inertia coupling properties of variable-speed wind turbines

As outlined in Section 2.1.2, VSWTs employ mostly DFIGs, IGs, and SGs. The IG and SG are connected to the grid through a FRC which decouples the generator from the system frequency. Therefore, any frequency changes will not affect the speed of the generator and hence there is no change in the power output. Therefore, no inertial coupling exists in FRC based WTs. In the case of a DFIG based WT, the stator is directly connected to the grid whereas the rotor is connected to the grid through a PRC. No inertial coupling exists in a DFIG based WT because the torque/speed control is performed by the rotor side converter, which is decoupled from the system frequency [76-79]. Even though VSWTs do not possess inertial coupling, frequency response can still be emulated by introducing a supplementary control loop.

2.4.2. Frequency support options

In the literature, there are essentially two different approaches to provide system frequency support by VSWTs, namely by providing inertia coupling or by the step response. The concept behind inertia coupling is to force the rotor speed to follow the system frequency [76, 79, 80]. The step response is a predefined increase in either the torque or power to provide an immediate short term increase in generation power [79, 81, 82].

2.4.2.1. Inertial coupling

The magnitude of the inertial frequency response of a WT is dependent on the inertia coupling characterised by the amount by which the rotational speed changes in response to a deviation in system frequency [80]. In the PRC and FRC based WTs the inertial coupling is obtained by adding a deceleration torque command to the generator controller given by [77, 79, 80, 83]

$$-\tau_{dec} = 2\mathrm{HK}_1 \frac{df}{dt} \tag{2.6}$$

where K_1 is a constant that is used to alter the effective size of the WT inertia, $^{df}\!/_{dt}$ is the rate of change of the system frequency and H[§] is the inertia constant of the WT. The block diagram showing the inertia coupling loop is shown in Figure 2.16.

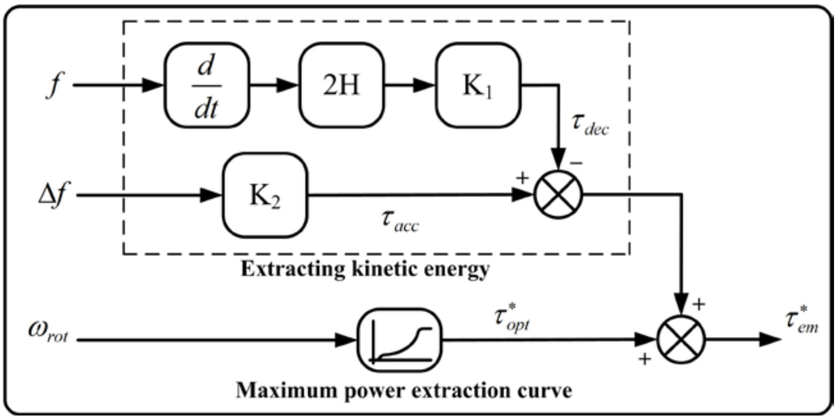

Figure 2.16: Auxiliary inertia coupling loop with τ_{acc} compensation

The operation of a VSWT during a frequency event with the auxiliary inertia coupling loop is shown in Figure 2.17. It is assumed that the wind speed is constant at 10 m/s and the WT is in steady-state at operation point A.

When there is a frequency event, the deceleration torque τ_{dec} becomes non-zero. This results in an increase in the net torque demand τ^{*}_{em} to the generator torque controller and a new operation point B is reached. At this point the power output from the generator increases proportionally to the deceleration torque. Assuming that the wind speed does not change (*i.e.,* aerodynamic torque available is constant), the extra power is extracted from the kinetic energy in the rotor. This forces the rotor to slow down and another operating point C is reached. At this speed, the maximum power extraction curve outputs a new reference torque (τ^{*}_{opt}) for the generator. The difference between the aerodynamic torque (point C) and the new generator torque reference (point D) results in an acceleration torque. This acts as a restoring torque for the speed change and the rotor accelerates. During this acceleration, the power output from the WT is less that the pre-frequency event which is undesirable during inertia response. In order to mitigate

---

[§] *Inertia constant (H) determines the time during which the WT can supply rated power by utilising the kinetic energy stored in the rotor and is defined as the ratio of total kinetic energy stored to the rated power* $\left(H = {}^{J\omega^2}\!/_{2S_{base}} \right)$ *[79].*

this effect, an additional term proportional to Δf in the inertia coupling loop was proposed in [77] and is shown in Figure 2.16. By choosing a suitable gain K_2, the start of the acceleration phase of the rotor can be delayed.

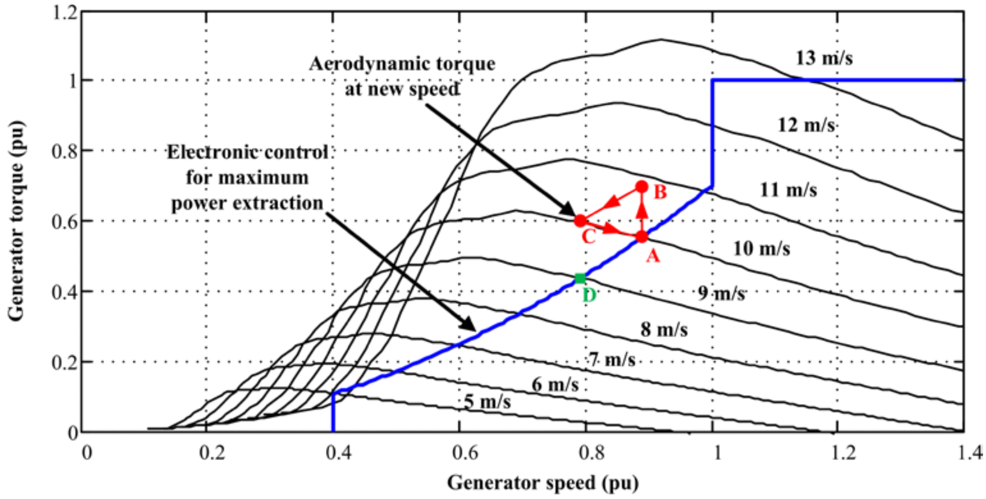

Figure 2.17: Operation of a VSWT during a frequency event with inertia coupling loop

2.4.2.2. *Step responses*

An alternative way for providing frequency support is to apply a step increase in torque [79] or in power [81, 82] to the generator controller. A block diagram showing an example of a torque step function for inertia response is shown in Figure 2.18.

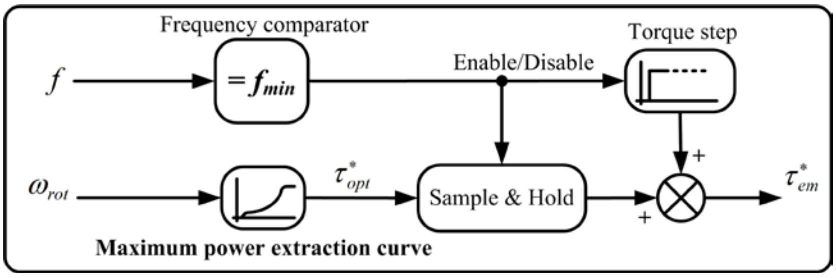

Figure 2.18: Example of inertia function using a step response in torque

The operation of a VSWT during a frequency event with a torque step response is shown in Figure 2.19. It is assumed that the wind speed is constant at 10 m/s and that the turbine is at a steady-state operation point A.

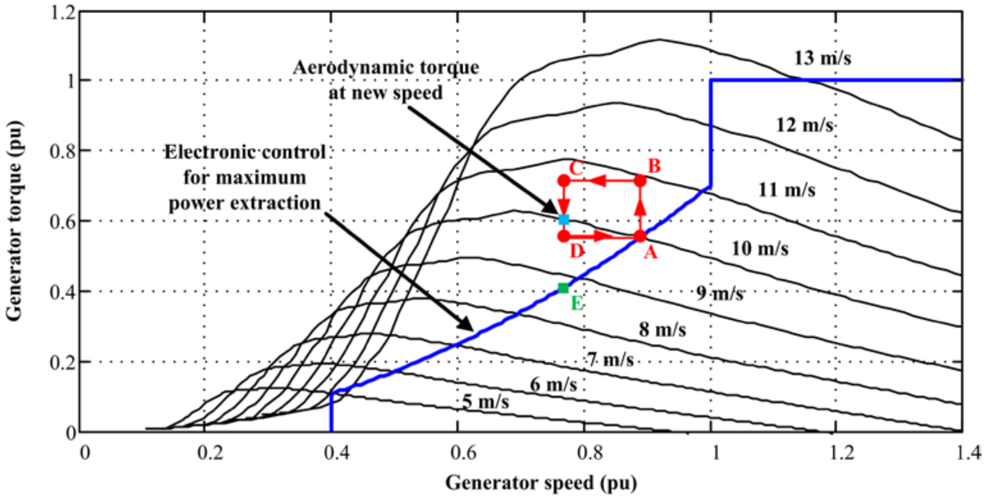

Figure 2.19: Operation of a VSWT during a frequency event with torque step loop

When the frequency comparator senses a drop in the system frequency (< f_{min}), the torque step and the sample and hold circuit are enabled simultaneously. This results in an increase in the generator reference torque τ^*_{em} by the magnitude of the torque step and causes the torque setpoint to move from A to B. The increase in the demanded generator torque causes a deceleration in the rotor from B to C as energy is extracted from the rotor. As opposed to the inertia coupling method, the optimal torque reference τ^*_{opt} does not vary as function of the rotor speed, but is held fixed by the sample and hold circuit. When the torque step goes back to zero, the resultant demanded torque to the generator is τ^*_{opt} from the sample and hold. This defines a new operation point D. At this point the imbalance between the aerodynamic torque and τ^*_{opt} is very small, hence the rotor speed can be assumed to remain constant. When the sample and hold is disabled the optimal torque τ^*_{opt} is updated from point A to point E. With the optimal torque reference updated, the aerodynamic torque is now considerably higher than τ^*_{opt} and the rotor accelerates back to operation point A.

In contrast with the inertia coupling method, the step response method is independent of the interaction with the optimal torque output from the maximum power extraction curve. This is because the step function and the sample and hold circuit set the generator torque set-point during frequency events. Moreover, the output of the step responses is not affected by any further changes in the system frequency once they are triggered. The reason for this is that the step is on for a pre-determined time [82]. Other methods for determining the ON time of the torque step are based on reaching a pre-defined point on the maximum power extraction curve [79] or a pre-determined minimum rotor speed limit [81].

A comparison of performance of the two different frequency support methods has been investigated in [79]. The power system used for the study was an islanded system consisting of an 8 MVA synchronous generator and a 1.5 MW VSWT. Results presented showed that all frequency support methods provide an improvement in the system frequency response. The rate of change of frequency and the minimum frequency reached were both improved when compared to system with no support. The torque step response helped to reduce the minimum frequency reached by 300 mHz, followed by the inertial coupling (200 mHz) and the power step (50 mHz). Although the performance of the torque step approach was the best in reducing the minimum frequency reached, it exhibited longer frequency recovery time compared to the unsupported and with inertial coupling support cases. On the other hand, the peak torque reached with the torque step was lower (120%) than with the inertial coupling (130%). The 30% increase might be problematic for the converter to supply the current especially in the regions close to rated power.

Chapter 3

Modelling and Simulation of a Variable-Speed Wind Turbine

Summary:

The objective of this chapter is to develop a dynamic mathematical model of a VSWT that is used for the design of the turbine controllers. Mathematical models of the aerodynamic conversion, drive-train, tower, pitch mechanism and permanent magnet synchronous generator are developed to enable steady-state and transient simulations. Different control strategies for controlling the voltage source converters are discussed. The controllers for the generator-side and grid-side converters are then designed using the root locus technique. Frequency response and step response analysis are carried out for each designed controller to assess its closed-loop performance. A pitch controller is also designed to limit the aerodynamic torque during operation at above rated wind speeds. A gain scheduling is derived and implemented in the pitch controller to compensate for the non-linear aerodynamic characteristics. This involves linearization of the wind turbine at an operation point. Finally a simulation with a wind step for both below and above rated wind conditions is performed to verify the wind turbine model and test the performance of the controllers designed.

3.1. Wind Turbine Modelling

A simplified FRC-PMSG based WT block diagram is shown in Figure 3.1. The model is composed of the following components: an aerodynamic model, a mechanical representation of a drive-train, tower and pitch system models, and an electrical model consisting of a PMSG, and a back-to-back VSC.

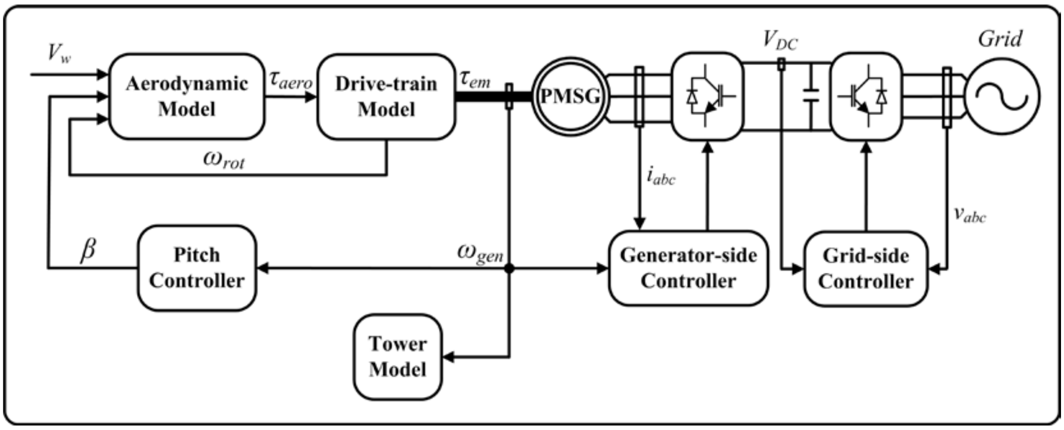

Figure 3.1: Block diagram of a FRC-PMSG based WT

3.1.1. Aerodynamic model

The aerodynamic torque τ_{aero} developed by a rotor of a WT is given by [13, 14]

$$\tau_{aero} = \frac{\rho A V_w^3 C_P(\beta, \lambda)}{2\omega_{rot}} \tag{3.1}$$

where ρ is the air density [kg/m^3], A is the area swept by the rotor [m^2], V_w is the wind speed [m/s], ω_{rot} is the rotor speed [rad/s] and C_P is the power coefficient, which is a function of the blade pitch angle β [deg] and tip speed ratio λ.

The aerodynamic model used to represent the aerodynamic system is shown in Figure 3.2. This representation is simple and does not include any dynamic inflow effects, wind shear or tower shadowing. It is used solely to convert wind energy to aerodynamic torque.

The rotor speed (derived from the measured generator speed) and the wind speed are used to calculate the tip speed ratio λ. The resulting λ and the pitch angle β are used to map the corresponding C_P value, which is then used to calculate the aerodynamic torque τ_{aero}.

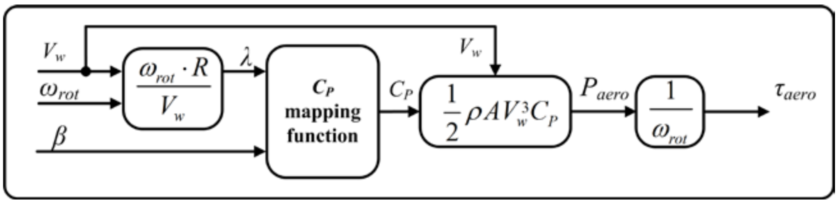

Figure 3.2: Aerodynamic system

The C_P mapping function can be obtained either by using a look-up table or an approximating function approach [84, 85]. In this work, a two dimensional look-up table obtained from a generic 2 MW WT model in Bladed® was used. A graphical representation of the look-up table is shown in Figure 3.3. The parameters of the 2 MW turbine model are given in Appendix A.1.

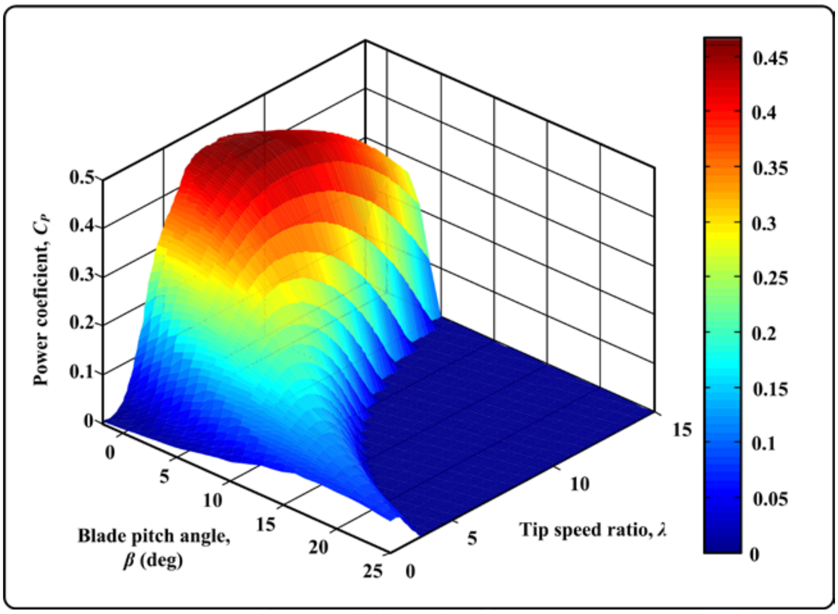

Figure 3.3: Representation of the C_P look-up table as a function of β and λ

3.1.2. Drive-train model

The aerodynamic torque is transferred to the generator shaft via the drive-train. This consists of a LSS that connects the WT rotor to the gearbox, a gearbox and a HSS that connects the gearbox to the generator. The gearbox is used to scale up the speed of the rotor to match the generator speed and to scale down the high torque present on the rotor shaft to an acceptable value for the generator.

The complexity of the mathematical model used to describe the drive-train depends on the analysis that is needed. For instance, when analysing the transient voltage stability of direct-drive WTs, a simple model (single lumped mass) can be used because the shaft system is relatively stiff [86]. On the other hand, for torsional vibrations analysis, dynamics from other parts have to be considered and more sophisticated representations are required. The common way to mathematically model the drive-train dynamics is to treat the system as a number of discrete masses (inertias) separated by springs defined by damping and stiffness coefficients [13].

In a WT drive-train, the dominant inertias are the rotor inertia on the LSS side and the generator, and the brake inertias on the HSS side [16, 87]. Hence, the drive-train can be modelled as a two-mass model, connected by a flexible shaft characterised by stiffness and damping coefficients [87, 88]. The two-mass model is illustrated in Figure 3.4.

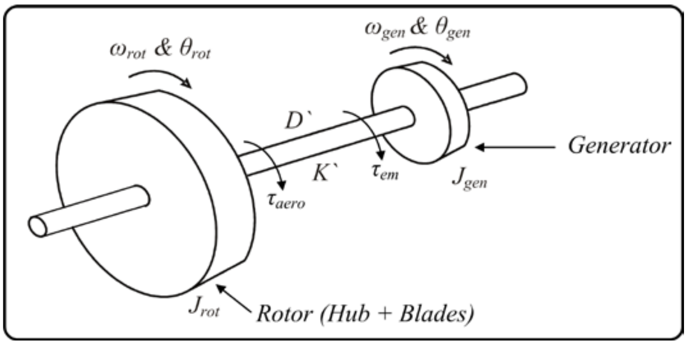

Figure 3.4: Two-mass model

The dynamics of the two-mass model referred to the LSS can be described by the following linear differential equations [51, 54, 89],

$$J_{rot}\frac{d}{dt}\omega_{rot} = \tau_{aero} - K'\left(\theta_{rot} - \frac{\theta_{gen}}{N}\right) - D'\cdot\frac{d}{dt}\left(\theta_{rot} - \frac{\theta_{gen}}{N}\right) \tag{3.2}$$

$$J_{gen}\frac{d}{dt}\frac{\omega_{gen}}{N} = -N\tau_{em} - K'\left(\frac{\theta_{gen}}{N} - \theta_{rot}\right) - D'\cdot\frac{d}{dt}\left(\frac{\theta_{gen}}{N} - \theta_{rot}\right) \tag{3.3}$$

$$\frac{d}{dt}\theta_{rot} = \omega_{rot} \qquad \frac{d}{dt}\theta_{gen} = \omega_{gen} \tag{3.4}$$

where ω_{rot} and ω_{gen} are the speeds of the rotor and generator [rad/s], θ_{rot} and θ_{gen} are the LSS and HSS angular position [rad], J_{rot} is the rotor inertia [kgm^2], J_{gen} is the generator inertia (referred to the LSS) [kgm^2] and N is the gearbox ratio. $K`$ and $D`$ are the equivalent LSS and HSS stiffness [Nm/rad] and damping [Nms/rad] coefficients referred to the LSS, given by

$$\frac{1}{K'}=\frac{1}{K_{LSS}}+\frac{1}{K_{HSS}\cdot N^2} \tag{3.5}$$

$$\frac{1}{D'}=\frac{1}{D_{LSS}}+\frac{1}{D_{HSS}\cdot N^2} \tag{3.6}$$

The natural frequency (drive-train torsional mode) of the two-mass model is given by

$$f_n=\frac{1}{2\pi}\sqrt{K'\left(\frac{1}{J_{rot}}+\frac{1}{J_{gen}}\right)} \tag{3.7}$$

The model was implemented in Simulink® as a state-space model given by

$$\begin{bmatrix}\dot{\omega}_{rot}\\ \left(\dot{\theta}_{rot}-\frac{\dot{\theta}_{gen}}{N}\right)\\ \dot{\omega}_{gen}\end{bmatrix}=\begin{bmatrix}-\frac{D'}{J_{rot}} & -\frac{K'}{J_{rot}} & \frac{D'}{NJ_{rot}}\\ 1 & 0 & -\frac{1}{N}\\ \frac{ND'}{J_{gen}} & \frac{NK'}{J_{gen}} & -\frac{D'}{J_{gen}}\end{bmatrix}\begin{bmatrix}\omega_{rot}\\ \left(\theta_{rot}-\frac{\theta_{gen}}{N}\right)\\ \omega_{gen}\end{bmatrix}+\begin{bmatrix}-\frac{1}{J_{rot}} & 0\\ 0 & 0\\ 0 & \frac{N^2}{J_{gen}}\end{bmatrix}\begin{bmatrix}\tau_{aero}\\ \tau_{em}\end{bmatrix}$$

$$y=\begin{bmatrix}0 & 0 & 1\end{bmatrix}\begin{bmatrix}\omega_{rot}\\ \left(\theta_{rot}-\frac{\theta_{gen}}{N}\right)\\ \omega_{gen}\end{bmatrix} \tag{3.8}$$

All drive-train parameters are included in Appendix A.1.

3.1.3. Tower model

A simple tower model that considers only the side-side bending mode was derived to observe the nacelle displacements during operation of the WT. The tower was modelled as a mass-less cantilever beam with a mass representing the rotor and the nacelle attached to its free end. This was represented with a mass-spring-damper system modelled by a 2nd order differential equation given by [13, 90]

$$m_{eff}\ddot{x}+D_t\dot{x}+K_tx=f(t) \tag{3.9}$$

where x is the top tower displacement [m], $\dot{x}$ is the velocity [m/s], $\ddot{x}$ is the acceleration [m/s^2], K_t is the stiffness coefficient [N/m], D_t is the damping coefficient

[Ns/m], m_{eff} is the effective mass at the tower top [kg] and f is an external forcing function [Nm].

In order to get the natural frequency of this simplified tower model close to that obtained from the detailed model in Bladed® (0.261 Hz), a refinement was made. An additional 23% of the tower mass was added to the top tower mass (nacelle mass including the rotor) as an adjustment to compensate for the model simplification [46, 47]. The natural frequency obtained with this adjustment was 0.262 Hz.

The tower model was expressed in the state-space general form and is given by

$$\begin{aligned} \begin{bmatrix} \dot{x}_1 \\ \dot{x}_2 \end{bmatrix} &= \begin{bmatrix} 0 & 1 \\ \dfrac{-K_t}{m_{eff}} & \dfrac{-D_t}{m_{eff}} \end{bmatrix} \begin{bmatrix} x_1 \\ x_2 \end{bmatrix} + \begin{bmatrix} 0 \\ \dfrac{1}{m_{eff}} \end{bmatrix} f \\ y &= \begin{bmatrix} 1 & 0 \end{bmatrix} \begin{bmatrix} x_1 \\ x_2 \end{bmatrix} \end{aligned} \tag{3.10}$$

where x_1 is the displacement at the tower top [m], $\dot{x}_1$ is the velocity [m/s] and $\dot{x}_2$ is the acceleration [m/s^2]. All tower parameters are given in Appendix A.1.

In order to observe how different rotor speeds affect the tower side-side movement, an external force (f) that has its frequency dependent on the rotor speed was derived. A non-homogenous rotor mass (mass imbalance in the rotor) was assumed. The mass imbalance was modelled as a mass m_{imb} located at radius r from the axis of rotation at angle θ_m with respect to blade A, as shown in Figure 3.5 [91].

The forces generated by the mass imbalance are gravitational (F_g) and centrifugal (F_c) forces. The centrifugal force produces a moment in the rotor plane that can drive the tower into resonance if its frequency matches the tower side-side mode.

The angular acceleration of the rotor is given by

$$\alpha(t) = \frac{d}{dt}\omega_{rot} = \frac{d^2\theta}{dt^2} \tag{3.11}$$

where ω_{rot} is the angular velocity [rad/s] and θ is the angular position of the rotor [rad]. The centripetal (radial) acceleration is given by

$$\alpha_{cen} = \omega_{rot}^2 r \tag{3.12}$$

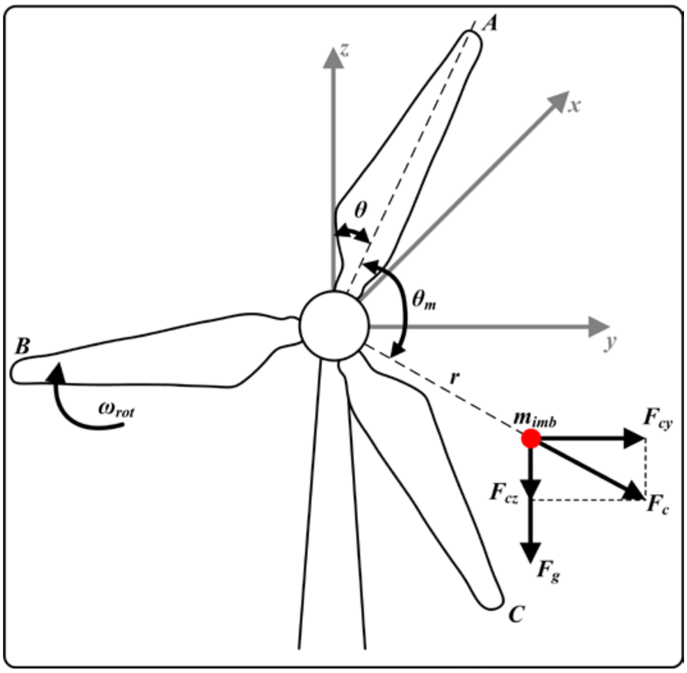

Figure 3.5: Rotor mass imbalance model

This centrifugal force is then given by

$$F_c = m_{imb}\alpha_{cen} = m_{imb}\omega_{rot}^2 r \tag{3.13}$$

Solving for the horizontal component of F_c yields

$$F_{cy} = F_c \sin(\omega_{rot} t + \theta + \theta_m) \tag{3.14}$$

which is the force responsible for the moment about the x-axis, given by

$$M_{xy} = F_{cy} H \tag{3.15}$$

where H is the height of the tower.

It can be noted from equation (3.14) that the horizontal component of the centrifugal force F_{cy} has a frequency dependent on the rotor speed. This was used as an external force acting on the tower to couple the rotor rotational speed with the side-side tower mode.

3.1.4. Pitch system model

A simple model for the pitch system is shown in Figure 3.6 and consists of an actuator model, modelled by a 1st order lag, a rate limiter acting on the demanded pitch angle and an angle limiter to set the minimum and maximum pitch angles [92]. The data of the pitch system is included in Appendix A.1.

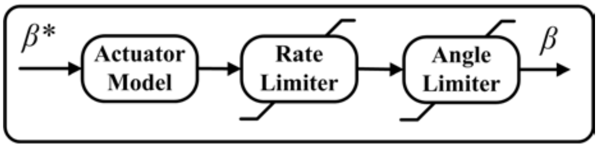

Figure 3.6: Pitch system model

The aim of the pitch system is to limit the aerodynamic torque not to exceed the maximum design ratings of the turbine when operating at above rated wind speeds. A pitch controller drives the pitch system to alter the blade pitch angle until the aerodynamic torque balances out the generator opposing torque. This ensures that the rotor speed of the turbine is kept constant at above rated wind speed [13]. At below rated wind speed the pitch angle is set to fine pitch to extract the maximum power available from the wind.

3.1.5. Generator model

The derivation of a PMSG model is included in Appendix B.1. In deriving this it was assumed that the stator windings are balanced with sinusoidal distributed magneto-motive force, saturation and parameters changes are neglected and no saliency is present. The equations for the generator in the *dq* frame are given by [93]

$$v_d = i_d R_s + \frac{d}{dt} i_d L_d - \omega_r L_q i_q \tag{3.16}$$

$$v_q = i_q R_s + \frac{d}{dt} i_q L_q + \omega_r L_d i_d + \omega_r \lambda_m \tag{3.17}$$

where ω_r is the electrical rotor speed [rad/s], L_d and L_q are the equivalent self-inductances of the stator in the *dq* frame [H], v_d and v_q are the equivalent stator voltages in the *dq* frame [V], λ_m is the flux linkage of the permanent magnet [Vs], and i_d and i_q are the equivalent stator currents in the *dq* frame [A]. It is worth noting that the swing equation of the generator has been included in the drive-train model equations (3.2) − (3.4).

The active and reactive powers in the *dq* frame assuming a balanced system (no zero sequence current) are given by

$$P = \frac{3}{2}\left(v_q i_q + v_d i_d\right) \tag{3.18}$$

$$Q = \frac{3}{2}\left(v_q i_d - v_d i_q\right) \tag{3.19}$$

and the electromagnetic torque of the machine assuming no saliency is given by

$$\tau_{em} = {}^{3}\!/_{2}\, n_{pp} \lambda_m i_q \tag{3.20}$$

where n_{pp} is the number of pair of poles.

The VSC, DC link capacitor and the grid were modelled using standard blocks from the SimPowerSystems library. The devices in the VSC were assumed ideal (*i.e.,* no on resistance and negligible turn on/off times).

All generator and VSC parameters are given in Appendix A.1.

3.2. Wind Turbine Controllers

The main controllers in a WT are the converter and the pitch controller. In this work a back-to-back VSC equipped with insulated-gate bipolar transistors (IGBTs) was used. Hence, the converter controller was split into two: one for the grid-side converter and the other for the generator-side converter.

3.2.1. Grid-side converter control

The main objectives of the grid-side converter are to transfer the power generated from the turbine to the utility grid and to control the power factor. There are two possible converter control strategies to accomplish this task: the load angle and magnitude control, and the vector control.

3.2.1.1. Load angle and magnitude control

The load angle and magnitude control strategy makes use of the steady-state power flow equations to control the supply of active and reactive power into the grid. The active and reactive power flow equations for this strategy are given by [23]

$$P_{grid} = \frac{V_{VSC} V_{grid}}{X_{grid}} \sin\delta \tag{3.21}$$

$$Q_{grid} = \frac{V_{VSC}^2}{X_{grid}} - \frac{V_{VSC} V_{grid}}{X_{grid}} \cos\delta \tag{3.22}$$

where P_{grid} is the active power flow to grid [W], Q_{grid} is the reactive power flow to grid [var], V_{VSC} is the voltage magnitude at the VSC terminals [V], V_{grid} is the magnitude of the grid voltage [V], X_{grid} is the total reactance between the converter and the grid [Ω] and δ is the phase angle between V_{VSC} and V_{grid} .

For a small phase angle δ equations (3.21) and (3.22) reduce to

$$P_{grid} = \frac{V_{VSC} V_{grid}}{X_{grid}} \delta \tag{3.23}$$

$$Q_{grid} = \frac{V_{VSC}^2}{X_{grid}} - \frac{V_{VSC} V_{grid}}{X_{grid}} = V_{VSC}\left(\frac{V_{VSC} - V_{grid}}{X_{grid}}\right) \tag{3.24}$$

The equations show that the active and reactive powers can be controlled almost independently by varying the phase angle and by the difference in voltage magnitudes. The equivalent circuit and the phasor diagram for the load angle and magnitude control scheme are shown in Figure 3.7.

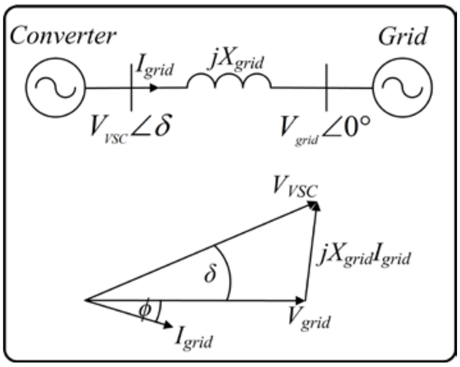

Figure 3.7: Equivalent circuit and phasor diagram of the load angle and magnitude control

3.2.1.2. Vector control

Vector or field-oriented control has been developed originally for high performance motor applications; nevertheless, the concept can be extended. In this case, this strategy is used to enable the converter to control the supply of active and reactive power to the grid independently [94]. This is achieved by orienting the reference frame with the supply voltage vector [95]. The phasor diagram for the vector control scheme is shown in Figure 3.8.

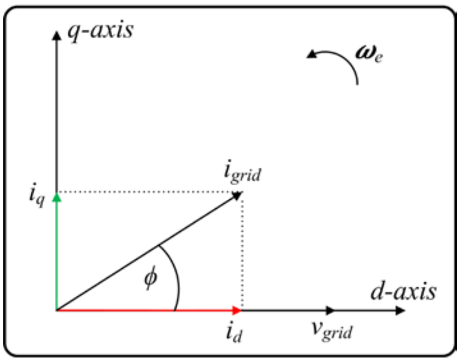

Figure 3.8: Phasor diagram of the grid-side converter

The supply voltage vector is aligned with the *d*-axis; hence, the *q*-axis component of the supply voltage is zero and the power equations (3.18) and (3.19) reduce to

$$P_{grid} = \frac{3}{2} v_d i_d \tag{3.25}$$

$$Q_{grid} = -\frac{3}{2} v_d i_q \tag{3.26}$$

These equations show that the active and reactive power can be controlled independently by controlling the *d* and *q*-axis currents, respectively.

Vector control was adopted for the grid-side converter, where the *d*-axis current was used to control the DC link voltage and thus the active power flow into the grid, and the *q*-axis current was used to control the reactive power flow. The derivation of the control loop is covered in detail in Appendix B.2. The block diagram of the vector control scheme for the grid-side converter is shown in Figure 3.9.

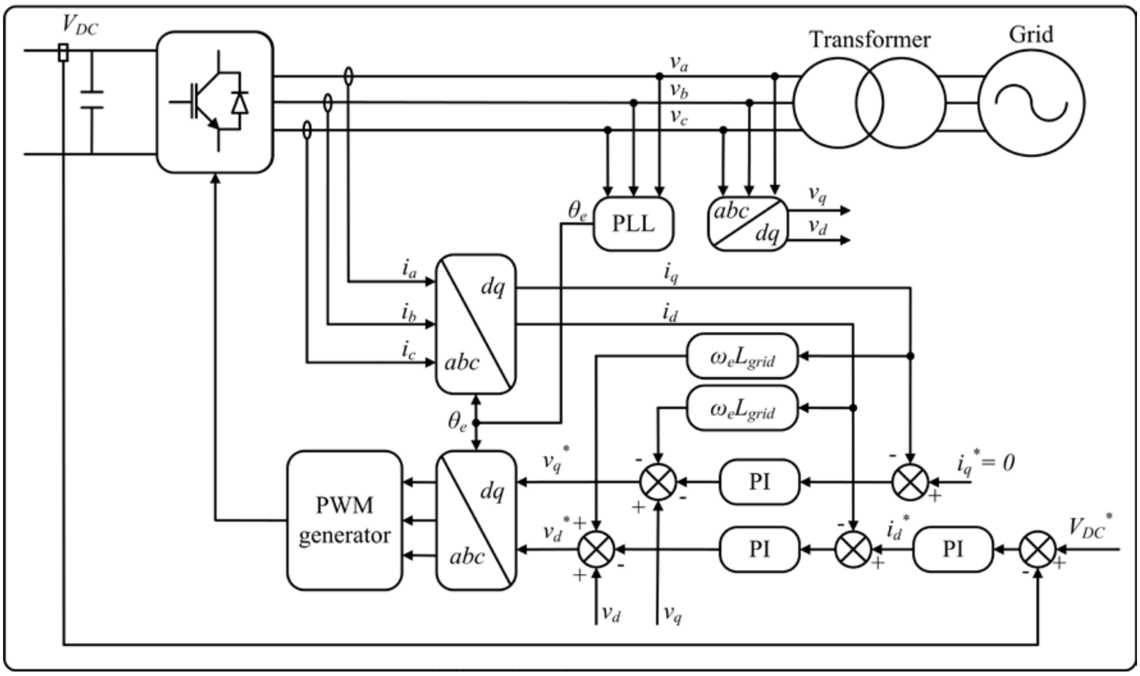

Figure 3.9: Vector control scheme for grid-side converter

The *d* and *q*-axis currents and voltages are computed from the instantaneous values (assuming a balanced system) using the transformation given by

$$\begin{bmatrix} i_d \\ i_q \end{bmatrix} = \frac{2}{3} \begin{bmatrix} \cos\theta_e & \cos\left(\theta_e - \frac{2\pi}{3}\right) & \cos\left(\theta_e + \frac{2\pi}{3}\right) \\ \sin\theta_e & \sin\left(\theta_e - \frac{2\pi}{3}\right) & \sin\left(\theta_e + \frac{2\pi}{3}\right) \end{bmatrix} \begin{bmatrix} i_a \\ i_b \\ i_c \end{bmatrix} \tag{3.27}$$

where θ_e is the electrical angle which was obtained using a phase locked loop (PLL).

The DC link voltage is measured and compared with a reference DC link voltage, V^*_{DC}. The error is then processed by a PI controller to obtain the reference *d*-axis current for the inner current loop. The *q*-axis current loop is identical to the *d*-axis loop except that the reference is set depending on the power factor required. In normal operation WTs operate at unity power factor (*i.e.*, $i_q = 0$); however, in some cases WTs are requested to supply reactive power to support the utility grid [89]. In such cases, the reference *q*-axis current is calculated using equation (3.26). The outputs of these current loops are the *d* and *q*-axis voltage references. The voltage equations (11.19) and (11.20) in Appendix B.2 show that the *d* and *q*-axis equations are coupled due to cross-coupling terms – $\omega_e L_{grid} i_q$ and $\omega_e L_{grid} i_d$ respectively. These terms were subtracted from their respective voltage reference in order to have independent control of the active and reactive power.

Furthermore, voltage feed-forward terms (v_d, v_q) were added to improve the system response. The resulting *d* and *q*-axis voltages are then transformed back to instantaneous grid voltage values which are used to generate the PWM signals for the converter.

3.2.1.3. Controller design

The tuning of all WT controllers was performed using the root locus technique. The percentage overshoot and the closed-loop bandwidth were used as design criteria for each controller. Then the SISO tool in MATLAB® was used to manually tune the controllers.

Current loop

The block diagram of the inner current control loop (*d*-axis) of the grid-side converter is illustrated in Figure 3.10. The block diagram and the transfer functions are also applicable to the *q*-axis current loop.

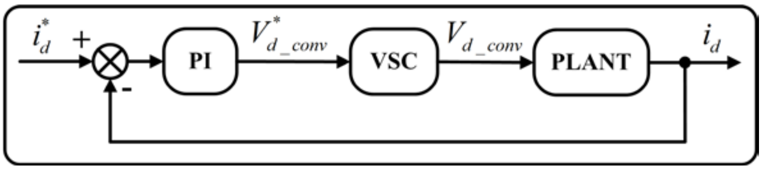

Figure 3.10: Block diagram of the *d*-axis current loop

The transfer functions for the current loop are given by

$$G_{PI}(s) = K_p + \frac{K_i}{s} \tag{3.28}$$

$$G_{VSC}(s) = \frac{V_{d\_conv}}{V_{d\_conv}^*} = \frac{1}{1 + s\,{}^{T_s}\!/_{2}} \tag{3.29}$$

$$G_{plant}(s) = \frac{i_d(s)}{v_{d\_conv}^*(s)} = \frac{1}{R_{grid} + sL_{grid}} \tag{3.30}$$

where K_p is the proportional gain, K_i is the integral gain and T_s is the sampling delay of the PWM generator [s]. The derivations of the transfer functions are included in Appendix B.3 and the current loop parameters are listed in Appendix A.1.

The design criteria for the current loop were to limit the percentage overshoot to approximately 20% and to have a bandwidth sufficiently high for achieving decoupling with the outer voltage loop. Hence, the bandwidth was set to 200 Hz. A root locus and a Bode plot of the current loop are illustrated in Figure 3.11.

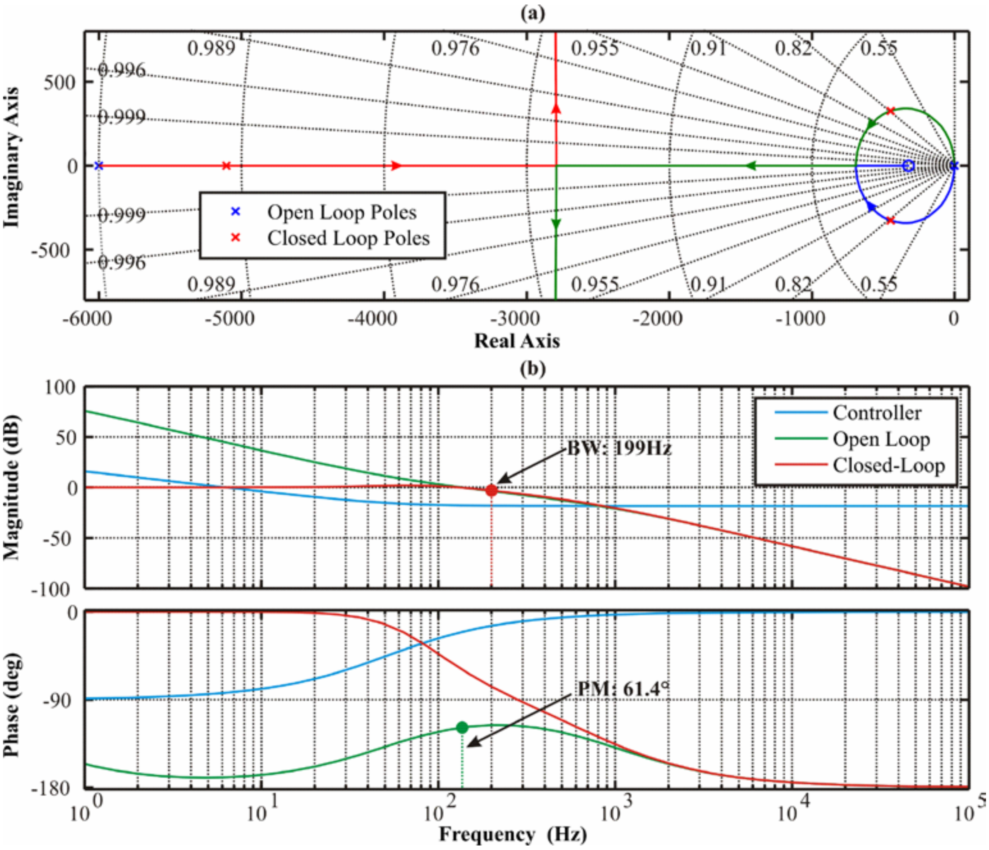

Figure 3.11: Grid-side current loop (a) Root Locus (b) Bode plot

The root locus in Figure 3.11(a) shows the open and the closed-loop poles of the system. The location of the closed-loop poles suggests that the system is 2nd order dominant. The damping ratio achieved with this design is 0.81, which gives an under-damped response. Moreover, from the Bode plot of Figure 3.11(b) it can be deduced that the system has good stability margins (GM = ∞, PM = 61.4°) and a bandwidth of 199 Hz.

In order to observe the behaviour of the system in the time-domain, a step response of the system was plotted and is shown in Figure 3.12. It can be noted that the percentage overshoot obtained was 20.7%. Therefore, this controller satisfies all the design criteria. The PI controller parameters are given in Appendix A.2, Table A-2.

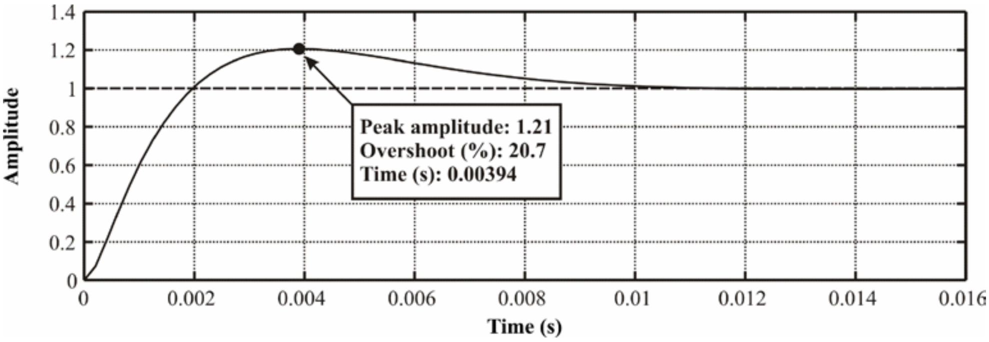

Figure 3.12: Grid-side current loop step response

Voltage loop

In order to have the outer voltage loop performance unaffected by the inner current loop, it was ensured that enough bandwidth separation exists between the two loops. In [96] it is suggested that adequate decoupling between the loops is achieved if the inner loop bandwidth is 5 to 20 times higher than that of the outer loop. If this is satisfied, the inner current loop can be neglected when tuning the voltage loop. The block diagram of the voltage loop is illustrated in Figure 3.13.

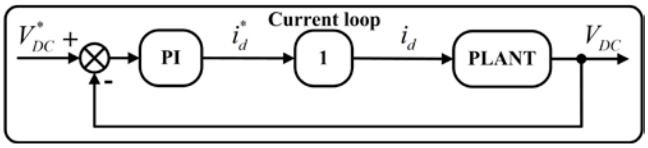

Figure 3.13: Block diagram of the voltage loop

The plant transfer function relating the DC voltage and the *d*-axis current was derived using equations (11.25) and (11.26) in Appendix B.2. Considering the load current (I_{load}) as a disturbance, then the plant transfer function in the Laplace domain is given by [94]

$$\frac{V_{DC}(s)}{i_d(s)} = \frac{3}{4}\frac{M_a}{sC} \tag{3.31}$$

where V_{DC} is the DC link voltage, i_d is the *d*-axis current, M_a is the modulation index of the converter and C is the DC link capacitor [mF].

The design criteria for the voltage controller were to limit the percentage overshoot to 20% and to have a closed-loop bandwidth 15 times lower than the current loop bandwidth. The PI controller parameters to meet these criteria are given in Appendix A.1, Table A-2.

The Bode plot of the voltage loop is shown in Figure 3.14, were it can be noted that the system exhibited good stability margins (GM = ∞, PM = 69.9°) and a closed-loop bandwidth of 13.88 Hz. Furthermore, the step response is shown in Figure 3.15, were it can be observed that the percentage overshoot achieved was 18%.

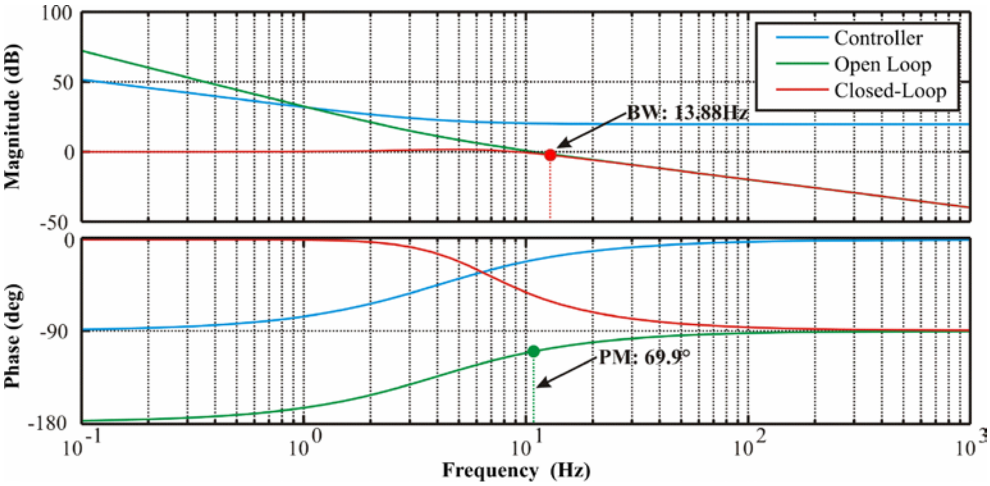

Figure 3.14: Grid-side voltage loop Bode plot

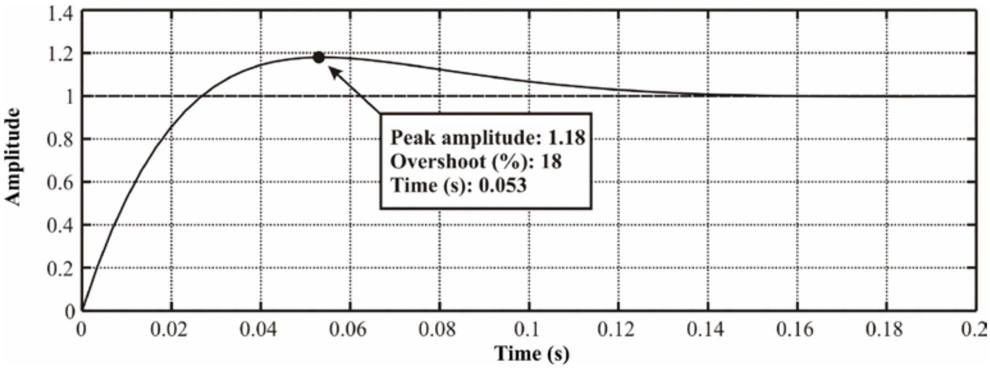

Figure 3.15: Grid-side voltage loop step response

3.2.2. Generator-side converter control

The conventional control scheme used in machines is vector control [97]. This scheme is used to decompose the stator current into a torque and a magnetic field generating components. There are different strategies that can be implemented with vector control, such as the unity power factor and the maximum torque per ampere control.

3.2.2.1. Unity power factor control

The main advantage of this strategy is that the generator operates at unity power factor and hence utilises the full VA rating of the converter for active power transfer [93]. The *q*-axis current is used to control the electromagnetic torque of the generator, whereas the *d*-axis current is used to compensate the reactive power demand of the generator.

Assuming that the generator is in steady-state and neglecting the resistive elements, the generator voltage equations (3.16) and (3.17) reduce to

$$\begin{aligned}
&v_d = -\omega_r L_q i_q \\
&v_q = \omega_r L_d i_d + \omega_r \lambda_m \\
&v_s = v_d + jv_q = -\omega_r L_q i_q + j\left(\omega_r L_d i_d + \omega_r \lambda_m\right) \ \textit{but for generating } i_d \textit{ and } i_q < 0 \\
&\therefore v_s = \omega_r L_q i_q + j\left(-\omega_r L_d i_d + \omega_r \lambda_m\right)
\end{aligned} \tag{3.32}$$

The phasor diagram for this control strategy is shown in Figure 3.16.

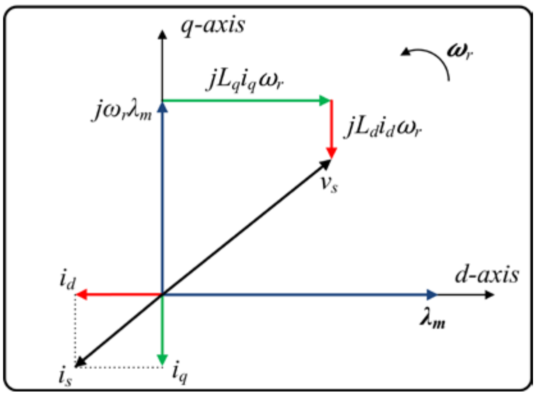

Figure 3.16: Phasor diagram for unity power factor control in *dq* frame

The drawback of this control strategy is that it is not optimised for torque production (not all the stator current is used for the generation of torque). Therefore, for the same generator torque, the copper losses are larger and the efficiency is less compared with the maximum torque per ampere control strategy [93].

3.2.2.2. Maximum torque per ampere control

The aim of this strategy is to control the stator current for torque generation only [92, 93]. Assuming that the machine has no saliency, then the torque of the PMSG is determined by the *q*-axis current only as given in equation (3.20). By making the *q*-axis current equal to the full stator current and the *d*-axis current to zero ($i_q = i_s$, $i_d = 0$), the generator stator current is entirely used for torque production.

Assuming that the generator is in steady-state and neglecting the resistive elements, the generator equations (3.16) and (3.17) reduce to

$$\begin{aligned} &v_s = v_d + jv_q = -\omega_r L_q i_q + j\omega_r \lambda_m \text{ ; but for generating } i_q < 0 \\ &\therefore v_s = \omega_r L_q i_q + j\omega_r \lambda_m \end{aligned} \tag{3.33}$$

The phasor diagram for this control strategy is shown in Figure 3.17. It can be noted that the reactive power demanded by the generator is not zero (*i.e.*, i_s and v_s are not in phase). Hence, the converter rating needs to be increased to cater for the increase in the apparent power ($S = P + jQ$) [92].

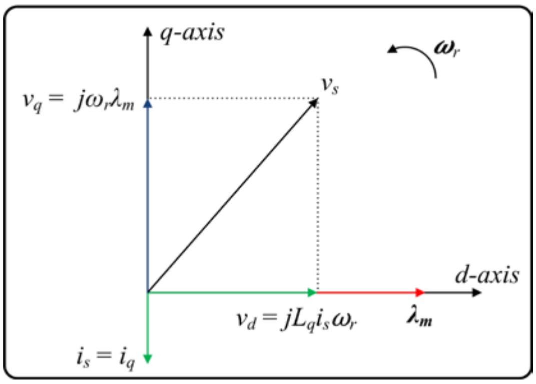

Figure 3.17: Phasor diagram for maximum torque per ampere control in *dq* frame

The maximum torque per ampere control strategy was used in this work and the block diagram of the scheme is shown in Figure 3.18.

The stator currents are first transformed into their equivalent *d* and *q*-axis currents in the rotor reference frame using the transformation given by

$$\begin{bmatrix} i_d \\ i_q \end{bmatrix} = \frac{2}{3} \begin{bmatrix} \cos\theta_r & \cos\left(\theta_r - \frac{2\pi}{3}\right) & \cos\left(\theta_r + \frac{2\pi}{3}\right) \\ \sin\theta_r & \sin\left(\theta_r - \frac{2\pi}{3}\right) & \sin\left(\theta_r + \frac{2\pi}{3}\right) \end{bmatrix} \begin{bmatrix} i_a \\ i_b \\ i_c \end{bmatrix} \tag{3.34}$$

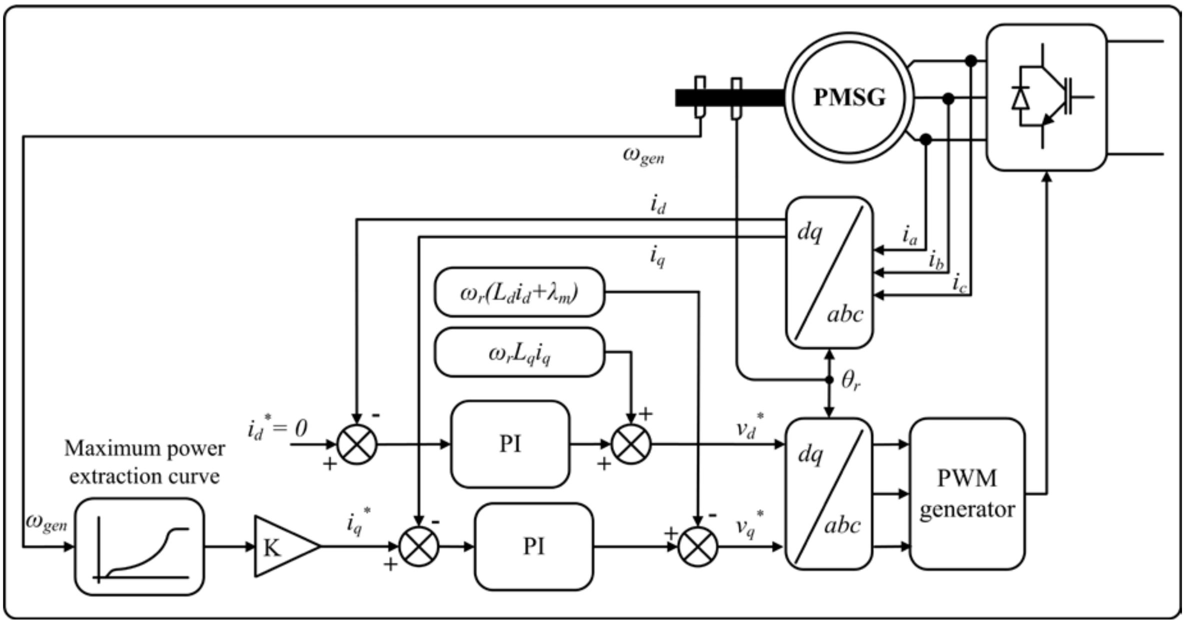

Figure 3.18: Vector control scheme for PMSG

The reference d-axis current (i_d^*) was set to zero, whereas the reference q-axis current (i_q^*) was computed using

$$i_q^* = \tau_{em}^* \frac{2}{3n_{pp} \cdot \lambda_m} \tag{3.35}$$

where τ_{em}^* is the optimal torque reference for maximum power extraction.

The optimal torque reference was obtained from a look-up table as explained in Section 3.1.1. The transformed stator currents (i_d, i_q) are then compared with the reference currents (i_d^*, i_q^*) and the errors are fed to their respective PI controller. The outputs of the PI controllers are the reference stator voltages in the *dq* frame to which cross-coupling compensation terms are added. These terms were included to ensure decoupling of the *d* and *q*-axis loops. Furthermore, the induced voltage due to the magnetic flux was also subtracted from the *q*-axis voltage reference. The resultant *d* and *q*-axis voltage references are then transformed back to the instantaneous stator voltages which are then used to generate the PWM signals for the converter.

3.2.2.3. Current controllers design

The block diagram of the current loops of the generator-side converter is identical to the inner current loop of the grid-side converter illustrated in Figure 3.10. Hence, the transfer functions are the same except for the plant transfer function, given by

$$G_{plant}(s) = \frac{i_d(s)}{v^*_{d\_conv}(s)} = \frac{1}{R_s + sL_d} \tag{3.36}$$

where R_s is the stator resistance [Ω] and L_d is the stator inductance [H]. The data for the current loop parameters is listed in Appendix A.1.

The same procedure and design criteria followed for the grid-side controller were used for the generator-side converter. However, in this case the bandwidth of the current loop was selected high enough to ensure decoupling with the mechanical system. The PI controller parameters for the generator-side converter are given in Appendix A.2, Table A-3.

The Bode plot for the system is shown in Figure 3.19. It can be observed that this controller design led to good stability margins (GM = ∞, PM = 65.2°) with a closed-loop bandwidth of 120 Hz.

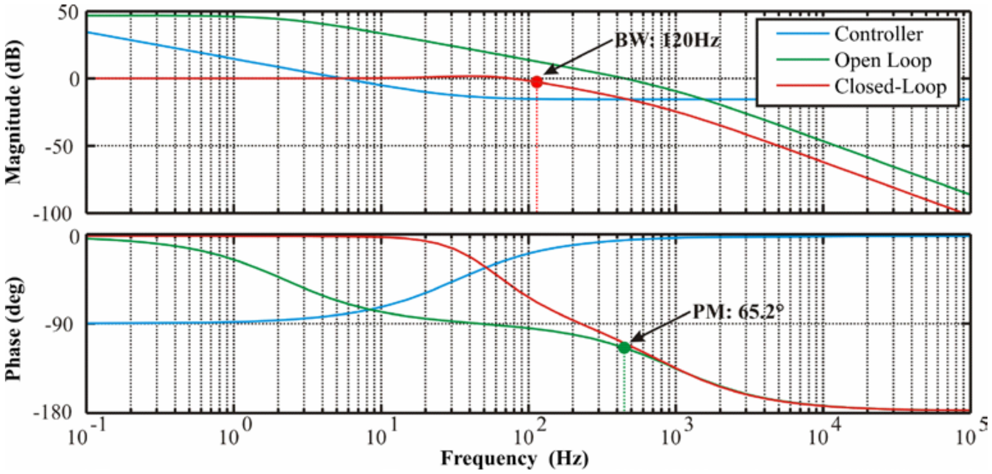

Figure 3.19: Generator-side current loop Bode plot

A step response of the system is shown in Figure 3.20, where it can be noted that the percentage overshoot obtained was 17.8%.

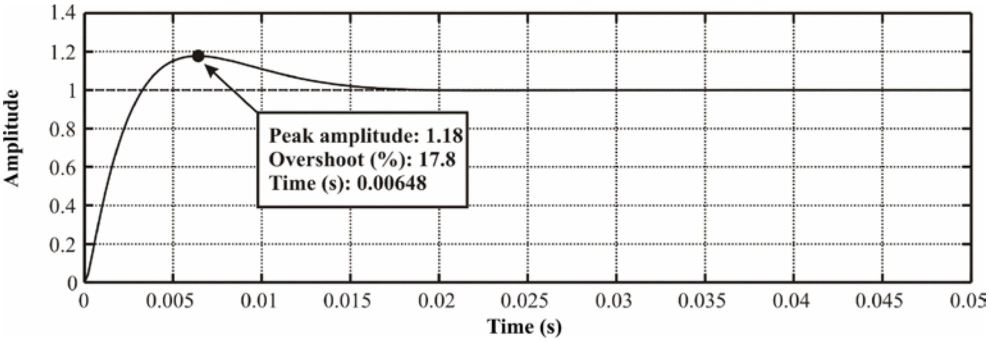

Figure 3.20: Generator-side current loop step response

3.2.3. Pitch Angle Controller Design

The block diagram of the pitch angle controller is shown in Figure 3.21. It consists of a PI controller equipped with an anti-windup circuit that generates a pitch angle reference β^* from the generator speed error. The pitch actuator follows this reference and changes the pitch angle which varies the aerodynamic torque accordingly. When the aerodynamic torque balances out the generator reaction torque, no acceleration torque is present and the generator speed is controlled.

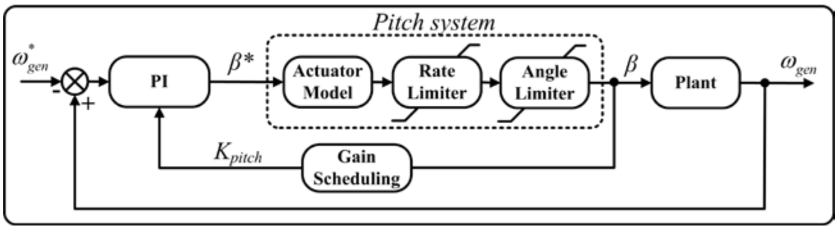

Figure 3.21: Pitch angle controller block diagram

The non-linear blocks of the rate and angle limiters and the gain scheduling were omitted for the control design. The derivation of the plant transfer function is included in Appendix C and is given by

$$\frac{\Delta\omega_{gen}(s)}{\Delta\beta(s)} = N\frac{{\partial\tau_{aero}}\big/{\partial\beta J_{tot}}}{\left(s - {\partial\tau_{aero}}\big/{\partial\omega_{rot} J_{tot}}\right)} \tag{3.37}$$

where N is the gearbox ratio, J_{tot} is the combined inertia of the rotor and generator referred to the LSS [kgm^2], ${\partial\tau_{aero}}\big/{\partial\beta}$ is partial derivative of the aerodynamic torque with respect to pitch angle [Nm/rad] and ${\partial \tau_{aero}}/{\partial \omega_{rot}}$ is the partial derivative of the aerodynamic torque with respect to the rotor speed [Nms/rad].

The actuator was modelled by a 1st order lag given by

$$G_{act}(s) = \frac{1}{1 + sT_{act}} \tag{3.38}$$

where T_{act} is the pitch actuator time constant [s].

A plot showing the variation of the aerodynamic torque as a function of the pitch angle and the wind speed (keeping the rotor speed constant) is shown in Figure 3.22. It is evident that the aerodynamic torque is highly non-linear. This implies that the partial derivatives in equation (3.37) are variable and will change depending on the operating point of the WT.

The WT was linearised at an operating point close to midway between the rated (12 m/s) and the cut-out (24 m/s) wind speeds, as indicated in Figure 3.22.

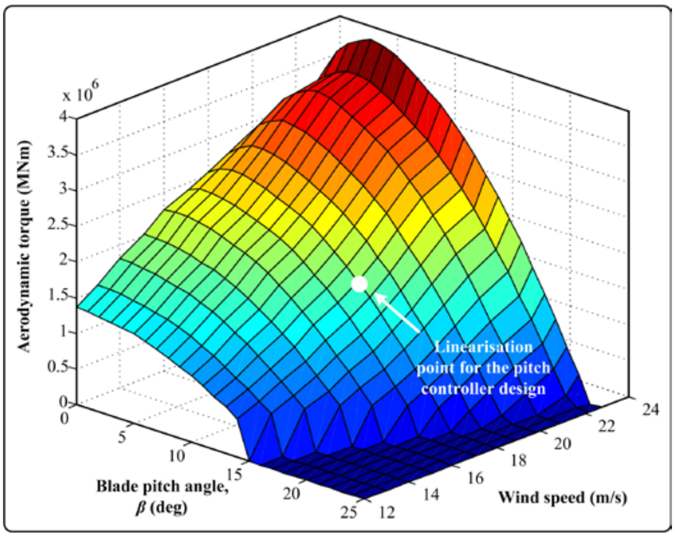

Figure 3.22: Aerodynamic torque variation with pitch angle and wind speed

The parameters at this operating point are β = 15.14°, ω_{rot} = 1.885 rad/s, V_w = 18 m/s, ${\partial \tau_{aero}}/{\partial \beta} = -1.04\times10^{7}$ Nm/rad and ${\partial \tau_{aero}}/{\partial \omega_{rot}} = -1.41\times10^{6}$ Nms/rad.

The design criteria across all the operation region of the pitch controller are the following: to limit the overshoot to around 20% to reduce excessive pitching action and to have a reasonable transient response (not exceeding the rate limiter in the pitch system). The PI controller parameters satisfying these criteria are given in Appendix A.2, Table A-4. The Bode plot for the pitch system is shown in Figure 3.23, where it can be noted that the system has good stability margins (GM = ∞, PM = 69.4°) and a bandwidth of 0.15 Hz.

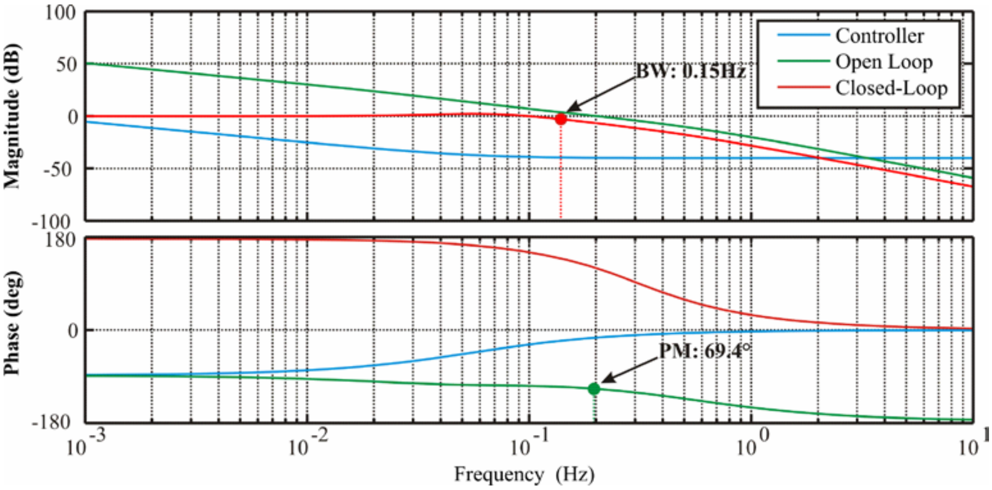

Figure 3.23: Pitch controller Bode plot

The pitch controller designed is only valid in the neighbourhood of the selected operation point. Hence, in order to ensure a good performance for all operating points above rated wind speed, the controller gains have to be continuously altered depending on the operating point. This was accomplished by using gain scheduling. A plot showing the variation of the partial derivative of τ_{aero} with respect to the pitch angle is shown in Figure 3.24.

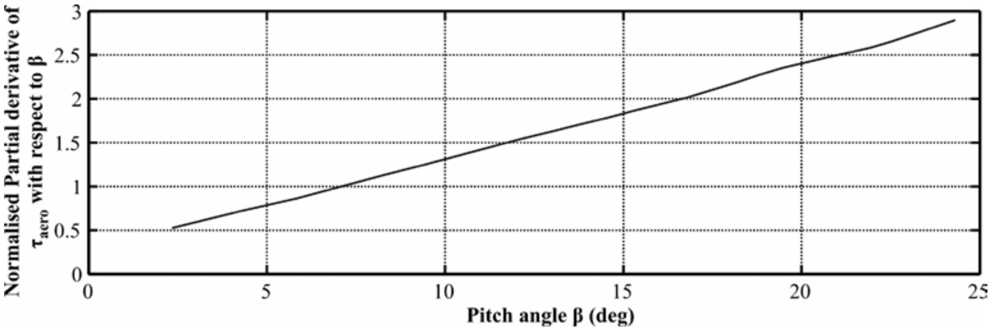

Figure 3.24: Partial derivative of the aerodynamic torque with respect to pitch angle

It can be observed that the relationship is quasi linear; hence, to compensate for such a variation, the PI controller gains were scaled linearly with the pitch angle [16]. A look-up table was constructed to scale the controller gains and is given in Appendix A.2, Table A-5. A step response for different operation points is shown in Figure 3.25.

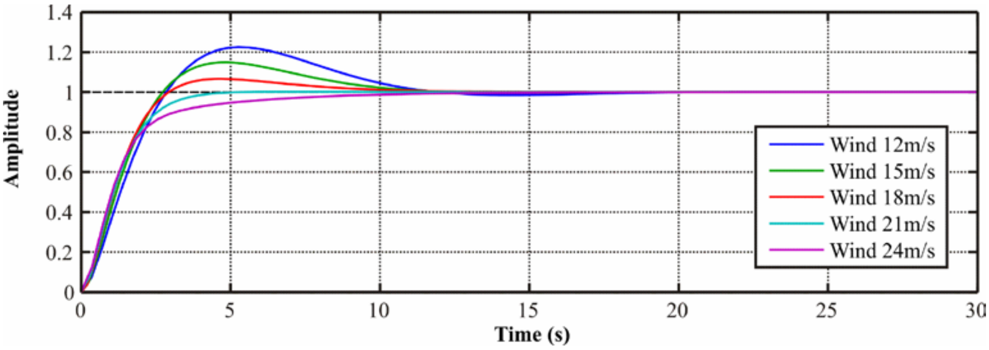

Figure 3.25: Pitch controller step response at different operating points

It can be noted that with this controller the overshoot reduces as the wind speed increases. A higher overshoot is more acceptable at low wind speeds, since the torque is less sensitive to the pitch angle. Nevertheless, high overshoot is unacceptable at high wind speeds since the torque is very sensitive to the pitch angle and might drive the system unstable.

3.3. Simulation Results

The WT model (illustrated in Figure 3.1) was implemented in Simulink® and is shown in Figure 3.26. The tower model was not relevant in this case so it was not included in the Simulink® model. A simulation with a wind step for cases below and above rated wind speeds was performed to evaluate the WT control system performance. The DC link voltage reference was set to 1400 V and the turbine was initially set to operate at unity power factor.

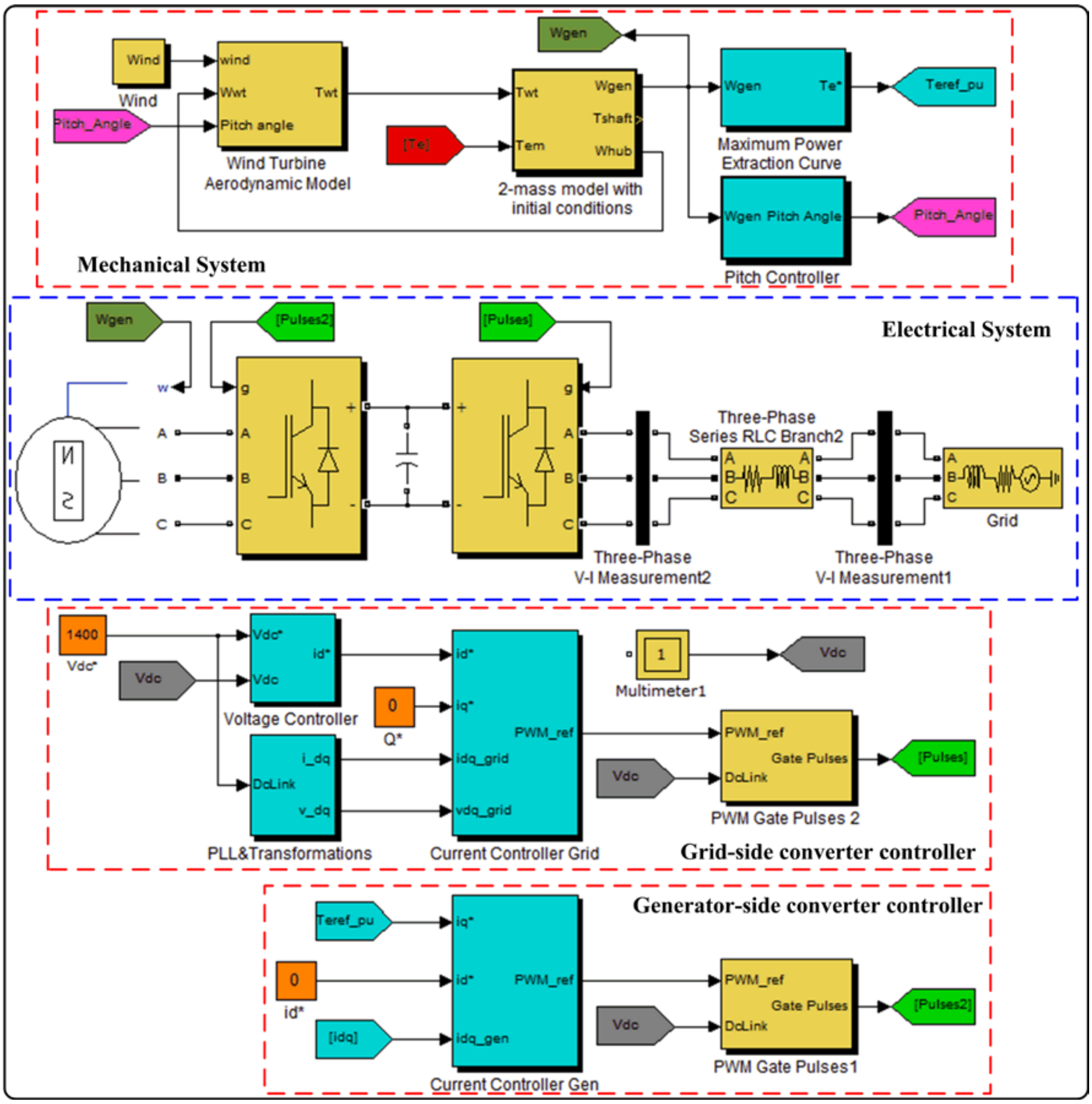

Figure 3.26: WT block diagram implemented in Simulink®

3.3.1. Below rated wind speed

The turbine was started with a wind speed ramp to soft start the turbine. The wind speed was left at a constant speed of 7 m/s to allow sufficient time for the WT to reach steady-state. At the 5 second mark a wind step from 7 to 9 m/s was applied as shown in Figure 3.27 (a).

It can be observed that when the wind step was applied to the turbine, the aerodynamic torque increased as illustrated in Figure 3.27 (b). Due to the imbalance between the aerodynamic and the generator reaction torques, the rotor started to accelerate. The increase in the rotor speed was reflected on the generator speed as illustrated by Figure

3.27 (c). The maximum power extraction function sensed the generator speed change and updated the reference torque demand to the generator. A new steady-state operating point was reached when the generator torque balances out the aerodynamic torque.

It is worth noting that throughout this simulation the pitch controller was inactive and the pitch angle was fixed at fine pitch (approx −2°) as shown in Figure 3.27 (d). The DC link voltage is shown in Figure 3.27 (e), where it can be observed that the grid-side converter controller managed to maintain the DC link voltage steady at 1400 V by exporting active power into the grid. The active and reactive powers are shown in Figure 3.27 (f). In this case there was no reactive power flowing into the grid as the WT was set to operate at unity power factor.

3.3.2. Above rated wind speed

The WT was started with a wind speed ramp until the speed reached 15 m/s. After allowing some time for the turbine to reach steady-state, a wind step from 15 m/s to 24 m/s was applied to the system as illustrated in Figure 3.28 (a). The reason for testing the WT for such a large wind step was to evaluate the performance of the pitch controller as it passes through different operating points.

When the wind step was applied to the turbine, the aerodynamic torque initially overshot as shown in Figure 3.28 (b). This led to an acceleration of the rotor and the generator as shown Figure 3.28 (c). During above rated wind speed operation, the aim of the pitch controller is to limit the aerodynamic power available from the wind and thus control the rotor and the generator speeds. Therefore, when the pitch controller sensed that the speed of the generator increased beyond its rated speed, it started to increase the pitch angle as shown in Figure 3.28 (d). As a consequence, the aerodynamic torque reduced (Figure 3.28 (b)) and a new steady-state was reached when the aerodynamic torque decreased enough to balance the generator rated torque. At this point the generator speed was brought back to its rated value. Similarly to the below rated case, no reactive power was exported to the grid as the WT was operating at unity power factor. Nevertheless, another simulation was performed to test the capability of the WT to supply reactive power to the grid. The reactive power demand was set to 0.75 Mvar and a wind step from 15 m/s to 24 m/s was applied to the system. The exported active and reactive powers are shown in Figure 3.29. It can be observed that the grid-side converter controller managed to control the amount of reactive power transferred to the grid according to the set-point chosen.

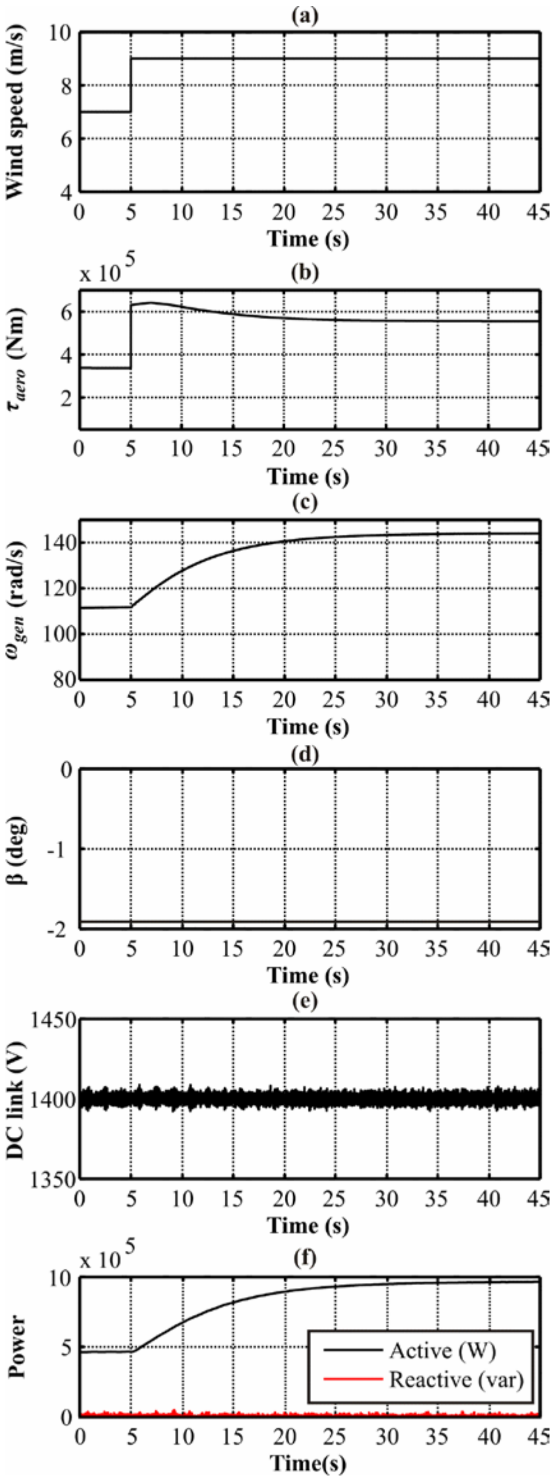

Figure 3.27: Wind step below rated

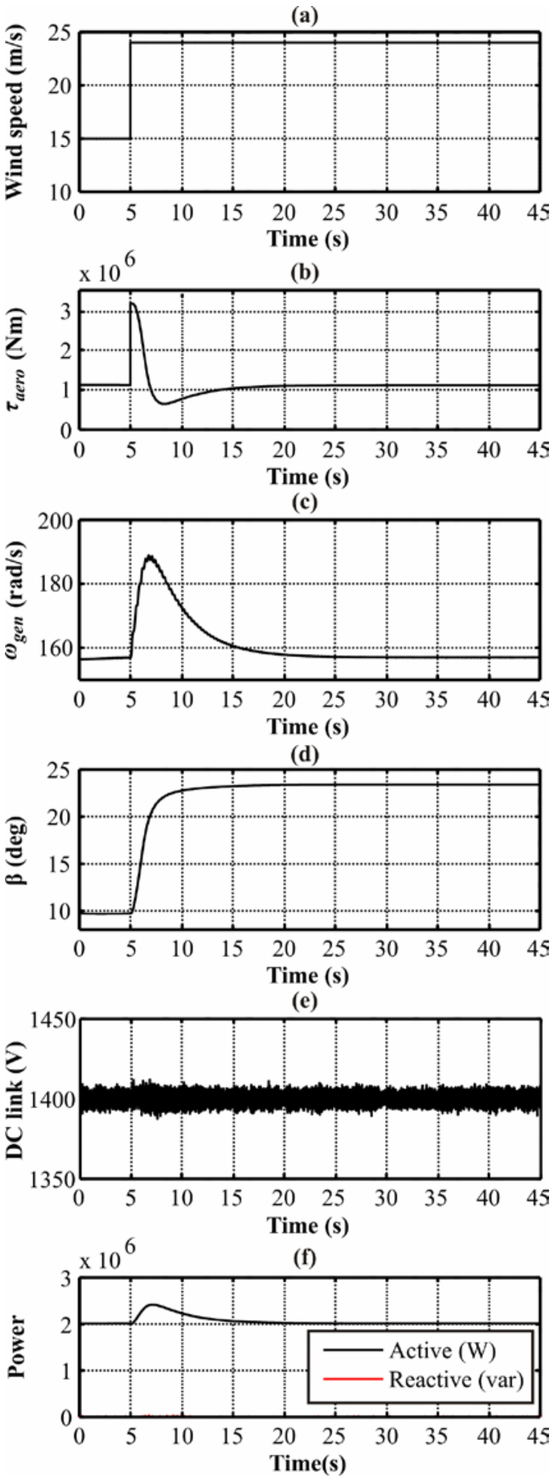

Figure 3.28: Wind step above rated

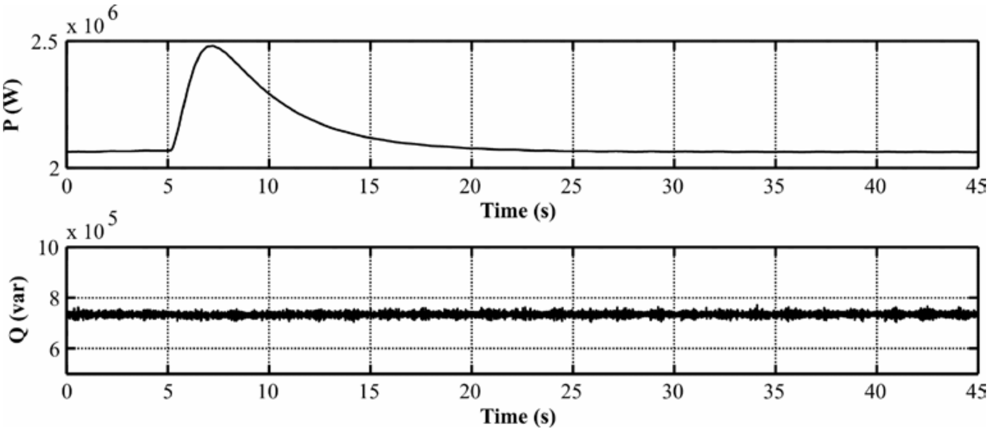

Figure 3.29: WT supplying active and reactive power

3.4. Conclusion

A simplified FRC-PMSG based VSWT model consisting of an aerodynamic, drive-train, tower, pitch and generator models was derived and implemented in Simulink®. A back-to-back VSC was used to connect the WT to the electrical grid.

The control scheme adopted for the back-to-back VSC was vector control. The unity power factor and the maximum torque per ampere control strategies were evaluated for the generator-side. In this case, the maximum torque per ampere control was adopted.

All WT controllers were designed using the root locus technique. In the case of the pitch controller design, linearization of the turbine at an operating point was necessary due to the highly non-linear dynamics. To compensate for these non-linearities, gain scheduling was applied to the pitch PI controller to ensure a satisfactory performance throughout all operating regions of the WT. Performance was assessed through Bode plots and step responses.

In order to verify the full WT model and its controllers, a simulation with a wind step for below and above rated wind speeds was performed. During below rated wind speed case, the generator-side controller managed to control the generator torque for maximum power extraction. The grid-side converter controlled the DC link voltage by exporting active power to the grid. During above rated wind speed, the generator torque was held fixed at rated torque and the speed of the generator was controlled by the pitch controller. The grid-side converter managed to control the DC link voltage effectively. A simulation to verify the capability of the WT to supply reactive power to the grid was also carried out. Results show that the turbine managed to transfer reactive power according to the desired set-point.

Results from the simulations performed confirmed that the performance of the simplified WT model was good. Hence, this turbine model can be used as the basis to design and test other auxiliary controls.

Chapter 4

Experimental Test Rig

Summary:

The objective of this chapter is to introduce the experimental test rig used for all experiments performed in this research. An overview of the hardware set-up is first given. This is followed by a discussion of the signal conditioning circuits used for the current and voltage measurements. The structure of the control system is then outlined. Finally, the hardware-in-the-loop experiment sequence is discussed.

Note:

The experimental test rig was manufactured by Cinergia based on the hardware design specifications supplied by us. The hardware commissioned was a manually operated test rig. The initialisation routine of the rig and the vector control algorithms for the back-to-back VSC were provided by Cinergia.

A dSPACE platform was subsequently interfaced to the test rig for conducting hardware-in-the-loop experiments, real-time plotting of variables and logging of measurements. Several noise problems were encountered during such interfacing. These were solved by using appropriate shielding and re-routing of some cables. Moreover, the PI parameters of the vector control algorithm had to be re-tuned to improve the system response.

4.1. Introduction

In this research study, a 1.2 kW experimental test rig that emulates a VSWT operation was used to validate the simulation results shown in Chapters 5−7. The block diagram of the test rig is shown in Figure 4.1.

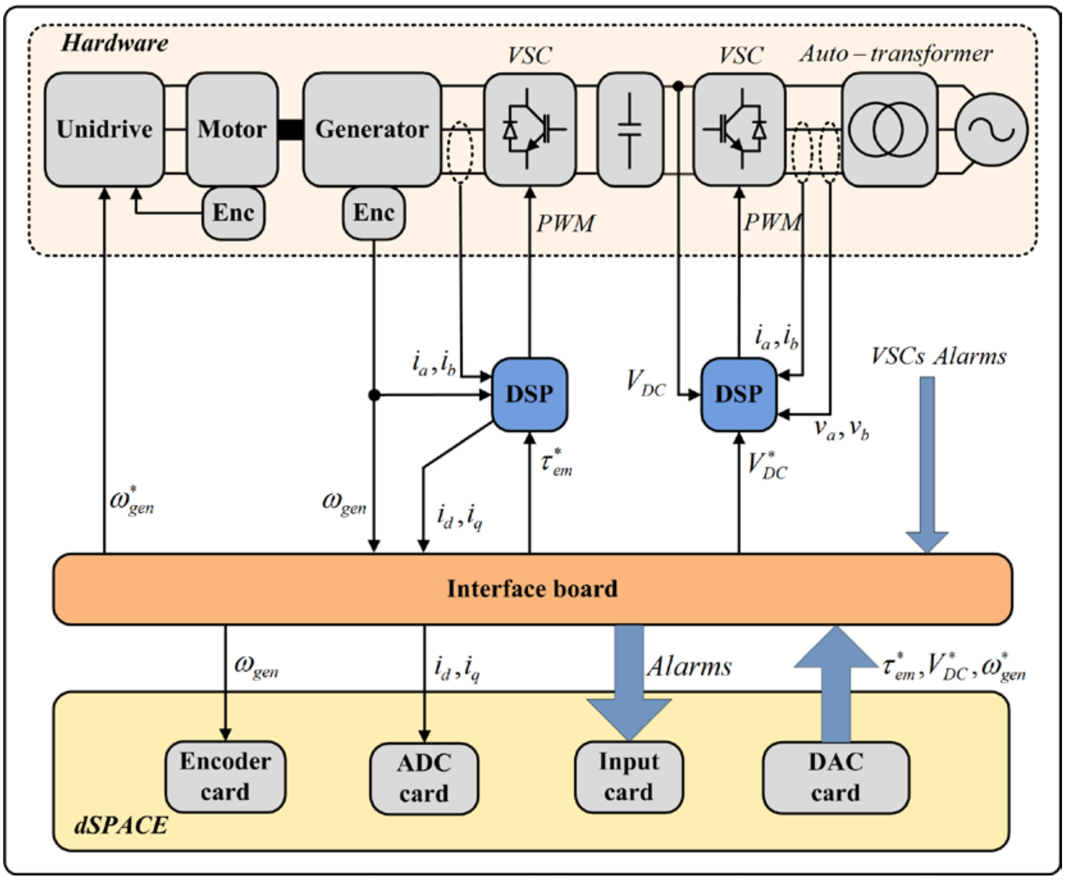

Figure 4.1: Experimental test rig block diagram

The test rig can be broadly divided into mechanical, electrical and control parts. The mechanical part consists of two AC brushless servo machines that are mechanically coupled by a flexible coupling. In this work, one machine was used as a motor and the other as a generator. The motor was controlled by an industrial variable-speed drive (Unidrive) and was configured in a closed-loop vector control to follow a set reference speed. The speed of the motor was used to emulate the speed of the HSS which drives the generator. Both machines have an integrated high resolution incremental encoder which provided the speed feedback for the control system. The output of the generator was connected to the grid through a FRC and an auto-transformer. In practice, the transformer is used to step up the output voltage of the WT to match the grid voltage;

however, in this case it was used to step-down the grid voltages for safety reasons. This enabled operation at a lower DC link voltage.

All the hardware components except for the motor-generator set were enclosed in a cabinet for safety reasons, as illustrated in Figure 4.2. The hardware data is included in Appendix E.1 and the cabinet electrical schematics are included in Appendix E.2.

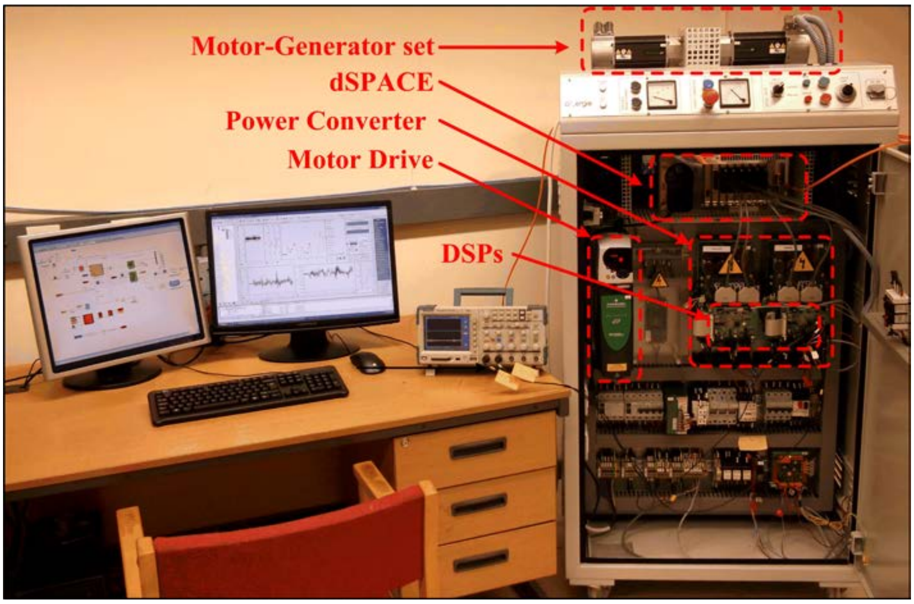

Figure 4.2: Experimental test rig

4.1.1. Power converter

The power converter consists of two identical VSCs arranged in a back-to-back configuration connected by a DC link capacitor bank. Each VSC unit comprises a power board, a driver board and a DSP controller. The schematics are included in Appendix E.3.

4.1.1.1. Power board

The power board consists of a Semikron module (SKiiP 23NAB12T4V1) mounted on a heatsink with forced ventilation, a pre-charge circuit and measurement circuits. The pre-charge circuit was used to charge the DC link capacitor bank from the grid through a resistor prior to switching on the converters. This prevented excessive charging current from flowing through the converter and cause damage. The pre-charge circuit consists of a contactor (LS_1) that shorts out a resistor (R_4) after the capacitor bank has charged up to a safe value (in this case 50 V). The pre-charge was performed from the grid-side converter using AC voltage which was rectified to DC through the freewheeling diodes of the converter. The capacitor bank of the generator-side converter was charged through two resistors (R_5 and R_6) from the rectified DC supply. These resistors are bypassed by a contactor (LS_2) once the pre-charge phase has finished. The pre-charge circuit is shown in the Power board –VSC schematic (sheet 2 of 4) in Appendix E.3 and is highlighted in grey.

The measurements carried out were used primarily for control and data logging purposes; however, in this case they were also used to provide protection for the VSCs. The measurements consisted of AC line to line voltages, phase currents, DC link voltage and the temperatures of the VSCs.

The AC voltage measurement circuits are based on an ISO124 isolation amplifier as shown in Figure 4.3. The purpose of this amplifier is to scale down the input voltage and to provide galvanic isolation between the input and output voltages. Identical circuits were used to measure the line to line voltages of the generator in the generator-side converter and the grid voltages in the grid-side converter.

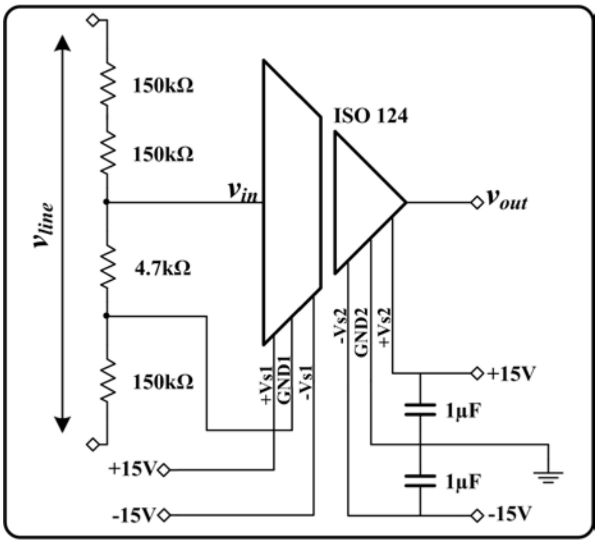

Figure 4.3: Voltage measurement circuit

The gain of this circuit is given by

$$\frac{v_{out}}{v_{in}} = \frac{4.7\ \mathrm{k\Omega}}{R_{tot}} = \frac{4.7\ \mathrm{k\Omega}}{454.7\ \mathrm{k\Omega}} = 0.0103 \tag{4.1}$$

where R_{tot} is the resistance across the input voltage [Ω].

The DC link voltage measurement is based on a Hall-effect transducer (LV 25/800), with a gain given by

$$\frac{v_{out}}{v_{in}} = 0.0084 \tag{4.2}$$

The AC current measurements are also based on Hall-effect transducers (LAH 25-NP). The gain is given by

$$\frac{i_{out}}{i_{in}} = 0.001 \tag{4.3}$$

These transducers were used to convert the phase currents of the generator and the grid to a lower current level. Moreover, they provided galvanic isolation between the input and output currents.

4.1.1.2. Driver board

The driver board consist of the VSC gate drivers and the alarm manager. The latter monitors the voltages, the currents and the temperature of the VSC and raises an alarm whenever an over rating of any of these variables is sensed. It also incorporates a current to voltage conversion circuit to convert the phase current measurements (performed in the power board) to voltage. The circuit is shown in Figure 4.4.

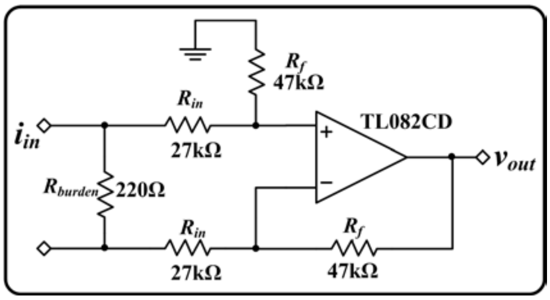

Figure 4.4: Current to voltage conversion circuit

The gain of the circuit is given by

$$\frac{v_{out}}{i_{in}} = \frac{R_{burden}R_f}{R_{in}} = \frac{220 \cdot 47\ \text{k}\Omega}{27\ \text{k}\Omega} = 383\ \text{V / A} \tag{4.4}$$

4.1.1.3. DSP board

The core of this board is a TMS320F2808 DSP that is used to perform vector control and the initialisation routine (pre-charging of the DC link) of the VSC. The DSP also monitors the alarm flag from the alarm manager and initiates a shut down procedure for the VSC whenever the alarm is raised. Apart from switching off the power devices, it discharges the DC link as a safety measure. This is performed through resistors (R_{13} and R_{14}) by enabling contactor LS_3. The DC link discharge circuit is shown in the Power board –VSC schematic (sheet 2 of 4) in Appendix E.3.

The board includes also a signal conditioning circuit for the voltage and current measurements to be compatible with the DSP. The voltage operation range of the analogue to digital converters in the DSP is from 0 − 3.3 V. Therefore, all the voltages and currents are conditioned in such a way to fit in this range. The signal conditioning circuit is shown in Figure 4.5. It consists of a scaling factor and a DC offset. The reason for the offset is because the measurements are AC quantities and hence cannot be read by the DSP.

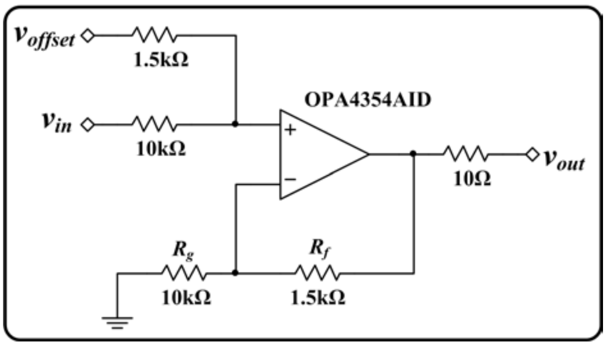

Figure 4.5: AC measurements signal conditioning circuit

The voltage at the non-inverting input (V^+) is given by

$$V^+ = \left(\frac{v_{in} - v_{offset}}{11.5\ \text{k}\Omega} \cdot 1.5\ \text{k}\Omega \right) + v_{offset} \tag{4.5}$$

The gain of the amplifier is given by

$$A_V = 1 + \frac{R_f}{R_g} = 1 + \frac{1.5\ \text{k}\Omega}{10\ \text{k}\Omega} = 1.15 \tag{4.6}$$

The offset voltage (v_{offset}) was set to half the voltage operating range (1.65 V); hence, the output voltage is given by

$$v_{out} = A_V \cdot V^+ = 0.15 v_{in} + 1.65 \tag{4.7}$$

In the case of the DC link voltage a similar circuit was used; however, the scaling factor and the offset were different (1.3 V and 0.3 V). The output voltage in this case is given by

$$v_{out} = A_V \cdot V^+ = 0.3 v_{in} + 0.3 \tag{4.8}$$

Considering all the signal conditioning performed on the voltage and current measurements the input voltages to the DSP are given by

$$\begin{aligned} v_{line}\ \text{measurment}: v_{out} &= \left[0.15\left(v_{line} \cdot 0.0103\right) + 1.65\right] \\ i_{ph}\ \text{measurment}: v_{out} &= \left[0.15\left(i_{ph} \cdot 0.383\right) + 1.65\right] \\ V_{DC}\ \text{measurment}: V_{out} &= \left[0.3\left(V_{DC} \cdot 0.0084\right) + 0.3\right] \end{aligned} \tag{4.9}$$

4.1.2. Control system

The control system was divided into low and high-level controllers. The task of the low-level controller was to control the power converter. This was split into a generator-side and a grid-side converter controller (each implemented in a dedicated DSP). The high-level controller was used to represent parts of the WT and its control system, and to provide reference set-points for the low-level controller. This was implemented in a dSPACE® rapid prototyping system.

4.1.1.4. Low-level controller

Each low-level controller main task was to control the VSC using a vector control scheme. A sine-weighted PWM with a carrier frequency of 10 kHz was used for both VSCs.

The strategy adopted for the generator-side converter was the maximum torque per ampere control. In this strategy, as explained in Section 3.2.2.2, the *q*-axis current was controlled to be equal to the generator stator current and the *d*-axis current to zero.

A similar strategy was used for the grid-side converter. The *d*-axis current was used to control the DC link voltage by exporting active power to the grid and the *q*-axis current was used to control the reactive power. In this case, the *q*-axis was set to zero for unity power factor operation. In addition to the vector control scheme, this controller had a phase-locked loop routine for synchronising the system with the grid and a DC link pre-charge routine.

The functions of the grid-side converter control algorithm are summarised in the state machine diagram of Figure 4.6. The generator-side converter algorithm state diagram is similar to this except that it does not contain the synchronisation and the pre-charge parts.

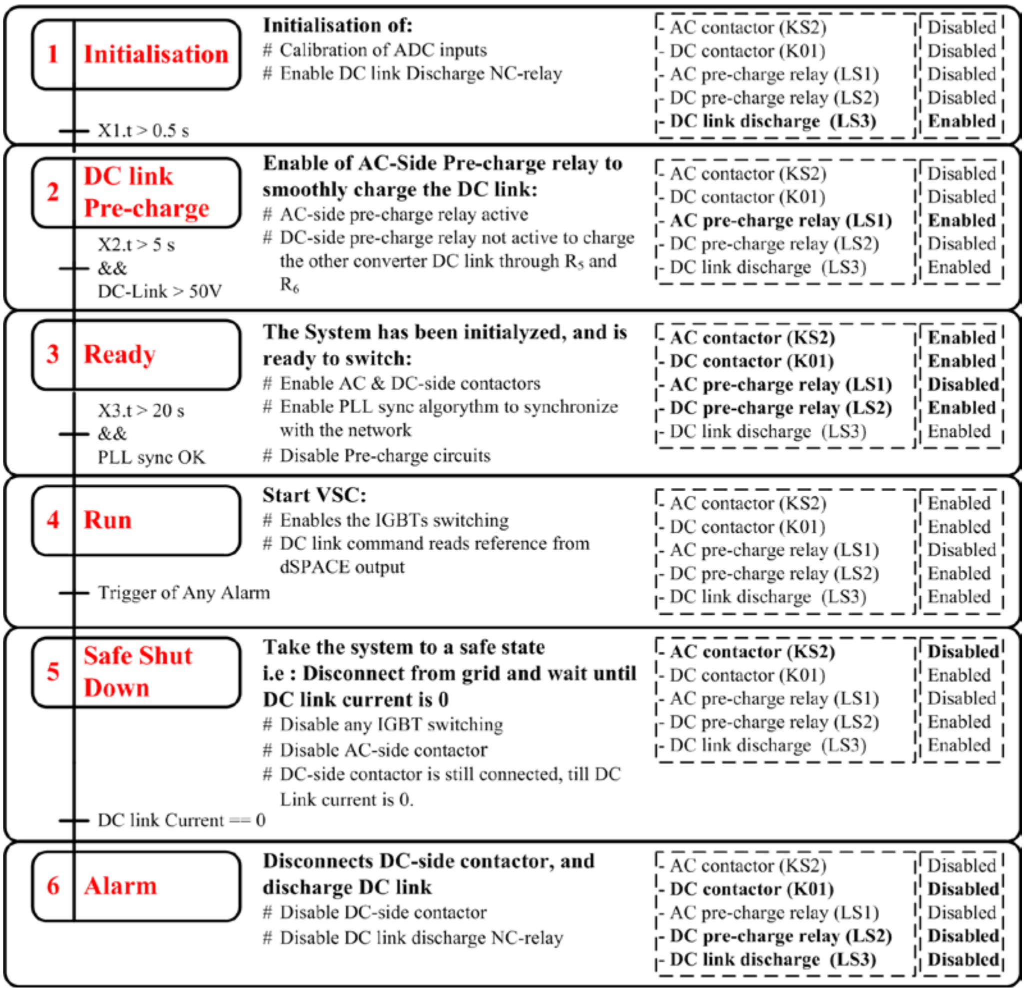

Figure 4.6: Grid-side converter algorithm state diagram

4.1.1.5. *High-level controller*

The high-level controller was implemented in a dSPACE® modular hardware platform based on a DS1005 processor board. The system included several input/output boards such as: analogue to digital conversion (DS2003), digital to analogue conversion (DS2103), encoder interface (DS3002) and digital input and output boards (DS4003).

This system was used to model parts of the WT such as the aerodynamics, the pitch system, the drive-train and the tower models. Moreover, the pitch controller, the torsional vibration damper and the inertial response controllers were also included as shown in Figure 4.7. The models and the control system were first developed in MATLAB/Simulink® and then converted to a suitable code for dSPACE® through the real-time workshop interface.

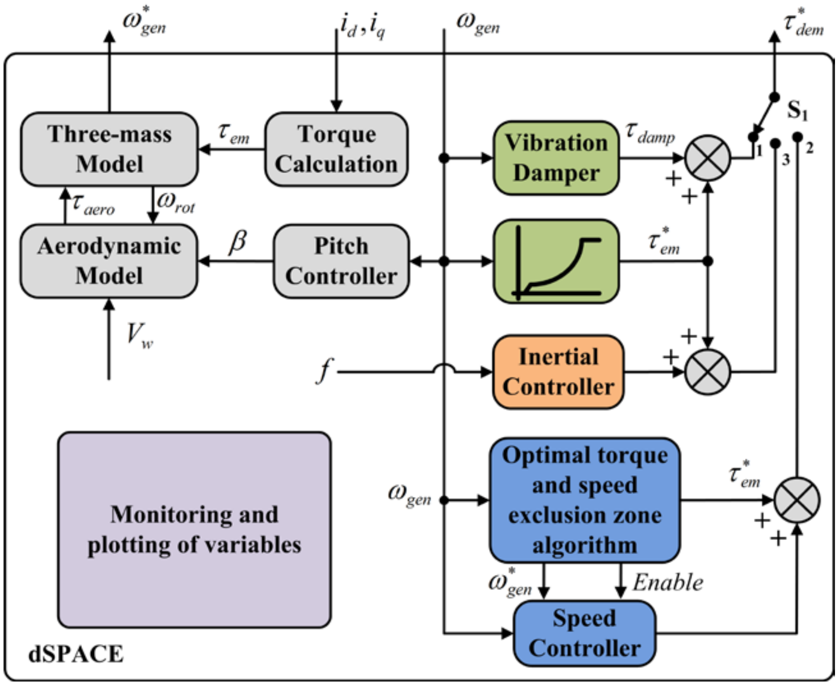

Figure 4.7: High-level controller block diagram

The inputs to the dSPACE® are the generator speed and the phase currents (*dq*) whereas the outputs are the reference speed to the motor drive (Unidrive) and the generator torque reference to the generator-side converter. The purpose of switch S_1 is to enable different options for generating the generator torque demand reference. This depends on the type of experiment carried out. Experiments related to torsional vibration damping (Chapter 5) the switch is set to position 1, for testing the speed exclusion zone algorithm

(Chapter 6) to position 2 and for testing the supplementary controller for inertial response (Chapter 7) to position 3.

A graphical user-interface was built in dSPACE® to control the experiment sequence and to be able to change set-points in real-time. This interface was also used for plotting of variables in real-time and for data acquisition. The data acquired from all experiments was exported and plotted in MATLAB®.

4.2. Hardware-in-the-loop experiment sequence

The hardware-in-the-loop block diagram for the torsional vibrations damping experiment is shown in Figure 4.8. It consists of a speed loop (blue) and a torque loop (red).

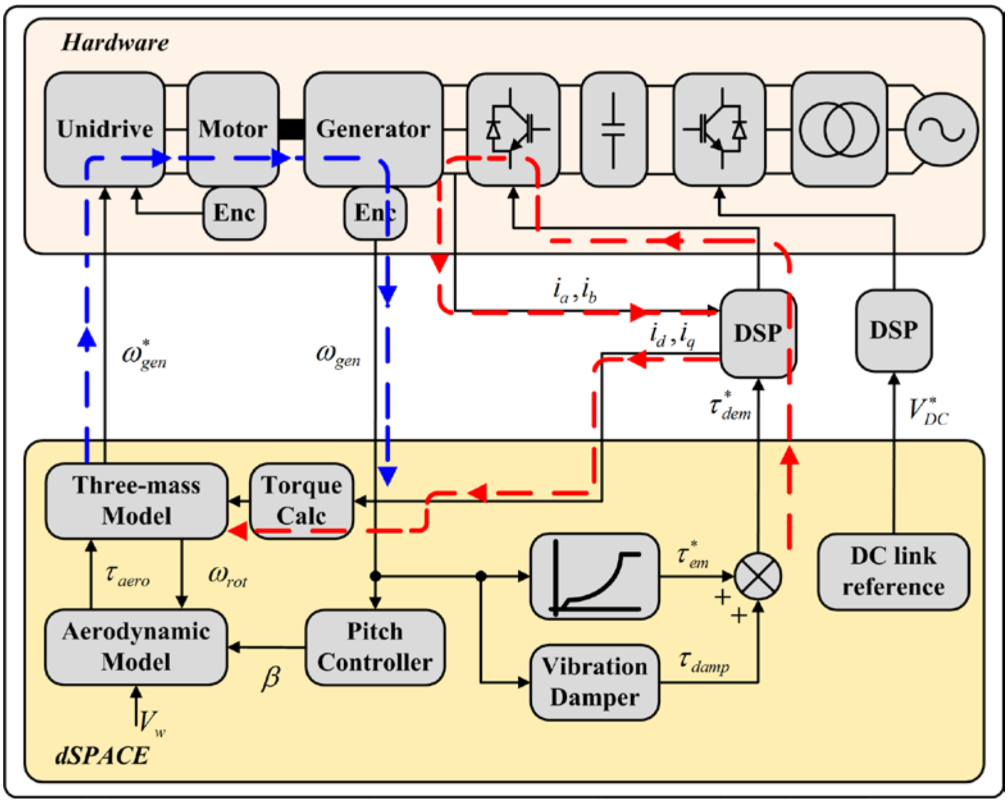

Figure 4.8: Block diagram of the hardware-in-the-loop experiment

The dSPACE® controller outputs the HSS speed (ω^*_{gen}) depending on the operating conditions of the WT. This is used as a speed reference to the motor drive (Unidrive) which controls the motor to the desired speed. Due to the mechanical coupling between the two machines the generator follows the motor speed. The generator speed is measured through an incremental encoder and read back into dSPACE®. The speed information is then used by the WT control system for the pitch controller, the optimal torque look-up table and the vibration damper. The reason for using the measured speed instead of the HSS speed directly was to introduce measurement noise and lag into the system.

In the case shown (torsional vibrations damping experiment), the turbine controller outputs the resultant torque from the optimal and damping torques (τ^*_{em}, τ_{damp}) as a reference (τ^*_{dem}) to the generator-side converter DSP. The DSP outputs the necessary gate signals to the VSC to control the generator to follow the reference torque. The generator phase currents (i_a, i_b) are measured by the DSP, converted to d and q-axis currents and sent to dSPACE®. The q-axis current is then used to calculate the generator reaction torque. This torque is inputted to the three-mass model to balance the aerodynamic torque (τ_{aero}) and damp any torsional vibrations present.

This experiment sequence is also valid for the other experiments (speed exclusion zone and inertial response). The only difference is the way the generator torque reference is generated.

4.3. Conclusion

This chapter described the hardware test rig used for the experimental testing conducted in this research. A brief overview of the hardware parts with particular focus on the signal conditioning circuits for the voltage and current measurements used in the VSCs units was given. The controller hierarchy used was discussed; the low-level controller was implemented in a DSP whereas the high-level controller was implemented in a dSPACE® environment. The dSPACE® platform enabled also data acquisition and real-time plotting of selected variables. Finally, the hardware-in-the-loop experiment sequence used for testing the torsional vibrations dampers was described. This was used also for the other experiments.

Chapter 5

Damping of Torsional Vibrations

Summary:

The objective of this chapter is to compare the performance of two different torsional vibration dampers when subjected to parameter variation and model uncertainty in a VSWT. First, a mechanical model that considers both shafts and blades flexibilities is derived. Then two torsional vibration dampers are designed: one uses a conventional design, based on BPFs and the other uses a model-based approach. A stability analysis is then performed to assess the system behaviour when parameter variation and model uncertainty are present in the mechanical model used for the design of the dampers. This is performed in the frequency domain using Nyquist plots. Sensitivity functions were then used to carry out performance analysis. Finally, simulations and experiments are carried out to test the performance of the torsional vibration dampers both with a wind step and a turbulent wind. The dampers are tested for cases when the torsional vibration frequencies are exactly known and when there is uncertainty present.

5.1. Introduction

In a VSWT, the drive-train torsional mode is usually very lightly damped because the mechanical damping from the gearbox and the generator is very small. Moreover, the aerodynamic damping provided by the in-plane blade modes and the structural damping is very small as well [63].

Torsional vibrations are most significant at high wind speeds during which the turbine is operating above rated wind speed. Typically, in this operating region, the generator torque and speed are held fixed at rated values. As a consequence, the inherent damping in the drive-train attributed to variable-speed operation is lost [13]. Therefore, any load changes such as turbulent wind and gusts can excite lightly damped modes resulting into large torque vibrations in the drive-train [43]. If such vibrations are left unaddressed, the drive-train components will be subjected to higher fatigue loads which ultimately may reduce their lifetime [12]. Moreover, if the torque vibrations are not addressed they will be converted into electrical power oscillations which are highly undesirable for the operation of the power system. This is because such oscillations may interact with modes in the power system [54, 86, 98].

Damping of torsional vibrations can be accomplished by either the pitch or the generator controllers. However, it has been reported that the generator torque controller is more effective for this task [62] and therefore it was employed in this work. A torsional vibration damper was included in the torque loop to generate a damping torque to provide auxiliary damping to the system [13, 16, 52, 63, 64, 99].

In order to design an effective torsional vibration damper, apart from the drive-train torsional mode frequency it is also important to consider the coupling to other modes, such as the blade in-plane symmetrical vibration mode [63]. This is because such vibration mode couples directly to the drive-train torsional mode and if it is excited, it will lead to torsional vibrations. The tower side-side mode is another mode that can couple with the drive-train mode [13]. Hence, when modelling the mechanical system to design the torsional damper it is important to consider all decisive modes that can possibly lead to torsional vibrations.

5.2. Mechanical Model

In the literature, a two-mass model is normally used to represent the mechanical system of a WT which takes into account only the shafts flexibilities and assumes that the blades are rigid [49-51, 89]. This representation is not adequate when studying torsional vibrations and for the design of torsional vibration dampers because the damper can exhibit inferior performance. In order to illustrate this, a simulation with two different dampers was performed on a quasi-realistic WT model in Bladed®. One was designed considering only the drive-train mode whereas the other one taking in account both the drive-train and the blade in-plane symmetrical modes.

In order to excite the WT modes, a wind step from 18 m/s to 24 m/s was applied to the turbine at 2 s. The LSS torque was recorded and used to assess the performance of the two torsional vibration dampers. Figure 5.1 illustrates the LSS torque of the system for the following cases: without any damping, with a damper designed considering one mode, and with a damper considering both modes.

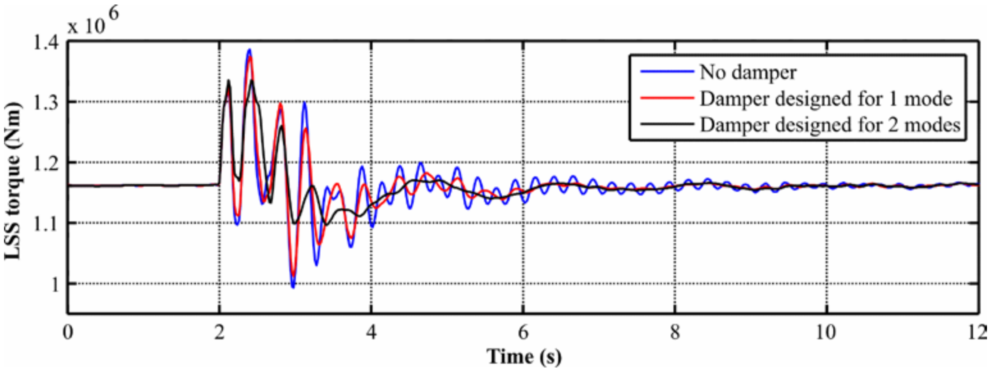

Figure 5.1: LSS torque for cases of no damper, damper designed considering one and both modes

It can be observed that although both dampers managed to damp the torque oscillations, the performance of the damper designed to damp both modes was better. The reason for this is attributed to the lack of damping offered to the blade-in plane mode by the damper designed considering the drive-train mode only. This is illustrated clearly in Figure 5.2, which shows an auto-spectral density plot of the LSS torques given in Figure 5.1. This was plotted in Bladed® and it measures the frequency content of a variable and helps to identify periodicities. It is evident from this plot that the damper designed considering the drive-train mode only, failed to address sufficiently the blade in-plane mode.

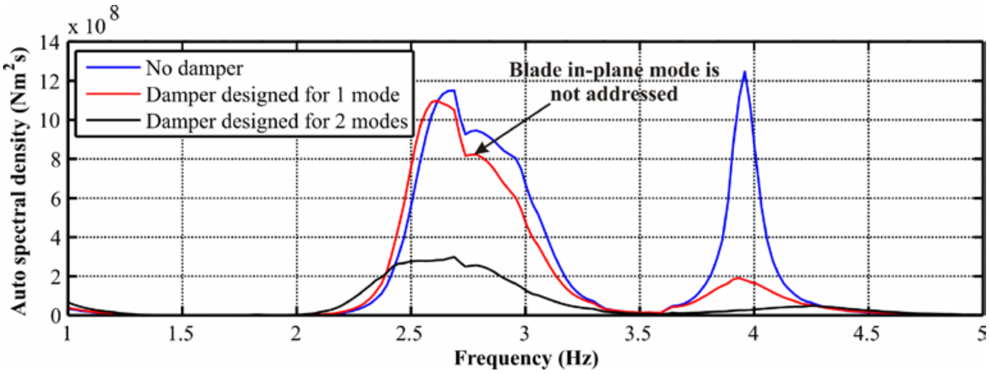

Figure 5.2: Auto-spectral density of the LSS torques of Figure 5.1

Although in this case the two mode frequencies are quite close to each other (2.54 Hz and 3.9 Hz), the difference in the dampers performance can still be observed. This difference would be more noticeable if the frequency modes are further apart.

Following this observation, a mechanical model that considers both the drive-train torsional and the blade in-plane symmetrical modes was used. A three-mass model was derived from first principles and is described in Appendix B.4. The dynamic equations of the three-mass model referred to the LSS including external torque components are given by [47, 100]

$$J_{blade}\frac{d}{dt}\omega_{rot} = \tau_{aero} - K_{bl}\left(\theta_{rot} - \theta_{hub}\right) - D_{bl}\cdot\frac{d}{dt}\left(\theta_{rot} - \theta_{hub}\right) \tag{5.1}$$

$$\begin{aligned} J_{hub}\frac{d}{dt}\omega_{hub} = -K_{bl}\left(\theta_{hub} - \theta_{rot}\right) - K_{sh}^{'}\left(\theta_{hub} - \frac{\theta_{gen}}{N}\right) - \\ D_{bl}\cdot\frac{d}{dt}\left(\theta_{hub} - \theta_{rot}\right) - D_{sh}^{'}\cdot\frac{d}{dt}\left(\theta_{hub} - \frac{\theta_{gen}}{N}\right) \end{aligned} \tag{5.2}$$

$$J_{gen}\frac{d}{dt}\frac{\omega_{gen}}{N} = -N\tau_{em} - K_{sh}^{'}\left(\frac{\theta_{gen}}{N} - \theta_{hub}\right) - D_{sh}^{'}\cdot\frac{d}{dt}\left(\frac{\theta_{gen}}{N} - \theta_{hub}\right) \tag{5.3}$$

$$\frac{d}{dt}\theta_{rot} = \omega_{rot} \tag{5.4}$$

$$\frac{d}{dt}\theta_{hub} = \omega_{hub} \tag{5.5}$$

$$\frac{d}{dt}\theta_{gen} = \omega_{gen} \tag{5.6}$$

where J_{blade} represents the inertia of the flexible part of the blade [kgm^2], J_{hub} represents the rigid part of the blade and hub [kgm^2], J_{gen} is the generator inertia [kgm^2] referred to LSS, ω_{gen}, ω_{rot} and ω_{hub} are the generator, rotor and LSS speeds [rad/s], K_{bl} and D_{bl} are the effective blade stiffness [Nm/rad] and damping [Nms/rad], K'_{sh} and D'_{sh} are the equivalent LSS and HSS stiffness [Nm/rad] and damping [Nms/rad] referred to the LSS and N is the gearbox ratio. All parameters are given in Appendix A.1, Table A-1.

5.3. Torsional Vibration Damper Design

Two different approaches were used to design the torsional vibration damper: the first one uses a conventional BPF-based design and the other a model-based design.

5.3.1. BPF-based torsional vibration damper

The block diagram of the BPF-based torsional damper is illustrated in Figure 5.3.

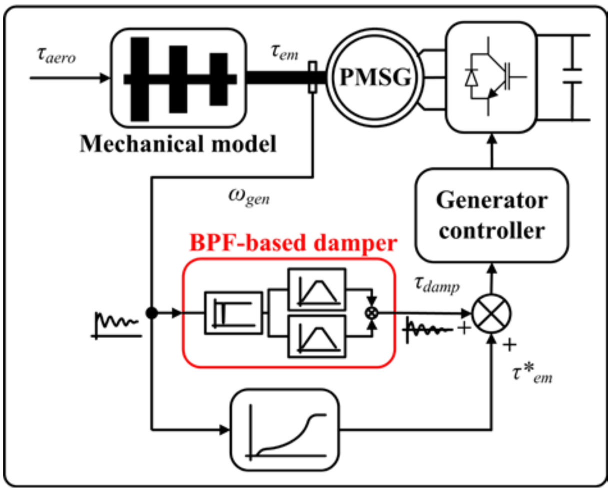

Figure 5.3: Block diagram of the BPF-based torsional damper

The idea behind this damper is to add a damping torque τ_{damp} at the torsional vibration frequencies to the generator torque reference τ^*_{em}. This damping torque is derived from a filtered version of the generator speed [64, 99]. Typically, either a band-pass or a high-pass filter is used to extract the vibration frequency from the generator speed [16, 52]. In the case of a BPF, it needs to provide enough gain in the pass band to damp torsional vibrations and minimum gain possible outside the bandwidth to limit the introduction of unwanted frequencies in the system such as multiples of the blade passing frequencies (3P and 6P) [13]. Hence, the BPF must have a narrow peak (low damping ratio) to limit the response outside its bandwidth. Moreover, it is important that the phase of the damping torque generated by the filter has a counteracting effect on the torque vibrations. If it is not exactly out of phase, the performance of the damper can be compromised. In such case, a low-pass filter is cascaded with the other filters to correct for the phase error [63].

The structure of the damper used in this work consists of a notch filter cascaded with two BPFs. Common practice suggests the use of one 2nd order BPF to extract the vibration frequency from the generator speed [16, 52, 65, 99]. However, since the nominal mode frequencies associated to the mechanical model equations (5.1) − (5.3) are relatively far apart (2.54 Hz and 3.7 Hz), two BPFs were used to address each frequency separately. This was done to avoid having a BPF with a high bandwidth, which is undesirable [13]. The transfer function of each BPF used is given by

$$G_{BPF}\left(s\right)=K_{BPF}\,\frac{2\zeta\omega_n s}{s^2+2\zeta\omega_n s+\omega_n^2} \tag{5.7}$$

where ζ is the damping ratio, ω_n is the resonant frequency [rad] and K_{BPF} is the DC gain.

The WT model considered in this work has a 6P blade passing frequency of 1.8 Hz. Although the BPF designed to address the blade in-plane mode frequency (2.54 Hz) has a narrow bandwidth it still exhibits significant response at the 6P. Hence, a notch filter of the form

$$G_{NF}\left(s\right)=\frac{s^2+2\zeta_1\omega_{nf}s+\omega_{nf}^2}{s^2+2\zeta_2\omega_{nf}s+\omega_{nf}^2} \tag{5.8}$$

was used in cascade with the BPFs to limit the damper response at such frequency [16]. ζ_1 and ζ_2 are the damping ratios that set the depth of the filter and ω_{nf} is the notch frequency. The parameters of the BPF and the notch filter are included in Appendix A.3.

In order to verify the design of the damper, a Bode plot of the system consisting of the plant (three-mass model transfer function from the generator speed to the generator torque) and the torsional damper on the feedback path was plotted and is shown in Figure 5.4. From the closed-loop response, it can be observed that the damper introduces enough damping in the system to suppress both the drive-train and the blade in-plane modes. This can be clearly observed from the location of the open loop and closed-loop poles in the root locus plot shown in Figure 5.5.

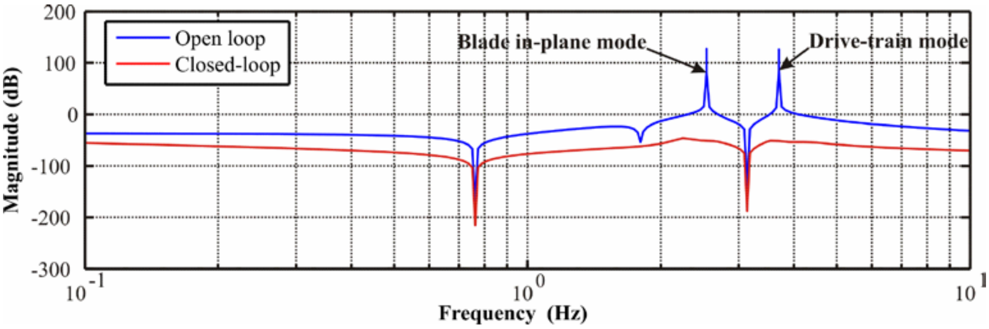

Figure 5.4: Bode plot - system with the BPF-based damper

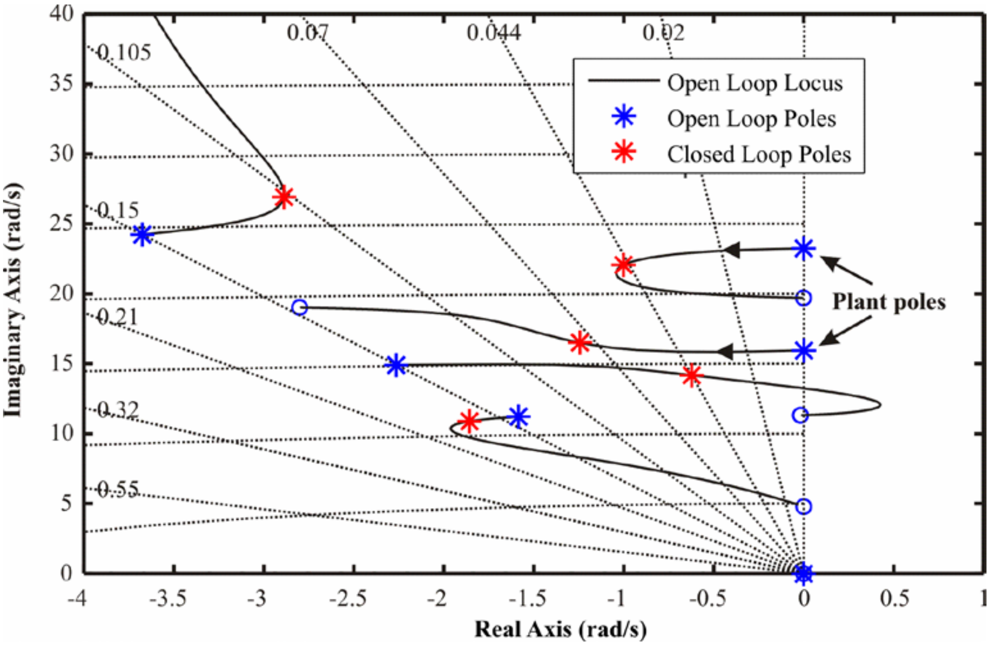

Figure 5.5: Root locus - system with the BPF-based damper

The plant open loop poles are close to the imaginary axis which implies that the system is lightly damped. Therefore, whenever the plant modes are excited by a slight disturbance, torsional vibrations will arise. These vibrations will take a long time to decay due to the low damping in the system. With the introduction of the damper the lightly damped plant poles move away from the axis as shown by the black arrows in Figure 5.5. Ultimately, this means that the damping of the plant increases; the larger the negative real part of the closed-loop poles, the higher is the damping.

5.3.2. Model-based torsional damper

An alternative approach for designing the torsional vibration damper is using pole placement with state feedback. Theoretically, this technique allows arbitrary placement of the closed-loop poles of the system [101]. By carefully selecting the location of the closed-loop poles, the damping of the system can be improved significantly.

The state feedback design approach requires information of all the states of the system. This is not realisable in practice because it is not economically feasible to have a sensor to measure each state and not all the states can be measured. Therefore, a state observer was used to estimate these states. The block diagram of the model-based torsional vibration damper is shown in Figure 5.6.

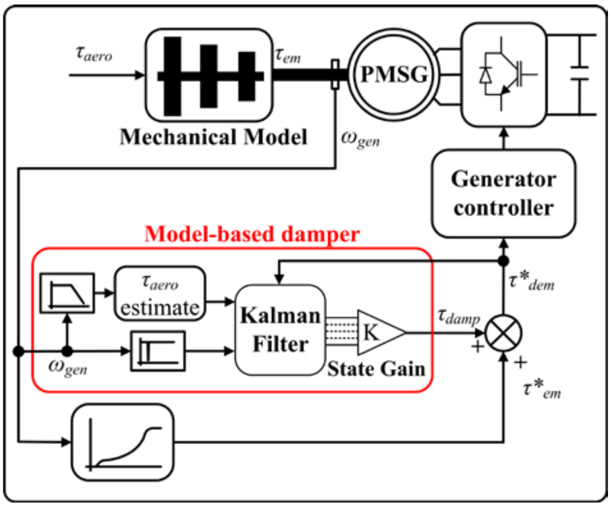

Figure 5.6: Block diagram of the model-based torsional damper

In order to achieve good state estimation despite having uncertainty in the model and measurement noise, a discrete-time KF was used. A KF is a linear filter described by a set of equations given by [102]

$$\hat{\mathbf{x}}_k^- = \mathbf{F}\hat{x}_{k-1} + \mathbf{G}\mathbf{u}_k \tag{5.9}$$

$$\mathbf{P}_k^- = \mathbf{F}\mathbf{P}_{k-1}\mathbf{F}^T + \mathbf{Q} \tag{5.10}$$

$$\mathbf{K}_k = \mathbf{P}_k^-\mathbf{H}^T\left(\mathbf{H}\mathbf{P}_k^-\mathbf{H}^T + \mathbf{R}\right)^{-1} \tag{5.11}$$

$$\hat{\mathbf{x}}_k = \hat{\mathbf{x}}_k^- + \mathbf{K}_k\left(y_k - \mathbf{H}\hat{\mathbf{x}}_k^-\right) \tag{5.12}$$

$$\mathbf{P}_k = \left(\mathbf{I} - \mathbf{K}_k\mathbf{H}\right)\mathbf{P}_k^- \tag{5.13}$$

where **F** and **G** are discretised plant state and input matrices, $\hat{\mathbf{x}}_{k-1}$ and $\mathbf{P}_{k-1}$ are the initial conditions for the states and the estimation error covariance, $\mathbf{K}_k$ is the KF gain, $\mathbf{P}_k$ is the estimation error covariance matrix, **H** is the output matrix, $\mathbf{u}_k$ is the input matrix, and y_k is the output.

A KF minimises the variance of the estimation error [102, 103]. Its successful implementation is ensured by having the three-mass model represented in the KF as accurately as possible. The closer the model within the KF structure is to the real plant, the better is the filter performance and thus the effectiveness of the damper. All input variables (ω_{gen}, τ^*_{dem}) were available to the damper except the aerodynamic torque (τ_{aero}) which had to be estimated. In the literature, this has been addressed by either augmenting the mechanical model with a state representing the unknown input [104, 105] or by solving differential equation (5.1) using the derivative of the rotor speed [106]. The derivative method was adopted in this work. Although through this approach the aerodynamic torque estimate is obtained in a simple way, it is very sensitive to measurement noise. In order to mitigate the problem of noise associated with derivatives, it is recommended that proper filtering is used either on the generator speed input or on the estimated aerodynamic torque [106]. In this case, a low-pass filter was used on the generator speed input to filter the noise at the source. Moreover, the speed measurement was passed through a similar notch filter as the one used in the BPF-based damper to eliminate any damper response at the 6P frequency. The design procedure and the structure of the model-based damper are included in Appendix D.

The Bode plot of the system with the model-based torsional vibration damper is shown in Figure 5.7. It can be observed that the damper suppresses both the drive-train and the blade in-plane modes as in the case of the BPF-based damper.

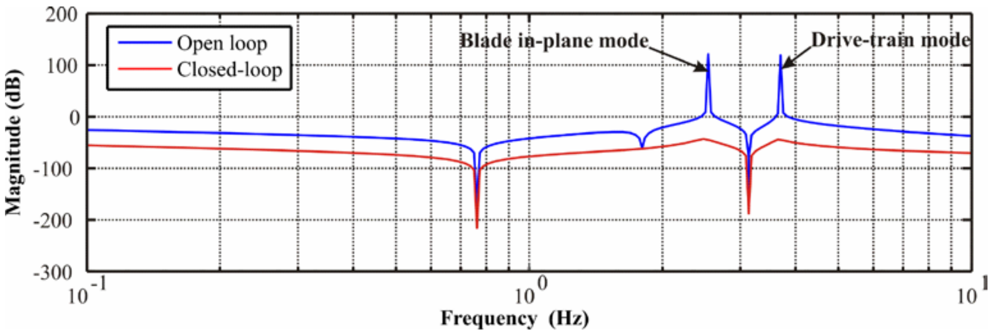

Figure 5.7: Bode plot - system with the model-based damper

5.4. Stability Analysis

A feedback control system that can remain stable under a specified range of process perturbations is said to possess robust stability [107]. According to [108], practical experience suggests that a GM of 10 dB and a PM of 60° are usually adequate stability margins.

Frequency domain tools, such as Nyquist analysis and Bode plots, can be used for analysing linear time-invariant systems. It is well known that a WT is a non-linear system mainly due to the non-linear aerodynamics [14]. Hence, for the stability analysis, only the torque loops shown in Figure 5.3 and Figure 5.6, which exclude the non-linear aerodynamics, were considered. By further neglecting non-linear terms in the three-mass model such as friction, the system can be assumed linear. Moreover, an additional simplification was performed by assuming that the electrical dynamics are at steady-state when addressing the mechanical dynamics (as electrical dynamics of the system are much faster than the mechanical). Therefore, the electrical subsystem (generator and converter) was simplified and modeled as a first-order lag, with a time constant $T_{lag} = {}^{L_q}\!/_{R_s}$ [51, 56]. The simplified torque loops that were considered for the stability analysis are shown in Figure 5.8.

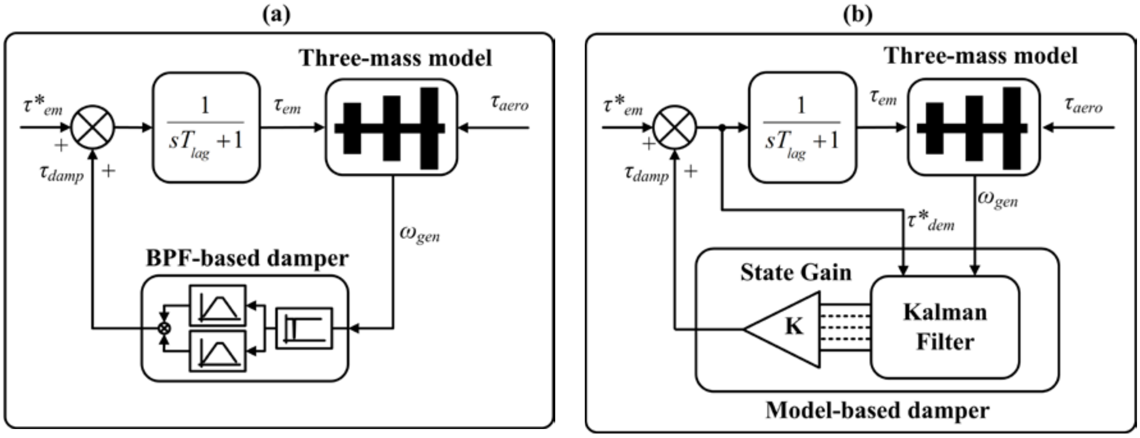

Figure 5.8: Simplified torque loops (a) BPF-based damper (b) Model-based damper

5.4.1. Vibration frequencies uncertainty

The stability analysis was carried out to identify regions of operation for which the system can potentially go unstable in the presence of model uncertainties and parameter variations. Model uncertainties are mainly due to the difference in the WT model (three-mass model) used for the design of the dampers and the actual turbine, whereas parameter variations are differences due to operating conditions of the WT, such as ice on the blades. Ultimately, model uncertainties and parameter variations are reflected as uncertainty in the torsional vibration frequencies. This means that the performance of the torsional vibration damper can be affected when implemented on the actual WT.

5.4.1.1. *Parameter variation*

During operation in icy weather conditions the rotor blades collect ice as they rotate. When ice starts accumulating on the blades, the mass of the blades increases. This leads to an increase in the rotor mass and hence the rotor inertia. A simulation in Bladed® showed that the rotor inertia increased by 18% for a three bladed 2 MW WT. As a consequence, the nominal blade in-plane mode (F_{1nom}) changed from 2.54 Hz to 2.4 Hz and the nominal drive-train mode (F_{2nom}) changed from 3.7 Hz to 3.49 Hz. This is illustrated in the Bode plot of Figure 5.9. The parameter variations in the WT due to ice on the blades and the three-mass model used to represent variations in the vibration frequencies are included in Appendix A.4.

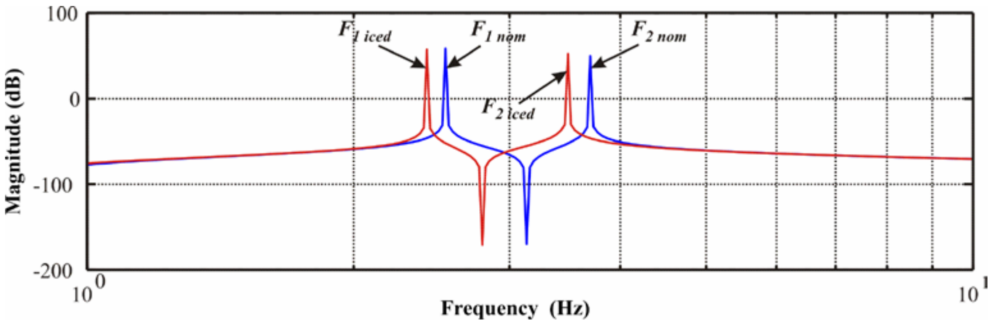

Figure 5.9: Torsional vibration frequencies – nominal and with ice on the blades

5.4.1.2. *Model uncertainty*

The accuracy of a model is dependent on the level of complexity used to describe a system. Model uncertainty may result from the simplification of the complex system for control design purposes and from parameters that are difficult to determine, such as hub stiffness, gearbox mountings, bedplate stiffness, etc. Due to the diversity of sources leading to model uncertainty, it is difficult to represent exactly how the torsional vibration frequencies are affected. Hence, a range of vibration frequency variations, bounded by ±0.25 Hz (±10% of F_{1nom}) were considered. The cases considered are tabulated in Table 5-1.

Table 5-1 : Cases for different uncertainty levels in the mode frequencies

	Three-mass Model	Modes Frequency Uncertainty		Resultant Modes Frequency [Hz]	
	Case	ΔF_{1nom}	ΔF_{2nom}	F_1	F_2
Set 1	1	–10%	10%	2.29	3.95
	2	–10%	0%	2.29	3.70
	3	–10%	–10%	2.29	3.45
	4	0%	10%	2.54	3.95
Nominal	5	0%	0%	2.54	3.70
Set 2	6	0%	–10%	2.54	3.45
	7	10%	10%	2.79	3.95
	8	10%	0%	2.79	3.70
	9	10%	–10%	2.79	3.45

A Bode diagram was plotted for each set of cases to illustrate the effect of uncertainty and is shown in Figure 5.10.

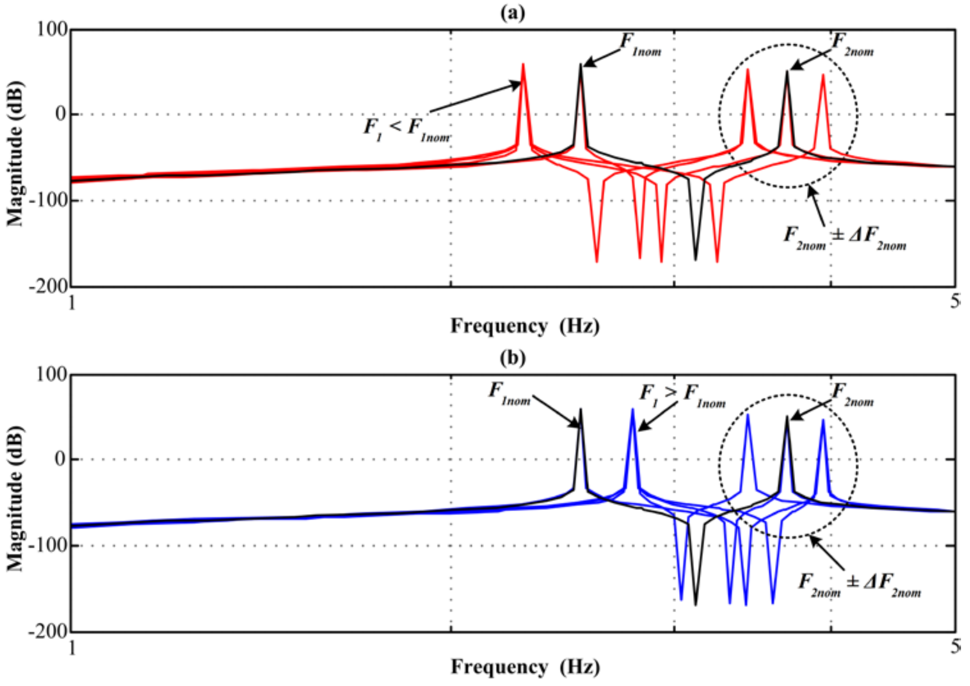

Figure 5.10: Bode plot for cases (a) $F_1 < F_{1nom}$ (b) $F_1 > F_{1nom}$ for all uncertainties in F_2

The cases were divided into two sets to facilitate the analysis and interpretation of results. The first set (shown in red) represents the cases when the uncertainty in F_1 is below the nominal ($F_1 < F_{1nom}$) for all uncertainties in F_2. The other set (shown in blue) represents the range of cases when the uncertainty in F_1 is above the nominal ($F_1 > F_{1nom}$) for all uncertainties in F_2. Case 5 represents the nominal three-mass model without any uncertainty (shown in black).

The uncertainty in the three-mass model was included through variations in stiffnesses and inertias (J_i and K_i) but not in the damping coefficients (D_i) since the latter has no effect on the mode frequencies.

5.4.2. Sensitivity functions

The Nyquist stability criterion was employed to evaluate the system stability with the two different vibration dampers. This criterion states that for a stable open loop plant (such as the one representing the torque loop), closed-loop stability is maintained as long as there are no encirclements of the critical point (–1, $j0$) [101]. The only drawback with this is that it fails to provide information on how close the Nyquist path is to (–1, $j0$). In order to provide a measure of the distance from the critical point to any point on the Nyquist trajectory, the sensitivity function S was used [101]. This is given by

$$S(j\omega) = \frac{1}{1+G(j\omega)C(j\omega)} = \frac{1}{1+L(j\omega)} \tag{5.14}$$

where $G(j\omega)$, $C(j\omega)$ and $L(j\omega)$ are the plant, the vibration damper and the open loop transfer functions, respectively. The term $1+L(j\omega)$ in equation (5.14) can be represented as a vector from the critical point to any point on the Nyquist path, $L(j\omega)$. The plant model uncertainty $\Delta G(j\omega)$ is represented as a disc with radius $\left|\Delta G(j\omega)C(j\omega)\right|$ centred at each ω evaluated. An uncertainty disc evaluated at a single ω is shown in Figure 5.11. The figure illustrates that as long as $\left|\Delta G(j\omega)C(j\omega)\right|$ is smaller than the distance $\left|1+L(j\omega)\right|$, the Nyquist path will not encircle the critical stability point (–1, $j0$) under the uncertainty bound $\Delta G(j\omega)$.

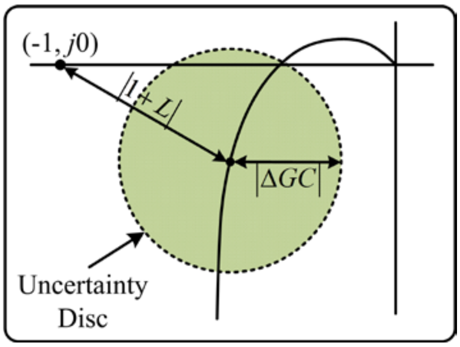

Figure 5.11: Nyquist plot showing model uncertainty *ΔG(jω)* [109]

The complementary sensitivity function *T* gives information on the amplification from the reference signal to the output signal. It is given by

$$T(j\omega)=\frac{G(j\omega)C(j\omega)}{1+G(j\omega)C(j\omega)} \tag{5.15}$$

This was used to determine the maximum uncertainty the system can experience without compromising stability [101]. Thus, the condition for the system to be robust stable is given by [109]

$$\begin{aligned}&\left|\Delta G(j\omega)C(j\omega)\right|<\left|1+L(j\omega)\right|\\&\Rightarrow\left|\Delta G(j\omega)\right|<\left|\frac{1+G(j\omega)C(j\omega)}{C(j\omega)}\right|\equiv\left|\frac{\Delta G(j\omega)}{G(j\omega)}\right|<\frac{1}{|T|}\text{ for }\forall\,\omega\geq 0\end{aligned} \tag{5.16}$$

5.4.3. Stability comparison of the system with the two different dampers

Stability analysis on the system with the different vibration dampers was performed only for the model uncertainty cases shown in Table 5-1. This was because the resulting deviation in the vibration frequencies due to ice on the blades lies within the boundary already considered through model uncertainty. This means that if stability is ensured for all cases in Table 5-1, then stability is also ensured for the system with ice on the blades.

The Nyquist plots for the system with the BPF-based torsional vibration damper for all cases of uncertainty are shown in Figure 5.12. For clarity only the positive frequencies are shown.

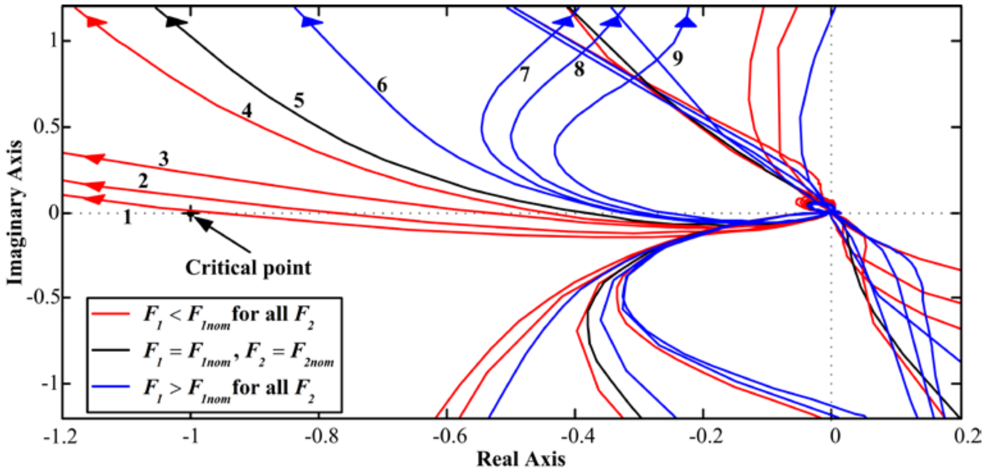

Figure 5.12: Nyquist plots of the system with the BPF-based torsional damper for all 9 cases

It can be observed that the phase and gain margins (PM = 34°, GM = 8 dB) of the system without any uncertainty (Case 5) are below the recommended values (60°, 10 dB) [108]. Moreover, as the lower mode frequency uncertainty was moved negatively (Cases 1 – 4), the stability margins decreased drastically. The worst condition was in Case 1, where the system approached the critical point (–1, *j*0), and as a consequence the stability margins deteriorated considerably (PM = 2.88°, GM = 1.09 dB). This result indicates that the Nyquist plot would encircle the critical point with a slight increase in either the damper gain or the level of uncertainty in the mechanical model, leading the system to instability. Although the system is stable for the given uncertainty bound (±0.25 Hz), its performance with the BPF-based damper is expected to deteriorate considerably when subjected to model uncertainty due to a large drop in stability margins.

The Nyquist plots for the system with the model-based torsional vibration damper for all 9 cases of uncertainty are shown in Figure 5.13. It can be noted that the Nyquist plot for Case 5 for the system with the model-based torsional damper features superior phase and gain margins (PM = 76.1°, GM ≈ ∞) over the BPF-based system. Moreover, an increase in the uncertainty level produced a relatively small change in stability margins. The worst case was again Case 1; however, the stability margins were still adequate (PM = 65°, GM ≈ ∞). Based on these attributes, the system with the model-based damper is expected to perform better than BPF-based torsional damper when model uncertainty is present. Besides that, the performance of the system with and without model uncertainty is not expected to change significantly.

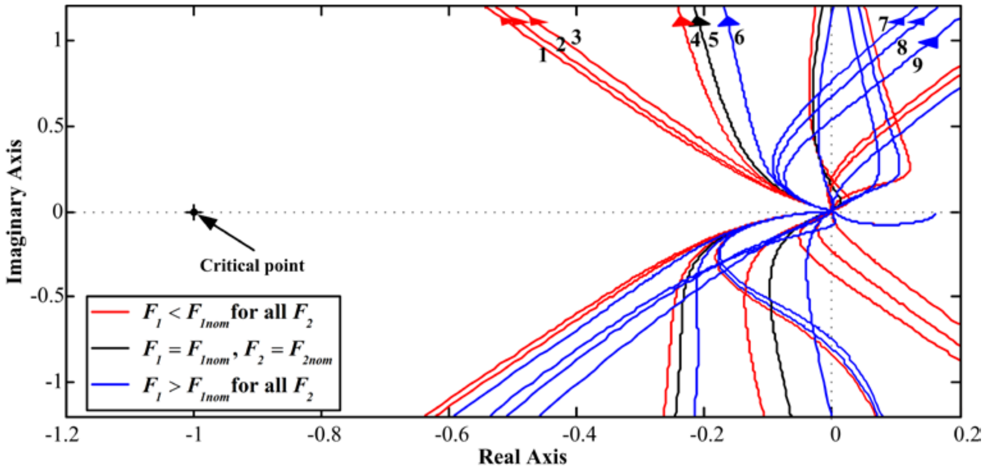

Figure 5.13: Nyquist plots of the system with the model-based torsional damper for all 9 cases

In order to quantify how much uncertainty the system can experience (with the different dampers) without compromising stability, the complementary sensitivity function was plotted. This is shown in Figure 5.14. Recalling from equation (5.16), the larger the magnitude of T is, the smaller the allowable disturbance is. Within the region of the vibration frequencies uncertainty (ΔF_{1nom} and ΔF_{2nom} in Figure 5.14), the magnitude of T for the system with the model-based damper is 0.95 whereas for the system with the BPF-based damper is 1.7. This implies that the maximum allowable uncertainty for the system with the model-based damper is $|\Delta G(j\omega)| = |1.05\times G(j\omega)|$, whereas for the system with the BPF-based damper is $|\Delta G(j\omega)| = |0.59\times G(j\omega)|$. This indicates that the system with the model-based damper can experience higher model uncertainty than the system with the BPF-based damper before becoming unstable. Hence, the system with the model-based damper is more robust than the system with the BPF-based damper.

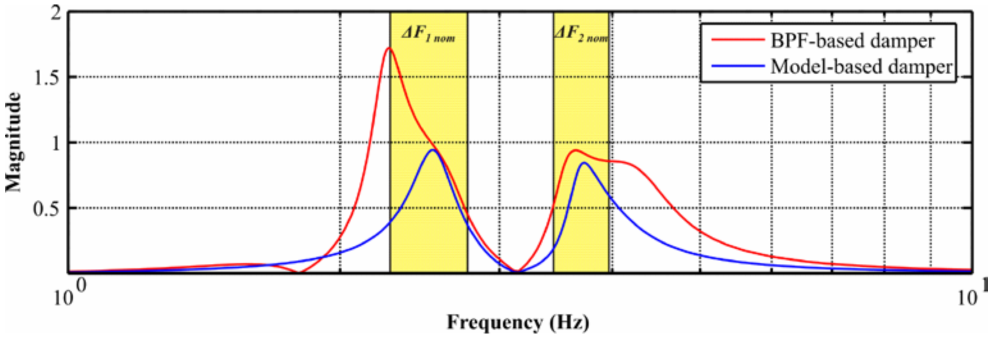

Figure 5.14: Complementary sensitivity function *T*

5.5. Performance Analysis

In addition to ensuring stability, it is also important to investigate whether the system possesses robust performance in the presence of vibration frequencies uncertainty. Robust performance can be defined as the low sensitivity of system performance with respect to model uncertainties and disturbances [110]. The system response to input disturbances, measurement noise and reference signal tracking was analysed. An equivalent block diagram of the system with unity feedback in the presence of disturbance, *d*, and measurement noise, *n*, is shown in Figure 5.15.

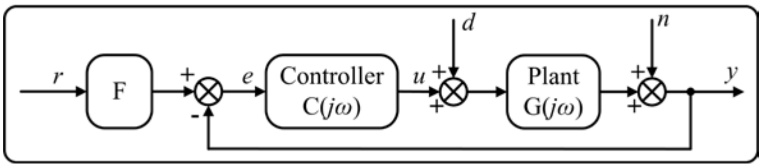

Figure 5.15: System block diagram with process disturbance, *d* and measurement noise, *n*

5.5.1. Disturbance rejection

The transfer function relating the output of the system, *y*, for a plant disturbance input, *d*, is given by

$$G_{YD}(j\omega) = \frac{Y(j\omega)}{D(j\omega)} = \frac{G(j\omega)}{1+G(j\omega)C(j\omega)} = S \cdot G(j\omega) \tag{5.17}$$

Hence, the magnitude of the sensitivity function *S* quantifies the amplification level provided by the system for disturbance *d* for all ω. Thus, the smaller *S* is the better the disturbance rejection becomes. In order to analyse the disturbance rejection for small changes in *G*(*jω*), equation (5.17) is differentiated:

$$\begin{aligned} &\frac{dG_{YD}(j\omega)}{dG(j\omega)} = \left(\frac{1+G(j\omega)C(j\omega)-G(j\omega)C(j\omega)}{(1+G(j\omega)C(j\omega))^2} \right) = S^2 = S \cdot \frac{G_{YD}(j\omega)}{G(j\omega)} \\ &\Rightarrow \frac{dG_{YD}(j\omega)}{G_{YD}(j\omega)} = S \cdot \frac{dG(j\omega)}{G(j\omega)} \end{aligned} \tag{5.18}$$

which shows that the effect of small variations (model uncertainties) in $G(j\omega)$ on G_{YD} $(j\omega)$ is also dependent on *S*.

Typically, plant disturbances are low frequency variations; hence, $|S(j\omega)|$ needs to be small at low frequencies. A plot of S at low frequencies is shown in Figure 5.16, where it can be observed that the system with the model-based damper exhibits better disturbance rejection than the BPF-based damper.

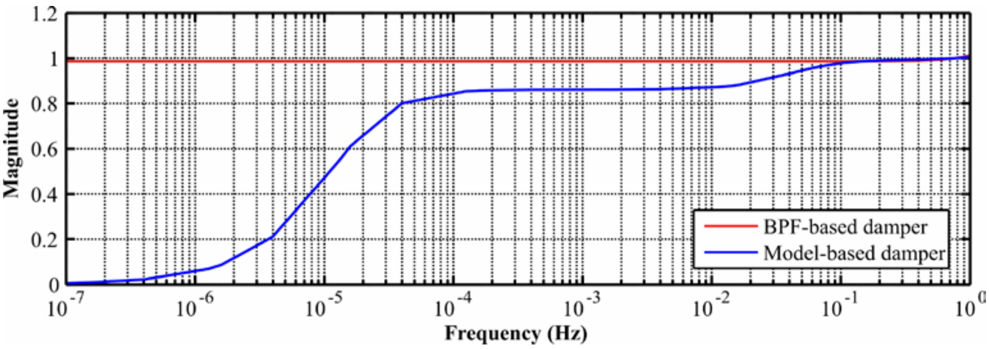

Figure 5.16: Sensitivity function *S* at low frequencies

It is also important for the system that the control actions for measurement noise are as small as possible. The transfer function that relates the controller action, u, and the noise input, n, is given by

$$G_{UN}(j\omega) = \frac{U(j\omega)}{N(j\omega)} = -\frac{C(j\omega)}{1+G(j\omega)C(j\omega)} = -\frac{T}{G(j\omega)} \tag{5.19}$$

Measurement noise is typically high frequency noise; thus, the complementary sensitivity function T has to be small at high frequencies to achieve low control actions [109]. A plot of T for high frequencies is shown in Figure 5.17.

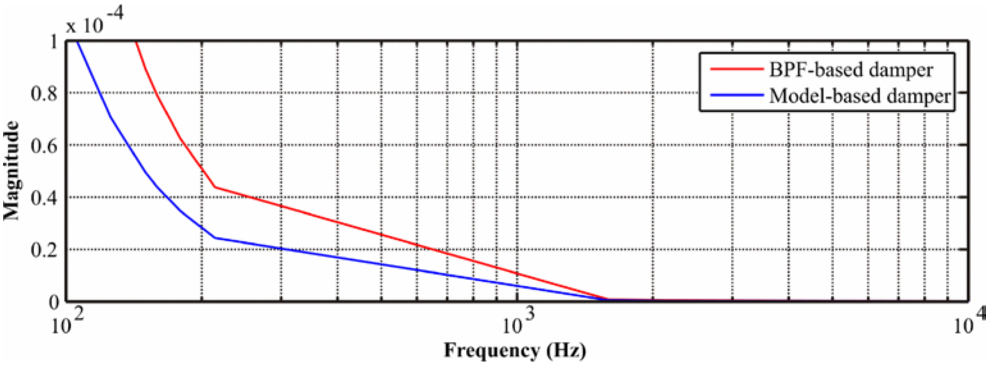

Figure 5.17: Complementary sensitivity function *T* at high frequency

It can be observed that both systems have good measurement noise rejection; however, the system with the model-based damper exhibits slightly better rejection. The variation of $G_{UN}(j\omega)$ with small variations in $G(j\omega)$ is also dependent on T, as given by

$$\begin{aligned}
&\frac{dG_{UN}(j\omega)}{dG(j\omega)}=\left(\frac{C(j\omega)^2}{\left(1+G(j\omega)C(j\omega)\right)^2}\right)=T\cdot\frac{G_{UN}(j\omega)}{G(j\omega)}\\
&\Rightarrow\frac{dG_{UN}(j\omega)}{G_{UN}(j\omega)}=T\cdot\frac{dG(j\omega)}{G(j\omega)}
\end{aligned}\tag{5.20}$$

Hence, the effects of plant variations on $G_{UN}(j\omega)$ are minimal since T is small at high frequencies, as shown in Figure 5.17.

5.5.2. Reference signal tracking

The closed-loop transfer function of the system is given by

$$G_{YR}(j\omega)=\frac{Y(j\omega)}{R(j\omega)}=\frac{F(j\omega)G(j\omega)C(j\omega)}{1+G(j\omega)C(j\omega)}\tag{5.21}$$

The variation of the $G_{YR}(j\omega)$ with small variations in $G(j\omega)$ is dependent on S as given by

$$\begin{aligned}
&\frac{dG_{YR}(j\omega)}{dG(j\omega)}=\frac{C(j\omega)F(j\omega)}{(1+G(j\omega)C(j\omega))^2}=S\cdot\frac{G_{YR}(j\omega)}{G(j\omega)}\\
&\Rightarrow\frac{dG_{YR}(j\omega)}{G_{YR}(j\omega)}=S\cdot\frac{dG(j\omega)}{G(j\omega)}
\end{aligned}\tag{5.22}$$

In order to have good tracking of the reference signal, it is important that S is unity everywhere except at the areas of potential resonances. A plot of the sensitivity function is shown in Figure 5.18.

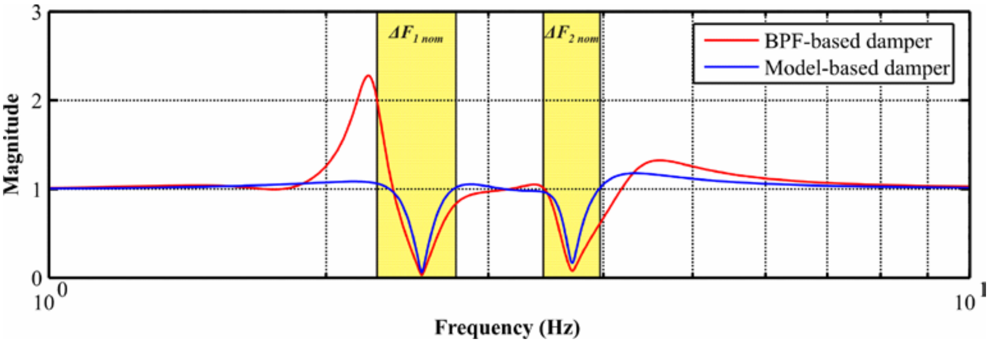

Figure 5.18: Sensitivity function *S*

It can be observed that the sensitivity function of the system with the BPF-based damper has a very high peak close to the area of uncertainty ΔF_{1nom}. This means that the system will amplify any frequencies where S is greater than unity. The sensitivity function for the system with the model-based damper is less than unity in most of the vibration frequency uncertainty areas. This indicates that any frequency within the area of uncertainty is damped.

The closed-loop Bode plots for the system with the two different dampers were plotted to observe how the system response is affected for all the cases (1−9) of vibration frequencies uncertainty. These are shown in Figure 5.19. It is evident from Figure 5.19(a) that there is a resonant peak for the system with the BPF-based damper. This is the effect of the sensitivity function being larger than unity close to the frequency uncertainty area, and implies that the performance of the BPF-based damper is being compromised. The closed-loop plots for the system with the model-based damper are shown in Figure 5.19(b). It can be noted that there are no resonant frequency peaks in this case, which gives an indication of good damping performance.

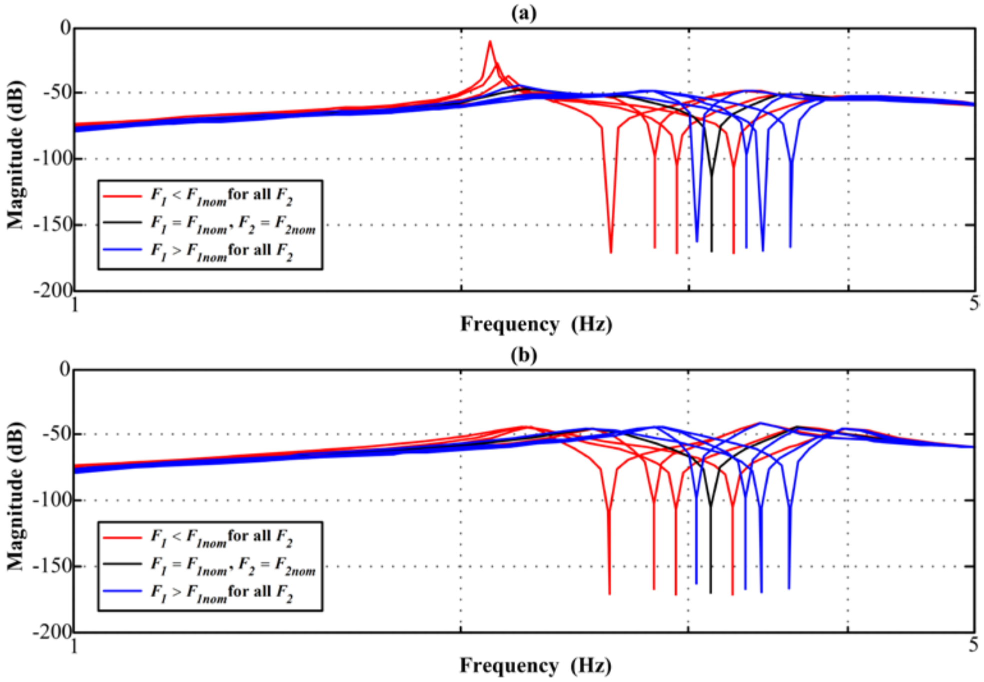

Figure 5.19: Closed-loop bode plots (a) system with the BPF-based damper (b) system with model-based damper

5.6. Simulation and Experimental Results

In order to compare the system performance with the two different torsional vibration dampers, a time domain simulation was performed. The comparison was carried out for three cases of vibration frequencies: nominal Case 5 (2.54 Hz and 3.7 Hz), when ice is present on the blades (2.4 Hz and 3.49 Hz) and with model uncertainty Case 1 (2.29 Hz and 3.95 Hz). The simulations were carried out in Simulink® using the WT model shown in Figure 5.20. A fixed-step solver was used for the simulation hence all transfer functions (*e.g.*, the three-mass model, the controllers and the torsional dampers) had to be converted to discrete-time. The discretization was performed using the Tustin (bi-linear approximation) method with a sampling time of 100μs.

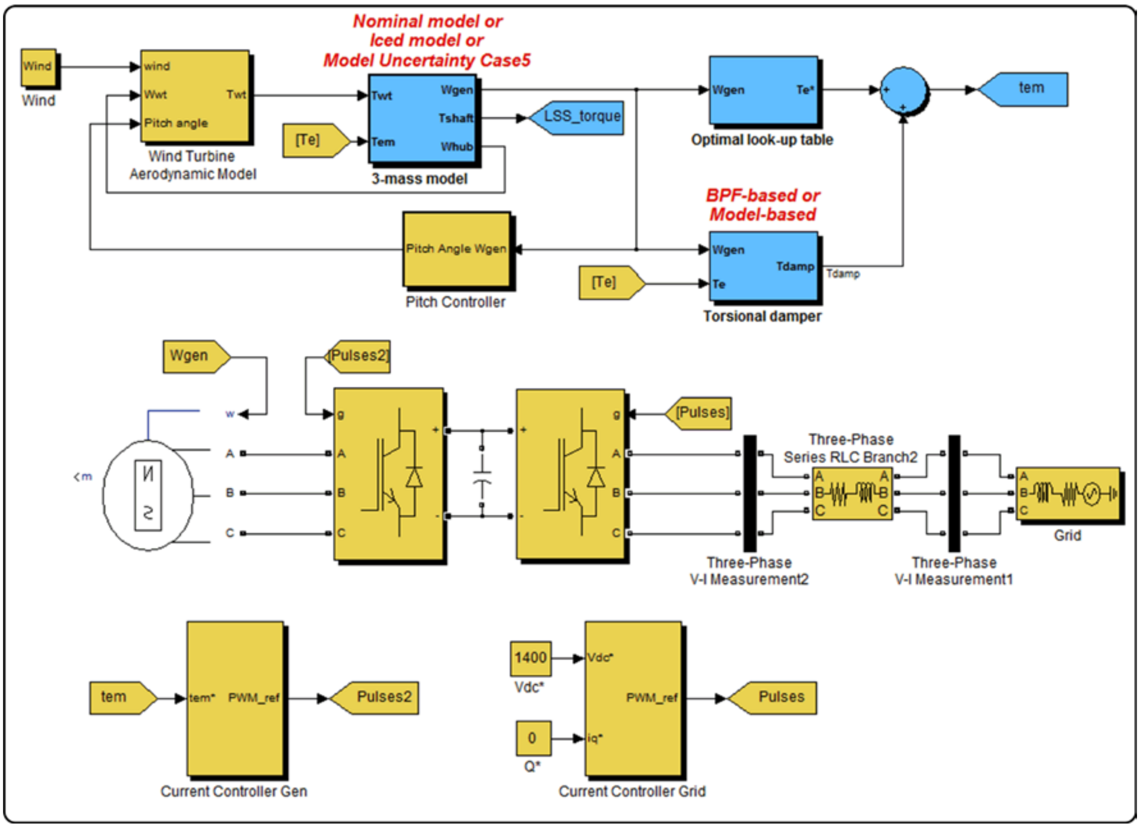

Figure 5.20: WT block diagram used for testing the torsional vibration dampers

A real-time hardware in the loop experiment was performed as outlined in Section 4.2. The experiments were carried out for the nominal model and the model with uncertainty (Case 1).

Simulations and experiments were conducted first with a wind step and then with a turbulent wind with a fixed mean. The LSS torque was recorded in all simulations and experiments and was used as a measure for comparing the performance of the two vibration dampers. In order to perform the simulations as realistically as possible, a zero mean white Gaussian noise with a standard deviation of 0.5 rad/s was added to the generator speed to mimic measurement noise. This was removed in all the experiments.

5.6.1. Wind step

In order to excite the modes that lead to torsional vibrations, a wind step from 14 m/s to 24 m/s was applied to the system at 5 s. Simulations were conducted for three cases: without a damper, with the BPF-based damper and with the model-based damper. On the other hand, the experiments were conducted for all cases except the case without a damper. The reason for this was to prevent damage to the system due to high torque oscillations.

5.6.1.1. Nominal model (Case 5)

The first simulation was performed using the nominal three-mass model with vibration frequencies of 2.54 Hz and 3.7 Hz. The simulation results for the three cases are shown in Figure 5.21. It can be observed that both dampers managed to damp the torque vibrations effectively within 5 s. This was confirmed from the experimental results as shown in Figure 5.22. A good performance from both dampers was expected since they were designed optimally to damp the nominal vibration frequencies (2.54 Hz and 3.7 Hz).

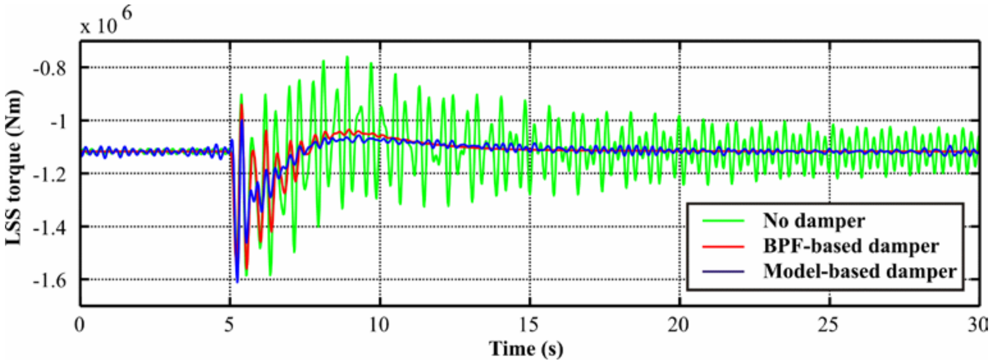

Figure 5.21: LSS torque – Nominal three-mass model – Simulation

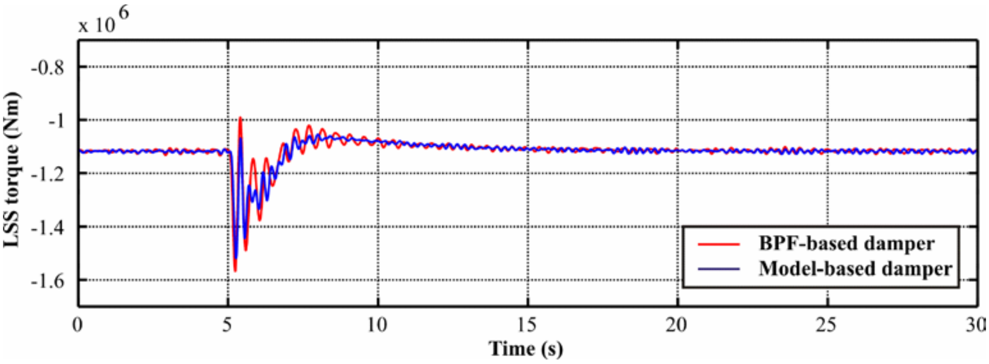

Figure 5.22: LSS torque – Nominal three-mass model – Experiment

In order to observe clearly the frequency content of the torque vibrations in all three cases, a power spectral density was plotted and is shown in Figure 5.23. It is evident that although both dampers managed to damp the torque vibrations effectively, the model-based damper performance was slightly better.

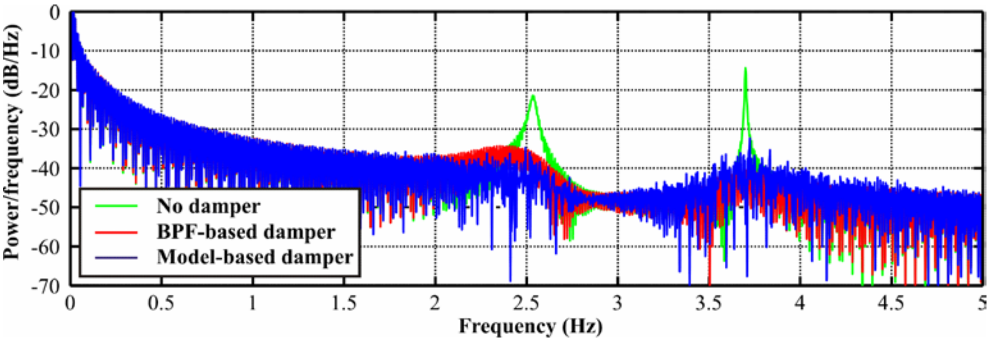

Figure 5.23: LSS torque power spectral density – Nominal three-mass model

5.6.1.2. *Model with iced blades*

The parameters of the three-mass model were changed to represent the effect of ice on the blades and the same simulation outlined in Section 5.6.1.1 was carried out. In this case, the vibration frequencies were 2.4 Hz and 3.49 Hz. The LSS torque for the system for all three cases is shown in Figure 5.24.

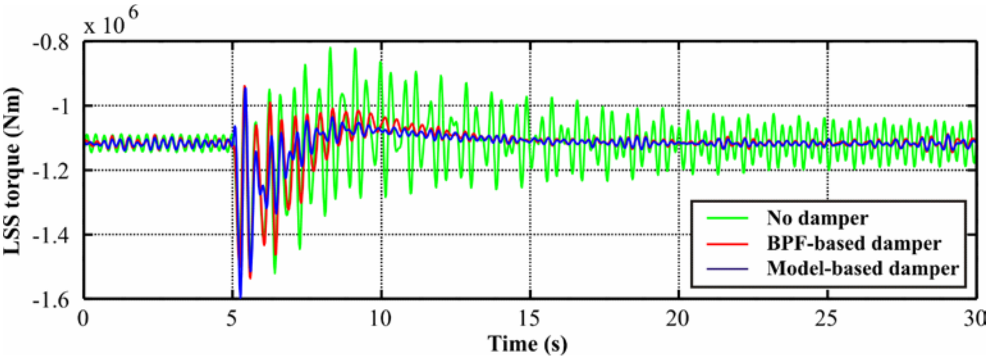

Figure 5.24: LSS torque – Three-mass model with ice on the blades – Simulation

As in the case with the nominal vibration frequencies, both dampers managed to damp the torque vibrations. However, in the case of the BPF-based damper, the amplitudes of the torque vibrations were higher and sustained slightly longer. In the case of the model-based damper the torque vibrations were damped in the same time but exhibited lower amplitudes. The results are clearly shown in the power spectral density plot in Figure 5.25.

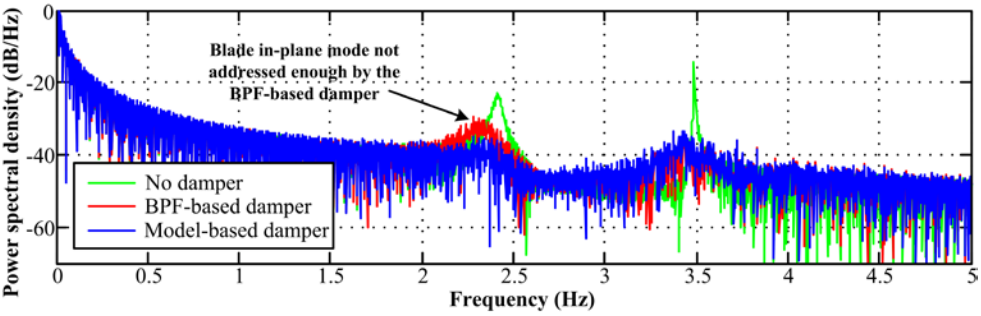

Figure 5.25: LSS torque power spectral density – Three-mass model with ice on the blades

From this plot, it is evident that the reason for the slight drop in performance of the BPF-based torsional damper was because it failed to address the blade in-plane mode effectively. This result suggests that the performance of the BPF-based damper can deteriorate when parameter variation such as ice on the blades is present. Nevertheless, the model-based damper managed to suppress effectively both the drive-train and blade in-plane modes. Moreover, the difference in performance of this damper in the presence of parameter variation when compared to the model with nominal vibration frequencies was insignificant.

5.6.1.3. Model with uncertainty (Case 1)

In this case, the parameters of the three-mass model were changed to reflect the uncertainty Case 1 with vibration frequencies of 2.29 Hz and 3.95 Hz as outlined in Section 5.4.1.2. The simulation results for the system are shown in Figure 5.26.

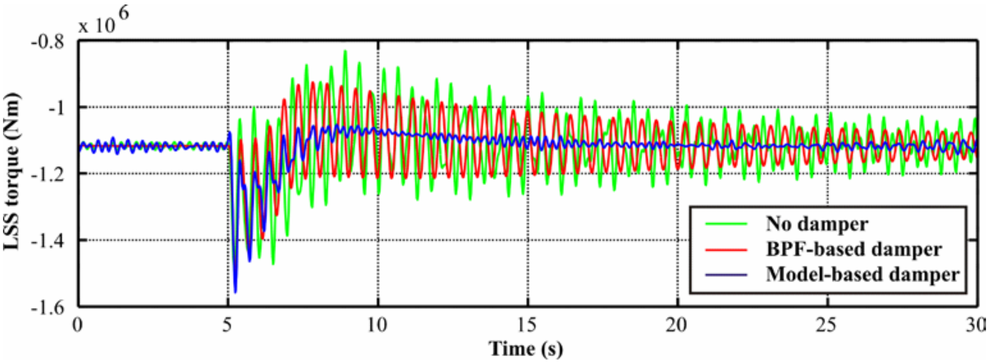

Figure 5.26: LSS torque – Three-mass model with uncertainty Case 1 – Simulation

It can be observed that the performance of the BPF-based damper has been compromised since it failed to damp the torque vibrations. Nevertheless, the model-based damper maintained a good performance. The experimental results are in agreement with the simulations performed and are shown in Figure 5.27.

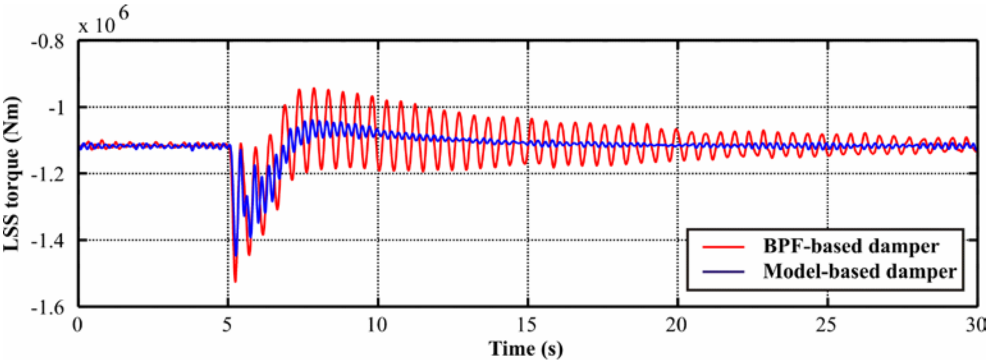

Figure 5.27: LSS torque – Three-mass model with uncertainty Case 1 – Experiment

In order to analyse why the BPF-based damper exhibits such a performance, a power spectral density was plotted and is shown in Figure 5.28.

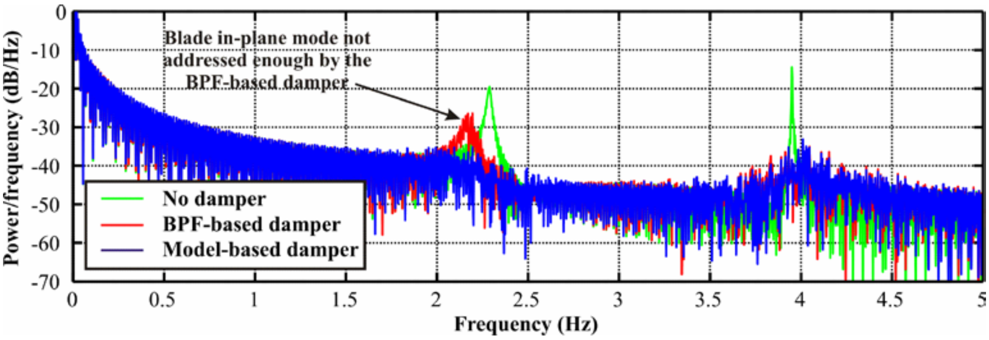

Figure 5.28: LSS torque power spectral density – Three-mass model with uncertainty Case 1

This plot revealed that BPF-based damper failed to address adequately the blade in-plane vibration frequency and as a consequence a peak appears in the neighbourhood of this vibration frequency. The reason for this is because the BPFs in the damper were not tuned for this frequency. Under this circumstance, the damper tends to offset the vibration frequency rather than damping it. This confirms the analysis done in Section 5.5.2. Therefore, in order to improve the BPF-based damper performance, re-tuning is necessary. On the other hand, the model-based damper maintained a good performance despite the uncertainty in the vibration frequencies. Hence, no re-tuning of the damper is necessary. This attribute shows the superiority of the model-based damper over the BPF-based damper.

5.6.2. Turbulent wind

In reality, a WT is exposed to turbulent winds and wind gusts rather than wind steps. Therefore, to test the performance of the two dampers in a more realistic environment, the experiments for the nominal and the model uncertainty Case 1 were carried out again. This time a turbulent wind with a mean of 18 m/s was used as shown in Figure 5.29.

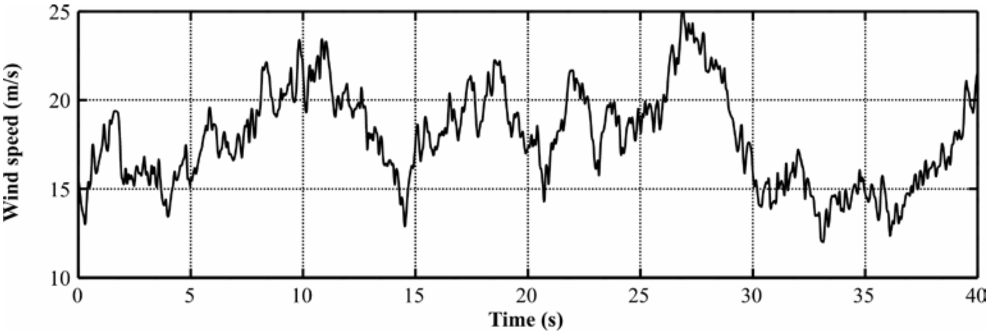

Figure 5.29: Turbulent wind with 18 m/s mean

The experimental results for the system with the nominal vibration frequencies are shown in Figure 5.30. It can be noted that the torque vibrations on the LSS in the case of the model-based damper are somewhat smaller than in the case of the BPF-based damper.

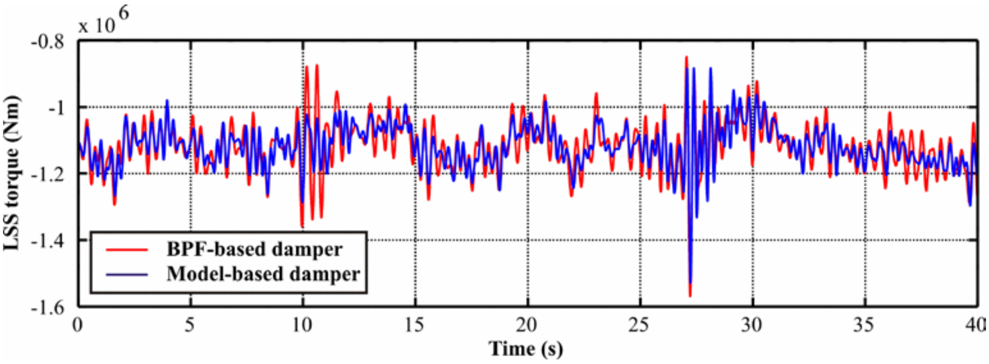

Figure 5.30: LSS torque – Nominal three-mass model – Turbulent wind

The results for the three-mass model with vibration frequency uncertainty Case 1 are shown in Figure 5.31. It can be clearly observed that the BPF-based vibration damper failed to damp the torsional vibrations. This can be noted from the increase in the LSS torque amplitudes. On the other hand, the performance of the model-based damper was good and its performance was superior to the BPF-based damper in both occasions.

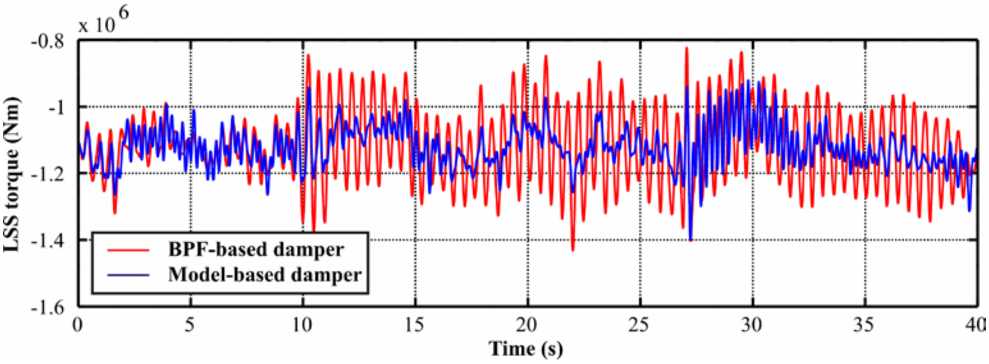

Figure 5.31: LSS torque – Three-mass model with uncertainty Case 1 – Turbulent wind

5.7. Conclusion

A performance comparison of two torsional vibration damper design approaches has been conducted through analysis, simulations and a real-time experiment. The results obtained are all in good agreement.

Stability and performance analyses have been conducted on the system with the two dampers. This was performed to evaluate the robustness of the system when parameter variation and model uncertainties are present in the model used to design the vibration dampers.

The stability analysis showed that without any parameter variation or model uncertainty, the system exhibited good stability margins with both damper designs. Nevertheless, when model uncertainty was introduced the stability margins of the system dropped considerably. On the other hand, the stability margins of the system with the model-based damper have hardly changed when model uncertainty was introduced. The analysis was confirmed by assessing the complementary sensitivity function of the system with the two dampers.

An analysis was also carried out to assess the effect of parameter variation and model uncertainty on the system performance. The system with the model-based damper showed better rejection of disturbance and measurement noise than the system with the BPF-based damper. Moreover, the system featuring the model-based damper showed good attenuation of torsional vibrations in all the area of frequency uncertainty, whereas the system with the BPF-based damper showed amplification in some of the uncertainty area. The effect was clearly observed in the closed-loop response plots.

To verify the stability and performance analysis, a time domain simulation and a real-time experiment were conducted. Both the simulation and experimental results showed that the performance of the model-based torsional damper was not affected in the presence of parameter variation and model uncertainty. However, the performance of the BPF-based damper deteriorated slightly in the presence of parameter variation and was compromised when model uncertainty was introduced. Correspondingly, the BPF-based torsional damper had to be re-tuned to recover the damping performance achieved when tested with nominal vibration frequencies. No re-tuning was necessary in the case of the model-based damper. Therefore, due to its unaffected performance, the model-based torsional damper eliminates re-tuning procedures associated with the conventional BPF-based damper designs. The downside of the model-based damper is that the design process is more challenging than that of the conventional BPF-based damper.

Chapter 6

Avoiding Side-Side Tower Resonance

Summary:

This chapter addresses the mitigation of additional fatigue loads on the tower caused by the excitation of the tower side-side bending mode at a particular rotor speed. The concept of a speed exclusion zone to prevent the rotor from operating close to the tower mode is first discussed. This is followed by an introduction of the algorithm for the generator controller that includes a maximum power extraction function and a speed exclusion zone. A flowchart of this algorithm is also presented. The dynamic amplification factor concept is then introduced for choosing the width of the speed exclusion zone. Next, the simple tower model is validated against a detailed tower model in Bladed®. In order to observe the effectiveness of the algorithm, it is tested for various turbulent wind speeds through simulations and experiments. Finally, a comparison in terms of the tower vibrations and annual energy yield for different speed exclusion zone widths is conducted.

6.1. Introduction

As WT sizes for offshore applications are continuously getting larger (presently 5–7 MW), the PMSG based VSWT with a FRC is gaining popularity [111]. Such turbines have a large region of variable-speed operation which is desirable for maximising the output power and reducing loads. However, VSWTs have to deal with resonant frequencies within their rotor speed range. Therefore, a larger variable-speed region would restrict the area adequate for the location of the tower modes, in particular the side-side bending mode [13, 112, 113].

When the tower side-side mode is close or within either the rotor rotational speed (1P) or the blade passing frequency (3P) regions, the tower is excited and starts vibrating. Consequently, the fatigue loads on the tower increase, and therefore, its lifetime can be compromised. Moreover, these vibrations can couple with the drive-train torsional mode and trigger torsional vibrations [63, 114, 115]. In order to eliminate these potential problems, the tower side-side mode frequency is generally designed away from the 1P and the 3P frequencies [13, 113]. In [42], it was suggested that if this tower mode frequency is ±10% away from the 1P and 3P frequency ranges, resonance problems are avoided. Nevertheless, this is not always possible.

Tower designs are generally classified according to their first bending mode frequencies (f_n) as shown in Figure 6.1. A very-soft tower design is defined when f_n < 1P, a soft-stiff tower when 1P < f_n < 3P and a stiff-stiff when f_n > 3P.

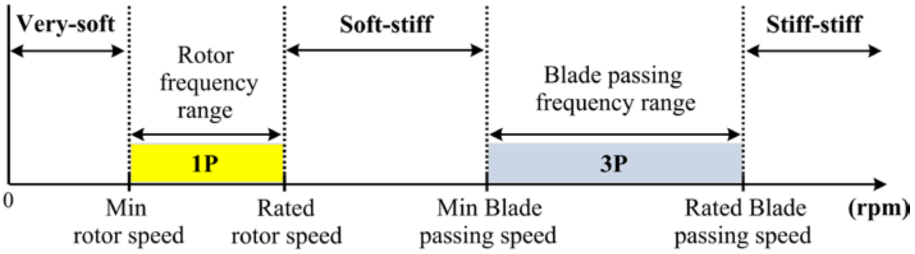

Figure 6.1: Design options for the tower first bending mode frequencies [113]

With such tower design options resonance problems can be avoided; however, there are problems associated with each of them. The very-soft option is difficult to adopt due to strength requirements and its susceptibility to excitation by waves. The stiff-stiff option is not economically feasible due to the large amount of material needed for the increased stiffness [13, 116, 117]. The soft-stiff design is a compromise between the two: cost effective with good stiffness. However, this design is difficult to achieve for large offshore WTs (> 5 MW) with a monopile foundation at large water depths. This is due to limitations on pile diameters and tower wall thicknesses [113]. Therefore, for such turbines the alternative option for the side-side tower mode frequency is within the 1P region. However, in this case, resonance will occur if the rotor rotational frequency is close to this tower mode.

In this work, the side-side tower mode frequency is 0.262 Hz (Section 3.1.3) which lies within the 1P operation region (10.2 – 18 rpm). The Campbell diagram in Figure 6.2 shows the critical rotor speed (15.72 rpm) at which the side-side tower mode is excited. Operation at a rotor speed in close proximity to this tower mode is very undesirable and has to be avoided. This was accomplished by implementing a speed exclusion zone in the generator control algorithm.

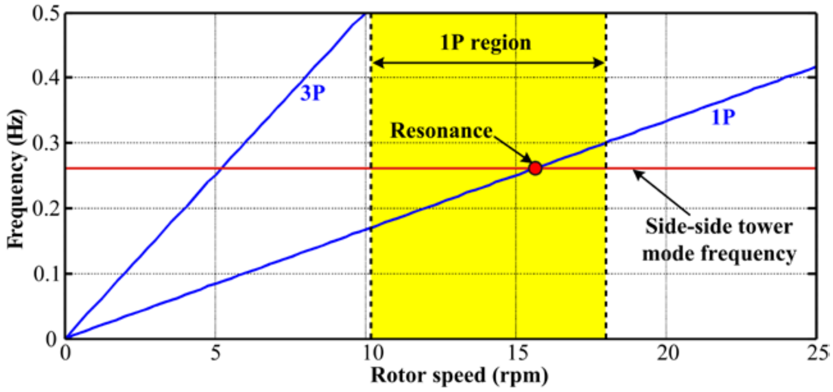

Figure 6.2: Campbell diagram showing the side-side tower resonance problem

6.2. Speed Exclusion Zone

A speed exclusion zone can be defined as an area within the variable-speed region of a WT where the generator is not allowed to operate for sustained periods. This is exemplified in Figure 6.3, were the variable-speed region is split into two parts (B–C and F–G) separated by a restricted speed zone bounded by two constant speed boundaries (C–D and E–F). The generator control algorithm then takes the decision of when and how fast to cross the speed exclusion zone depending on the reaction torque demanded from the generator.

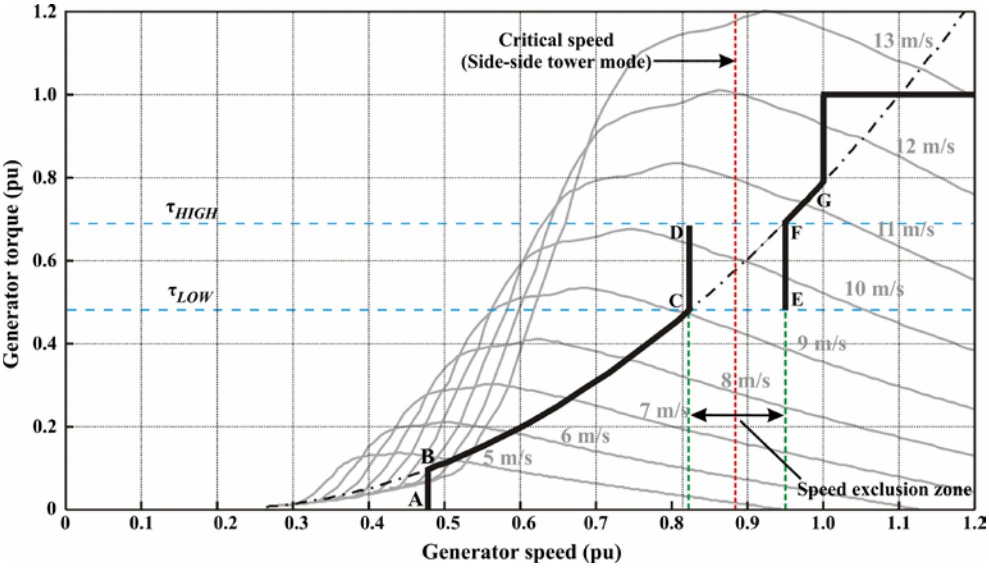

Figure 6.3: Characteristic of a VSWT showing the speed exclusion zone

During the variable-speed region (B–C), the generator is torque controlled and its speed is allowed to vary to extract the maximum available power from the wind. When the generator speed reaches the lower speed boundary (C), the generator speed is held fixed and the torque is allowed to vary along (C–D) in order to balance the aerodynamic torque. When the generator torque demand exceeds an upper limit (τ_{HIGH}) for a pre-defined hysteresis time (t_{HYS}), the algorithm initiates the procedure for crossing the speed exclusion zone. This is performed by gradually increasing the generator speed from D to F, until it exceeds the higher speed boundary. In region (F–G) the WT resumes variable-speed operation. When the wind speed falls, the aerodynamic torque drops and the generator torque demand is reduced in order to follow the optimal torque set-point. As a consequence the generator slows down until it reaches the upper speed boundary. At this point the speed is held fixed at the boundary (E–F). When the demanded generator torque drops below the lower torque limit (τ_{LOW}) for the pre-defined hysteresis time, the generator speed is ramped down from E to C until it becomes lower than the lower speed boundary. At this point the WT resumes variable-speed operation.

A hysteresis time was included in the algorithm to prevent frequent crossing through the critical speed. The choice of the hysteresis time is site specific because it is directly related to the level of wind turbulence present. This means that for sites with large turbulence intensities the hysteresis time has to be longer than for low turbulence sites.

6.3. Generator Controller Algorithm

The primary objective of the generator torque controller during below rated wind speed is to achieve maximum power extraction. In this case, the controller was assigned also the objective of preventing side-side tower resonance. In order to achieve both goals, the optimal generator torque for maximum power extraction was no longer derived from a look-up table (given in Section 3.1.1), but was implemented as an algorithm. The generator controller consists of a cascaded speed and torque controller as shown in Figure 6.4.

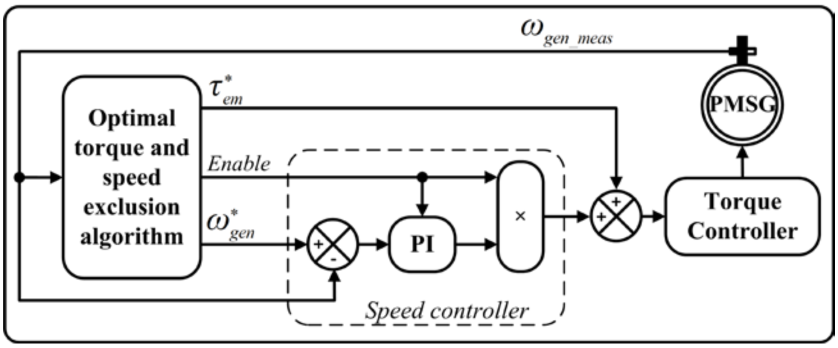

Figure 6.4: Block diagram of the generator controller

For the variable-speed regions (B–C and F–G), the generator is operated in torque control. Hence, the algorithm sets the *'Enable'* line low to simultaneously disable the output of the speed controller and the integrator of the PI to prevent integral windup. At the same time, the algorithm outputs an optimal torque reference (τ^*_{em}) for the generator controller proportional to the square of the measured generator speed as given by [63]

$$\tau^*_{em} = \left(\frac{\rho \pi R^5 C_P}{2\lambda^3 N^3} \right) \omega^2_{gen} = G_{opt} \cdot \omega^2_{gen} \tag{6.1}$$

where R is the blade radius [m], ρ is the air density [kg/m^3], ω_{gen} is the generator speed [rad/s], N is the gearbox ratio, λ is the tip speed ratio, C_P is the power coefficient and G_{opt} is the optimal gain.

During operation along the fixed-speed regions (C–D and E–F) the generator is speed controlled. In such case, the algorithm drives the *'Enable'* line high to enable the speed loop and outputs a speed reference ω^*_{gen} according to which fixed-speed boundary it is in. At the same time τ^*_{em} is held constant at the optimal torque corresponding to this speed.

When crossing the speed exclusion zone, the speed loop is left on and the speed reference is gradually ramped up/down until the other boundary speed is reached. In order to ensure that the generator does not end up operating within the speed exclusion zone for prolonged periods, the crossing sequence cannot be interrupted unless the generator has crossed to the other boundary.

The flow chart of the generator controller algorithm including the speed exclusion zone is shown in Figure 6.5.

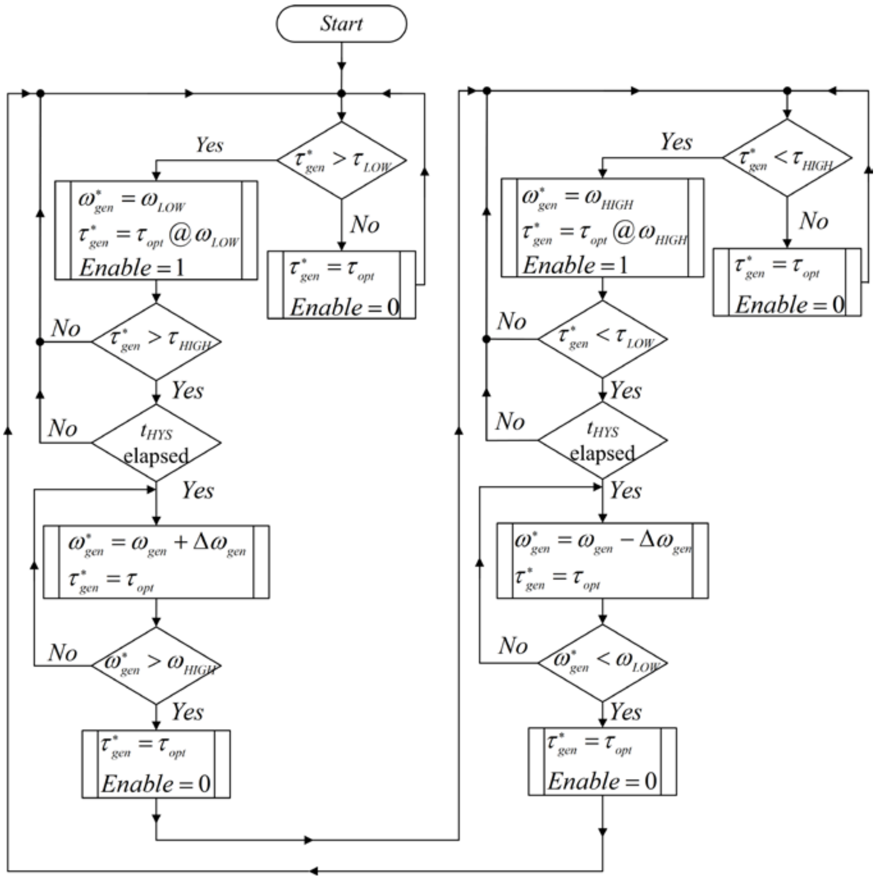

Figure 6.5: Flow chart of the speed exclusion zone algorithm

The choice of the PI controller gains for the speed controller is crucial. This is because high PI gains would imply that the speed is controlled tightly to the set reference at the expense of large torque variations. This is highly undesirable since large torque variations are reflected as large power variations. Hence, a compromise was reached.

All parameters and the PI gains for the speed controller are included in Appendix A.1 and Appendix A.2, Table A-3, respectively.

6.4. Determination of the Speed Exclusion Zone Width

In order to determine the width of the speed exclusion zone, an analysis using the dynamic amplification factor was carried out. This was performed to find out how close the rotor speed can be to the tower mode frequency without causing excessive tower oscillations. The dynamic amplification factor gives information on how much the displacement responses are amplified as a function of the load frequency. For a single degree of freedom (as in this case) the dynamic amplification factor is given by [46]

$$\text{Dynamic amplification factor}\,(f) = \frac{1}{\sqrt{\left(1-\left({f}/{f_n}\right)^2\right)^2+\left(2\zeta\, {f}/{f_n}\right)^2}} \tag{6.2}$$

where f is the frequency of the load, f_n and ζ are the resonant frequency and the damping ratio of the tower. This factor describes how under-damped the oscillations or resonance are in a system. When this factor approaches zero (*i.e.*, $f >> f_n$), the load has less effect on the tower; hence, no oscillations are observed. As the factor approaches unity (*i.e.*, $f << f_n$), the load on the tower is regarded as static. However, when it is larger than unity, an amplification of the tower oscillations is noted. A dynamic amplification factor plot for the tower used in this work is shown in Figure 6.6.

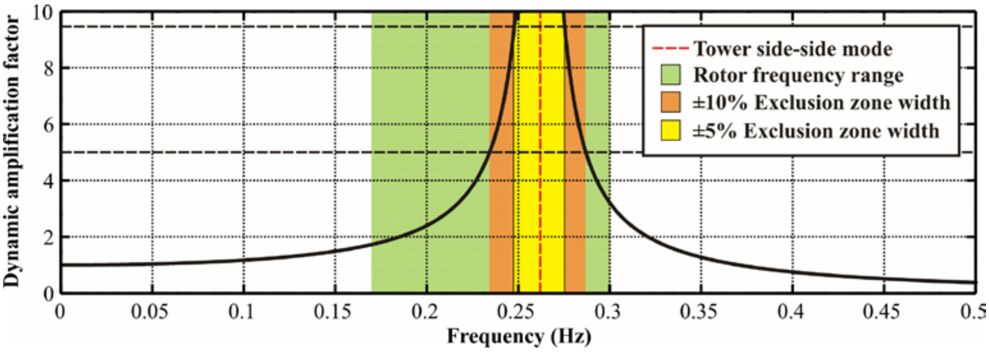

Figure 6.6: Dynamic amplification factor of the tower

It can be observed that the amplification is larger than unity throughout the whole rotor speed range; hence, amplification of the oscillations will occur. Due to the low damping present in the tower (0.005), the amplification approaches 100 as the rotor speed approaches the side-side tower mode (0.262 Hz). This means that the tower oscillations will be amplified by 100 times. Although with this amplification the system will still be stable, the fatigue loads on the tower are increased considerably.

In order to reduce the amplification to acceptable values, two speed exclusion zone widths were defined: ±5% and ±10% (shown in Figure 6.6). At the boundaries of these zones, the dynamic amplification factor reduces from 100 to 9.5 and 5, respectively. It is worth noting that it is possible to reduce further the amplification factor by increasing the width of the speed exclusion zone. However, this is undesirable because it reduces the variable-speed operating region where the WT can maximise the extracted power.

6.5. Tower Model Validation

To observe the effect of different rotor speeds on the tower and the effectiveness of the speed exclusion zone algorithm, a simplified tower model was derived as outlined in Section 3.1.3. Furthermore, a forcing function that couples the tower model to the rotor speed was also derived. This was accomplished by assuming a mass imbalance (m_{imb}) in the rotor located at a radius (r) from the axis of rotation. The magnitude of the forcing function was achieved by comparing the nacelle displacements from the simple tower model with a detailed model in Bladed® using the same initial conditions. Simulations with different values of $m_{imb} \cdot r$ at different steady wind speeds (7.5, 8, 8.5, 9 and 9.5 m/s) were performed. A simulation with a mean turbulent wind speed of 8.5 m/s was also performed. The results of the nacelle displacements for both models when the $m_{imb} \cdot r$ value was 176 kg·m are shown in Figure 6.7.

It can be observed that for steady wind speed cases (Figure 6.7 (a) − Figure 6.7 (e)) there is a good correlation between the two models. However, there was a slight discrepancy in the nacelle displacement when the two models were tested with a turbulent wind speed, as shown in Figure 6.7 (f). This was due to other mode frequencies present in the nacelle displacement of the detailed tower model. This was confirmed in Bladed® by performing a spectral analysis on the nacelle displacement. Moreover, this analysis showed that the side-side tower mode has shifted from 0.262 Hz to 0.244 Hz. This was due to the coupling of the tower mode to other component modes in the WT.

Although the nacelle displacement of the simple model deviated slightly due to the order of the model used and the coupling to other modes, the model was still adequate to investigate the effects of the rotor speed on the side-side tower resonance.

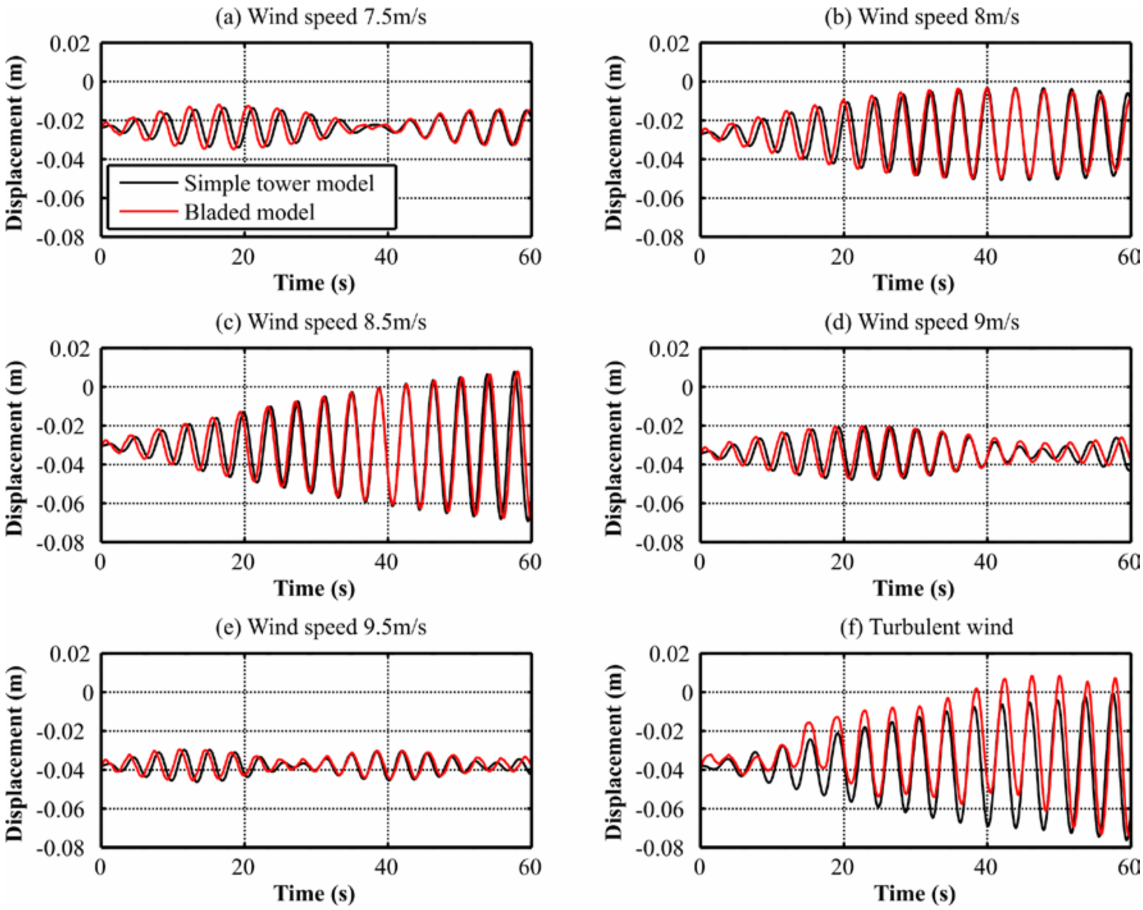

Figure 6.7: Nacelle displacements (a-e) Fixed wind speed (f) Turbulent wind speed

6.6. Simulation and Experimental results

In order to observe the effectiveness of the speed exclusion zone, a time domain simulation was performed with a fixed and variable mean turbulent wind. The wind turbulence model used was based on Kaimal spectra with a turbulence intensity of 12%. Moreover, a simulation to compare the performance of the system with ±5% and ±10% speed exclusion zone widths was conducted. The simulations were carried out in

Simulink® using the WT model shown in Figure 6.8. A real-time hardware in the loop experiment as outlined in Section 4.2 was also performed.

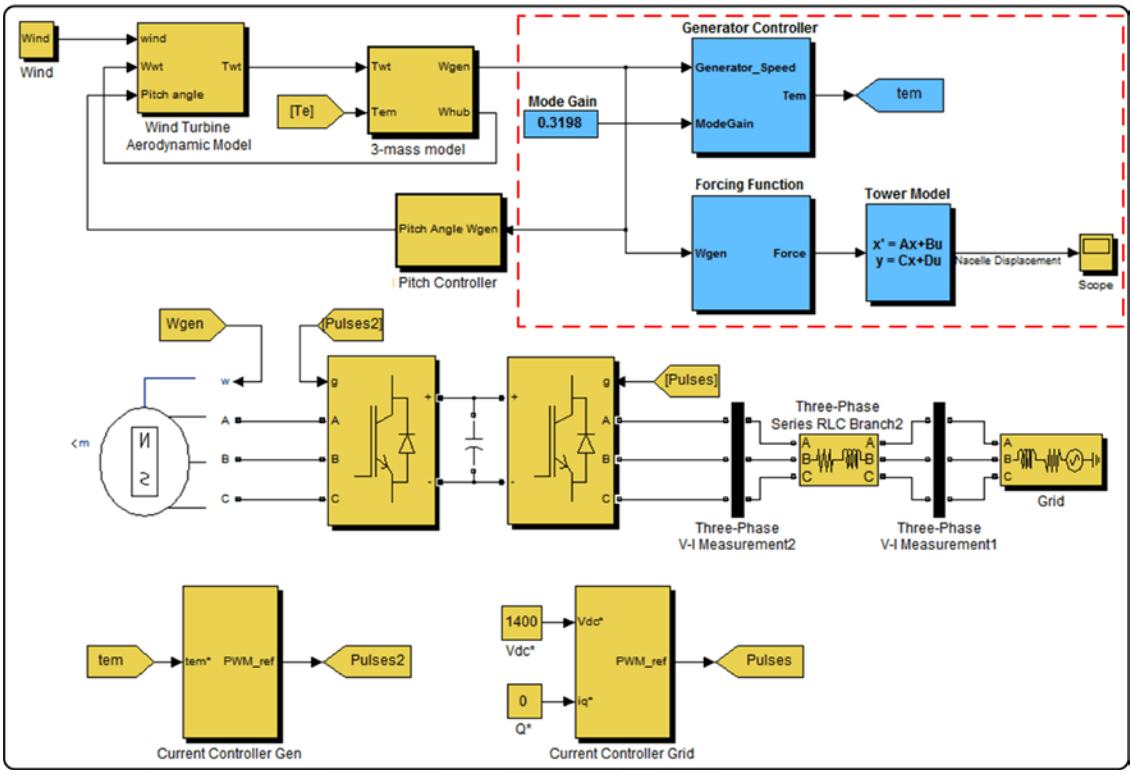

Figure 6.8: WT block diagram used for testing the speed exclusion zone

6.6.1. Fixed mean turbulent wind

A simulation with a turbulent wind speed with a mean of 8.5 m/s was performed. This wind speed was used because it corresponds to the critical rotor speed at which the side-side tower mode is excited. In this case, the width of the speed exclusion zone was set to ±10% the critical speed (0.262 Hz). The nacelle displacement was recorded to assess the tower oscillations with and without the speed exclusion zone. The simulation results are shown in Figure 6.9 and the experimental results are shown in Figure 6.10.

The results from the simulations and experiments were in good agreement and showed that the nacelle displacements were considerably lower when the speed exclusion zone was employed. This means that the magnitude of the tower oscillations is lower and hence the tower experiences less fatigue loads. In the case without the speed exclusion zone, whenever the generator speed matched the critical speed, the tower mode was excited and the nacelle displacement increased.

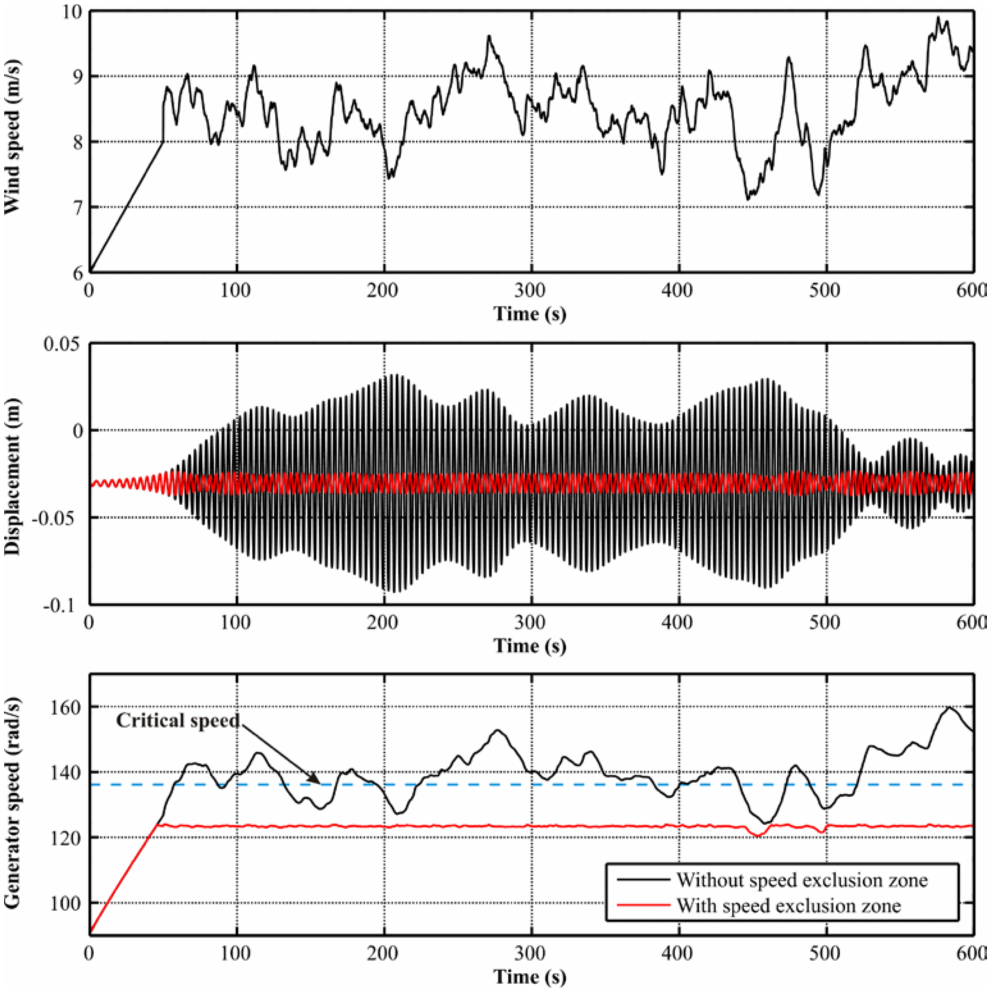

Figure 6.9: Simulation with a turbulent wind with a mean of 8.5 m/s

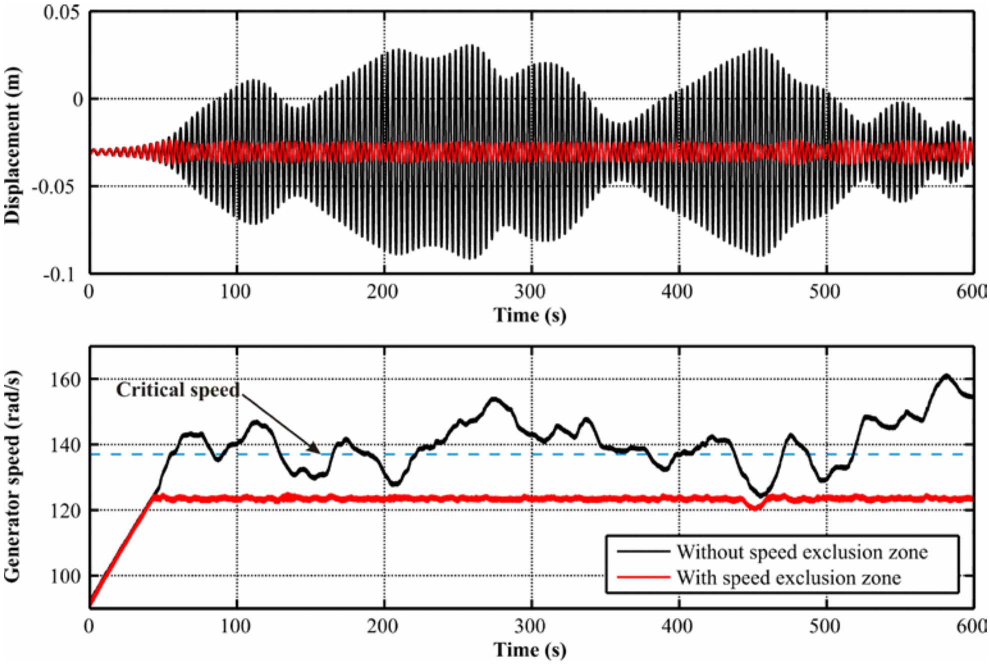

Figure 6.10: Experiment with a turbulent wind with a mean of 8.5 m/s

6.6.2. Variable mean turbulent wind

The simulation results for a turbulent wind speed with a varying mean ranging from 7.5 − 9 m/s are shown in Figure 6.11. This wind mean variation was introduced to enable the generator to cross the speed exclusion zone and to observe the effect on the nacelle displacement during such an event. A width of ±10% for the speed exclusion zone and a hysteresis time of 10 s were used.

From the simulation results it can be observed that the system equipped with the speed exclusion zone exhibited lower nacelle excursions. However, when compared to the previous case (turbulent wind with fixed mean), it can be noted that the nacelle displacement increased slightly during the crossing of the speed exclusion zone. This was because during crossing, the generator speed momentarily equalled the critical speed (at 260 and 460 s) and hence the tower mode was slightly excited.

The experimental results are shown in Figure 6.12. Although these results are in good agreement with the simulations, it can be noted that in the experiment case the generator crossed the speed exclusion zone faster. This faster speed response can be attributed to the lower inertia of the generator used in the experiment.

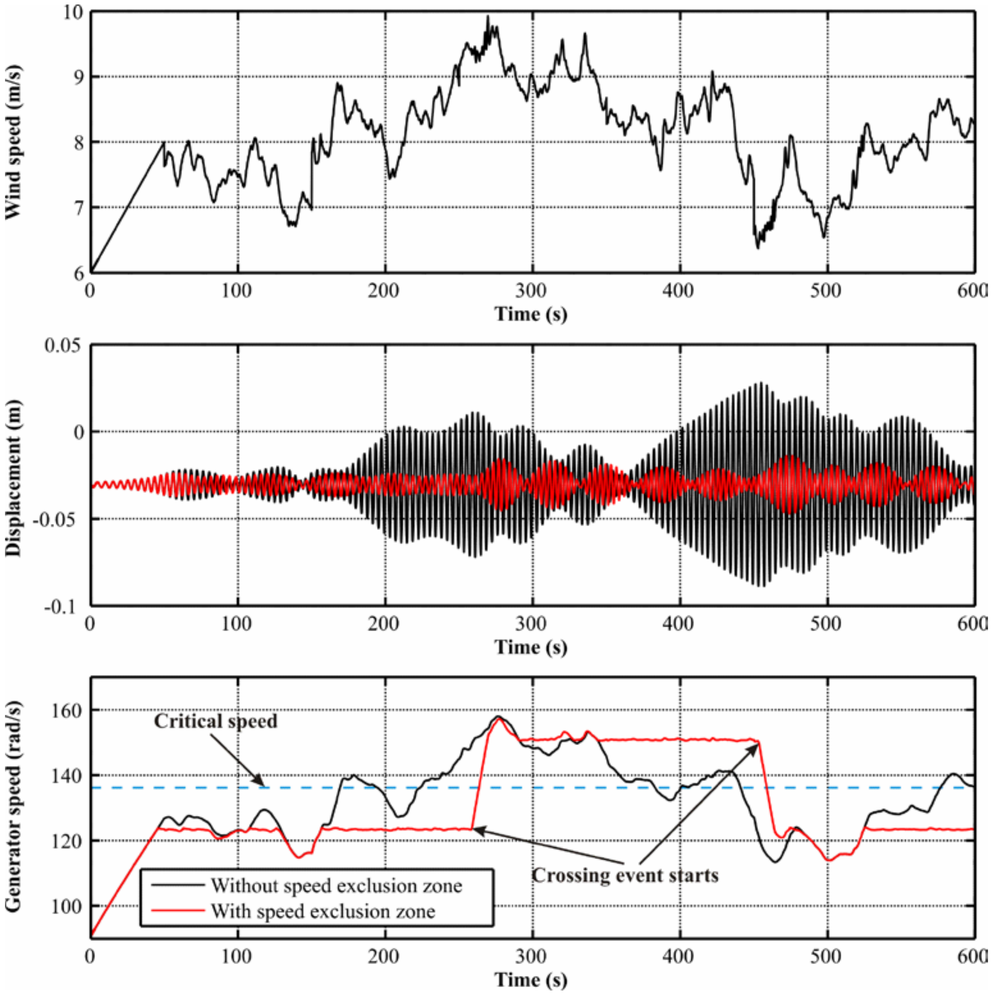

Figure 6.11: Simulation with a varying mean turbulent wind

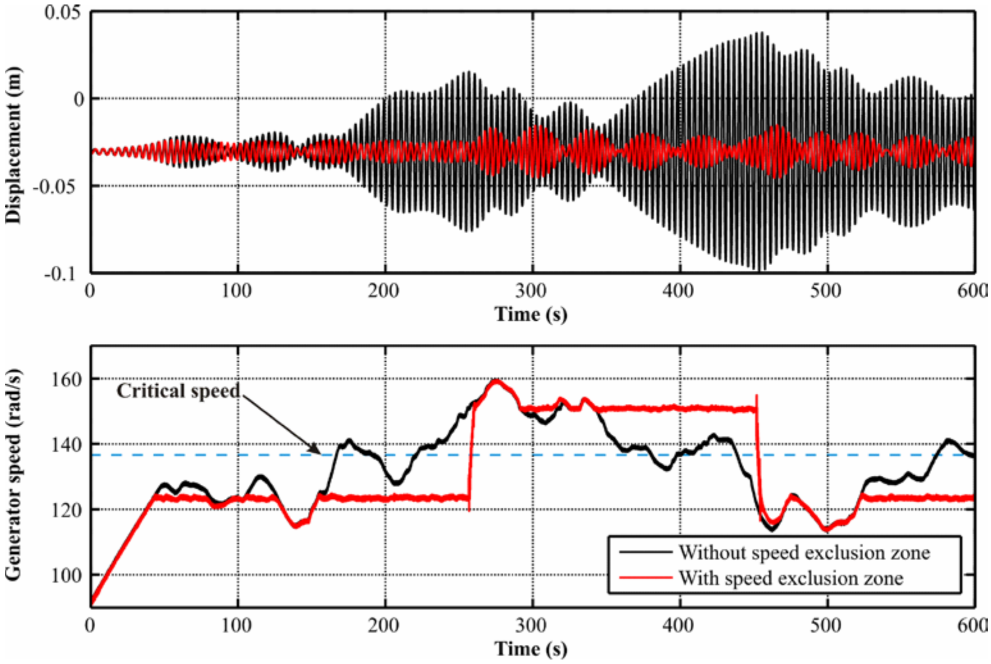

Figure 6.12: Experiment with a varying mean turbulent wind

6.6.3. Effect of different speed exclusion zone widths

In order to observe the effect of having different speed exclusion zone widths, simulations with no speed exclusion zone and two different exclusion zone widths (±10% and ±5%) were performed. For better interpretation of results the study was carried out with a steady wind speed varying from 6.5 − 9.5 m/s. In this case, apart from the nacelle displacement, the output power was also recorded. As the power rating of the simulated system (2 MW) and laboratory model (1.2 kW) are quite different, the output power was converted to pu on the respective machine base. The simulation and experimental results are shown in Figure 6.13 and Figure 6.14, respectively.

Simulation and experimental results showed that when the wind speed was between 6.5 and 8.2 m/s, the WT had the same output power and identical nacelle displacement in all three cases (without, with ±5% and ±10% speed exclusion zone).

As the wind speed increased, the system with the ±10% exclusion zone was the first to hold the generator speed fixed at its lower boundary. When the wind speed increased further, the system with the ±5% exclusion zone followed and held the generator speed fixed. Results showed that as the width of the speed exclusion zone was reduced, the system exhibited larger nacelle displacements. This was because the fixed-speed boundaries with the ±5% width are closer to the critical speed than in the case of ±10%. Hence, the forcing function frequency is closer to the tower frequency. Moreover, it was observed that the power output increased when width was reduced from ±10% to ±5%.

Figure 6.15 illustrates an expanded time plot (80 − 130 s) of the output power from the experiment results (Figure 6.14). This time range corresponds to the region during which both systems are operating at fixed speed at their respective lower boundaries. In this region, it can be observed that the output power of the system with a speed exclusion zone width of ±5% is 0.01pu higher than that with a width of ±10%. This means that for a 5 MW WT, the power loss at the lower fixed speed boundary amounts to 50 kW. Similarly, when the generator is operating at the upper fixed speed boundary the difference in output power for the two width cases is 0.005pu.

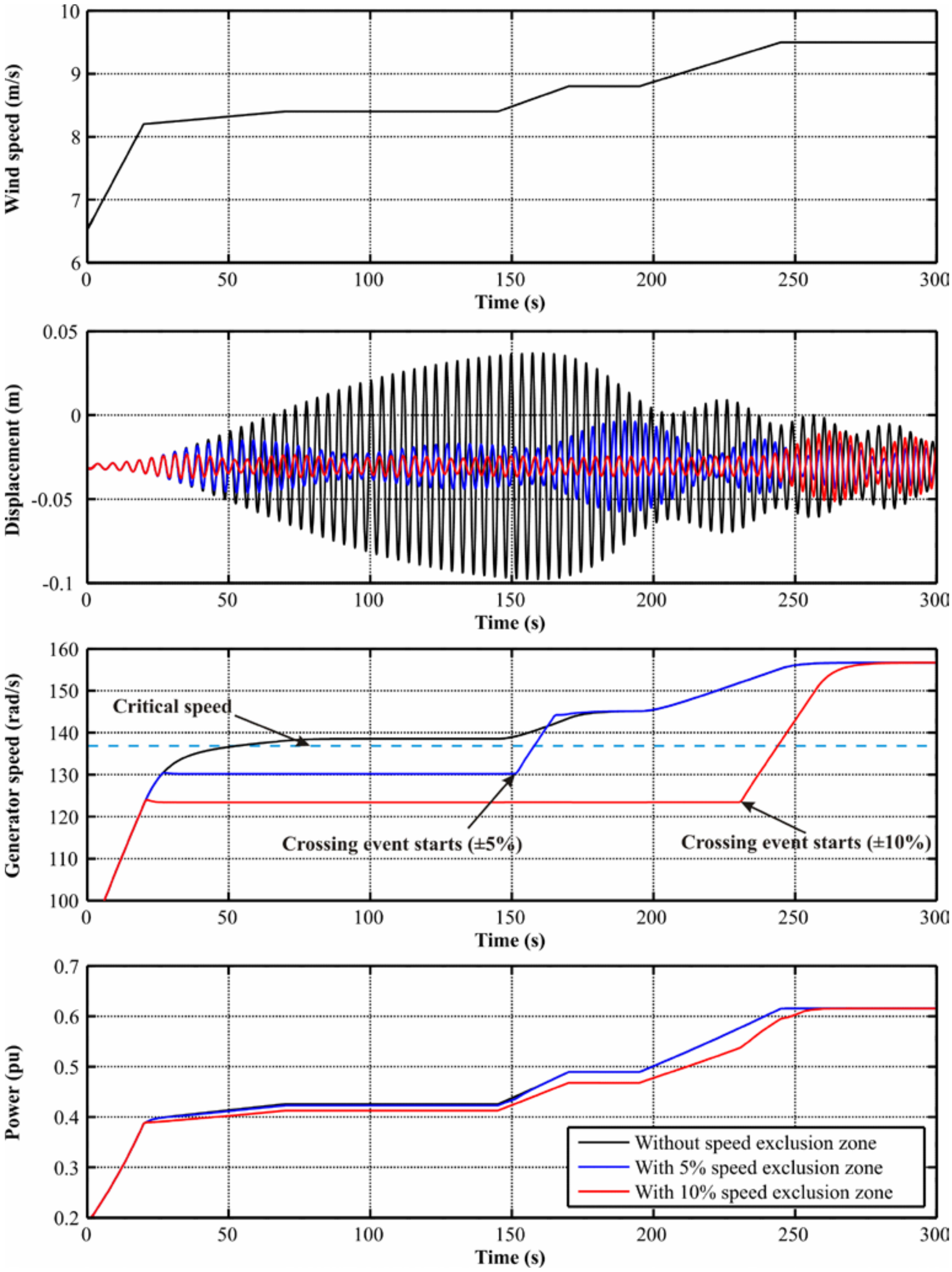

Figure 6.13: Simulation results for ±5% and ±10% speed exclusion zone

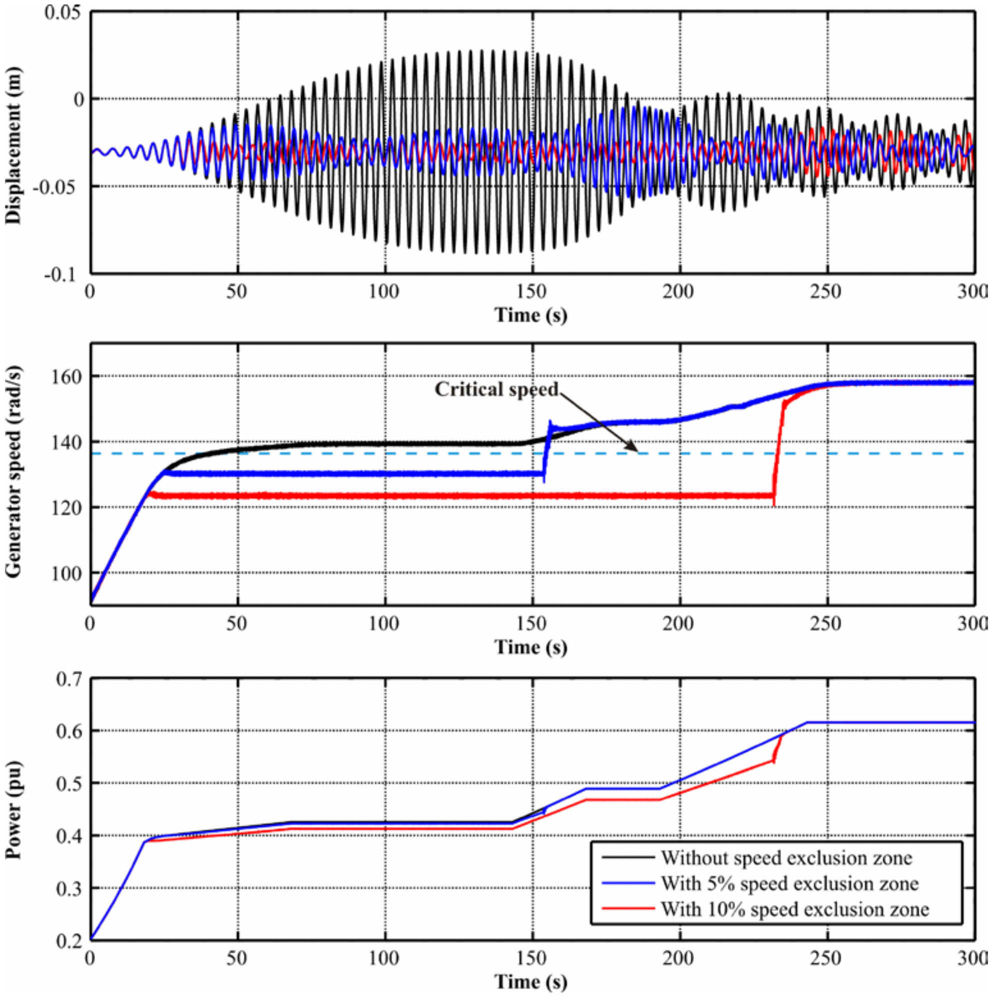

Figure 6.14: Experimental results for ±5% and ±10% speed exclusion zone

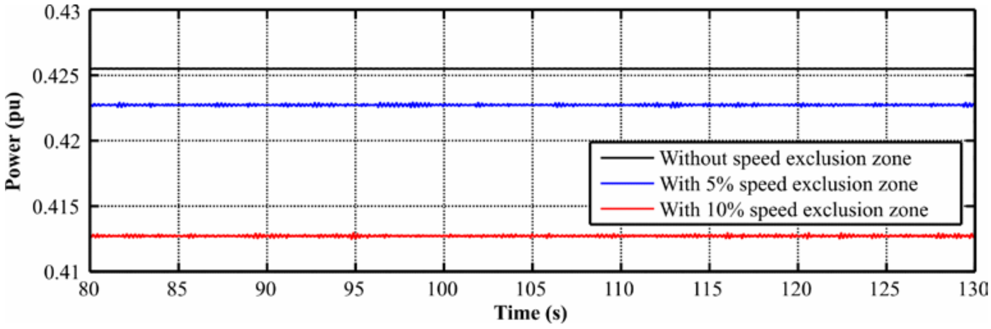

Figure 6.15: Expanded plot of the output power

To quantify the annual energy loss with different speed exclusion zone widths, the wind distribution gathered from the offshore mast FINO1 was used. The Weibull distribution is shown in Figure 6.16 [118]. The range of wind speeds for the two speed exclusion zone widths during which the WT will be operating at the fixed-speed boundaries is also shown.

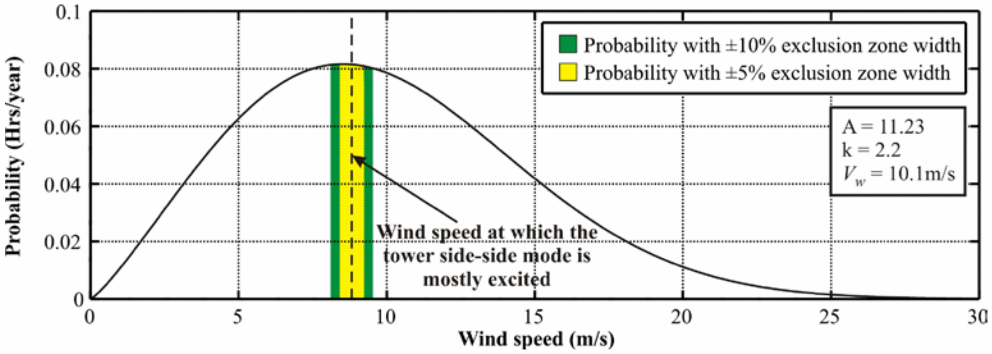

Figure 6.16: Weibull distribution for the wind data measured at FINO1 at 100 m height

Using this wind speed distribution, the probabilities that the WTs will be operating at the fixed-speed boundaries for the exclusion zone width cases (±5% and ±10%) are 6% and 11.36%, respectively. Table 6-1 shows the energy loss for a 5 MW WT assuming 100% availability of the WT for the following cases:

- Case 1: WTs are operating at the lower fixed-speed boundary at all times (*i.e.*, WT_1 (−5%) for 6% and WT_2 (−10%) for 11.36% of the total probable time)
- Case 2: WTs are operating at the upper fixed-speed boundary at all times (*i.e.*, WT_1 (+5%) for 6% and WT_2 (+10%) for 11.36% of the total probable time)
- Case 3: WTs are operating for the same time at the lower and upper fixed-speed boundaries (*i.e.*, WT_1 (−5%) for 3% and (+5%) for 3%, WT_2 (−10%) for 5.68% and (+10%) for 5.68% of the total probable time)

Table 6-1: Annual energy yield for different speed exclusion zone widths

	Annual Energy for different widths (MWh)			**Energy loss (MWh)**
	No exclusion zone	**±5%**	**±10%**	**(±5%) – (±10%)**
Case 1	26174	26170	26122	**48**
Case 2	26174	26168	26132	**36**
Case 3	26174	26169	26127	**42**

In all three cases, the results showed that by reducing the width of the speed exclusion zone from ±10% to ±5% a slightly higher energy is produced. In Case 3 for instance, the annual energy yield increased by 42 MWh (0.16%).

6.7. Conclusion

A speed exclusion zone algorithm was designed to prevent the generator from operating at the critical speed where the tower side-side mode can be excited. The displacement at the tower top was used to investigate the effectiveness of the algorithm.

Results for turbulent wind speed with a mean of 8.5 m/s showed that the nacelle displacement was reduced with the speed exclusion zone. The effect of having the speed of the generator momentarily equal to the tower mode during the crossing of the speed exclusion zone was also assessed. Results showed that the tower mode was excited slightly during crossing; however, the nacelle displacements were still lower than in the case without the speed exclusion zone.

An evaluation of the effect of having different speed exclusion zone widths was also performed. Results showed that reducing the width from ±10% to ±5% contributed to larger nacelle displacements. This was because the fixed-speed boundaries of the speed exclusion zone were closer to the critical speed. On the other hand, the gain in annual energy yield was only 0.16% when the width was reduced from ±10% to ±5%.

A speed exclusion zone algorithm prevents tower resonance and thus alleviates excess fatigue loads in the tower. A compromise between the energy lost (wide zone) and the increase in tower fatigue loads (narrow zone) has to be reached in order to set the width of the speed exclusion zone.

Chapter 7

Inertial Response

Summary:

This chapter focuses on the provision of inertial response from a FRC-PMSG based WTs and wind farms. An inertial response controller is first presented. The contributions of the loops within this controller are then discussed. Simulations for below and above rated wind speeds are performed for various parameters (gains and delays) of the inertial response controller. A simplified WT model is then developed. A simulation is performed to validate the inertial response achieved from this model against that obtained from a detailed WT model and from experimental results. The simple WT representation is then used to construct a wind farm model. A coordinated inertial response from each WT in the wind farm is then performed. Finally, the inertial response from a FRC-PMSG based wind farm is compared to a fixed-speed IG based wind farm.

7.1. Introduction

The integration of wind energy into an existing power system brings about technical and regulatory challenges. System inertia is one of the important technical aspects that needs investigation. This is because it determines the sensitivity of the power system for changes in the system frequency due to supply and demand imbalances.

Modern WTs operate at variable-speed to maximise the power extracted from the wind. To accomplish this task, such turbines typically employ generators that are connected to the grid through either a PRC or a FRC. As opposed to synchronous turbo generators, synchronous machines and induction machine loads, a VSWT does not contribute to system inertia. Therefore, as VSWTs start replacing power plants, the system inertia will decrease. This may create difficulties in containing the system frequency after a frequency event.

Although VSWTs do not provide natural inertial response, by using appropriate supplementary control action on their generator torque controllers, it is possible to force a VSWT to contribute to system inertia.

7.2. Inertial Response from a FRC-based WT

The kinetic energy stored in a rotor of a VSWT is given by

$$E_{KE} = \frac{1}{2} J \omega_{rot}^2 \tag{7.1}$$

where J is the inertia of the rotor [kgm^2] and ω_{rot} is the rotor speed [rad/s]. The power is given by

$$P = \frac{dE_{KE}}{dt} = J \omega_{rot} \frac{d\omega_{rot}}{dt} \tag{7.2}$$

This can be expressed in terms of the per unit inertia constant H as [23]

$$\begin{aligned} P &= \left(\frac{2HS_{base}}{\omega_{rated}^2} \right) \omega_{rot} \frac{d\omega_{rot}}{dt} \\ \Rightarrow \bar{P} &= 2H \bar{\omega}_{rot} \frac{d\bar{\omega}_{rot}}{dt} \end{aligned} \tag{7.3}$$

where the bar means that the variable is in pu.

Equation (7.3) shows that whenever there is a change in the rotor speed a corresponding change in power occurs. Therefore, the energy stored in the rotor can be used by the WT to provide inertial response. However, in a FRC based VSWT the rotor speed is controlled through the generator controller and is not affected by any changes in system frequency. This means that for such turbines the rotor speed change has to be emulated through the generator torque controller.

7.2.1. Emulated inertial response

In order to obtain inertial response in FRC-PMSG based WT, a supplementary control signal τ_{dec} proportional to the rate of change of the system frequency $\left({df}/{dt} \right)$ was added to the generator torque controller as shown in Figure 7.1.

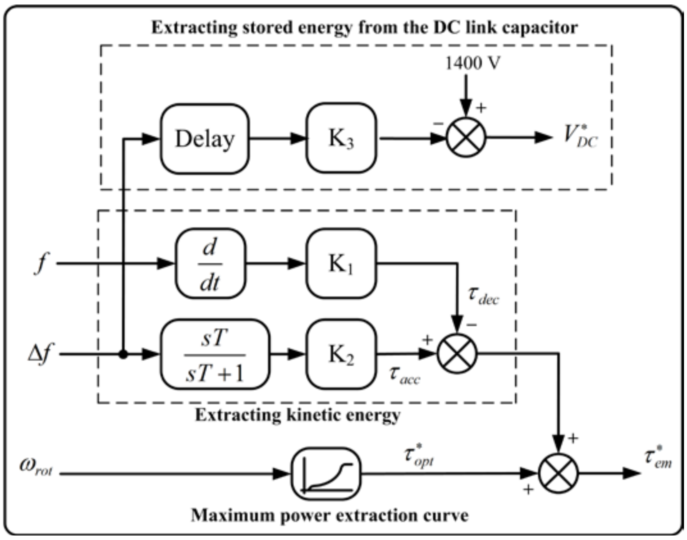

Figure 7.1: Inertial response controller

When there is a frequency drop, the auxiliary control action applies a deceleration torque τ_{dec} to the generator (proportional to ${df}/{dt}$) which forces the rotor to slow down. This results in a period of over-power production due to the extraction of kinetic energy from the rotor as shown in Figure 7.2.

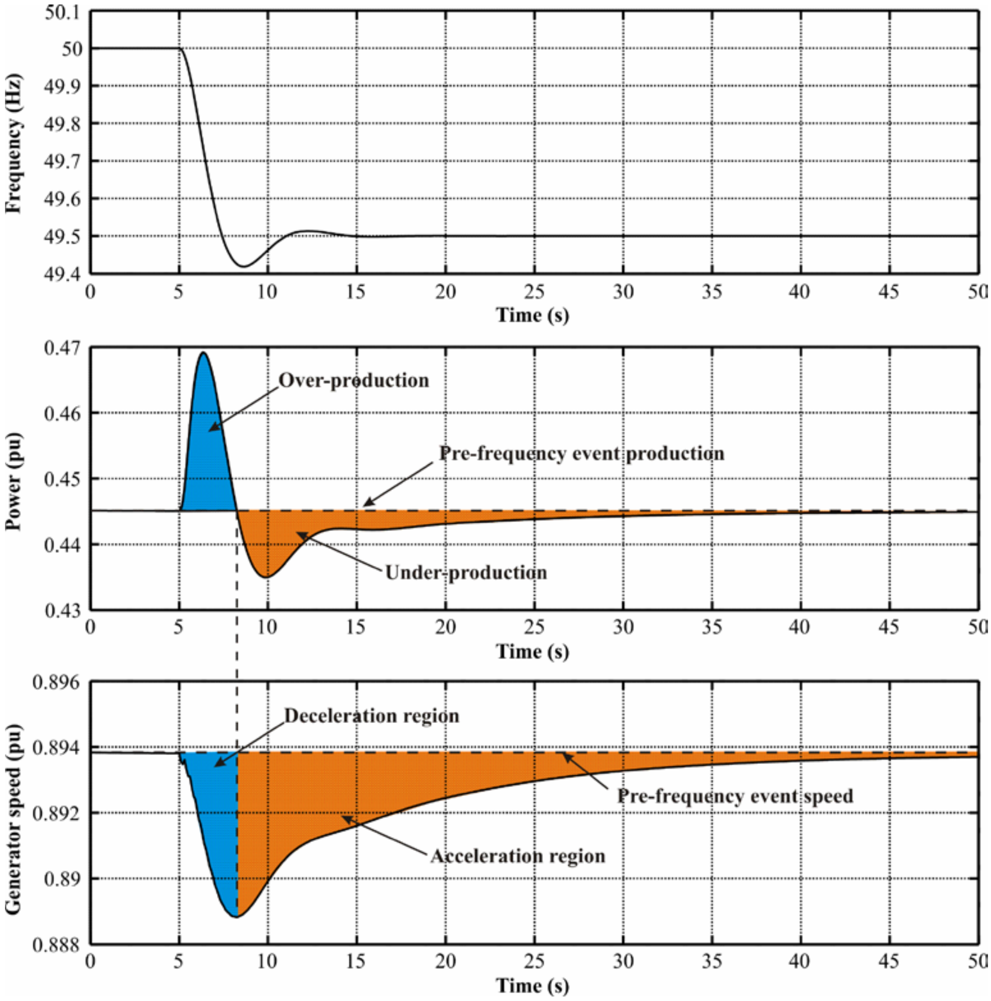

Figure 7.2: Inertial response using only τ_{dec}

Following the deceleration of the rotor, the WT reaches a new steady-state operating point were the generator torque reference is lower than the available aerodynamic torque ($\tau_{aero} > \tau_{em}$) assuming the wind speed does not change. This torque imbalance leads to the acceleration of the rotor during which the WT output power drops below the pre-frequency event level (recovery period). This is shown in Figure 7.2.

The most critical period in an inertial response is during the first 10 s (5 − 15 s) as the power system needs support to arrest the collapsing frequency. Unfortunately, after a short over-production (3 s) a period of under-production follows. This drop in output power is undesirable because it will contribute further to the increase in mismatch between generation and demand.

In order to minimise this shortcoming, an additional torque term τ_{acc} proportional to Δf was used. The problem of the deceleration torque loop is that τ_{dec} decays to zero as soon as ${}^{df}\!/_{dt} \rightarrow 0$, even though the system frequency has not been restored. The idea behind the τ_{acc} loop is to delay the start of the rotor acceleration period and thus the period of under-production. In order to accomplish this, a high-pass filter with a time constant of 2 s was included. The effect of this loop on the demanded generator torque is shown in Figure 7.3. It is worth noting that apart from the increase in the peak torque demand (0.03 to 0.039pu), the time at which the acceleration of the rotor starts has been delayed by 1 s (8.5 to 9.5 s).

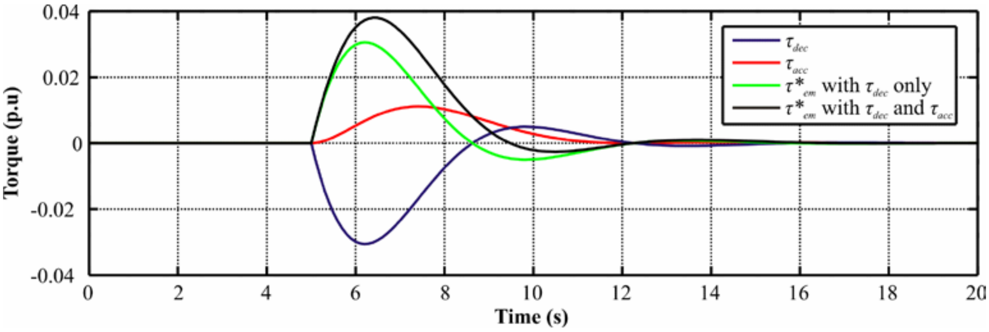

Figure 7.3: Torque contributions from the different loops

Another possible option to improve the inertial response is to extract some of the stored energy from the DC link capacitor bank. In this case, an additional loop that generates a reduction in the DC link voltage reference proportional to Δf (delayed by 2.5 s) was used. This is shown in the uppermost loop of the inertial response controller in Figure 7.1. Under normal operation the DC link voltage was maintained at 1400 V.

7.2.2. Simulation results

In order to observe the inertial response of a FRC-based WT, time domain simulations were performed using the WT model shown in Figure 7.4. Different inertial responses were obtained by changing the gains K_1, K_2 and K_3 and the delay setting for DC link energy extraction loop. A frequency deviation of 0.5 Hz at 5 s was applied to the inertial response controller to mimic a frequency change in a power system as shown in Figure 7.5 (a).

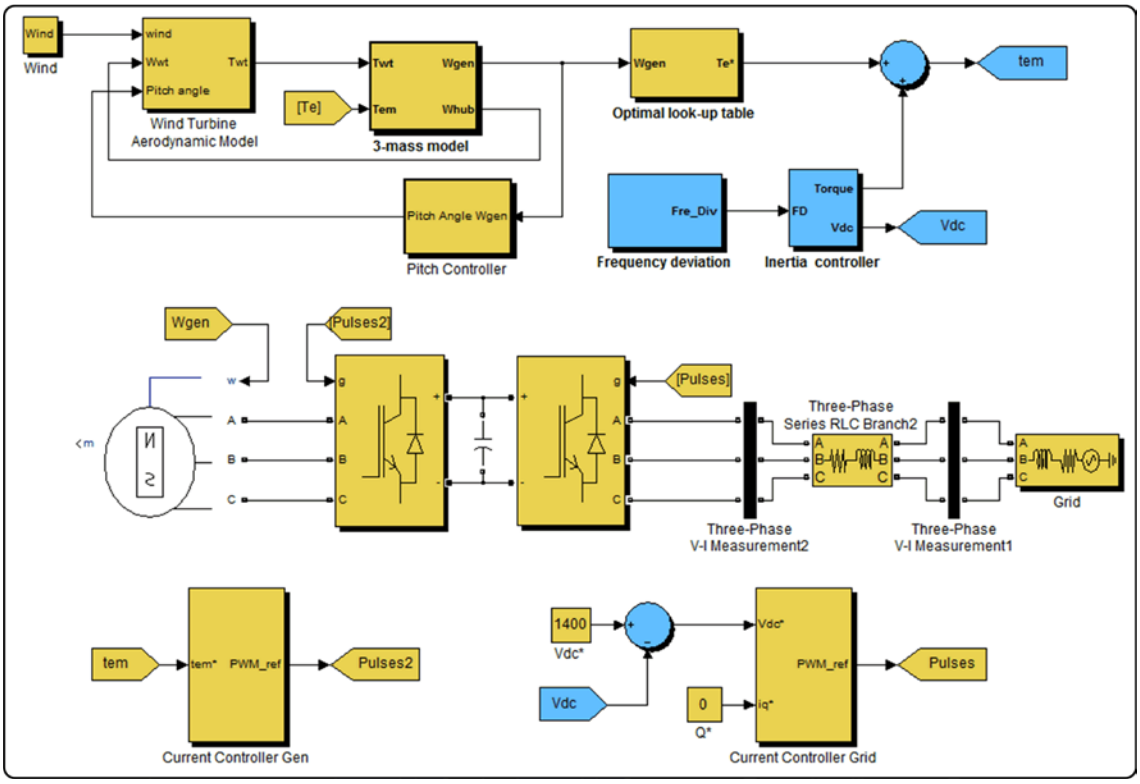

Figure 7.4: WT block diagram used for testing the inertial response

The first simulation was performed with a fixed wind speed of 8.5 m/s to observe the inertial response of the WT when it is operating below rated wind speed. The response obtained is shown in Figure 7.5 (b).

It can be observed that the inertial response with the additional torque term τ_{acc} (red) is better than in the case with the τ_{dec} loop only (green). An increase in peak power of approximately 0.01pu and a 0.7 s longer time before the rotor starts accelerating was noted.

Further improvement was obtained by utilising some of the energy stored in the DC link capacitor. With a delay of 2.5 s, there was no increase in peak power; however, the time during which the WT was over-producing was slightly increased (cyan). In this case, the energy in the DC link capacitor was just used to delay further the start of the rotor acceleration phase and hence the region of under-production. When the delay was reduced from 2.5 s to 1 s (purple), an increase in the peak power output at the expense of shorter over-production period was obtained.

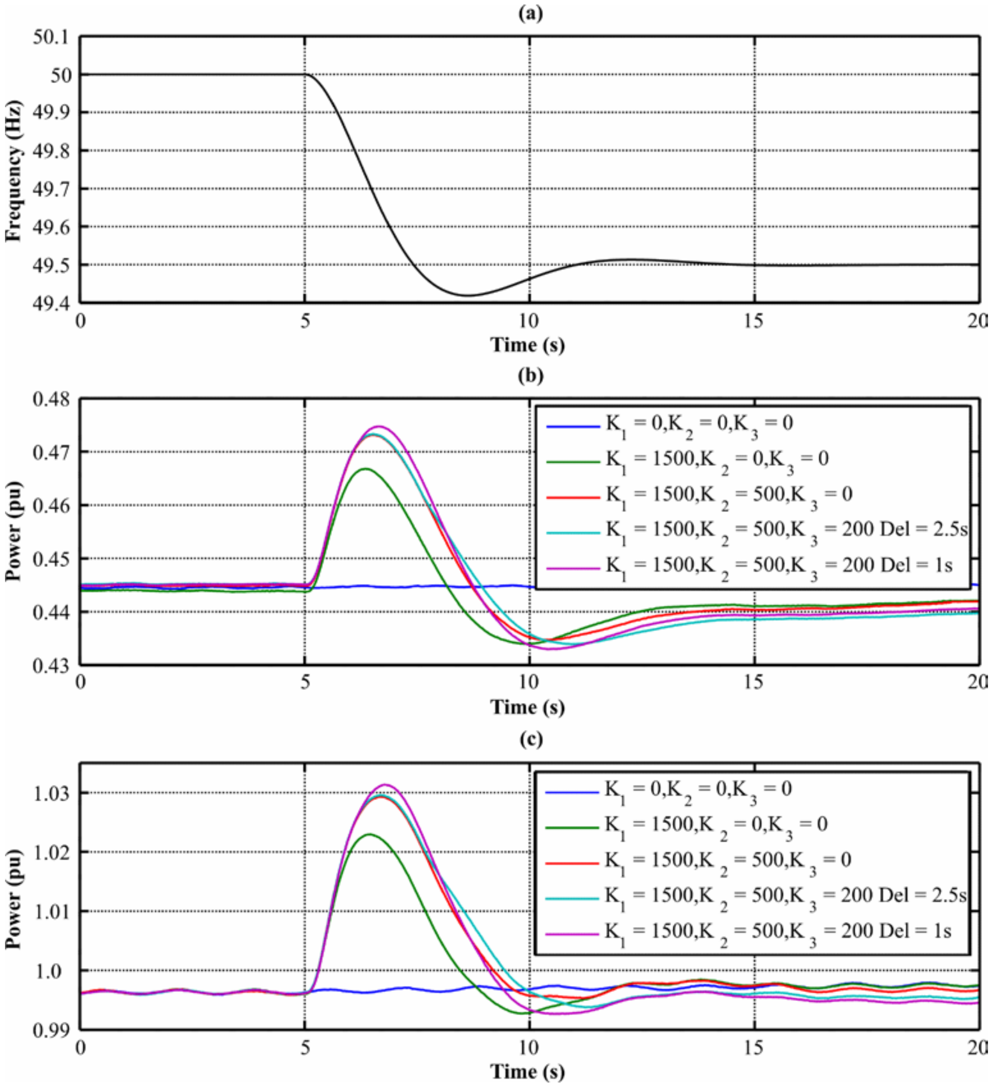

Figure 7.5: (a) Frequency event – Power output (b) below rated wind speed (c) above rated wind speed

The inertial response obtained for above rated wind speed of 20 m/s is shown in Figure 7.5 (c). Similarly to the below rated wind speed case, it is evident that an improvement in the inertial response was achieved with the introduction of the τ_{acc} and the DC link energy extraction loops. It is worth noting that in above rated wind speed cases, the converters should have a transient power capability of 3% above their continuous rating. Another important observation is that the recovery power dip (after the delivery of the power burst) is smaller than in the case of below rated wind speed. The reason for this can be explained using Figure 7.6.

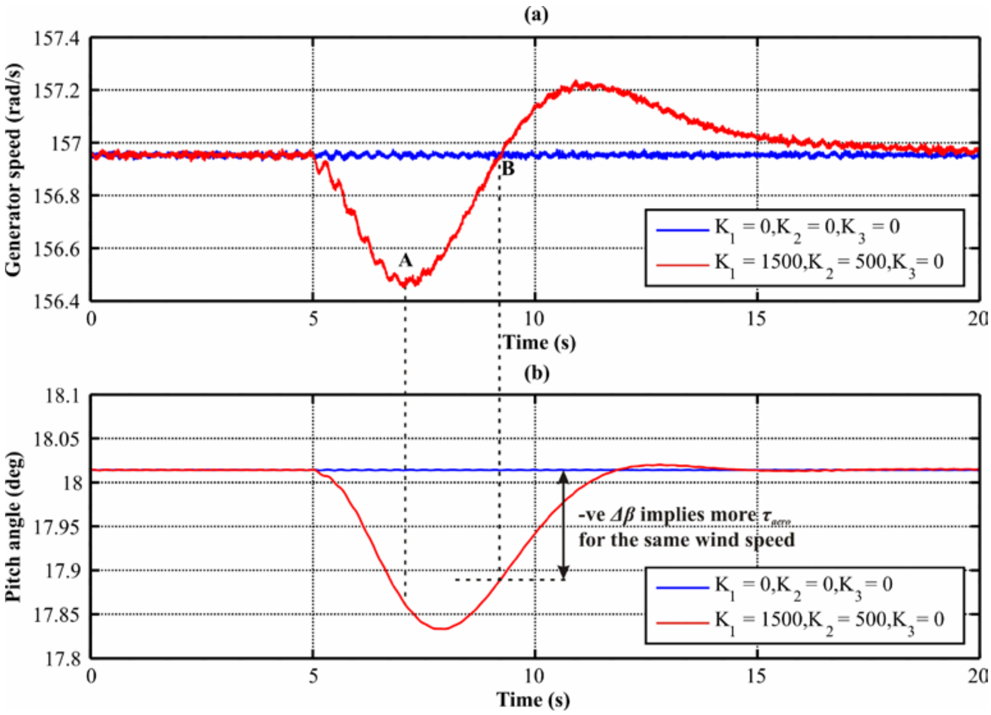

Figure 7.6: (a) Generator speed and (b) Pitch angle during an inertial response

When the pitch controller senses a drop in generator speed (due to extraction of kinetic energy from the rotor), it reduces the pitch angle to control the speed back to rated (5 – 8 s). At point A, the generator speed starts its recovery. For a wind speed of 20 m/s the pitch angle to balance the aerodynamic torque and the generator opposing torque is approximately 18.02° but at point A it is still at 17.86°. As a consequence the imbalance between the aerodynamic and generator torque will be much higher resulting into a faster acceleration of the generator towards rated speed. This results in a smaller recovery power dip (Figure 7.5 (c)). At point B, the generator reaches rated speed but the pitch angle is still not at steady state hence the speed overshoot.

7.3. Inertial response from wind farms

In the previous section, an inertial response from a single WT was demonstrated. One of the main concerns of this response is the period of under-production after inertial response has been provided. Although individual WTs provide rather poor inertial response performance within the first 3 − 4 s, a wind farm could provide a better inertial response as it has a large number of generators and each operating differently. This operation diversity of generators can be used to provide a coordinated inertial response from a wind farm using a SCADA system.

A typical wind farm control consists of a SCADA system that integrates individual turbine information into the wind farm control and monitoring functions. A SCADA system allows the wind farm operator to monitor and control each WT and regulate the active and reactive power or power factor of the wind farm in a coordinated manner. Turbines should be able to accept plant level control commands in real-time and follow control references. For instance, the wind farm power controller accepts reference values from the transmission system operator and then sends individual power commands to each WT through the SCADA system.

7.3.1. Simplified WT model for modelling the wind farm

As discussed previously, the inertial response loop modifies the torque set-point of the generator controller. Since maximum torque per ampere strategy is used for the generator, only the *q*-axis current affects torque generation (assuming no saliency). Therefore the *q*-axis voltage equation (3.17) can be simplified to

$$\frac{d}{dt}i_q = -\frac{R_s}{L_q}i_q + \frac{v_q - \omega_{gen}\lambda_m}{L_q} \tag{7.4}$$

Rearranging equation (7.4) and multiplying by L_q/R_s yields

$$\frac{L_q}{R_s}\frac{d}{dt}i_q + i_q = \frac{v_q - \omega_{gen}\lambda_m}{R_s} \tag{7.5}$$

In the Laplace domain, equation (7.5) is expressed as

$$\left(\frac{L_q}{R_s}s + 1\right)i_q = \frac{v_q - \omega_{gen}\lambda_m}{R_s} \tag{7.6}$$

The simplified model of FRC-PMSG based WT with the inertial response controller is shown in Figure 7.7. F_1 and F_2 are $\frac{2}{3n_{pp}\lambda_m}$ and $\frac{3}{2}n_{pp}\lambda_m$, respectively. All parameters are included in Appendix A.1 and the generator current controller (PI) parameters are given in Appendix A.2, Table A-3.

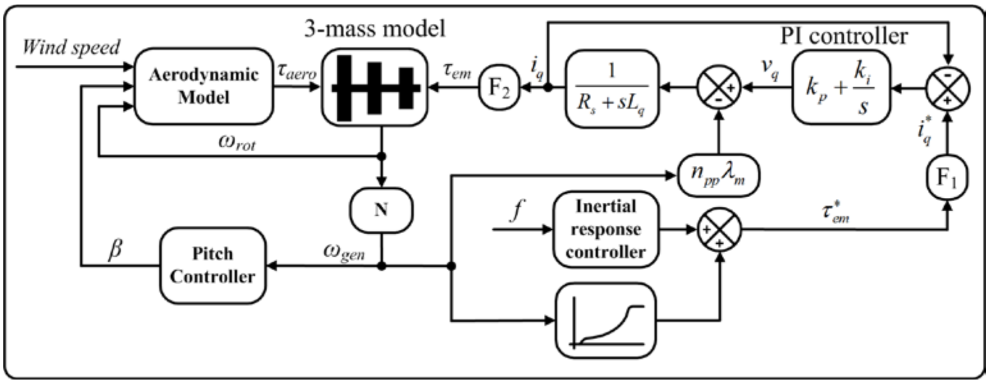

Figure 7.7: Block diagram of the simplified WT with the inertial response controller

7.3.2. Validation of the simplified WT model

In order to validate the simplified WT model, a simulation of an inertial response was performed in Simulink® for the detailed (shown in Figure 7.4) and the simplified WT models (shown in Figure 7.7) with a wind speed of 8.5 m/s. The frequency change shown in Figure 7.8 was applied to the inertial control loop at 5 s in both model cases. Moreover, a real-time hardware in the loop experiment was performed as outlined in Section 4.2.

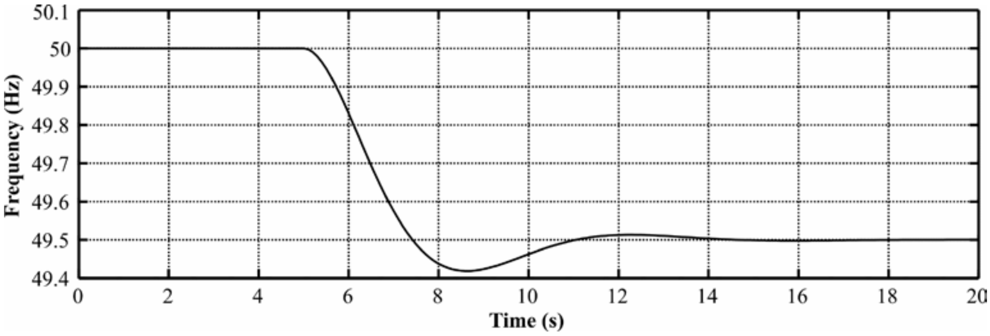

Figure 7.8: Frequency deviation

As the rating of the simulated system (2 MW) and laboratory model (1.2 kW) are quite different, the inertial response obtained was converted to per unit on the respective machine bases (2 MW and 1.2 kW) and is shown in Figure 7.9. A substantial agreement among the inertial responses obtained can be observed. Hence, the simplified WT representation was used to model a wind farm to analyse its inertial response when subjected to a frequency event.

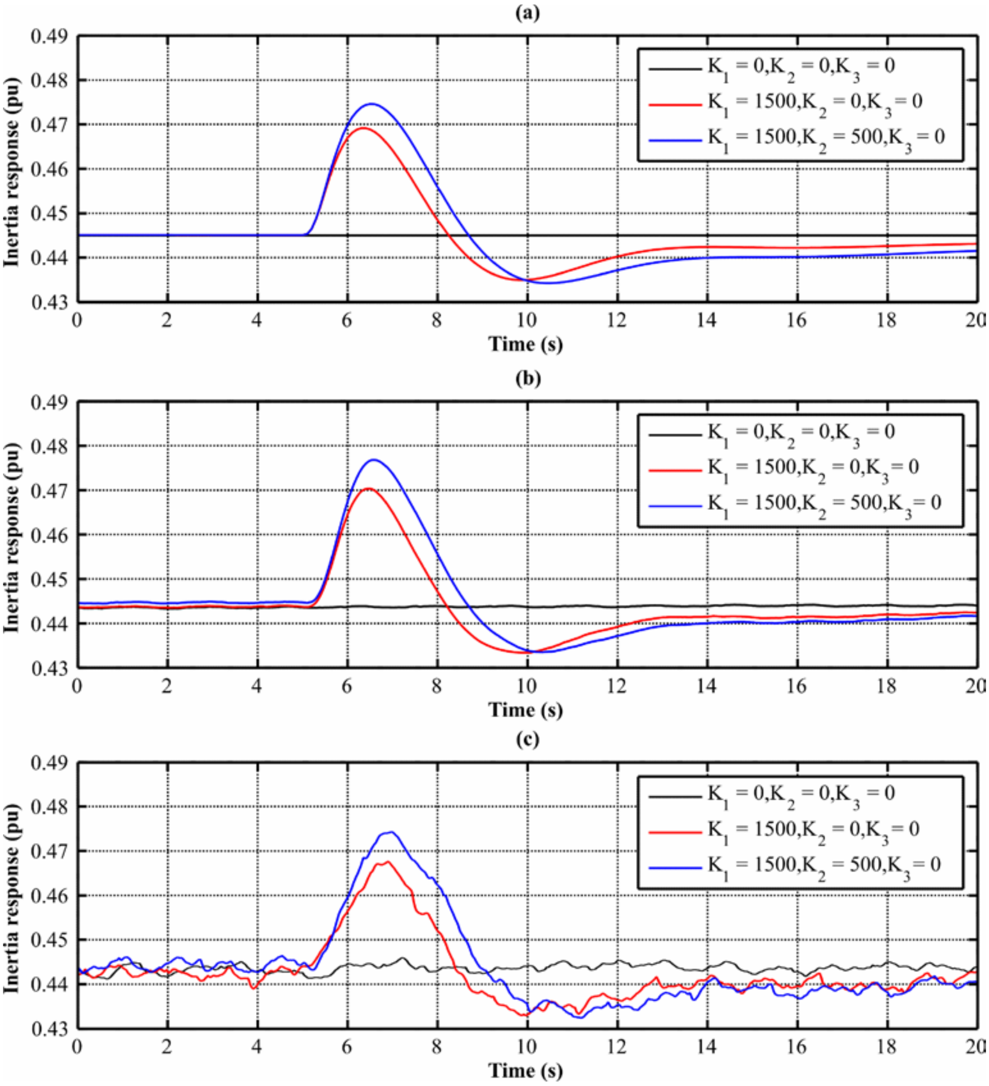

Figure 7.9: Inertial response (a) Simulation simple model (b) Simulation detailed model (c) Experiment

7.3.3. Simulation of wind farm inertial response

In order to demonstrate wind farm inertial response, an offshore wind farm that is connected to the terrestrial grid through a high-voltage DC link was considered. In this case, it was assumed that the SCADA sitting on the collector platform has real-time information about the status of each WT and the latency in the communication network is negligible.

Depending on the operating wind speed, a number of WTs are clustered by the SCADA to send inertial response commands. For instance WTs operating at lower wind speeds (4 − 6 m/s) will act on the measured frequency signal directly, whereas WTs operating at higher wind speed bands will receive slightly delayed frequency signal. The reason of clustering the WTs this way can be explained using Figure 7.5. The turbines operating below rated wind speed have a larger recovery power dip (under-production) which can be compensated by the inertial response from other turbines. As the recovery dip of the WTs operating above rated wind speed is lower, scheduling them last will reduce the recovery dip of the entire wind farm.

In this demonstration, 10 clusters representing different wind speed bands (4 m/s − 24 m/s) were used as shown in Figure 7.10. Each WT in the wind farm was modelled using the simplified model shown in Figure 7.7. The system was simulated in Simulink$^{®}$ and the frequency signal shown in Figure 7.11 was used for the first cluster (4 − 6 m/s). This signal was delayed to the other clusters operating a higher wind speed ($f + del_x$). Due to the simplicity of the WT model used, the inertial response controller was limited to the τ_{dec} and τ_{acc} loops only.

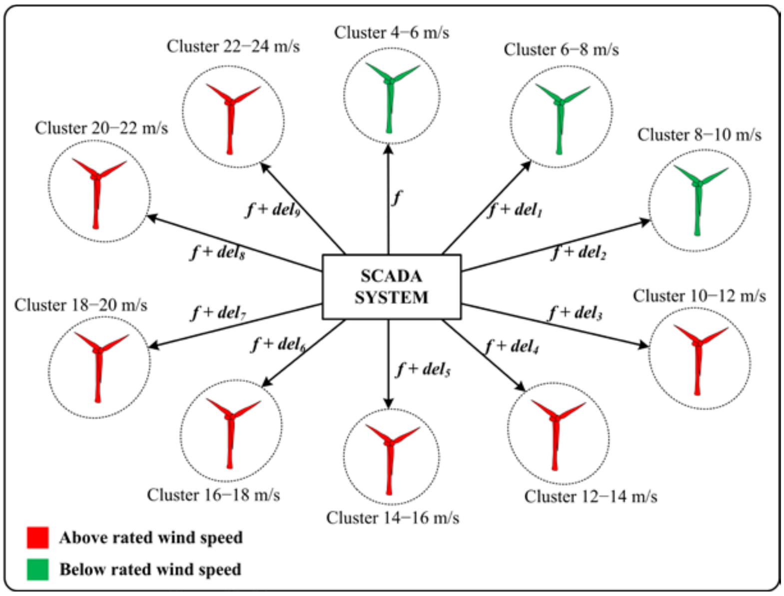

Figure 7.10: System considered for the wind farm inertial response

The inertial response of the wind farm for frequency signals with different delays between clusters for $K_1 = 1500$ and $K_2 = 500$ is shown in Figure 7.11. It shows the response for the following conditions: when a fixed delay of 1 s or 1.5 s between two clusters exists, and when the delay between two clusters was variable with increasing intervals of 0.15 s (starting at 0.15 s between the first two clusters, 0.3 s between the next two clusters, etc) and 0.25 s (starting at 0.25 s, then 0.5 s, etc). It can be observed that the wind farm managed to support the grid during the critical period (0 − 10 s) in all the different delay cases shown. The best performance was obtained with a variable delay with an increasing interval of 0.15 s.

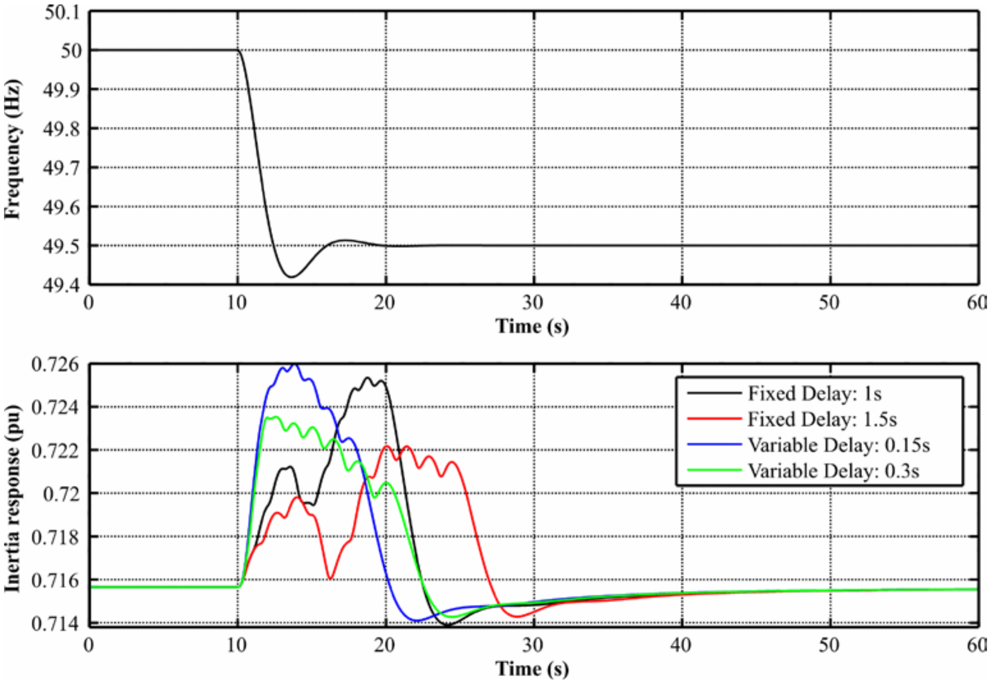

Figure 7.11: Inertial response from the wind farm

In order to demonstrate the flexibility and the improved performance that can be provided by a FRC-PMSG based wind farm, the response of the system shown in Figure 7.11 was compared to a response from a wind farm equipped with fixed-speed IG WTs. In this simulation it was assumed that the inertia constant of the IG-based WTs is 6 s. In order to obtain the same peak inertial response from the FRC-PMSG based wind farm as in the case of the fixed-speed IG based wind farm, the values of K_1 and K_2 were modified. For turbine clusters operating below rated wind speed, the gains were set to $K_1 = 5000$ and $K_2 = 3000$ whereas for the clusters operating at above rated wind speed the gains were set lower ($K_1 = 2000$ and $K_2 = 1200$) in order not to exceed the ratings of the turbines. A variable delay with an increasing interval of 0.15 s was used. Figure 7.12 shows the response obtained from the fixed-speed IG and the FRC-PMSG based wind farms. It can be observed that the peak inertial response of the FRC-PMSG based wind farm is comparable to the fixed-speed IG based wind farm and the over-production period was delayed from about 4 s (fixed-speed IG based WT) to about 15 s (FRC-PMSG based WT).

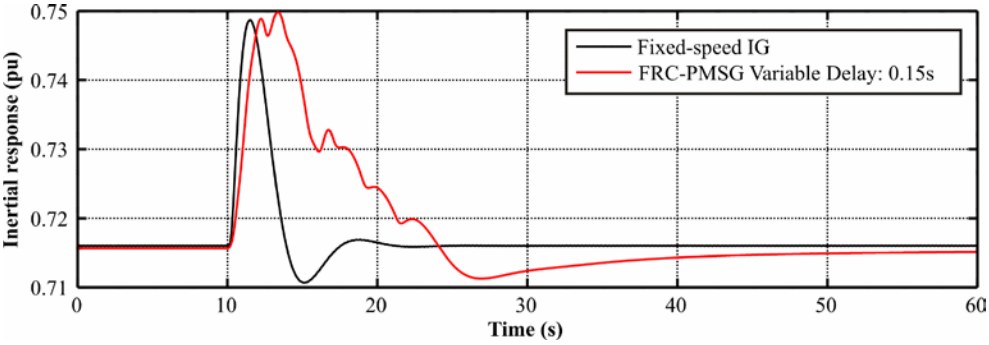

Figure 7.12: Comparison of inertial response from fixed-speed IG and FRC-PMSG based wind farms

7.4. Conclusion

The possibility of providing inertial response from FRC-PMSG based WTs was demonstrated through simulations and experiments. Supplementary control signals were added to generator-side and grid-side VSC to extract the kinetic energy stored in the rotating mass and the energy stored in the DC link capacitor. The control method used to extract the stored energy in the DC link capacitor was based on changing the DC link voltage reference. The delay used in this control loop is an important design parameter as it affected the peak power transferred into the grid during a frequency event.

A detailed model with full representation of the back-to-back VSC of the FRC-PMSG based WT and a laboratory prototype were used to show that emulated inertial response of about 0.03pu of the active power output during a frequency event can be provided for 3 − 4 s. This is comparable to the inertial response provided by a FSIG having an inertia constant of 6 s.

In order to demonstrate the possibility of coordinating the inertial response from each WT in a wind farm, a simplified WT model was developed and validated against the inertial response obtained from the detailed model and experimental results. The simplified model was then used to represent a wind farm with 10 clusters of WTs operating at different wind speeds. Using this model, it was demonstrated that the peak inertial response and the duration can be varied by changing the delay introduced to the frequency signal and gains of the inertial response control loop of each WT. By varying both the frequency signal delays and the inertial response control gains, it was shown that the peak emulated response provided by the FRC-PMSG based wind farm could be comparable to a fixed-speed IG based wind farm. Moreover, the starting time of the recovery period was delayed from about 4 s (fixed-speed IG based WT) to about 15 s (FRC-PMSG based WT). Following that in the FRC-PMSG based wind farm the recovery starts after 10 s, it means that collectively each turbine supports the frequency recovery of the power system.

Even though in this study it was assumed that the latency of the communication network is negligible, it is worth noting that latency only affects the first few clusters (depending on the delay) as the other clusters only act on delayed signals.

Chapter 8

Conclusion

Summary:

This chapter summarises the conclusions drawn from this research work, highlights the contributions, lists the publications made and outlines some recommendations for future work.

8.1. Conclusion

During the last decade, wind energy generation increased steadily and is expected to become one of the predominant energy sources in the coming future. Therefore, apart from ensuring a smooth transition from conventional power plants to wind power plants, the industry is striving to improve the cost-effectiveness of WTs thereby reducing the cost of wind energy.

The first part of this research addresses the mitigation of fatigue loads in the drive-train and the tower of a VSWT. The reduction of such loads helps to prevent premature failures of turbine components and hence increases the reliability of WTs. Ultimately, this means that the cost associated with component replacement, maintenance and energy lost due to the turbine downtime is reduced. This contributes towards the reduction of the cost of energy.

The second part deals with the provision of inertial response from VSWTs and wind farms. This ensures that the loss of inertia in the power system when migrating from conventional to wind power plants is mitigated. This contributes towards the achievement of a smooth transition when large penetration of wind energy replaces conventional power plants.

8.1.1. Wind turbine model

A 2 MW FRC-PMSG based VSWT model was derived and implemented in Simulink®. The turbine model was represented by an aerodynamic, drive-train, tower, pitch, generator and a back-to-back VSC models. The WT parameters used for all the models are not linked to any specific turbine but were obtained from a generic 2 MW WT model in Bladed®.

The control of the WT was accomplished by three coordinated controllers: a torque controller (generator-side converter), a DC link voltage and power factor controller (grid-side converter) and a pitch controller. All the controllers were designed using the root locus technique.

Simulation results showed that the performance of WT model with these controllers was good throughout a range of operating conditions. During below rated wind speeds, the generator-side controller controlled the generator torque for maximum power extraction whereas the grid-side converter controlled the DC link voltage by exporting active power to the grid. On the other hand, at above rated wind speeds, the generator torque was held fixed at rated torque and the generator speed was controlled by the pitch controller.

The performance obtained from the WT model was good and hence it was used for testing other supplementary control schemes.

8.1.2. Experimental test rig

A 1.2 kW experimental test rig was used to verify the simulation results obtained in this research. It consisted of two AC brushless servo machines coupled together; one used as a motor and the other as a generator. The motor was used to emulate the HSS speed which drove the generator. The generator was connected to the grid through a back-to-back VSC and an auto-transformer. The transformer was used to lower the grid voltage for safety reasons. The control system of the test rig was split into two: the vector control schemes of the generator and grid-side converters were implemented in separate DSPs whereas the turbine control system was implemented in a dSPACE® platform. All user interface and data acquisition was performed through the same platform.

A hardware-in-the-loop experiment was performed to supplement most of the simulations presented in this work. The experiment results achieved were in good agreement with the simulations obtained.

8.1.3. Damping of torsional vibrations

Torsional vibrations in a WT occur mainly due to the flexibilities of the shafts in the drive-train. Nevertheless, some of the blade bending modes (symmetrical in-plane) couple directly with the drive-train dynamics. In order to represent both the drive-train torsional mode and the blades in-plane modes, a three-mass model was used.

Two torsional vibration dampers based on the conventional design approach (BPFs) were designed. One considered the torsional mode only whereas the other considered both modes. Simulations conducted in Bladed® showed that the performance of the damper designed to address both modes was considerably better than the other. This result indicated that for torsional vibration damping studies both modes have to be considered.

A model-based vibration damper was proposed. It was designed using pole placement with state feedback using a state observer. The damping performance of this damper was compared to the conventional design through analysis, simulations and experiments.

Stability analysis showed that the stability margins of the system with the conventional damper deteriorated slightly when parameter variation was present and dropped considerably when model uncertainty was introduced. The stability margins of the system with the model-based damper have hardly changed. A performance analysis was also conducted. Results demonstrated that the system featuring the model-based damper showed attenuation of torsional vibrations throughout both frequency uncertainty areas. On the other hand, the system with the conventional damper exhibited amplification in one part of the uncertainty areas.

Simulation and experimental results confirmed the stability and performance analysis. Results showed that the performance of the proposed damper compared to the conventional was considerably better, particularly when model uncertainty was present in the system. The conventional damper failed to damp the vibrations adequately and had to be re-tuned to recover its damping performance. No re-tuning was necessary in the case of the model-based damper.

Apart from providing a superior damping performance, the model-based damper can be used to eliminate re-tuning procedures associated with the conventional damper.

8.1.4. Avoiding side-side tower resonance

Due to different design constraints (pile diameter, tower wall thickness and height), the tower bending modes are sometimes located close or within the rotor rotational frequency operating range. This implies that whenever the rotor speed frequency coincides with the side-side tower mode, resonance occurs. This has a detrimental effect on the tower lifetime due to the increase in fatigue loads. In order to limit this increase, a speed exclusion zone algorithm was designed. It consisted of a region within the variable-speed region of a WT where the rotor has restricted operation for sustained periods.

Simulation and experimental results for a range of turbulent wind speeds showed the effectiveness of this algorithm in reducing tower oscillations. During the crossing of the speed exclusion zone, the rotor speed momentarily equalled the critical speed and the tower mode was slightly excited. However, the tower oscillations were still lower that the case without the speed exclusion zone.

Results also showed that the zone width had an impact on both the tower oscillations magnitude and the power output of the WT. It was observed that with a wider zone, not only the magnitude of the tower oscillations was reduced but also the power generated by the WT. Therefore, it was concluded that although the main scope of the speed exclusion zone was to alleviate the tower from excess fatigue loads, a compromise between the energy lost (wide zone) and the increase in tower fatigue loads (narrow zone) needs to be reached.

8.1.5. Inertia response

It is well known that VSWTs, particularly the FRC-based WTs do not provide any natural inertial response due to the decoupling of the rotor speed from the grid frequency. One of the requirements of modern Grid Codes is that WTs and wind farms have to provide additional active power during a frequency event to limit the rate of change of frequency.

An auxiliary controller was designed to provide inertial response from a FRC-PMSG based WT. The kinetic energy stored in the rotor and the energy stored in the DC link capacitor was used to aid the power system in containing the system frequency. Simulation and experimental results showed that with this auxiliary controller the VSWT provided some inertial response. However, this was not enough to be complaint with the primary response requirements.

The possibility of achieving a coordinated inertial response from each WT within a wind farm was assessed. A wind farm model was designed using simplified WT representations operating at different wind speeds. Results showed that the additional power output from an FRC-PMSG based wind farm was comparable to a fixed-speed

IG based wind farm. Moreover, the starting time of the recovery period was delayed to more than 10 s, meaning that the collective contribution of each WT within the wind farm supported the frequency recovery of the power system.

8.2. Summary of Contributions

- A simplified WT model was derived and implemented in Simulink®. A vector control scheme was adopted for both the generator-side and the grid-side converters. A pitch controller was also designed.
- A hardware-in-the-loop experimental test rig was set-up and used to validate all the simulation results.
- Simulation results in Bladed® showed that for torsional vibrations studies, correct representation of the relevant modes is necessary to ensure good performance of the vibration damper.
- A model-based torsional vibration damper was proposed and designed. Simulation and experimental results showed superior damping performance of this damper over the conventional BPF-based damper. Moreover, due the robustness exhibited by this damper, it can be used to eliminate re-tuning procedures associated with the conventional damper during commissioning of WTs.
- A speed exclusion zone algorithm was designed to prevent side-side tower resonance. Simulation and experimental results confirmed the effectiveness of the algorithm in reducing tower oscillations.
- A supplementary control was used for the provision of inertial response from a FRC-PMSG based WT. Moreover, it was demonstrated that a coordinated inertial response from each WT in a wind farm can be used to support frequency recovery of a power system.

8.3. Recommendations for further work

The recommendations for future work are subdivided into lists according to the main areas of the contributions done in this research. Each list outlines a number of research items as a way of furthering the findings in this research work.

Damping of torsional vibrations

- Including the proposed model-based torsional damper on a quasi-realistic WT model in Bladed®. This would enable assessment and comparison of the effectiveness of this damper *vis-à-vis* the conventional damper in reducing loads on different components, such as blades, shafts, gearbox, etc. Fatigue analysis can also be performed within the software platform.
- Implementation of the proposed damper on an actual WT to test the performance of the damper in a real system. This would enable testing the potential of the model-based damper in eliminating re-tuning procedures during commissioning of WTs and its performance in the presence of parameter variation.

Avoiding side-side tower resonance

- Integrating the speed exclusion zone algorithm in the WT controller in Bladed®. This would enable an in-depth assessment of the algorithm capabilities in reducing loads on the tower. A fatigue analysis of the tower with and without the speed exclusion zone would give a clearer picture of the effectiveness of the algorithm.
- Developing of an optimisation tool that relates the energy lost and the fatigue loads on the tower. Depending on the wind speed data gathered from the site and the allowable fatigue loads on the tower, the tool would help the designer to optimally choose the width of the speed exclusion zone. Moreover, the possibility of having an asymmetric zone can also be considered in the optimisation tool.
- Maximising the WT power output during operation at the fixed-speed boundaries by varying the pitch angle to optimise the tip speed ratio. During below rated wind speed operation, the WT operates at an optimal tip speed ratio of 8.1 (pitch angle of -0.25°) to maximise the power coefficient C_P. When the rotor speed is held fixed by the algorithm and the wind speed increases, the tip speed ratio drops. When it drops below 8, a pitch angle of -0.25° no longer gives the maximum C_P. Figure 8.1 shows that by changing the pitch angle to -0.5° a higher C_P can be achieved for a tip speed ratio lower than 8.

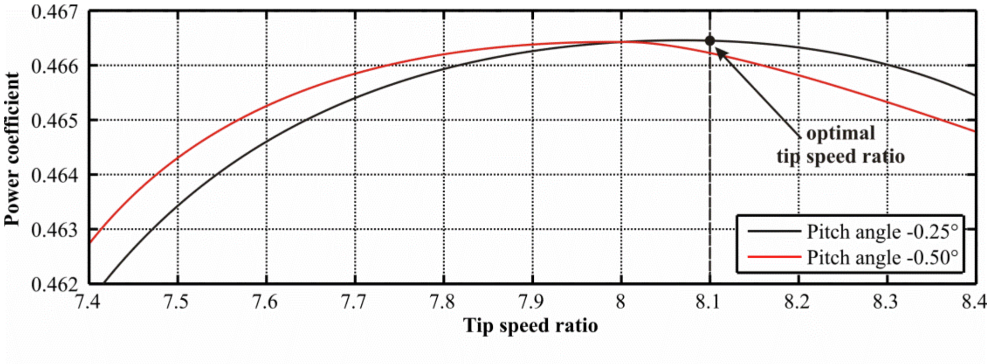

Figure 8.1: Variation of the power coefficient with tip speed ratio for different pitch angles

Inertial response

➢ Improving the wind farm inertial response by optimising the clustering of the WTs, the frequency delayed signals applied to each cluster and the gains of inertial control loop.

➢ Developing of a power system model to conduct a more realistic assessment of the wind farm capability to help containing the collapsing system frequency. In this work, the frequency deviation to trigger inertial response has been emulated. With a power system model, the frequency of the power system can be made to vary naturally by causing an imbalance in the power generation and demand.

➢ Integrating the inertial response controller in Bladed® for assessing the loads experienced by WT components such as drive-train, blades and tower during a frequency event. The response of the inertial controller to a frequency deviation is a sudden increase in the demanded torque reference to the generator. The sharp increase can trigger modes within the WT, particularly those that couple with the torsional mode of the drive-train.

References

[1] European Environment Agency (EEA). (2011, 8th Dec 2012). *Emissions from public electricity and heat production*. Available: http://www.eea.europa.eu/data-and-maps/indicators/emissions-co2-so2-nox-from-1/assessment-1

[2] European Union. (2009, 10th Sep 2012). *Directive on the promotion of the use of energy from renewable sources, DIRECTIVE 2009/28/EC,* . Available: http://eur-lex.europa.eu/LexUriServ/LexUriServ.do?uri=OJ:L:2009:140:0016:0062:EN:PDF

[3] The European Wind Energy Association. (2012, 29th Nov 2012). *Wind in Power 2011 European statistics.* Available: http://www.ewea.org/fileadmin/files/library/publications/statistics/Wind_in_power_2011_European_statistics.pdf

[4] The European Wind Energy Association. (2011, 8th Dec 2012). *Pure Power - Wind energy targets for 2020 and 2030.* Available: http://www.ewea.org/fileadmin/files/library/publications/reports/Pure_Power_III.pdf

[5] P. Gardner, A. Garrad, L. F. Hansen, P. Jamieson, C. Morgan, F. Murray, A. Tindal, J. I. Cruz, L. Arribas, and N. Fichaux. (2009, 8th Dec 2012). *WIND ENERGY - THE FACTS* Available: http://www.wind-energy-the-facts.org/

[6] N. Fichaux, J. Beurskens, P. H. Jensen, and J. Wilkes. (2011, *UpWind Design limits and solution for very large wind turbines.* Available: http://www.ewea.org/fileadmin/ewea_documents/documents/upwind/21895_UpWind_Report_low_web.pdf

[7] P. Jamieson, *Innovation in Wind Turbine Design*: John Wiley & Sons Ltd, 2011.

[8] K. Z. Ostergaard, P. Brath, and J. Stoustrup, "Gain-scheduled Linear Quadratic Control of Wind Turbines Operating at High Wind Speed," in *IEEE International Conference on Control Applications, CCA*, 2007, pp. 276-281.

[9] L. Fingersh, M. Hand, and A. Laxson. (2006, 8th Dec 2012). *Wind Turbine Design Cost and Scaling Model* Available: http://www.nrel.gov/wind/pdfs/40566.pdf

[10] S. Sheng. (2011, 5th Jul 2012). *Wind Turbine Drivetrain Condition Monitoring*. Available: http://www.nrel.gov/docs/fy12osti/52908.pdf

[11] M. Molinas, J. A. Suul, and T. Undeland, "Extending the Life of Gear Box in Wind Generators by Smoothing Transient Torque With STATCOM," *IEEE Transactions on Industrial Electronics*, vol. 57, pp. 476-484, 2010.

[12] P. Cazelitz, W. Kleinkauf, T. Kruger, J. Petschenka, M. Reichard, and K. Storzel, "Reduction of fatigue loads on wind energy converters by advanced control methods," in *EWEC*, Dublin, Ireland, 1997.

[13] T. Burton, D. Sharpe, N. Jenkins, and E. A. Bossanyi, *Wind Energy Handbook*, 2 ed.: John Wiley & Sons Ltd, 2001.

[14] J. F. Manwell, J. G. McGowan, and A. L. Rogers, *Wind Energy Explained*, 1 ed.: John Wiley & Sons Ltd, 2002.

[15] B. Fox, D. Flynn, L. Bryans, N. Jenkins, D. Milborrow, M. O'Malley, R. Watson, and O. Anaya-Lara, *Wind Power Integration: Connection and system operational aspects* vol. 50: The Institution of Engineering and Technology, 2007.

[16] E. A. Bossanyi, "The Design of closed loop controllers for wind turbines," *Wind Energy*, vol. 3, pp. 149-163, 2000.

[17] Vestas. (2012, 17th Aug 2012). *Product Brochure*. Available: http://www.vestas.com

[18] Siemens. (2010, 18th Oct 2010). *Product Brochure*. Available: http://www.energy.siemens.com

[19] Gamesa. (2010, 18th Oct 2010). *Product Brochure*. Available: http://www.gamesacorp.com

[20] F. Blaabjerg, Z. Chen, R. Teodorescu, and F. Iov, "Power Electronics in Wind Turbine Systems," in *Power Electronics and Motion Control Conference, 2006. IPEMC 2006. CES/IEEE 5th International*, 2006, pp. 1-11.

[21] H. Li and Z. Chen, "Overview of different wind generator systems and their comparisons," *IET Renewable Power Generation,* , vol. 2, pp. 123-138, 2008.

[22] C. Zhe, J. M. Guerrero, and F. Blaabjerg, "A Review of the State of the Art of Power Electronics for Wind Turbines," *IEEE Transactions on Power Electronics,*, vol. 24, pp. 1859-1875, 2009.

[23] O. Anaya-Lara, N. Jenkins, J. Ekanayake, P. Cartwright, and M. Hughes, *Wind Energy Generation Modelling and Control* 1ed. Chichester: John Wiley and Sons, 2009.

[24] L. H. Hansen, L. Helle, F. Blaabjerg, E. Ritchie, S. Munk-Nielsen, H. Bindner, P. Sørensen, and B. Bak-Jensen. (2001, 15th Nov 2012). Conceptual survey of Generators and Power Electronics for Wind Turbines

[25] D. A. Torrey, "Variable-reluctance generators in wind-energy systems," in *Power Electronics Specialists Conference. PESC '93 Record., 24th Annual IEEE*, 1993, pp. 561-567.

[26] R. Cardenas, R. Pena, M. Perez, J. Clare, G. Asher, and P. Wheeler, "Control of a switched reluctance generator for variable-speed wind energy applications," *IEEE Transactions on Energy Conversion,*, vol. 20, pp. 781-791, 2005.

[27] (2002, 28th October 2012). *Historic Documentation on a Wind Power Project* Available: http://www.windpowerphotos.com/w-form/windform.htm

[28] B. B. Jensen, n. Mijatovic, and A. B. Abrahamsen, "Development of superconducting wind turbine generators," presented at the EWEA 2012, Copenhagen, 2012.

[29] A. B. Abrahamsen, N. Mijatovic, E. Seiler, T. Zirngibl, C. Træholt, P. B. Nørgård, N. F. Pedersen, N. H. Andersen, and J. Østergård, "Superconducting wind turbine generators," *Superconductor Science and Technology*, vol. 23, p. 034019, 2010.

[30] P. N. Barnes, M. D. Sumption, and G. L. Rhoads, "Review of high power density superconducting generators: Present state and prospects for incorporating YBCO windings," *Cryogenics,* vol. 45, pp. 670-686, 2005.

[31] P. Kurronen, M. Haavisto, and J. Pyrhönen, "Challenges in applying permanent magnet (PM) technology to wind power generators " in *EWEC*, Brussels, 2010.

[32] E. d. Vries. (April 2012) The evolution of wind turbine drive systems. *Windpower Montly*.

[33] S. Schmidt and A. Vath, "Comparison of Existing Medium-speed Drive Train Concepts with a Differential Gearbox Approach " in *EWEA 2012*, Copenhagen, 2012.

[34] E. d. Vries. (July 2011) Wind Tech: Electrical generators - Doubly-fed induction vs permanent magnet. *Windpower Montly*.

[35] P. J. Tavner, F. Spinato, G. J. W. v. Bussel, and E. Koutoulakos, "Reliability of Different Wind Turbine Concepts with Relevance to Offshore Application," in *EWEA 2008*, Brussles, 2008.

[36] F. Spinato, P. J. Tavner, G. J. W. van Bussel, and E. Koutoulakos, "Reliability of wind turbine subassemblies," *IET Renewable Power Generation,,* vol. 3, pp. 387-401, 2009.

[37] H. Polinder, F. F. A. van der Pijl, G. J. de Vilder, and P. J. Tavner, "Comparison of direct-drive and geared generator concepts for wind turbines," *IEEE Transactions on Energy Conversion,,* vol. 21, pp. 725-733, 2006.

[38] A. Allcock. (2010, 25th Nov 2012). *Opportunity dawns* Available: http://www.machinery.co.uk/machinery-features/wind-energy-uk-manufacturing/23856/

[39] G. Hatch. (2008, 25th Nov 2012). *How Does The Use Of Permanent Magnets Make Wind Turbines More Reliable?* Available: http://www.terramagnetica.com/2009/08/03/how-does-using-permanent-magnets-make-wind-turbines-more-reliable/

[40] N. McDonald. (2011, 25th Nov 2012). *Wind Turbines: Direct Drive vs. Gearbox* Available: http://cenvironment.blogspot.co.uk/2011/04/wind-turbines-direct-drive-vs-gearbox.html

[41] The Switch. (2012, 10th Nov 2012). *FusionDrive– Smartest gear and generator combination.* Available: http://www.theswitch.com/wind-power/fusiondrive/

[42] DNV/Riso, *Guidelines for Design of Wind Turbines*, 2 ed., 2002.

[43] M. Hau. (2010, 10th Apr 2011). *Promising Load Estimation Methodologies.* Available: http://www.upwind.eu/pdf/D5.2_PromisingLoadEstimationMethodologies.pdf

[44] British Standard Institution (1980), "BS 61400 - 1 Wind turbines – Part 1: Design Requirements," London.

[45] G. Lloyd, "Guidline for the Certification of Wind Turbines," Germanischer Lloyd, Hamburg, 2010, p. 384.

[46] C. F. Beards, *Structural Vibration: Analysis and Damping*. New York: John Wiley & Sons 1996.

[47] C. M. Harris, *Shock and vibration handbook*, 6 ed.: McGraw Hill, 1996.

[48] P. N. Paraskevopoulos, *Modern Control Engineering*. New York: Marcel Dekker, 2002.

[49] A. D. Hansen and G. Michalke, "Modelling and control of variable-speed multi-pole permanent magnet synchronous generator wind turbine," *Wind Energy,* vol. 11, pp. 537-554, 2008.

[50] X. Zuo-xia, L. Li-zhe, G. Heng-yi, and W. Xiao-dong, "Damping Control Study of the Drive Train of DFIG Wind Turbine," in *International Conference on Energy and Environment Technology, (ICEET)*, 2009, pp. 576-579.

[51] H. Geng, D. Xu, B. Wu, and G. Yang, "Active Damping for PMSG-Based WECS With DC-Link Current Estimation," *IEEE Transactions on Industrial Electronics,*, vol. 58, pp. 1110-1119, 2011.

[52] E. A. Bossanyi, "Wind Turbine Control for Load Reduction," *Wind Energy,* vol. 6, pp. 229-244, 2003.

[53] W. Johnson, *Helicopter theory*: Dover publications, 1980.

[54] G. Ramtharan, "Control of Variable speed wind generators," PhD Thesis, The University of Manchester, 2008.

[55] B. Jasniewicz. (2009, 26th Jun 2011). *Integrated wind turbine design*. Available: www.upwind.eu/

[56] H. Geng, D. Xu, B. Wu, and G. Yang, "Comparison of oscillation damping capability in three power control strategies for PMSG-based WECS," *Wind Energy,* vol. 14, pp. 389-406, 2011.

[57] H. De Battista, P. F. Puleston, R. J. Mantz, and C. F. Christiansen, "Sliding mode control of wind energy systems with DOIG-power efficiency and torsional dynamics optimization," *IEEE Transactions on Power Systems,* vol. 15, pp. 728-734, 2000.

[58] A. J. G. Westlake, J. R. Bumby, and E. Spooner, "Damping the power-angle oscillations of a permanent-magnet synchronous generator with particular reference to wind turbine applications," *IEE Proceedings - Electric Power Applications,* vol. 143, pp. 269-280, 1996.

[59] O. Wasynczuk, D. T. Man, and J. P. Sullivan, "Dynamic Behavior of a Class of Wind Turbine Generators during Random Wind Fluctuations," *IEEE Power Engineering Review,* vol. PER-1, pp. 47-48, 1981.

[60] S. Jöckel, B. Hagenkort, T. Hartkopf, M. Ruckh, and H. Schneider, "Direct-Drive Synchronous Generator System for Offshore Wind Farms with Active Drive-Train Damping by Blade Pitching," presented at the EWEC, Copenhagen, 2001.

[61] A. D. Wright, "Modern Control Design for Flexible Wind Turbines " PhD Thesis, National Renewable Energy Laboratory NREL, Colorado, 2004.

[62] A. D. Wright and L. J. Fingersh, "Part I: Control Design, Implementation, and Initial Tests " NREL, Technical Report NREL/TP-500-42437 2008.

[63] E. A. Bossanyi. (2009, 17th Aug 2011). *Controller for 5MW reference turbine*. Available: www.upwind.eu/

[64] M. Laubrock, T. P. Woldmann, and S. Bilges, "Method for the active damping of the drive train in a wind energy plant," United States Patent US 7,501,798 B2, Mar 10, 2009.

[65] P. Nielsen, "Damping of drive train oscillations by DC-Link absorption means," International Patent WO 2011/045263, Apr 21, 2011.

[66] F. Iov, R. Teodorescu, F. Blaabjerg, B. Andersen, J. Birk, and J. Miranda, "Grid Code Compliance of Grid-Side Converter in Wind Turbine Systems," in *Power Electronics Specialists Conference, PESC '06. 37th IEEE,* 2006, pp. 1-7.

[67] H. Geng, D. Xu, B. Wu, and G. Yang, "Active damping for torsional vibrations in PMSG based WECS," in *Applied Power Electronics Conference and Exposition (APEC), 25th Annual IEEE*, 2010, pp. 2126-2131.

[68] A. D. Wright and K. A. Stol, "Designing and Testing Controls to Mitigate Dynamic Loads in the Controls Advanced Research Turbine " presented at the ASME Wind Energy Symposium Reno, Nevada, 2008.

[69] J. Jun-Keun and S. Seung-Ki, "Kalman filter and LQ based speed controller for torsional vibration suppression in a 2-mass motor drive system," *IEEE Transactions on Industrial Electronics*, vol. 42, pp. 564-571, 1995.

[70] NationalGrid. (2004, 22nd June 2012). *GB Security and Quality of Supply Standard V1.0* Available: http://www.nationalgrid.com/NR/rdonlyres/A775F864-C341-4E80-8A60-0B9BD2EDD78A/1950/GB_SQSS_V1.pdf

[71] ENTSO-E. (2011, 27th October 2011). *Grid Connection Applicable to all Generators* Available: http://www.entsoe.eu/resources/network-codes/requirements-for-generators/

[72] I. A. Erinmez, D. O. Bickers, G. F. Wood, and W. W. Hung, "NGC experience with frequency control in England and Wales-provision of frequency response by generators," in *Power Engineering Society 1999 Winter Meeting, IEEE*, 1999, pp. 590-596 vol.1.

[73] National Grid. (2012, Nov 2012). *THE GRID CODE*. Available: http://www.nationalgrid.com/uk/Electricity/Codes/gridcode/gridcodedocs/

[74] Hydro-Quebec. (2009, 11th July 2012). *Transmission provider technical requirements for the connection of power plants to the Hydro-Quebec transmission system* Available: http://www.hydroquebec.com/transenergie/fr/commerce/pdf/exigence_raccordement_fev_09_en.pdf

[75] NationalGrid. (2010, 22nd June 2012). *NGC Frequency response technical sub-group*. Available: http://www.nationalgrid.com/NR/rdonlyres/F0793C0C-9617-49B1-98D4-FAC711F344ED/44455/Meeting2Presentation.pdf

[76] J. Ekanayake and N. Jenkins, "Comparison of the response of doubly fed and fixed-speed induction generator wind turbines to changes in network frequency," *IEEE Transactions on Energy Conversion*, vol. 19, pp. 800-802, 2004.

[77] G. Ramtharan, J. B. Ekanayake, and N. Jenkins, "Frequency support from doubly fed induction generator wind turbines," *IET Renewable Power Generation*, vol. 1, pp. 3-9, 2008.

[78] L. Holdsworth, J. Ekanayake, and N. Jenkins, "Power system frequency response from fixed speed and doubly fed induction generator based wind turbines," *Wind Energy*, vol. 7, pp. 21-35, 2004.

[79] M. Kayikci and J. V. Milanovic, "Dynamic Contribution of DFIG-Based Wind Plants to System Frequency Disturbances," *IEEE Transactions on Power Systems*, vol. 24, pp. 859-867, 2009.

[80] G. Lalor, A. Mullane, and M. O'Malley, "Frequency control and wind turbine technologies," *IEEE Transactions on Power Systems* vol. 20, pp. 1905-1913, 2005.

[81] G. C. Tarnowski, P. C. Kjar, P. E. Sorensen, and J. Ostergaard, "Variable speed wind turbines capability for temporary over-production," in *Power & Energy Society General Meeting, 2009. PES '09. IEEE*, 2009, pp. 1-7.

[82] N. R. Ullah, T. Thiringer, and D. Karlsson, "Temporary Primary Frequency Control Support by Variable Speed Wind Turbines; Potential and Applications," *IEEE Transactions on Power Systems,,* vol. 23, pp. 601-612, 2008.

[83] J. F. Conroy and R. Watson, "Frequency Response Capability of Full Converter Wind Turbine Generators in Comparison to Conventional Generation," *IEEE Transactions on Power Systems,* vol. 23, pp. 649-656, 2008.

[84] S. Heier and R. Waddington, *Grid Integration of Wind Energy Conversion Systems*: John Wiley & Sons, 2006.

[85] A. Rolan, A. Luna, G. Vazquez, D. Aguilar, and G. Azevedo, "Modeling of a variable speed wind turbine with a Permanent Magnet Synchronous Generator," in *Industrial Electronics, 2009. ISIE 2009. IEEE International Symposium on*, 2009, pp. 734-739.

[86] V. Akhmatov, "Analysis of dynamic behaviour of electric power systems with large amount of wind power," PhD Thesis, Technical University of Denmark, 2003.

[87] F. Iov, A. D. Hansen, P. Sørensen, and F. Blaabjerg, *Wind Turbine Blockset in Matlab/Simulink General Overview and Description of the Models*: Aalborg University, 2004.

[88] G. Michalke, "Variable Speed Wind Turbines Modelling, Control, and Impact on Power Systems ", PhD Thesis, Technischen Universität Darmstadt , 2008.

[89] A. D. Hansen and G. Michalke, "Multi-pole permanent magnet synchronous generator wind turbines' grid support capability in uninterrupted operation during grid faults," *Renewable Power Generation, IET,* vol. 3, pp. 333-348, 2009.

[90] E.L. van der Hooft, P. Schaak, and T.G. van Engelen, "*Wind turbine control algorithms: DOWEC-F1F1-EH-03-094/0,*" ECN-C-03-111, December 2003.

[91] J. Niebsch, R. Ramlau, and T. T. Nguyen, "Mass and Aerodynamic Imbalance Estimates of Wind Turbines," *Energies,* vol. 3, pp. 696-710, 8th April 2010.

[92] G. Michalke, A. D. Hansen, and T. Hartkopf, "Control strategy of a variable speed wind turbine with multipole permanent magnet synchronous generator " in *Ewec 2007,* 2007.

[93] R. Krishnan, *Permanent Magnet Synchronous and Brushless DC Motor Drives*, 1 ed.: Taylor & Francis group, 2010.

[94] R. Pena, J. C. Clare, and G. M. Asher, "Doubly fed induction generator using back-to-back PWM converters and its application to variable-speed wind-energy generation," *Electric Power Applications, IEE Proceedings -,* vol. 143, pp. 231-241, 1996.

[95] R. Pena, R. Cardenas, R. Blasco, G. Asher, and J. Clare, "A cage induction generator using back to back PWM converters for variable speed grid connected wind energy system," in *Industrial Electronics Society, 2001. IECON '01. The 27th Annual Conference of the IEEE*, 2001, pp. 1376-1381 vol.2.

[96] M. Liserre, F. Blaabjerg, and A. Dell'Aquila, "Step-by-Step Design Procedure for a Grid-Connected Three-Phase PWM Voltage Source Converter," *International Journal of Electronics,* vol. 91, pp. 445-460, 2004.

[97] W. Leonhard, *Control of Electric Drives*, 3rd ed.: Springer, 2001.

[98] V. Akhmatov, "Variable-Speed Wind Turbines with Doubly-Fed Induction Generators, Part I: Modelling in dynamic simulation tools," *Wind Engineering*, vol. 26, pp. 171-188, 2002.

[99] S. Suryanarayanan, A. Avangliano, and C. Barbu, "Vibration damping method for variable speed wind turbines," United States Patent US 7,423,352 B2, Dec 18, 2007.

[100] W. T. Thomas, "Theory of vibration with applications," 4th ed: Chapman & Hall, 1993, pp. 131-145, 268-337.

[101] K. Ogata, *Modern Control Engineering*, 3 ed.: Prentice-Hall, 1997.

[102] G. Welch and G. Bishop. (2001, Oct. 27 2011). *An Introduction to the Kalman Filter*. Available: www.cs.unc.edu/~welch/media/pdf/kalman_intro.pdf

[103] D. Simon, *Optimal State Estimation*, 1 ed. Canada: John Wiley & Sons, 2006.

[104] B. Boukhezzar and H. Siguerdidjane, "Nonlinear Control of a Variable-Speed Wind Turbine Using a Two-Mass Model," *IEEE Transactions on Energy Conversion*, vol. 26, pp. 149-162, 2011.

[105] D. Bourlis and J. A. M. Bleijs, "A wind speed estimation method using adaptive Kalman filtering for a variable speed stall regulated wind turbine," in *IEEE 11th International Conference on Probabilistic Methods Applied to Power Systems (PMAPS)*, 2010, pp. 89-94.

[106] K. Z. Østergaard, P. Brath, and J. Stoustrup, "Estimation of effective wind speed " *Journal of Physics: Conference Series*, vol. 75, pp. 1-9, 2007.

[107] J. R. Leigh, *Control Theory*, 1 ed. vol. 64. London, United Kingdom: Institution of Engineering and Technology, 2004.

[108] D. J. Leith and W. E. Leithead, "Implementation of wind turbine controllers," *International Journal of Control*, vol. 66, pp. 349-380, 1997.

[109] K. J. Aström and R. M. Murray, *Feedback Systems: An Introduction for Scientists and Engineers*. Oxfordshire: Priceton University Press, 2008.

[110] C. C. Tsui, *Robust Control System Design: Advanced State Space Techniques* 2nd ed.: Marcel Dekker, 2004.

[111] E. d. Vries. (2011) Wind Power - Special report: Offshore Technogy. *Windpower Montly*. 36. Available: www.windpowermontly.com.

[112] S. Siegfriedsen, "Method for Operating Offshore Wind Turbine Plants based on Frequency of their Towers," 2005.

[113] T. Fischer. (2011, May. 30 2012). *Offshore Foundations and Support Structures*. Available: www.upwind.eu/

[114] C. Carrillo, A. E. Feijoo, J. Cidras, and J. Gonzalez, "Power fluctuations in an isolated wind plant," *Energy Conversion, IEEE Transactions on*, vol. 19, pp. 217-221, 2004.

[115] T. Thiringer and J. A. Dahlberg, "Periodic pulsations from a three-bladed wind turbine," *Energy Conversion, IEEE Transactions on*, vol. 16, pp. 128-133, 2001.

[116] E. Hau, *Wind Turbines: Fundamentals, Technologies, Applications, Economics*, 2 ed. Berlin: Springer, 2006.

[117]L. V. Andersen, M. J. Vahdatirad, M. T. Sichani, and J. D. Sørensen, "Natural frequencies of wind turbines on monopile foundations in clayey soils-A probabilistic approach," *Computers and Geotechnics*, vol. 43, pp. 1-11, 2012.

[118]A. Beeken, T. Neumann, and A. Westerhellweg. (2008, 25th Nov 2012). *Five years of operation of the first offshore wind research platform in the german bight – FINO1*. Available: http://www.dewi.de/dewi/fileadmin/pdf/publications/Publikations/5_Beeken.pdf

[119]E. A. Bossanyi, *GH Bladed User Manual*, 2009.

[120]G. Lloyd, "Rules and Regulations IV, Non-marine technology, Part 1 - Wind Energy, Section 2," Germanischer Lloyd, Hamburg, 1993.

[121]I. Boldea, *Synchronous generators*: Taylor & Francis Group, 2006.

[122]N. Mohan, T. M. Undeland, and W. P. Robbins, *Power Electronics - Converters, Applications and Design*, 2nd ed.: John Wiley & Sons, 1995.

[123]H. Li and Z. Chen, "Transient Stability Analysis of Wind Turbines with Induction Generators Considering Blades and Shaft Flexibility," in *33rd Annual Conference of the IEEE Industrial Electronics Society*, Taiwan, 2007, pp. 1604-1609.

[124]J. Doyle and G. Stein, "Robustness with observers," *IEEE Transactions on Automatic Control*, vol. 24, pp. 607-611, 1979.

Appendix A

Parameters

A.1. Wind Turbine

Table A-1: WT parameters

Rotor:	**Generator**:
Radius (R): 40 m	Rating: 2 MW
Rated Speed: 18 rpm	Inertia referred to LSS (J_{gen}): 416633 kgm^2
Number of blades: 3	Poles pairs (n_{pp}): 2
Inertia rotor,(J_{rot}): 6.028×10^6 kgm^2	Rated frequency: 50 Hz
Inertia blades, (J_{blade}): 3.9196×10^6 kgm^2	Stator resistance (R_s): 4.523 mΩ
Inertia hub, (J_{hub}): 2.1094×10^6 kgm^2	Stator inductance ($L_d = L_q$): 322 µH
Effective blade stiffness (K_{bl}): 4.598×10^8 Nm/rad	Magnet flux (λ_m): 1.75 Vs
Effective Mass (m_{eff}): 105.6 tons	
Drive-train:	**Converters**:
LSS stiffness (K_{LSS}): 1.6×10^6 Nm/rad	DC link capacitor (C): 90,000 µF
LSS damping (D_{LSS}): 2.5×10^5 Nms/rad	DC link voltage: 1400 V
HSS stiffness (K_{HSS}): stiff	Modulation index (M_a): 0.8
HSS stiffness (D_{HSS}): stiff	Switching frequencies (F_s): 3 kHz
Gearbox ratio (N): 83.33:1	PWM sampling delay (T_s): 333µs
Tower:	**Grid**:
Mass (m_t): 175 tons	Grid line to line rms voltage (V_{LL}): 690 V
Height (H): 101.5 m	Grid coupling inductance (L_{grid}): 500 µH
Stiffness (K_t): 418645 N/m	Grid coupling resistance (R_{grid}): 0.4 mΩ
Damping (D_t): 2496 Ns/m	
Pitch:	**Other**:
Actuator time constant (T_{act}) = 0.3 s	Air density (ρ): 1.225 kg/m^3
Angle limits = [Min Max] = [−2° 90°]	Cut-in wind speed: 4 m/s
Pitch rate limit = ±8°	Cut-out wind speed: 24 m/s
	Rated wind speed: 12 m/s
	Optimal gain (G_{opt}): 0.3198

A.2. Converters and Pitch Controllers

Table A-2: Grid-side controller

Current Loop:

Proportional gain $K_p = 0.122$

Integral gain $K_i = 39.3$

Voltage Loop:

Proportional gain $K_p = 9.6$

Integral gain $K_i = 240$

Table A-3: Generator-side controller

Current Loop:

Proportional gain $K_p = 0.166$

Integral gain $K_i = 33.95$

Speed Loop:

Proportional gain $K_p = 2000$

Integral gain $K_i = 1000$

Table A-4: Pitch controller

Speed Loop:

Proportional gain $K_p = 9.86\times10^{-3}$

Integral gain $K_i = 3.4\times10^{-3}$

Table A-5: Pitch controller gain scheduling

Pitch Angle (deg)	Gain Divisor
0	1.0
4.4	1.0
5.9	1.0
7.2	1.0
8.3	1.1
9.4	1.2
10.3	1.3
11.3	1.4
12.1	1.5
13.0	1.6
13.8	1.7
14.6	1.8
15.3	1.9
16.1	1.9
16.8	2.0
17.5	2.1
18.1	2.2
18.8	2.3
19.5	2.4
20.1	2.4
20.7	2.5
21.3	2.5
22.0	2.6
22.6	2.7
23.2	2.7
23.7	2.8
24.3	2.9

A.3. Torsional Dampers

Table A-6: BPF-based damper

BPF 1:	**BPF 2:**	**NF:**
$K_{BPF1} = 400$	$K_{BPF1} = 400$	$\zeta_1 = 0.0015$
$\zeta = 0.15$	$\zeta = 0.15$	$\zeta_2 = 0.14$
$\omega_n = 15.07$ rad/s	$\omega_n = 24.5$ rad/s	$\omega_{nf} = 11.31$ rad/s

Table A-7: Model-based damper

NF:
$\zeta_1 = 0.0015$ $\zeta_2 = 0.14$ $\omega_{nf} = 11.31$ rad/s
LPF:
Time constant (T_{LPF}): 2.5×10^{-3} s
State-Feedback gain:
$\mathrm{K} = \begin{bmatrix} 6.363\times10^{4} & -4.299\times10^{5} & -1.363\times10^{4} & 1.816\times10^{5} & -5.999\times10^{2} \end{bmatrix}$
Kalman filter gain:
$\mathrm{K_k} = \begin{bmatrix} 2.5405\times10^{-7} & -8.4615\times10^{-10} & -3.2144\times10^{-6} & 1.8842\times10^{-7} & 0.0795 \end{bmatrix}$
Covariance Matrices
Measurement Noise (**R**) = 0.25
Process Noise ($\mathbf{Q}_f$) = $\begin{bmatrix} 2.5\times10^{-11} & 0 & 0 & 0 & 0 \\ 0 & 3\times10^{-15} & 0 & 0 & 0 \\ 0 & 0 & 6.22\times10^{-12} & 0 & 0 \\ 0 & 0 & 0 & 2.42\times10^{-11} & 0 \\ 0 & 0 & 0 & 0 & 1.65\times10^{-3} \end{bmatrix}$

A.4. Wind Turbine Iced Model

These parameters were obtained from a generic 2 MW WT model in Bladed®. The density of ice used was 700 kg/m^3 [42] and the tip chord was set 0.9. The tip chord was calculated as outlined by [45, 119, 120]. This is defined as the chord length at the blade tip, linearly extrapolated from the blade contour.

Table A-8: Parameter changes in the model due to ice on the blades

WT model

Blade	No Ice	With Ice
Mass (kg):	6547	7073
Moment of inertia (kgm^2):	2005657	2380130

Rotor	No Ice	With Ice
Mass (kg):	33640	35218
Moment of inertia (kgm^2):	6028970	7152388

Table A-9: Parameter changes in the three-mass model due to ice on the blades

Three-mass model

Inertia (J_{blade}): 4.2148×10^6 kgm^2

Inertia (J_{hub}): 2.9376×10^6 kgm^2

Inertia (J_{gen}): 416633 kgm^2

LSS stiffness (K_{LSS}): 1.6×10^6 Nm/rad

Effective blade stiffness (K_{bl}): 4.7355×10^8 Nm/rad

Appendix B

Derivations

B.1. Permanent magnet synchronous generator

Figure B.1 illustrates the reference frames for a PMSG, which are the stationary ($\alpha\beta$) and the rotor frame (dq), which rotates at the rotor angular electrical speed ω_r.

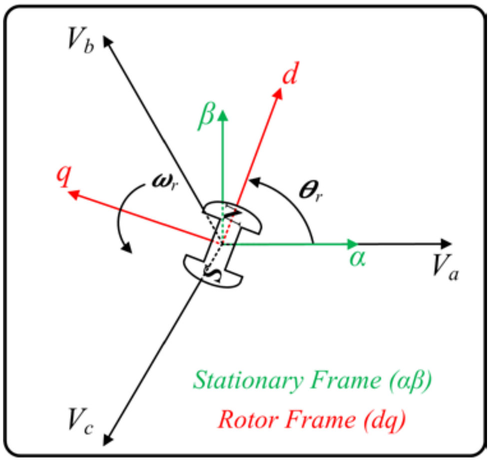

Figure B.1: Reference frames

The following assumptions are being made: stator winding produce sinusoidal mmf distribution, the supply is balanced and no saliency is present in the generator ($L_d = L_q$). The stator instantaneous voltage equations are given by

$$v_a = i_a R_s + \frac{d}{dt}\lambda_a \tag{11.1}$$

$$v_b = i_b R_s + \frac{d}{dt}\lambda_b \tag{11.2}$$

$$v_c = i_c R_s + \frac{d}{dt}\lambda_c \tag{11.3}$$

where v_a, v_b and v_c are the stator voltages [V]; i_a, i_b and i_c are the stator currents [A]; and λ_a, λ_b and λ_c are the flux linkages [Vs]. These flux linkages consists of the self-excitation and mutual flux linkages resulting from other winding current and the magnet source [93] as given by

$$\begin{aligned}\lambda_a &= L_{aa}i_a + L_{ab}i_b + L_{ac}i_c + \lambda_m \cos\theta_r \\ \lambda_b &= L_{ab}i_a + L_{bb}i_b + L_{bc}i_c + \lambda_m \cos\left(\theta_r - 120°\right) \\ \lambda_c &= L_{ac}i_a + L_{bc}i_b + L_{cc}i_c + \lambda_m \cos\left(\theta_r + 120°\right)\end{aligned} \tag{11.4}$$

Assuming a balanced system, a three-phase system can be represented as a two-phase system using the Clarke transformation given by [121]

$$\begin{bmatrix} v_\alpha \\ v_\beta \end{bmatrix} = \frac{2}{3}\begin{bmatrix} 1 & -\cos\left(\pi/3\right) & -\cos\left(\pi/3\right) \\ 0 & \sin\left(\pi/3\right) & -\sin\left(\pi/3\right) \end{bmatrix}\begin{bmatrix} v_a \\ v_b \\ v_c \end{bmatrix} \tag{11.5}$$

which yield the following equations in the *αβ* frame,

$$v_\alpha = i_\alpha R_s + \frac{d}{dt}\lambda_\alpha \tag{11.6}$$

$$v_\beta = i_\beta R_s + \frac{d}{dt}\lambda_\beta \tag{11.7}$$

$$\lambda_\alpha = i_\alpha L_{\alpha\alpha} + i_\beta L_{\alpha\beta} + \lambda_m \cos\theta_r \tag{11.8}$$

$$\lambda_\beta = i_\beta L_{\beta\beta} + i_\alpha L_{\beta\alpha} + \lambda_m \sin\theta_r \tag{11.9}$$

where v_α and v_β are the equivalent stator voltages in the *αβ* frame [V], i_α and i_β are the equivalent stator currents in the *αβ* frame [A], λ_α and λ_β are the equivalent flux linkages in the *αβ* frame [Vs], $L_{\alpha\alpha}$ and $L_{\beta\beta}$ are the equivalent self-inductances of the stator in the *αβ* frame [H], $L_{\alpha\beta}$ and $L_{\beta\alpha}$ are the equivalent mutual inductances in the *αβ* frame [H], λ_m is the flux produced by magnet [Vs], θ_r is the electrical rotor position [rad], and R_s is the stator resistance [Ω]. It is worth nothing that for a cylindrical and smooth rotor with no saliency, the mutual inductance between the *α* and *β* axis windings is zero [93].

As it can be noted from equations (11.8) and (11.9) the stator flux linkages are dependent on the rotor position θ_r. By changing from the stationary frame to the rotor reference frame the flux linkages become independent of the rotor position. This leads to a more compact and simple system equations [93, 121].

In order to transform any two-phase vector from the *αβ* frame to the *dq* frame, the following transformation is used [93]

$$\begin{bmatrix} v_d \\ v_q \end{bmatrix} = \begin{bmatrix} \cos\theta_r & \sin\theta_r \\ -\sin\theta_r & \cos\theta_r \end{bmatrix} \begin{bmatrix} v_\alpha \\ v_\beta \end{bmatrix} \tag{11.10}$$

Applying transformation (11.10) to equations (11.6) − (11.9) yields the following stator voltage equations in the *dq* frame,

$$v_d = i_d R_s + \frac{d}{dt} i_d L_d - \omega_r L_q i_q \tag{11.11}$$

$$v_q = i_q R_s + \frac{d}{dt} i_q L_q + \omega_r L_d i_d + \omega_r \lambda_m \tag{11.12}$$

where ω_r is the electrical rotor speed [rad/s], L_d and L_q are the equivalent self-inductances of the stator in the *dq* frame [H], v_d and v_q are the equivalent stator voltages in *dq* frame [V], λ_m is permanent magnet flux linkage [Vs], and i_d and i_q are the equivalent stator currents [A].

When transforming from a three-phase system to a two-phase system the power has to remain invariant. Therefore, for a two-phase system a factor of 1.5 times needs to be included in the power equation to have the equivalent power of a three-phase system. Hence, the active and reactive power in the *dq* frame assuming a balanced system (no zero sequence current) are given by

$$P_{(dq)} = \frac{3}{2}\left(v_q i_q + v_d i_d\right) \tag{11.13}$$

$$Q_{(dq)} = \frac{3}{2}\left(v_q i_d - v_d i_q\right) \tag{11.14}$$

Substituting equations (11.11) and (11.12) in (11.13) yields

$$P_{(dq)} = {}^{3}\!/_{2}\left[R_s\left(i_q^2 + i_d^2\right) + \left(L_d i_d \, {}^{d}\!/_{dt}\, i_d + L_q i_q \, {}^{d}\!/_{dt}\, i_q\right) + \omega_r\left(\lambda_m + \left(L_d - L_q\right) i_d\right) i_q\right] \tag{11.15}$$

It can be noted from the right-hand side of equation (11.15) that the terms corresponding to the resistive losses, rate of change of magnetic energy stored and the air gap power can be easily identified. The electromagnetic torque is given by dividing the air gap power by the mechanical speed,

$$\tau_{em} = \frac{P_{(dq-airgap)}}{\omega_{mech}} = {}^{3}\!/_{2}\, n_{pp}\left[\lambda_m + \left(L_d - L_q\right) i_d\right] i_q \tag{11.16}$$

where n_{pp} is the number of pole pairs. Since it was assumed that the machine has no saliency, *i.e.*, $L_d = L_q$, the electromagnetic torque reduces to

$$\tau_{em} = {}^{3}\!/_{2}\, n_{pp} \lambda_m i_q \tag{11.17}$$

B.2. Grid-side converter control loop

Figure B.2 illustrates the grid-side converter schematic.

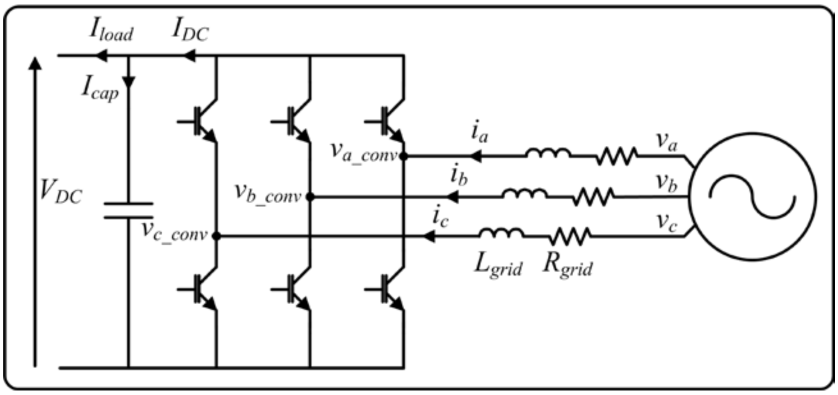

Figure B.2: Grid-side converter schematic

Figure B.2 is described by [94]

$$\begin{bmatrix} v_a \\ v_b \\ v_c \end{bmatrix} = R_{grid} \begin{bmatrix} i_a \\ i_b \\ i_c \end{bmatrix} + L_{grid} \frac{d}{dt} \begin{bmatrix} i_a \\ i_b \\ i_c \end{bmatrix} + \begin{bmatrix} v_{a\_conv} \\ v_{b\_conv} \\ v_{c\_conv} \end{bmatrix} \tag{11.18}$$

where v_a, v_b and v_c are the grid phase voltages [V]; i_a, i_b and i_c are the grid phase currents [A]; v_{a_conv}, v_{b_conv} and v_{c_conv} are the converter input voltages [V]; and R_{grid} and L_{grid} are the resistance [Ω] and inductance [H] between the converter and the grid.

The equations in the *dq* reference frame are

$$v_d = i_d R_{grid} + L_{grid} \frac{d}{dt} i_d - \omega_e L_{grid} i_q + v_{d\_conv} \tag{11.19}$$

$$v_q = i_q R_{grid} + L_{grid} \frac{d}{dt} i_q + \omega_e L_{grid} i_d + v_{q\_conv} \tag{11.20}$$

where ω_e is the synchronous frequency [rad/s], v_d and v_q are the grid voltages in *dq* frame [V], i_d and i_q are the grid currents in *dq* frame [A], and v_{d_conv} and v_{q_conv} are the converter voltages in *dq* frame [V].

Assuming a lossless converter, $P_{in} = P_{out}$, where P_{in} is the DC power stored in the DC link and P_{out} is the power flowing into the grid. The power equality equation is given by

$$V_{DC} I_{DC} = {}^{3}\!/_{2}\, v_d i_d \tag{11.21}$$

where V_{DC} is voltage [V] and I_{DC} is current [A] in the DC link.

For a three-phase inverter operating in the linear modulation region (*i.e.*, $M_a \leq 1.0$), the peak value of the fundamental voltage component in one inverter leg is given by [122]

$$\hat{v}_{ph} = M_a \frac{V_{DC}}{2} \tag{11.22}$$

where M_a is the amplitude modulation ratio and $\hat{v}_{ph}$ is the peak grid phase voltage [V]. The phase voltage in the *dq* reference frame is given by

$$\hat{v}_{ph} = v_d + j v_q \tag{11.23}$$

However, $v_q = 0$ since the phase voltage is aligned with the *d*-axis. Hence, the *d*-axis voltage can be expressed as

$$v_d = \hat{v}_{ph} = M_a \frac{V_{DC}}{2} \tag{11.24}$$

Substituting equation (11.24) into (11.21) and solving for I_{DC} yields

$$I_{DC} = \frac{3M_a}{4} i_d \tag{11.25}$$

The DC link voltage equation is given by

$$C \frac{dV_{DC}}{dt} = I_{DC} - I_{load} \tag{11.26}$$

From equation (11.25) and (11.26), it can be noted that the DC link voltage can be controlled by I_{DC} through the *d*-axis current i_d.

B.3. Grid-side current loop

The PI transfer function in the *s*-domain is given by [101]

$$G_{PI}(s) = K_p + \frac{K_i}{s} \tag{11.27}$$

where K_p is the proportional gain and K_i is the integral gain.

The VSC was assumed ideal so that the transfer function can be modelled as a delay depending on the type of sampling in the PWM scheme. In this work a double-update PWM scheme is used, which implies that the duty-cycle of the PWM signal is updated twice per period. Hence, the VSC was modelled by a lag of half the PWM switching frequency T_s, given by

$$G_{VSC}(s) = \frac{V_{d\_conv}}{V^*_{d\_conv}} = \frac{1}{1 + s\, {T_s}/{2}} \tag{11.28}$$

The plant transfer function can be derived by rearranging equation (11.19). In order to cancel the cross-coupling terms, the feed-forward terms are compensated before going into the converter as shown in bold on the left hand side of equation (11.29):

$$v_d + \boldsymbol{\omega_e L_{grid} i_q} \mathbf{-}\, \boldsymbol{v_{d\_conv}} = i_d R_{grid} + L_{grid}\frac{d}{dt} i_d \tag{11.29}$$

Assuming no delay in the converter,

$$v^*_{d\_conv} = v_d + \omega_e L_{grid} i_q - v_{d\_conv} = i_d R_{grid} + L_{grid}\frac{d}{dt} i_d \tag{11.30}$$

and hence the plant transfer function is given by

$$G_{plant}(s) = \frac{i_d(s)}{v^*_{d\_conv}(s)} = \frac{1}{R_{grid} + sL_{grid}} \tag{11.31}$$

The same plant transfer function applies for the q-axis current loop.

B.4. Three-mass model

The representation of the blade bending dynamics is a complex phenomenon attributed to the non-uniform distribution of the mass, stiffness and twist angle of the blade. Hence, in order to simplify the rotor dynamics, the blades in-plane bending dynamics were represented as a simple torsional system as illustrated in Figure B.3.

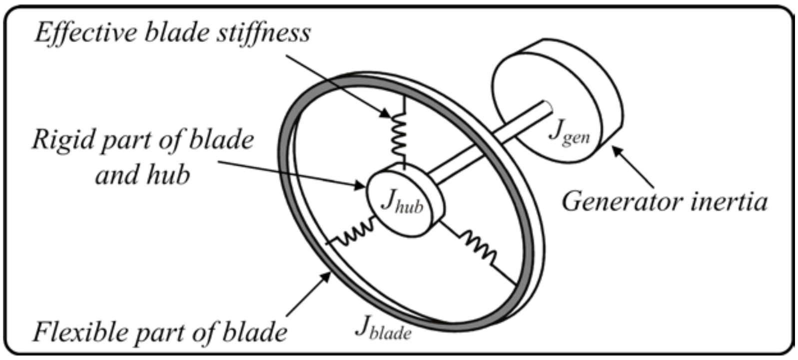

Figure B.3: Representation of the rotor as a simple torsional system

Since the blade in-plane bending occurs well away from the hub, the blades can be split in two parts, a rigid and a flexible part. The rigid part blade inertia was included with the hub inertia. This was connected to the inertia of the flexible part of the blade via three springs representing the effective stiffness of the blade [54, 123].

The simplified rotor structure in Figure B.3 can be represented by a three-mass model as shown in Figure B.4.

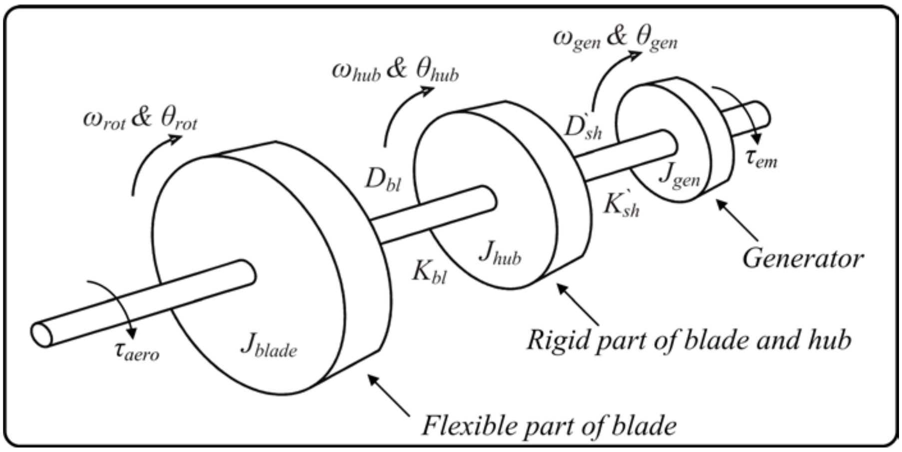

Figure B.4: Three-mass model representation

where J_{blade} represents the inertia of the flexible part of the blade [kgm^2], J_{hub} represents the hub and the rigid blade part [kgm^2], J_{gen} represents the generator inertia [kgm^2] referred to LSS, K_{bl} and D_{bl} represent the effective blade stiffness [Nm/rad] and damping [Nms/rad], $K`_{sh}$ and $D`_{sh}$ represent the resultant of the low-speed and high-speed shafts stiffness [Nm/rad] and damping [Nms/rad] respectively and N is the gearbox ratio.

The dynamic equations referred to the LSS including external torque components are given by [47, 100]

$$J_{blade}\frac{d}{dt}\omega_{rot} = \tau_{aero} - K_{bl}\left(\theta_{rot} - \theta_{hub}\right) - D_{bl}\cdot\frac{d}{dt}\left(\theta_{rot} - \theta_{hub}\right) \tag{11.32}$$

$$\begin{aligned} J_{hub}\frac{d}{dt}\omega_{hub} &= -K_{bl}\left(\theta_{hub} - \theta_{rot}\right) - K_{sh}^{'}\left(\theta_{hub} - \frac{\theta_{gen}}{N}\right) \\ &\quad -D_{bl}\cdot\frac{d}{dt}\left(\theta_{hub} - \theta_{rot}\right) - D_{sh}^{'}\cdot\frac{d}{dt}\left(\theta_{hub} - \frac{\theta_{gen}}{N}\right) \end{aligned} \tag{11.33}$$

$$J_{gen}\frac{d}{dt}\frac{\omega_{gen}}{N} = -N\tau_{em} - K_{2}^{'}\left(\frac{\theta_{gen}}{N} - \theta_{hub}\right) - D_{2}^{'}\cdot\frac{d}{dt}\left(\frac{\theta_{gen}}{N} - \theta_{hub}\right) \tag{11.34}$$

$$\frac{d}{dt}\theta_{rot} = \omega_{rot} \tag{11.35}$$

$$\frac{d}{dt}\theta_{hub} = \omega_{hub} \tag{11.36}$$

$$\frac{d}{dt}\theta_{gen} = \omega_{gen} \tag{11.37}$$

The generator inertia J_{gen}, the resultant shafts stiffness $K`_{sh}$ and the total rotor inertia $J_{blade} + J_{hub}$ are known quantities. In order to determine the effective inertia and stiffness of the blade (J_{blade}, K_{bl}), the equations for the natural frequency of vibration (f_1, f_2) were used. These are given by

$$f_1, f_2 = \frac{1}{2\pi}\left[-\frac{b}{2} \pm \frac{\sqrt{b^2 - 4c}}{2}\right]^{0.5} \tag{11.38}$$

where $b = -\left[K_{bl}\left(\frac{1}{J_{blade}} + \frac{1}{J_{hub}}\right) + K_{sh}\left(\frac{1}{J_{hub}} + \frac{1}{J_{gen}}\right)\right]$ and $c = K_{bl}K_{sh}\left(\frac{J_{blade} + J_{hub} + J_{gen}}{J_{blade}J_{hub}J_{gen}}\right)$

The two vibration frequencies (f_1, f_2) in equation (11.38) were obtained by conducting a spectral analysis of the LSS torque in Bladed®. The frequency of the blade in-plane symmetrical mode was 2.54 Hz whilst the drive-train mode was 3.7 Hz. Substituting these values in equation (11.38) and solving for J_{blade}, J_{hub} and K_{bl} yield the effective blade parameters. These are given in Appendix A.1.

The model was implemented in Simulink® as a state-space model given by

$$A=\begin{bmatrix} -\dfrac{D_{bl}}{J_{blade}} & -\dfrac{K_{bl}}{J_{blade}} & \dfrac{D_{bl}}{J_{blade}} & 0 & 0 \\ 1 & 0 & -1 & 0 & 0 \\ \dfrac{D_{bl}}{J_{hub}} & \dfrac{K_{bl}}{J_{hub}} & \dfrac{-D_{bl}-D_{sh}^{'}}{J_{hub}} & -\dfrac{K_{sh}^{'}}{J_{hub}} & \dfrac{D_{sh}^{'}}{NJ_{hub}} \\ 0 & 0 & 1 & 0 & -\dfrac{1}{N} \\ 0 & 0 & \dfrac{ND_{sh}^{'}}{J_{gen}} & \dfrac{NK_{sh}^{'}}{J_{gen}} & -\dfrac{D_{sh}^{'}}{J_{gen}} \end{bmatrix};B=\begin{bmatrix} -\dfrac{1}{J_{blade}} & 0 \\ 0 & 0 \\ 0 & 0 \\ 0 & 0 \\ 0 & \dfrac{N^2}{J_{gen}} \end{bmatrix};$$

$$C=\begin{bmatrix}0 & 0 & 0 & 0 & 1\end{bmatrix};D=0 \tag{11.39}$$

$$x=\left[\omega_{rot},\left(\theta_{rot}-\theta_{hub}\right),\ \omega_{hub},\left(\theta_{hub}-\theta_{gen}\right),\ \omega_{gen}\right]^T;u=\begin{bmatrix}\tau_{aero} & \tau_{em}\end{bmatrix}^T$$

Appendix C

Wind Turbine Linearization

The WT linearization was performed considering only the rotor rotational speed degree of freedom. A one-mass model is obtained, where the inertia of the rotor and the generator are lumped in a single mass. All parameters are referred to the LSS and the corresponding equations are given by

$$\tau_{aero} - N\tau_{em} = J_{tot}\frac{d}{dt}\omega_{rot} \tag{12.1}$$

$$J_{tot} = J_{rot} + N^2 J_{gen} \tag{12.2}$$

where τ_{aero} is the aerodynamic torque [Nm], τ_{em} is the generator torque [Nm], ω_{rot} is the rotor speed [rad/s], J_{rot} and J_{gen} are the rotor and generator inertias [kgm^2] and N is the gearbox ratio.

The aerodynamic torque is a non-linear function of the wind speed, pitch angle and the rotor speed. In order to obtain a linear approximation, the non-linear torque function is expanded in a Taylor series about an operating point in terms of V_w, β and ω_{rot}. Ignoring higher order terms (*h.o.t.s*), the series is given by

$$\tau_{aero} = \tau_{aero}\left(V_{w\_0}, \beta_0, \omega_{rot\_0}\right) + \frac{\partial \tau_{aero}}{\partial V_w}\Delta V_w + \frac{\partial \tau_{aero}}{\partial \beta}\Delta\beta + \frac{\partial \tau_{aero}}{\partial \omega_{rot}}\Delta\omega_{rot} + h.o.t.s \tag{12.3}$$

where V_{w_0}, β_0 and ω_{rot_0} are the nominal wind speed, pitch angle and rotor speed at the chosen operating point; ΔV_w, $\Delta\beta$ and $\Delta\omega_{rot}$ are the respective perturbations and $\frac{\partial \tau_{aero}}{\partial V_w}, \frac{\partial \tau_{aero}}{\partial \beta}, \frac{\partial \tau_{aero}}{\partial \omega_{rot}}$ are the partial derivatives evaluated at the chosen operating point.

Let the change in the aerodynamic torque be represented by

$$\Delta\tau_{aero} = \tau_{aero}\left(V_w, \beta, \omega_{rot}\right) - \tau_{aero}\left(V_{w\_0}, \beta_0, \omega_{rot\_0}\right) \tag{12.4}$$

then,

$$\Delta\tau_{aero} = \frac{\partial\tau_{aero}}{\partial V_w}\Delta V_{wind} + \frac{\partial\tau_{aero}}{\partial\beta}\Delta\beta + \frac{\partial\tau_{aero}}{\partial\omega_{rot}}\Delta\omega_{rot} \tag{12.5}$$

Assuming that the generator torque is constant and that the rotor exhibits no acceleration at equilibrium, then

$$\tau_{aero}\left(V_{w\_0}, \beta_0, \omega_{rot\_0}\right) = N\tau_{em} \tag{12.6}$$

Substituting equations (12.3) and (12.6) into equation (12.1) yields,

$$\frac{\partial\tau_{aero}}{\partial V_w}\Delta V_w + \frac{\partial\tau_{aero}}{\partial\beta}\Delta\beta + \frac{\partial\tau_{aero}}{\partial\omega_{rot}}\Delta\omega_{rot} = J_{tot}\Delta\frac{d}{dt}\omega_{rot} \tag{12.7}$$

Assuming that at the chosen operating point the wind speed is constant, then equation (12.7) is simplified to

$$\frac{\partial\tau_{aero}}{\partial\beta}\Delta\beta + \frac{\partial\tau_{aero}}{\partial\omega_{rot}}\Delta\omega_{rot} = J_{tot}\Delta\frac{d}{dt}\omega_{rot} \tag{12.8}$$

Taking the Laplace transform of equation (12.8), the transfer function in the *s*-domain for the effect of the pitch angle β on the rotor speed ω_{rot} is given by

$$\frac{\Delta\omega_{rot}(\mathrm{s})}{\Delta\beta(s)} = \frac{\dfrac{\partial\tau_{aero}}{\partial\beta J_{tot}}}{\left(\mathrm{s} - \dfrac{\partial\tau_{aero}}{\partial\omega_{rot}J_{tot}}\right)} \tag{12.9}$$

Appendix D

Model-based damper design

A detailed block diagram of the structure of the model-based torsional damper is shown in Figure D.1.

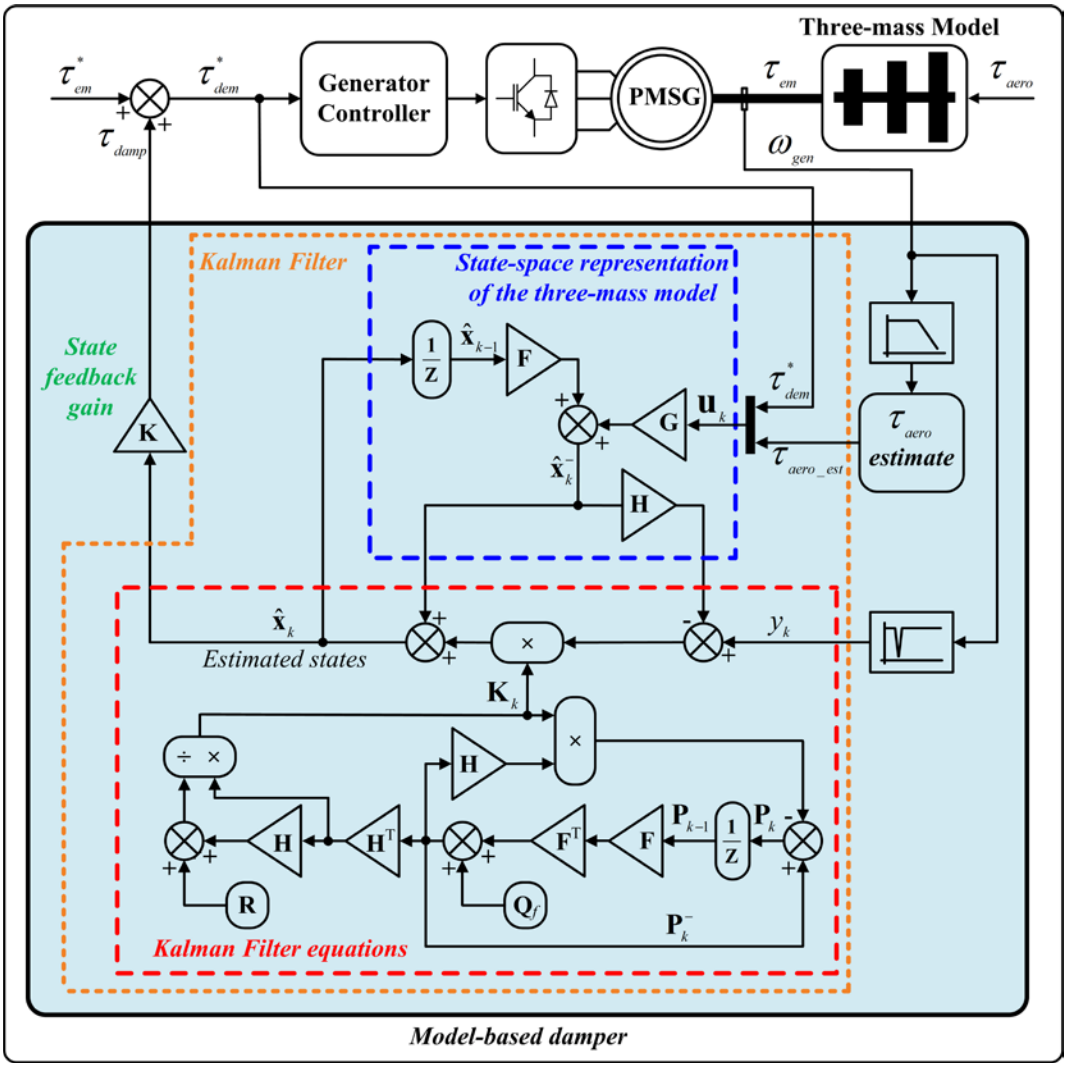

Figure D.1: Detailed structure of the model-based torsional vibration damper

The structure of the model-based vibration damper can be divided into three sections: the KF equations, the plant representation (three-mass model) and the state feedback controller. The procedure to the design the damper was split in two parts. First it was assumed that the states vector ($\hat{\mathbf{x}}_k$) was available and designed the state-feedback controller to determine the state feedback gain **K.** Then the KF was designed to estimate the state vector ($\hat{\mathbf{x}}_k$).

D.1. Full state feedback controller design

In full state feedback, the control law is a linear combination of the system states given by

$$\tau_{dem}^{*} = \tau_{gen}^{*} - \left(K_1\omega_{rot} + K_2\left(\theta_{rot} - \theta_{hub}\right) + K_3\omega_{hub} + K_4\left(\theta_{hub} - \theta_{gen}\right) + K_5\omega_{gen}\right) \qquad (13.1)$$

where K_1, K_2, K_3, K_4 and K_5 are the elements of state feedback gain **K**.

In order to be able to place the system poles arbitrarily in the complex plane the system need to be controllable.

Controllability test:

In order for a system to be completely controllable,

$$\left[\mathbf{B}\ \ \mathbf{AB}\ \ \mathbf{A}^2\mathbf{B}\ \ \mathbf{A}^3\mathbf{B}\ \ \mathbf{A}^4\mathbf{B}\ .....\right]$$

must be full rank [101], were **A** and **B** are the system and input matrices respectively. For a system matrix **A** (three-mass model) and input matrix **B** (generator torque only) given by

$$\mathbf{A} = \begin{bmatrix} 0 & -117 & 0 & 0 & 0 \\ 1 & 0 & -1 & 0 & 0 \\ 0.1 & 218 & -0.23 & -76 & 0 \\ 0 & 0 & 1 & 0 & -0.0120 \\ 0 & 0 & 50 & 32001 & -0.6 \end{bmatrix} \mathbf{B} = \begin{bmatrix} 0 \\ 0 \\ 0 \\ 0 \\ 0.0167 \end{bmatrix}$$

the system is full rank so the plant is completely controllable.

The damping of a system can be increased by increasing the real negative part of the eigenvalues (poles). The optimal location of these poles is rather difficult to find and usually techniques such as linear quadratic regulator are used to trade-off performance with actuator use [62]. In this case, the locations of the closed-loop poles were chosen close to the ones achieved in the BPF-based damper. The state feedback gains corresponding to these pole locations are given in Table D-1.

Table D-1: State feedback gains

Feedback coefficient	Gains
K1	6.363×10^{4}
K2	-4.299×10^{5}
K3	-1.363×10^{4}
K4	1.816×10^{5}
K5	-5.999×10^{2}

D.2. State Observer Design

In order to be able to estimate the state variables of a linear time-invariant system from measurable variables, the system need to be completely observable.

Observability test:

In order for a system to be completely observable,

$$\begin{bmatrix} \mathbf{C} \\ \mathbf{CA} \\ \mathbf{CA}^2 \\ \mathbf{CA}^3 \\ \mathbf{CA}^4 \end{bmatrix}$$

must be full rank [101], were **A** and **C** are the system and output matrices respectively. For a system matrix **A** (three-mass model) and output matrix C given by

$$\mathbf{A} = \begin{bmatrix} 0 & -117 & 0 & 0 & 0 \\ 1 & 0 & -1 & 0 & 0 \\ 0.1 & 218 & -0.23 & -76 & 0 \\ 0 & 0 & 1 & 0 & -0.0120 \\ 0 & 0 & 50 & 32001 & -0.6 \end{bmatrix} \mathbf{C} = \begin{bmatrix} 0 & 0 & 0 & 0 & 1 \end{bmatrix}$$

the system is full rank so the plant is completely observable.

A KF was used for the estimation of the system (three-mass model) states. In KF theory, it is assumed that the plant is susceptible to process noise which in this case is parametric uncertainty in the model (discrepancies in the values of turbine parameters between the modelled and the actual) and that the output measurement is subjected to measurement noise. Provided that the plant and measurement noise are Gaussian, zero-mean, uncorrelated white noise then the KF is the best filter that minimises the variance of the state estimation error [102, 103]. The KF can be implemented both in continuous and discrete time. In this work a discrete-time KF was used. In order to derive an optimal estimator, a few mathematical assumptions are made about the plant and the unknown disturbances.

Assumption 1: The mechanical model (three-mass model) used is sufficiently accurate

Assumption 2: The disturbances are stochastic, zero mean with known input and output noise covariance matrices **Q** and **R**

From these assumptions, the KF minimises the expected value (mean) of the 2-norm state estimate error. If the error between the true and the estimated state is denoted as $\tilde{x}_k$ and given by

$$\tilde{x}_k = x_k - \hat{x}_k \tag{13.2}$$

then the expected value of the 2-norm estimation error is given by

$$min\ E[\tilde{x}_k \tilde{x}_k^T] \tag{13.3}$$

The general problem that a discrete KF addresses is to estimate the states of a discrete-time process that is governed by a linear stochastic difference equation given by [102]

$$\mathbf{x}_k = \mathbf{F}\mathbf{x}_{k-1} + \mathbf{G}\mathbf{u}_k + \omega_{k-1} \tag{13.4}$$

with a measurement equation

$$\mathbf{z}_k = \mathbf{H}\mathbf{x}_k + v_k \tag{13.5}$$

where ω_k and v_k are random variables representing the process and measurement noise $\left[\omega_k \sim \mathrm{N}(0, \mathbf{Q}_k) \text{ and } v_k \sim \mathrm{N}(0, \mathbf{R}_k)\right]$ respectively, **F**, **G** and **H** are the discrete-time equivalent matrices of the system matrix **A**, the input matrix **B** and the output matrix **C,** respectively.

The equations for the discrete-time KF can be split into two groups, namely time update equations and the measurement update equations. The time update equations are responsible to predict the current states ($\hat{\mathbf{x}}_k^-$) and the error covariance ($\mathbf{P}_k^-$) estimates for the next time step before the measurement is available [102]. These are given by

$$\hat{\mathbf{x}}_k^- = \mathbf{F}\hat{\mathbf{x}}_{k-1} + \mathbf{G}\mathbf{u}_k \tag{13.6}$$

$$\mathbf{P}_k^- = \mathbf{F}\mathbf{P}_{k-1}\mathbf{F}^T + \mathbf{Q} \tag{13.7}$$

where $\hat{\mathbf{x}}_{k-1}$ and $\mathbf{P}_{k-1}$ are the initial conditions for the states and the estimation error covariance. The measurement update equations are then responsible to incorporate the measurement into the predicted estimates to obtain an improved estimate of the states ($\hat{\mathbf{x}}_k$) [102]. These equations are given by

$$\mathbf{K}_k = \mathbf{P}_k^-\mathbf{H}^T(\mathbf{H}\mathbf{P}_k^-\mathbf{H}^T + \mathbf{R})^{-1} \tag{13.8}$$

$$\hat{\mathbf{x}}_k = \hat{\mathbf{x}}_k^- + \mathbf{K}_k\left(y_k - \mathbf{H}\hat{\mathbf{x}}_k^-\right) \tag{13.9}$$

$$\mathbf{P}_k = \left(\mathbf{I} - \mathbf{K}_k\mathbf{H}\right)\mathbf{P}_k^- \tag{13.10}$$

where $\mathbf{K}_k$ is the Kalman gain and $\mathbf{P}_k$ is the estimation error covariance matrix, $\mathbf{R}$ is the measurement noise covariance, $\mathbf{H}$ is the output matrix and y_k is the measurement. Equation (13.8) shows that the larger the measurement noise $\mathbf{R}$ the smaller is the Kalman gain $\mathbf{K}_k$. This implies that low credibility is given to the measurement y_k when computing the next state estimate $\hat{\mathbf{x}}_k$.

The second assumption made earlier was that the noise covariance matrices $\mathbf{Q}$ and $\mathbf{R}$ are known. The measurement noise covariance matrix $\mathbf{R}$ was easily determined by taking some off-line sample measurements and then computing the variance of the measurement noise. In this case, $\mathbf{R}$ is a scalar value since the measurement equation (13.5) is composed of only the generator speed measurement. The standard deviation of the measurement noise was set to 0.5 rad/s. The process noise covariance $\mathbf{Q}$ is generally more difficult to determine since it is not possible to observe the process being estimated. The process noise covariance $\mathbf{Q}$ is a matrix which is often adequate to let it be simply diagonal. A sensible approach to determine the $\mathbf{Q}$ matrix was to make an initial guess of the entries. Then the state estimation was run offline and the diagonal entries adjusted by systematic trial and error.

Although the state-feedback controller and the KF have strong robustness properties when used individually, robustness is drastically reduced when they are used together. To overcome this problem, the loop transfer recovery method is normally used to recover some of the robustness properties. In this work, the adjustment procedure that was proposed in [124], was used. The original full-state feedback loop was achieved by modifying the design of the KF, were the uncertainties in the plant were represented by additional process noise as given by

$$\mathbf{Q}_f = \mathbf{Q} + q^2\mathbf{Q} \tag{13.11}$$

where $\mathbf{Q}$ is the original process noise covariance matrix, $q^2\mathbf{Q}$ is the additional fictitious noise matrix and $\mathbf{Q}_f$ is the resultant process noise covariance matrix.

The term q was increased iteratively until the open loop response with the KF became close to that obtained with full-state feedback. With this additional fictitious process noise, the KF would interpret it as less confidence in the system model and correspondingly would put more credibility on the measurement and less emphasis on the process model. The downside of adding this fictitious noise is poorer performance of the filter should the process model be correct [103]. The $\mathbf{R}$ and $\mathbf{Q}_f$ entries that led to good performance of the KF are given by

$$\mathbf{R} = 0.25, \mathbf{Q}_f = \begin{bmatrix} 2.56\times10^{-11} & 0 & 0 & 0 & 0 \\ 0 & 3\times10^{-15} & 0 & 0 & 0 \\ 0 & 0 & 6.22\times10^{-12} & 0 & 0 \\ 0 & 0 & 0 & 2.42\times10^{-11} & 0 \\ 0 & 0 & 0 & 0 & 1.65\times10^{-3} \end{bmatrix}$$

Appendix E

Hardware

E.1. Hardware data

Table E-1: Power components specifications

AC brushless machines:

Rated power: 1.2 kW
Rated voltage: 400 V
Rated torque: 3.9 Nm
Rated speed: 3000 rpm
Stator resistance (ph-ph): 6.8 Ω
Stator inductance (ph-ph): 24.3 mH
Kt: 1.6 Nm/A
Ke: 98 V/krpm
Encoder: Incremental with 4096 ppr

Variable-speed drive:

Rated power: 2.2 kW
Rated voltage: 400 V

VSC:

Rated power: 10 kVA
Rated voltage: 400 V
DC link voltage (max): 800 V
AC Current (max): 15 A
Switching frequency (max): 10 kHz
Capacitor bank: 1020 µf

Auto-transformer:

Rated power: 5 kW
Rated voltage input: 400 V
Output voltage: 0 – 400 V

Input/Output inductors (L_1, L_2):

Rated current: 6.3 A
Inductance: 3.5 mH

E.2. Cabinet electrical schematic

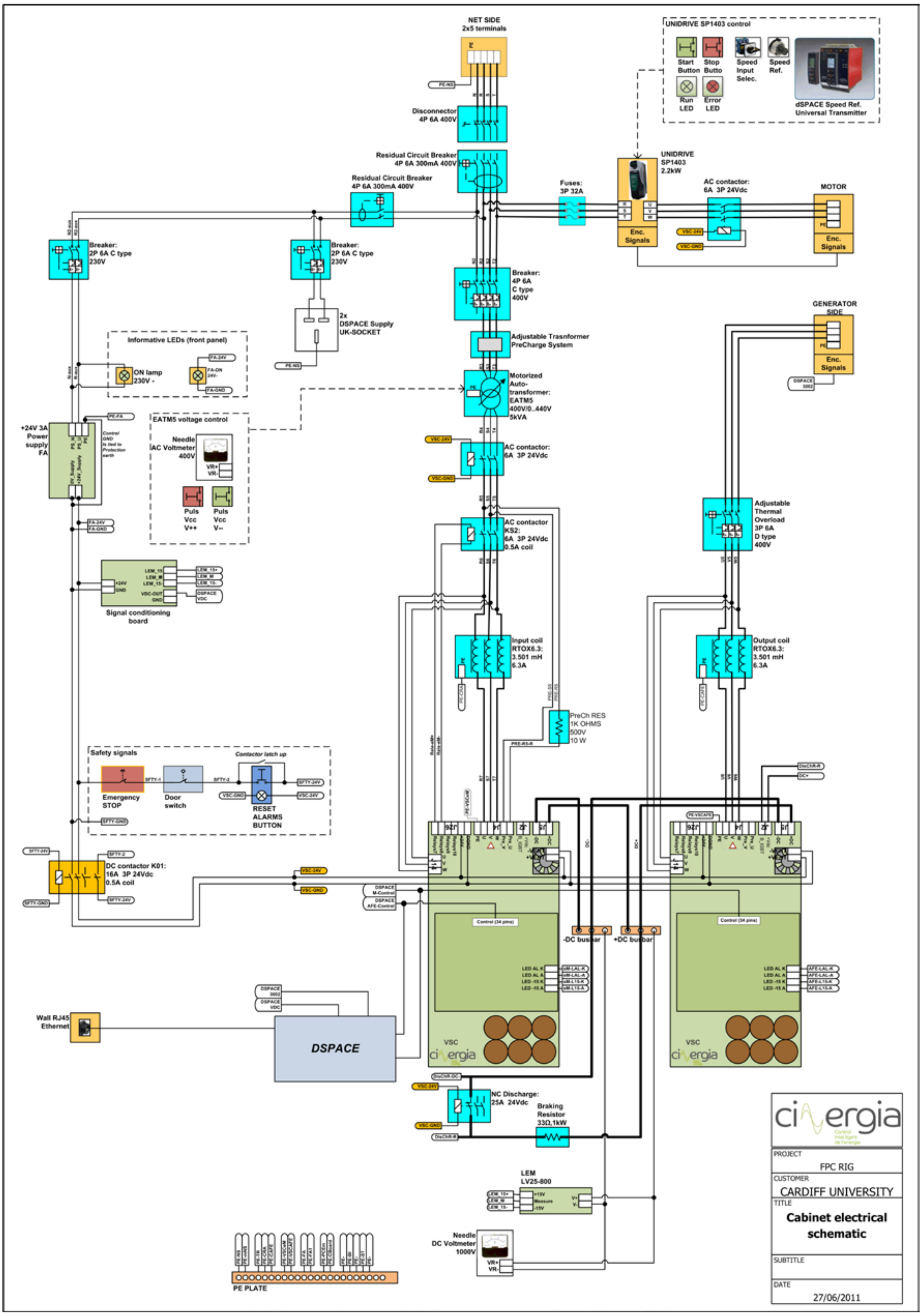

E.3. Power converter (Power, Driver and DSP boards)

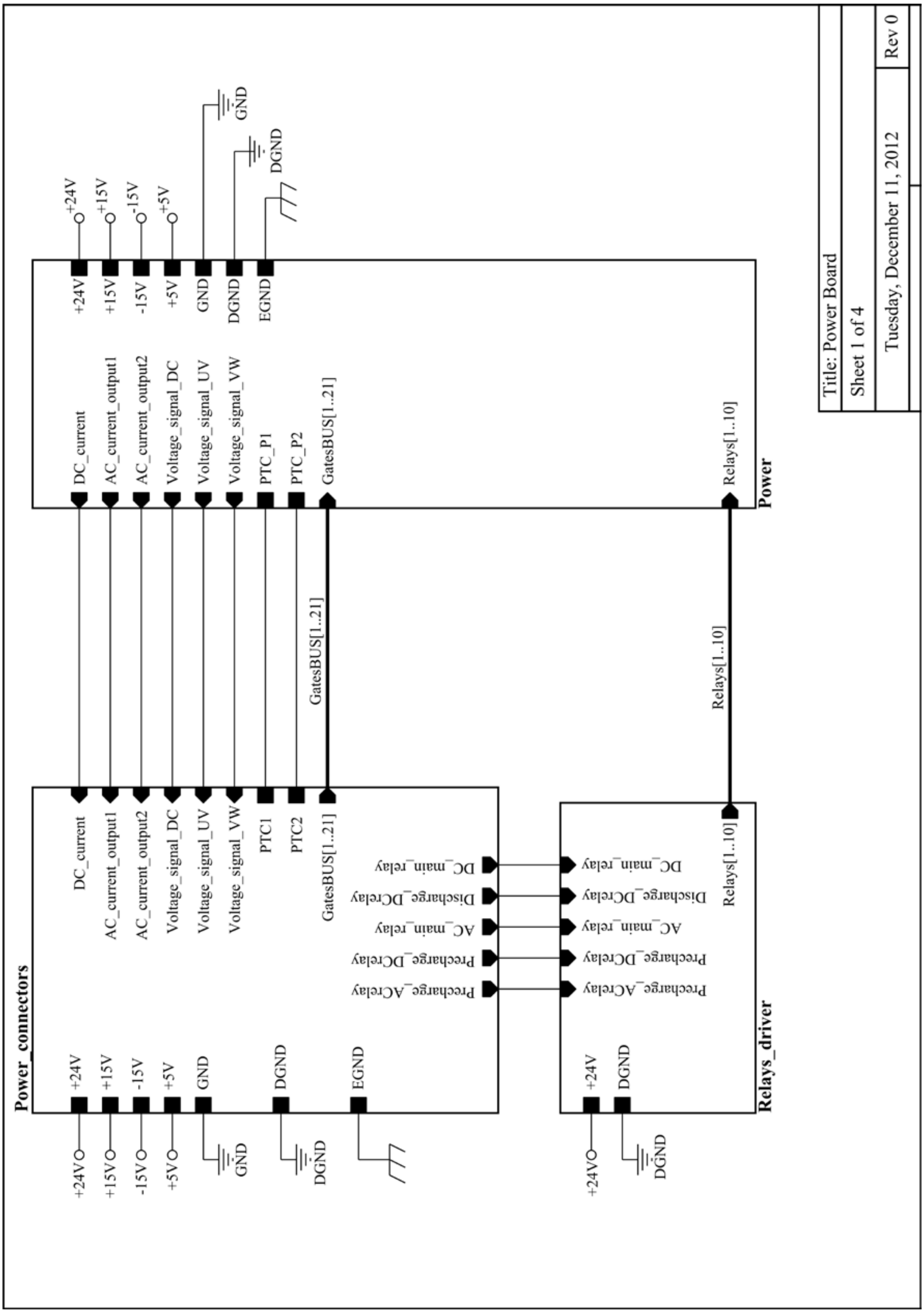

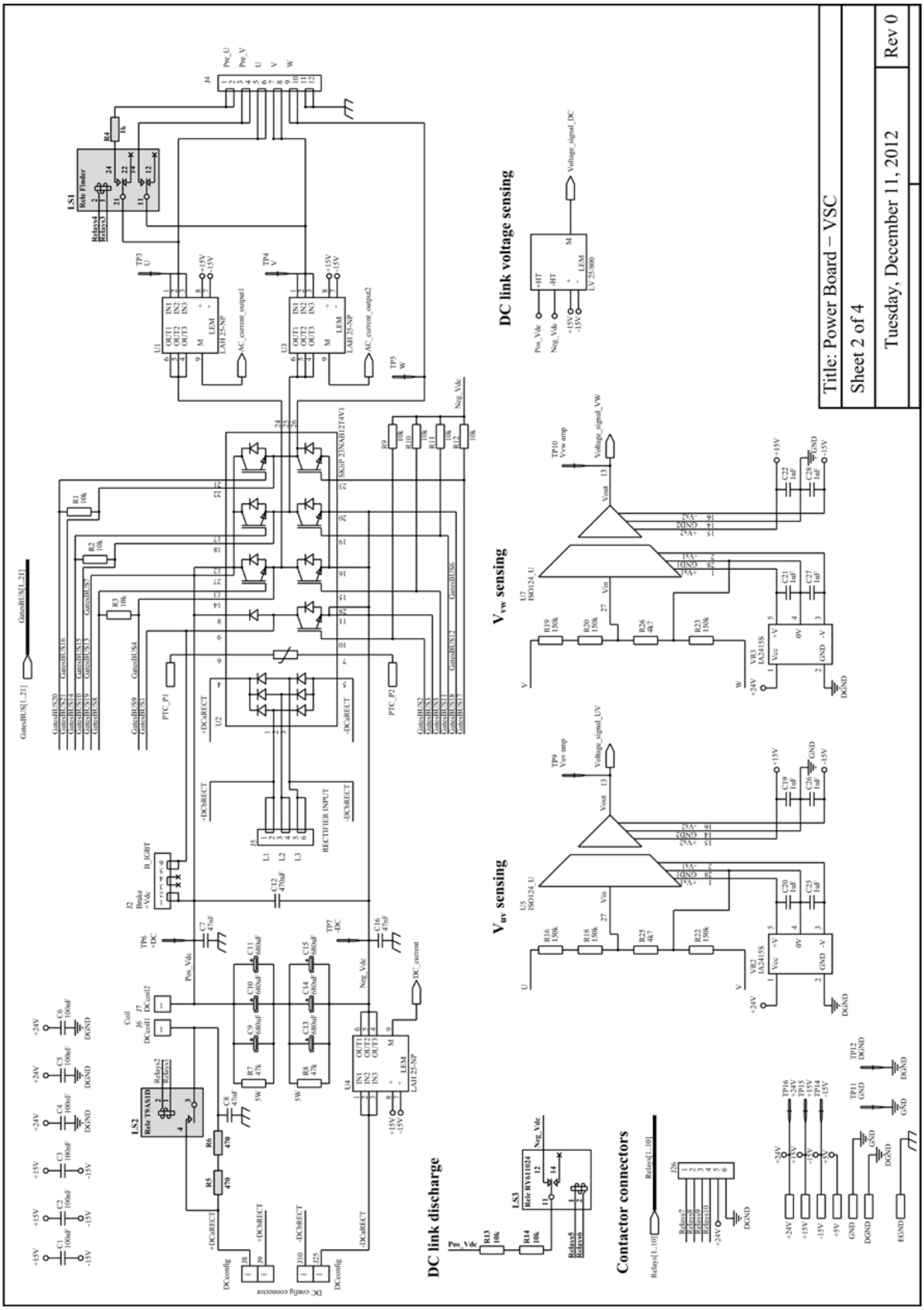
Title: Power Board – VSC
Sheet 2 of 4
Tuesday, December 11, 2012
Rev 0
DC link voltage sensing
Vvw sensing
Vuv sensing
DC link discharge
Contactor connectors
LS1 Rele Finder
LS2 Rele T9AS1D
LS3 Rele RY611024
LAH 25-NP
LV 25/800
ISO124_U
IA2415S
RECTIFIER INPUT
SKiiP 23NAB12T4V1
GatesBUS[1..21]
Relays[1..10]
Voltage_signal_DC
Voltage_signal_VW
Voltage_signal_UV
AC_current_output1
AC_current_output2
DC_current
Pos_Vdc
Neg_Vdc
DC config connector

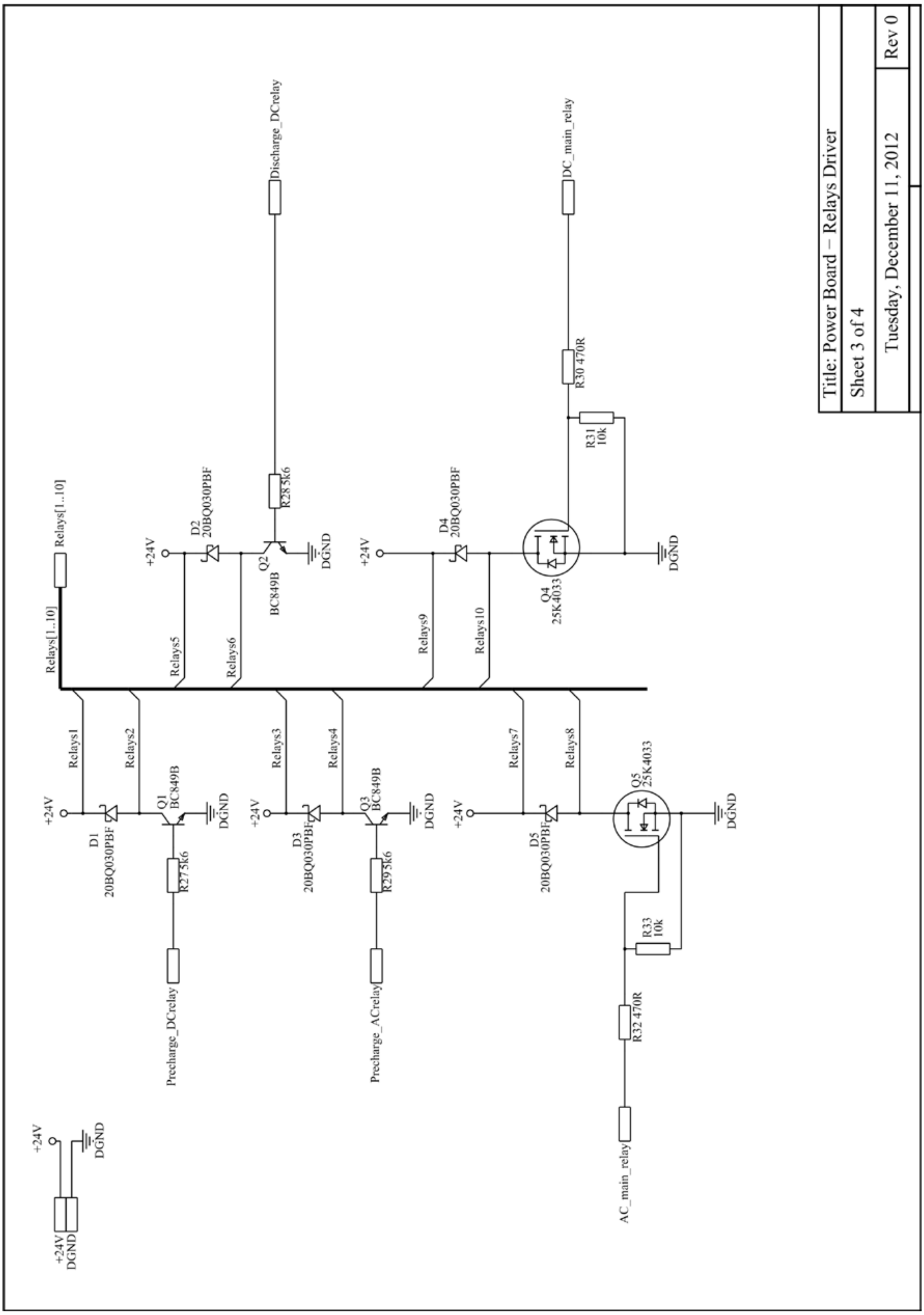
Title: Power Board – Relays Driver
Sheet 3 of 4
Tuesday, December 11, 2012
Rev 0
Relays[1..10]
Relays1
Relays2
Relays3
Relays4
Relays5
Relays6
Relays7
Relays8
Relays9
Relays10
+24V
DGND
D1 20BQ030PBF
D2 20BQ030PBF
D3 20BQ030PBF
D4 20BQ030PBF
D5 20BQ030PBF
Q1 BC849B
Q2 BC849B
Q3 BC849B
Q4 25K4033
Q5 25K4033
R27 5k6
R28 5k6
R29 5k6
R30 470R
R31 10k
R32 470R
R33 10k
Precharge_DCrelay
Precharge_ACrelay
Discharge_DCrelay
DC_main_relay
AC_main_relay

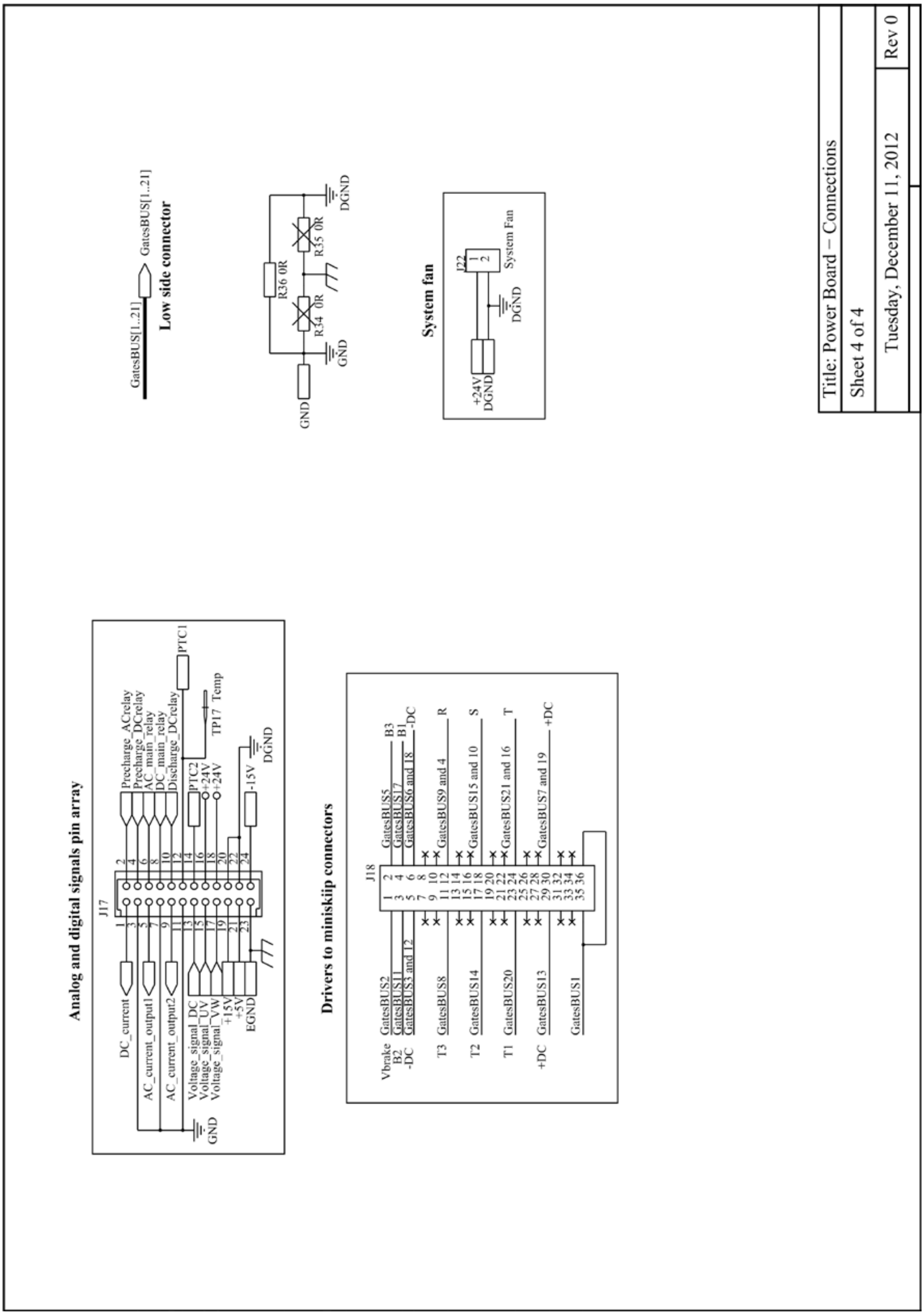
Analog and digital signals pin array
J17
DC_current
AC_current_output1
AC_current_output2
Voltage_signal_DC
Voltage_signal_UV
Voltage_signal_VW
+15V
+5V
EGND
GND
Precharge_ACrelay
Precharge_DCrelay
AC_main_relay
DC_main_relay
Discharge_DCrelay
PTC1
PTC2
+24V
+24V
TP17 Temp
-15V
DGND
Drivers to miniskiip connectors
J18
Vbrake
B2
-DC
T3
T2
T1
+DC
GatesBUS2
GatesBUS11
GatesBUS3 and 12
GatesBUS8
GatesBUS14
GatesBUS20
GatesBUS13
GatesBUS1
GatesBUS5
GatesBUS17
GatesBUS6 and 18
GatesBUS9 and 4
GatesBUS15 and 10
GatesBUS21 and 16
GatesBUS7 and 19
B3
B1
-DC
R
S
T
+DC
Low side connector
GatesBUS[1..21]
GatesBUS[1..21]
GND
R36 0R
R34 0R
R35 0R
DGND
DGND
System fan
J22
System Fan
+24V
DGND
DGND
Title: Power Board – Connections
Sheet 4 of 4
Tuesday, December 11, 2012
Rev 0

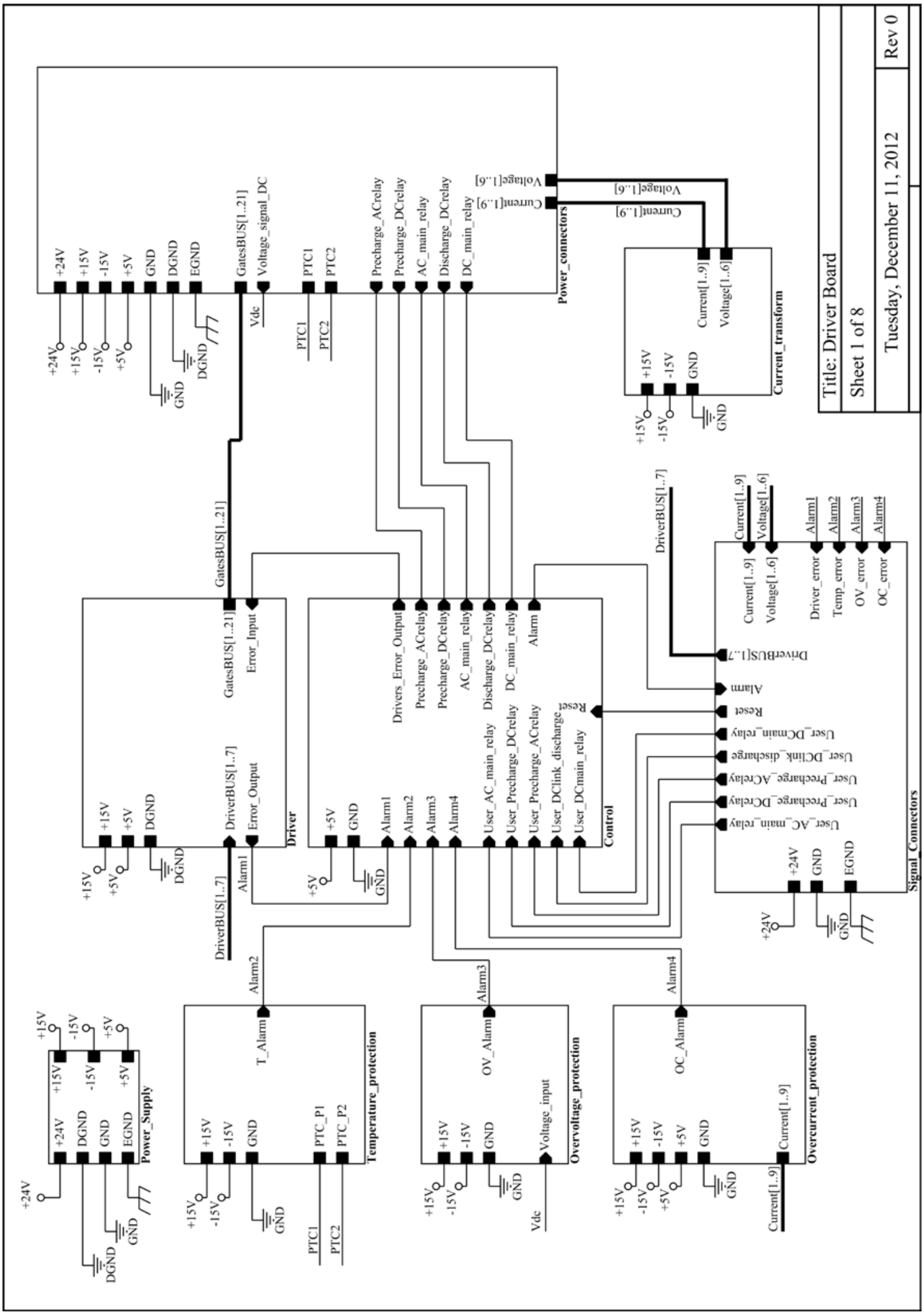
Title: Driver Board
Sheet 1 of 8
Tuesday, December 11, 2012
Rev 0
Power_connectors
+24V
+15V
-15V
+5V
GND
DGND
EGND
GatesBUS[1..21]
Voltage_signal_DC
PTC1
PTC2
Precharge_ACrelay
Precharge_DCrelay
AC_main_relay
Discharge_DCrelay
DC_main_relay
Current[1..9]
Voltage[1..6]
Vdc
Current_transform
Driver
Error_Input
DriverBUS[1..7]
Error_Output
Alarm1
Control
Drivers_Error_Output
Alarm
Reset
Alarm2
Alarm3
Alarm4
User_AC_main_relay
User_Precharge_DCrelay
User_Precharge_ACrelay
User_DClink_discharge
User_DCmain_relay
Signal_Connectors
Driver_error
Temp_error
OV_error
OC_error
Power_Supply
Temperature_protection
T_Alarm
PTC_P1
PTC_P2
Overvoltage_protection
OV_Alarm
Voltage_input
Overcurrent_protection
OC_Alarm

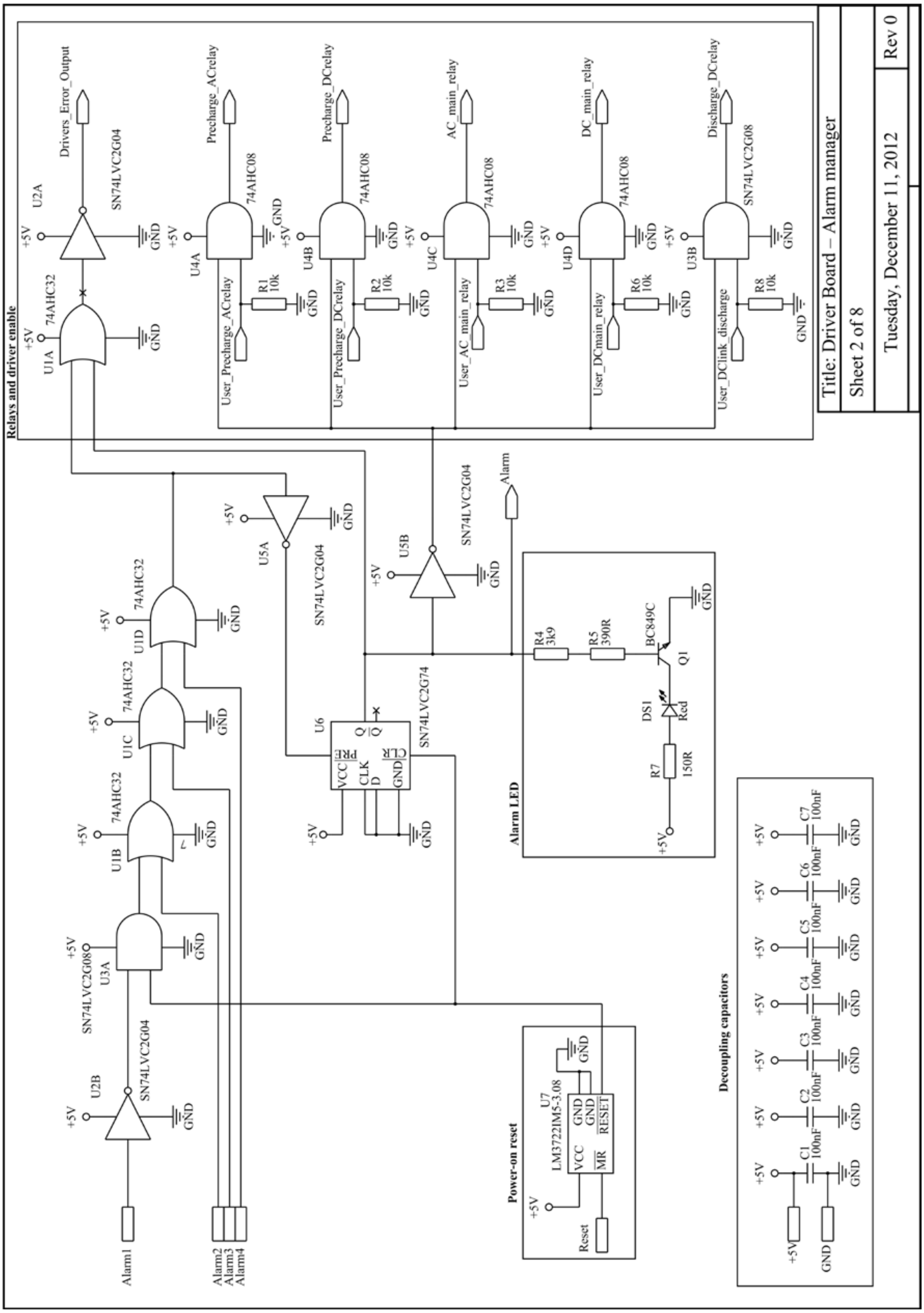
Title: Driver Board – Alarm manager
Sheet 2 of 8
Tuesday, December 11, 2012
Rev 0
Relays and driver enable
Drivers_Error_Output
Precharge_ACrelay
Precharge_DCrelay
AC_main_relay
DC_main_relay
Discharge_DCrelay
User_Precharge_ACrelay
User_Precharge_DCrelay
User_AC_main_relay
User_DCmain_relay
User_DClink_discharge
U1A 74AHC32
U2A SN74LVC2G04
U4A 74AHC08
U4B 74AHC08
U4C 74AHC08
U4D 74AHC08
U3B SN74LVC2G08
R1 10k
R2 10k
R3 10k
R6 10k
R8 10k
+5V
GND
Alarm
U5A SN74LVC2G04
U5B SN74LVC2G04
U1B 74AHC32
U1C 74AHC32
U1D 74AHC32
U3A SN74LVC2G08
U2B SN74LVC2G04
U6 SN74LVC2G74
VCC
PRE
CLK
D
GND
CLR
Q
Alarm LED
R4 3k9
R5 390R
BC849C
Q1
DS1 Red
R7 150R
Alarm1
Alarm2
Alarm3
Alarm4
Power-on reset
U7 LM3722IM5-3.08
VCC
MR
GND
GND
RESET
Reset
Decoupling capacitors
C1 100nF
C2 100nF
C3 100nF
C4 100nF
C5 100nF
C6 100nF
C7 100nF

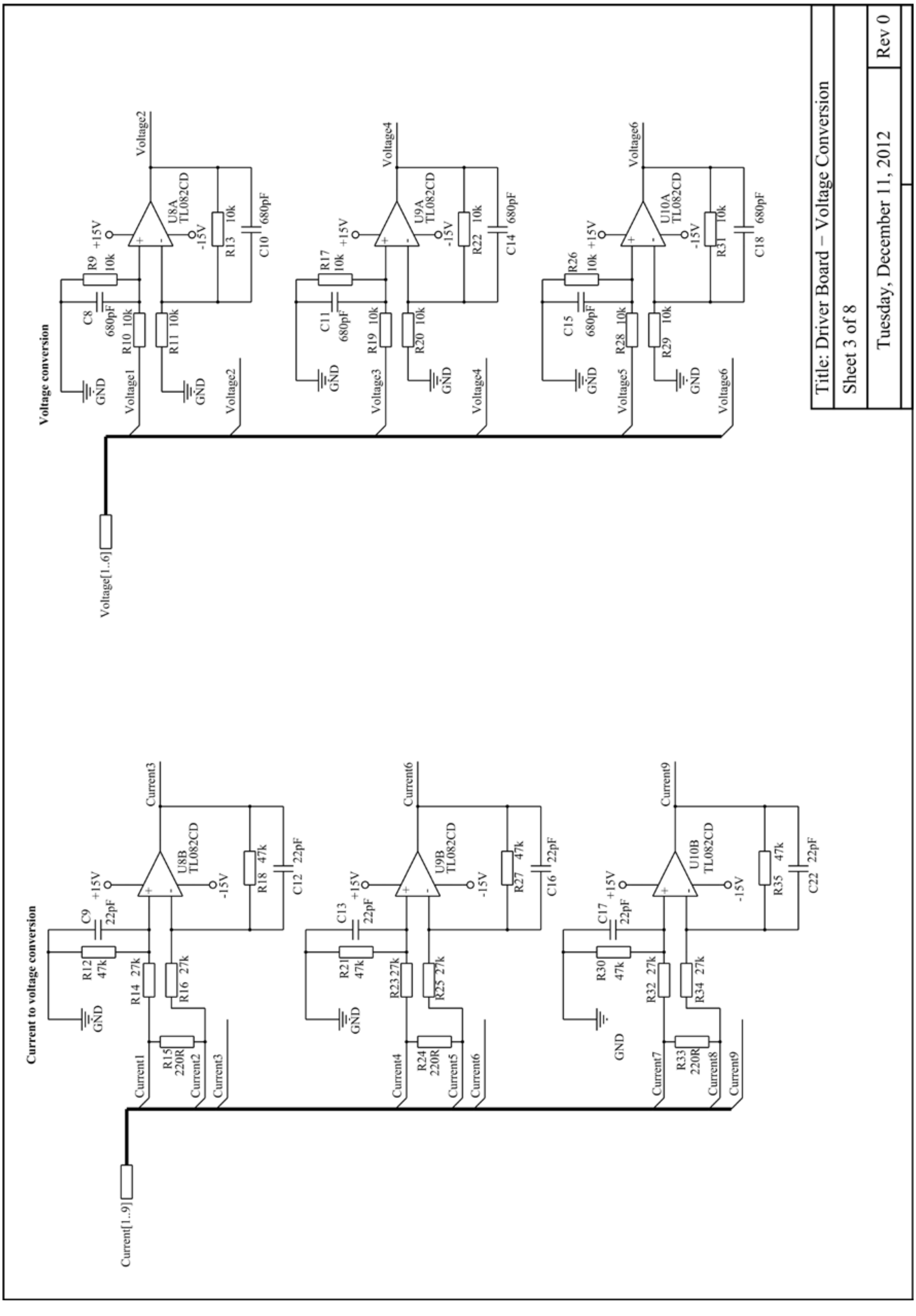
Title: Driver Board – Voltage Conversion
Sheet 3 of 8
Tuesday, December 11, 2012
Rev 0
Voltage conversion
Voltage[1..6]
Voltage1
Voltage2
Voltage3
Voltage4
Voltage5
Voltage6
U8A TL082CD
U9A TL082CD
U10A TL082CD
+15V
-15V
GND
R9 10k
C8 680pF
R10 10k
R11 10k
R13 10k
C10 680pF
R17 10k
C11 680pF
R19 10k
R20 10k
R22 10k
C14 680pF
R26 10k
C15 680pF
R28 10k
R29 10k
R31 10k
C18 680pF
Current to voltage conversion
Current[1..9]
Current1
Current2
Current3
Current4
Current5
Current6
Current7
Current8
Current9
U8B TL082CD
U9B TL082CD
U10B TL082CD
C9 22pF
R12 47k
R14 27k
R16 27k
R15 220R
R18 47k
C12 22pF
C13 22pF
R21 47k
R23 27k
R25 27k
R24 220R
R27 47k
C16 22pF
C17 22pF
R30 47k
R32 27k
R34 27k
R33 220R
R35 47k
C22 22pF

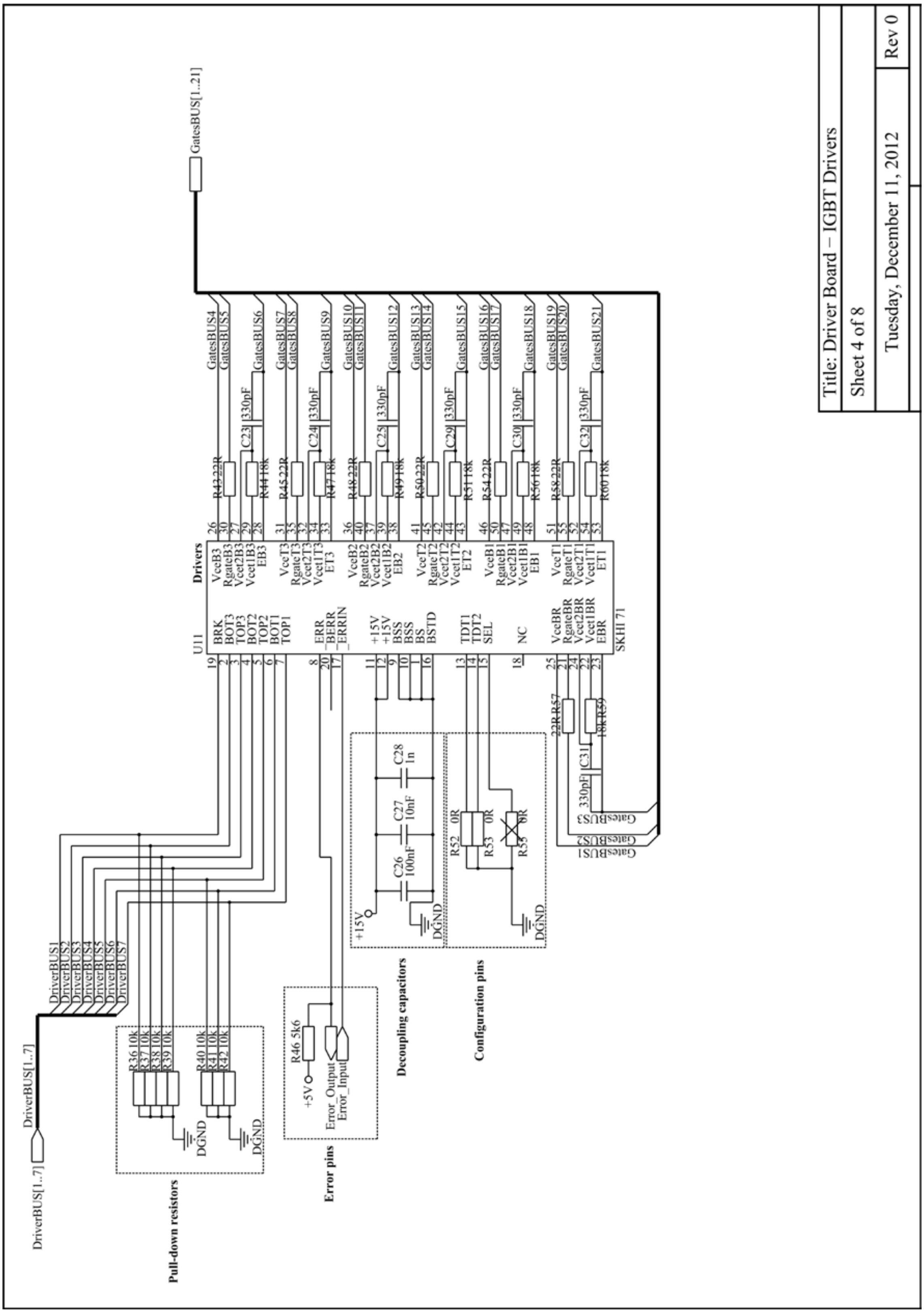
Title: Driver Board – IGBT Drivers
Sheet 4 of 8
Tuesday, December 11, 2012
Rev 0
GatesBUS[1..21]
DriverBUS[1..7]
DriverBUS1
DriverBUS2
DriverBUS3
DriverBUS4
DriverBUS5
DriverBUS6
DriverBUS7
Pull-down resistors
R36 10k
R37 10k
R38 10k
R39 10k
R40 10k
R41 10k
R42 10k
DGND
Error pins
R46 5k6
+5V
Error_Output
Error_Input
Decoupling capacitors
+15V
C26 100nF
C27 10nF
C28 1n
Configuration pins
R52 0R
R53 0R
R55 0R
U11
Drivers
SKHI 71
BRK
BOT3
TOP3
BOT2
TOP2
BOT1
TOP1
ERR
_BERR
_ERRIN
+15V
BSS
BS
BSTD
TDT1
TDT2
SEL
NC
VceBR
RgateBR
Vcet2BR
Vcet1BR
EBR
VceB3
RgateB3
Vcet2B3
Vcet1B3
EB3
VceT3
RgateT3
Vcet2T3
Vcet1T3
ET3
VceB2
RgateB2
Vcet2B2
Vcet1B2
EB2
VceT2
RgateT2
Vcet2T2
Vcet1T2
ET2
VceB1
RgateB1
Vcet2B1
Vcet1B1
EB1
VceT1
RgateT1
Vcet2T1
Vcet1T1
ET1
R43 22R
R44 18k
R45 22R
R47 18k
R48 22R
R49 18k
R50 22R
R51 18k
R54 22R
R56 18k
R58 22R
R60 18k
R57 22R
R59 18k
C23 330pF
C24 330pF
C25 330pF
C29 330pF
C30 330pF
C32 330pF
C31 330pF
GatesBUS1
GatesBUS2
GatesBUS3
GatesBUS4
GatesBUS5
GatesBUS6
GatesBUS7
GatesBUS8
GatesBUS9
GatesBUS10
GatesBUS11
GatesBUS12
GatesBUS13
GatesBUS14
GatesBUS15
GatesBUS16
GatesBUS17
GatesBUS18
GatesBUS19
GatesBUS20
GatesBUS21

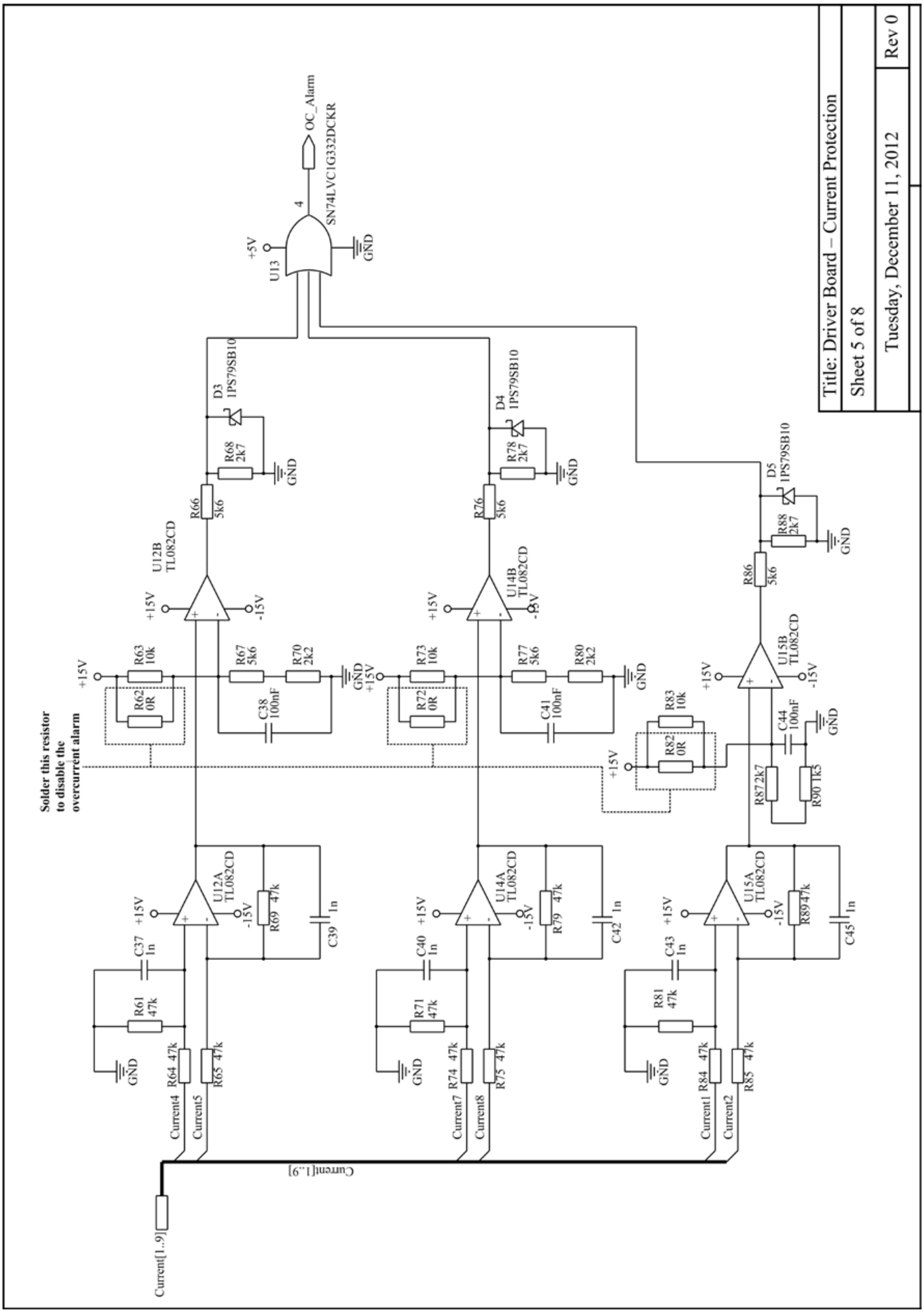
Title: Driver Board – Current Protection
Sheet 5 of 8
Tuesday, December 11, 2012
Rev 0
OC_Alarm
SN74LVC1G332DCKR
U13
+5V
GND
4
D3 1PS79SB10
D4 1PS79SB10
D5 1PS79SB10
R68 2k7
R78 2k7
R88 2k7
R66 5k6
R76 5k6
R86 5k6
U12B TL082CD
U14B TL082CD
U15B TL082CD
+15V
-15V
R63 10k
R62 0R
R67 5k6
R70 2k2
C38 100nF
R73 10k
R72 0R
R77 5k6
R80 2k2
C41 100nF
R83 10k
R82 0R
C44 100nF
R87 2k7
R90 1k5
Solder this resistor to disable the overcurrent alarm
U12A TL082CD
U14A TL082CD
U15A TL082CD
R69 47k
R79 47k
R89 47k
C39 1n
C42 1n
C45 1n
C37 1n
C40 1n
C43 1n
R61 47k
R71 47k
R81 47k
R64 47k
R65 47k
R74 47k
R75 47k
R84 47k
R85 47k
Current4
Current5
Current7
Current8
Current1
Current2
Current[1..9]

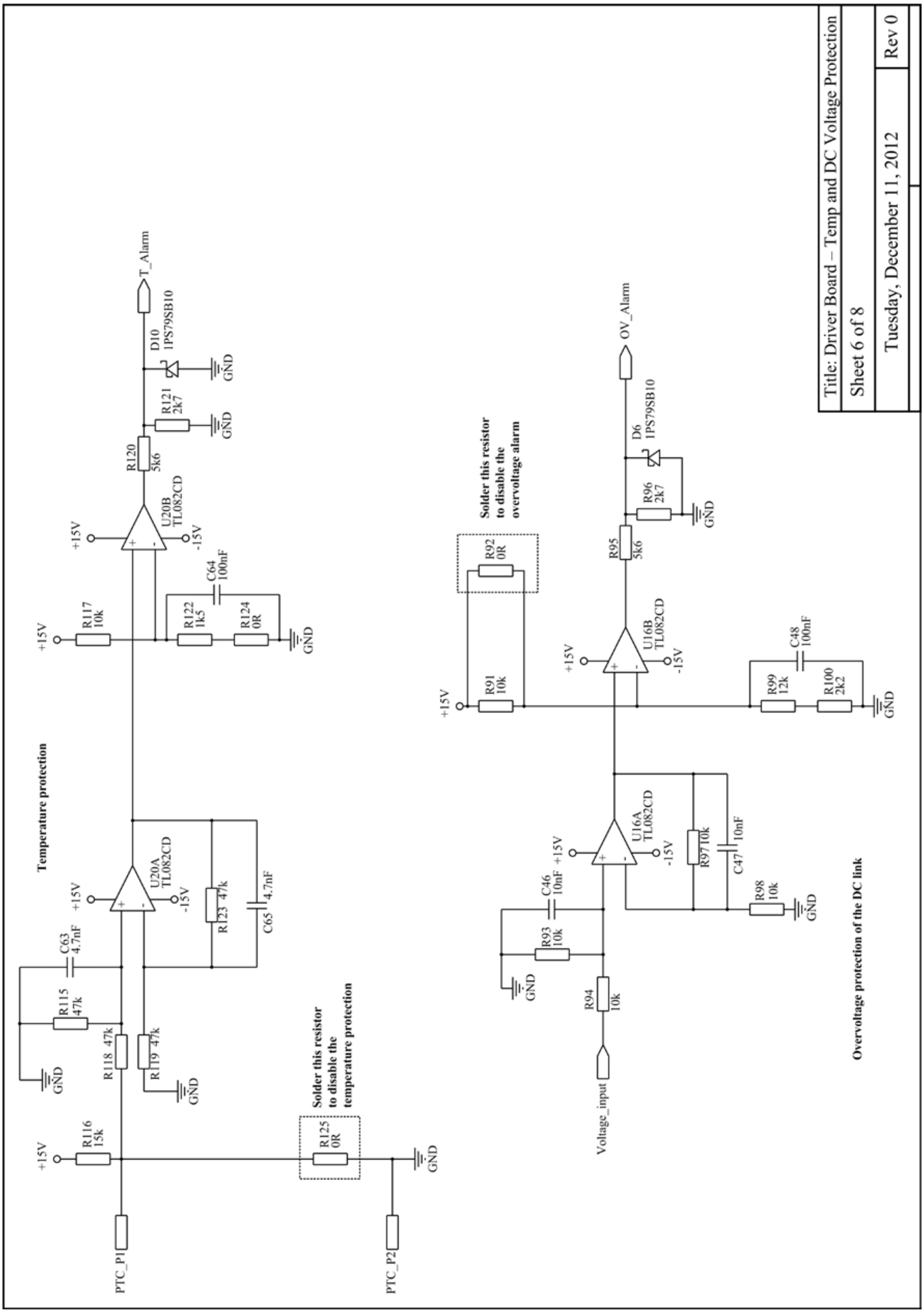
Title: Driver Board – Temp and DC Voltage Protection
Sheet 6 of 8
Tuesday, December 11, 2012
Rev 0
Temperature protection
Overvoltage protection of the DC link
Solder this resistor to disable the temperature protection
Solder this resistor to disable the overvoltage alarm
T_Alarm
OV_Alarm
PTC_P1
PTC_P2
Voltage_input
D10 1PS79SB10
D6 1PS79SB10
U20A TL082CD
U20B TL082CD
U16A TL082CD
U16B TL082CD
R115 47k
R116 15k
R117 10k
R118 47k
R119 47k
R120 5k6
R121 2k7
R122 1k5
R123 47k
R124 0R
R125 0R
R91 10k
R92 0R
R93 10k
R94 10k
R95 5k6
R96 2k7
R97 10k
R98 10k
R99 12k
R100 2k2
C63 4.7nF
C64 100nF
C65 4.7nF
C46 10nF
C47 10nF
C48 100nF
+15V
-15V
GND

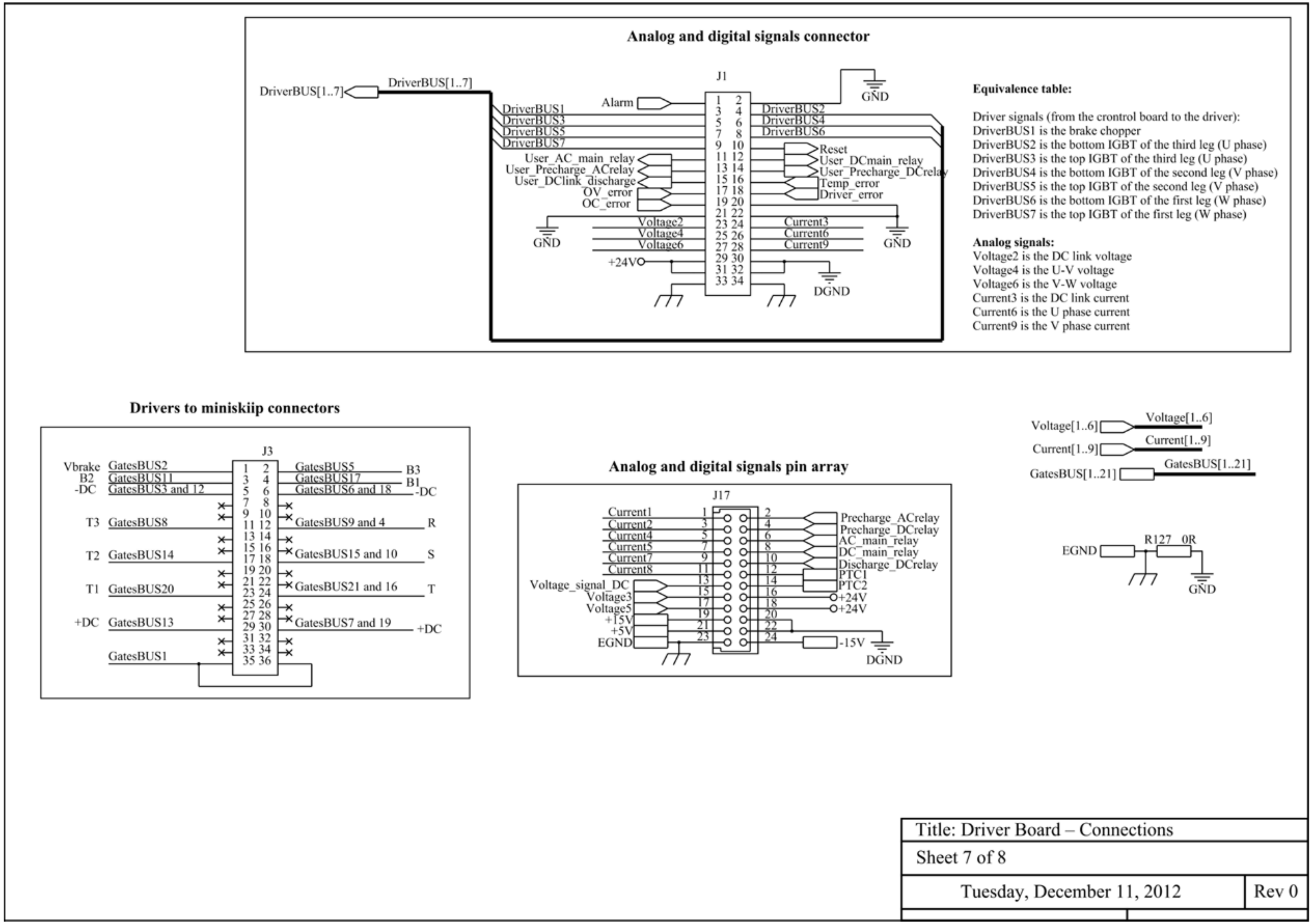

Equivalence table:

Driver signals (from the crontrol board to the driver):
DriverBUS1 is the brake chopper
DriverBUS2 is the bottom IGBT of the third leg (U phase)
DriverBUS3 is the top IGBT of the third leg (U phase)
DriverBUS4 is the bottom IGBT of the second leg (V phase)
DriverBUS5 is the top IGBT of the second leg (V phase)
DriverBUS6 is the bottom IGBT of the first leg (W phase)
DriverBUS7 is the top IGBT of the first leg (W phase)

Analog signals:
Voltage2 is the DC link voltage
Voltage4 is the U-V voltage
Voltage6 is the V-W voltage
Current3 is the DC link current
Current6 is the U phase current
Current9 is the V phase current

Title: Driver Board – Connections
Sheet 7 of 8
Tuesday, December 11, 2012
Rev 0

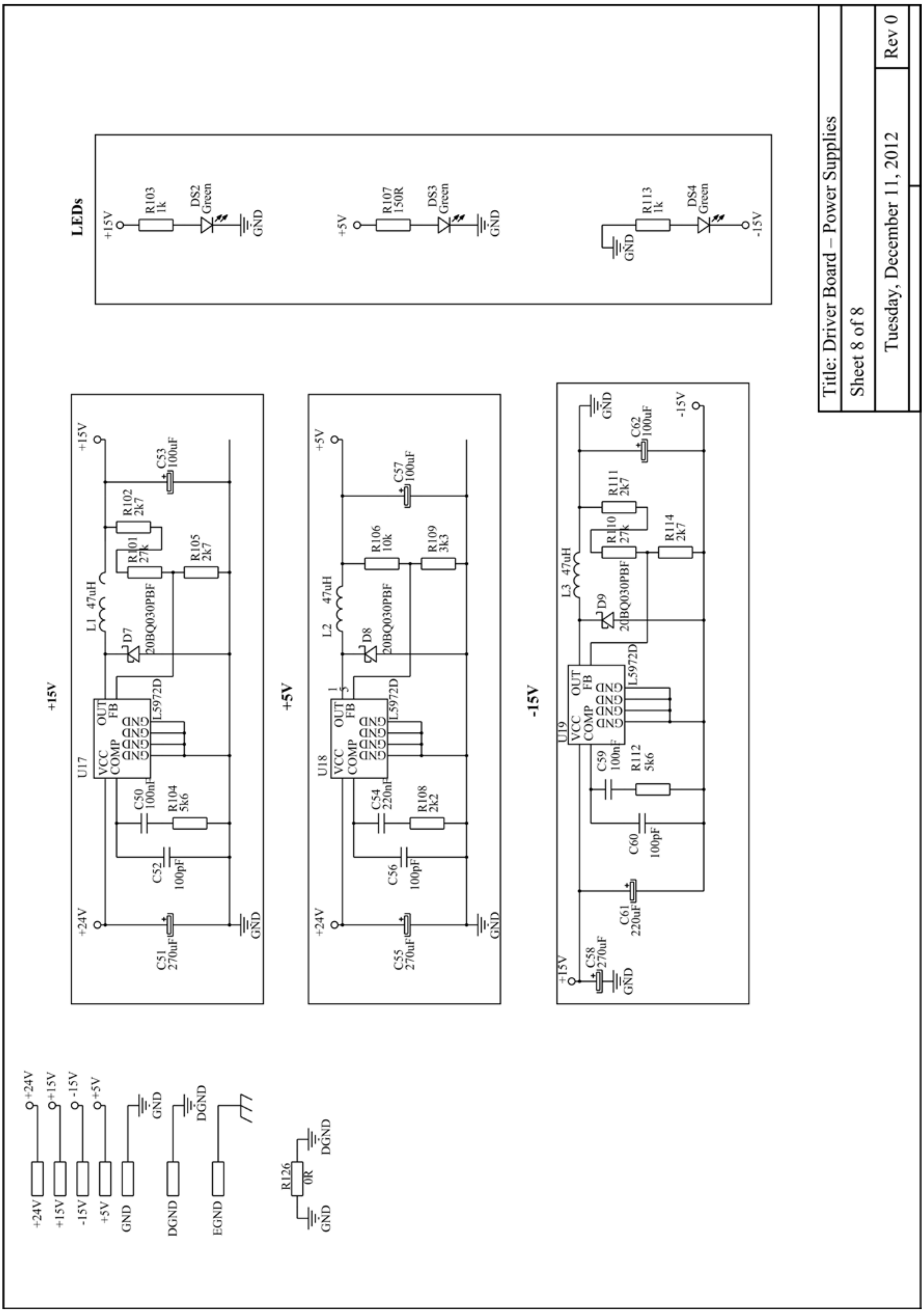
Title: Driver Board – Power Supplies
Sheet 8 of 8
Tuesday, December 11, 2012
Rev 0
LEDs
+15V
R103 1k
DS2 Green
GND
+5V
R107 150R
DS3 Green
R113 1k
DS4 Green
-15V
+15V
U17
VCC
COMP
OUT
FB
GND
L5972D
L1 47uH
D7 20BQ030PBF
R101 27k
R102 2k7
R105 2k7
C53 100uF
C50 100nF
R104 5k6
C52 100pF
C51 270uF
+24V
+5V
U18
L2 47uH
D8 20BQ030PBF
R106 10k
R109 3k3
C57 100uF
C54 220nF
R108 2k2
C56 100pF
C55 270uF
-15V
U19
L3 47uH
D9 20BQ030PBF
R110 27k
R111 2k7
R114 2k7
C62 100uF
C59 100nF
R112 5k6
C60 100pF
C61 220uF
C58 270uF
+24V
+15V
-15V
+5V
GND
DGND
EGND
R126 0R

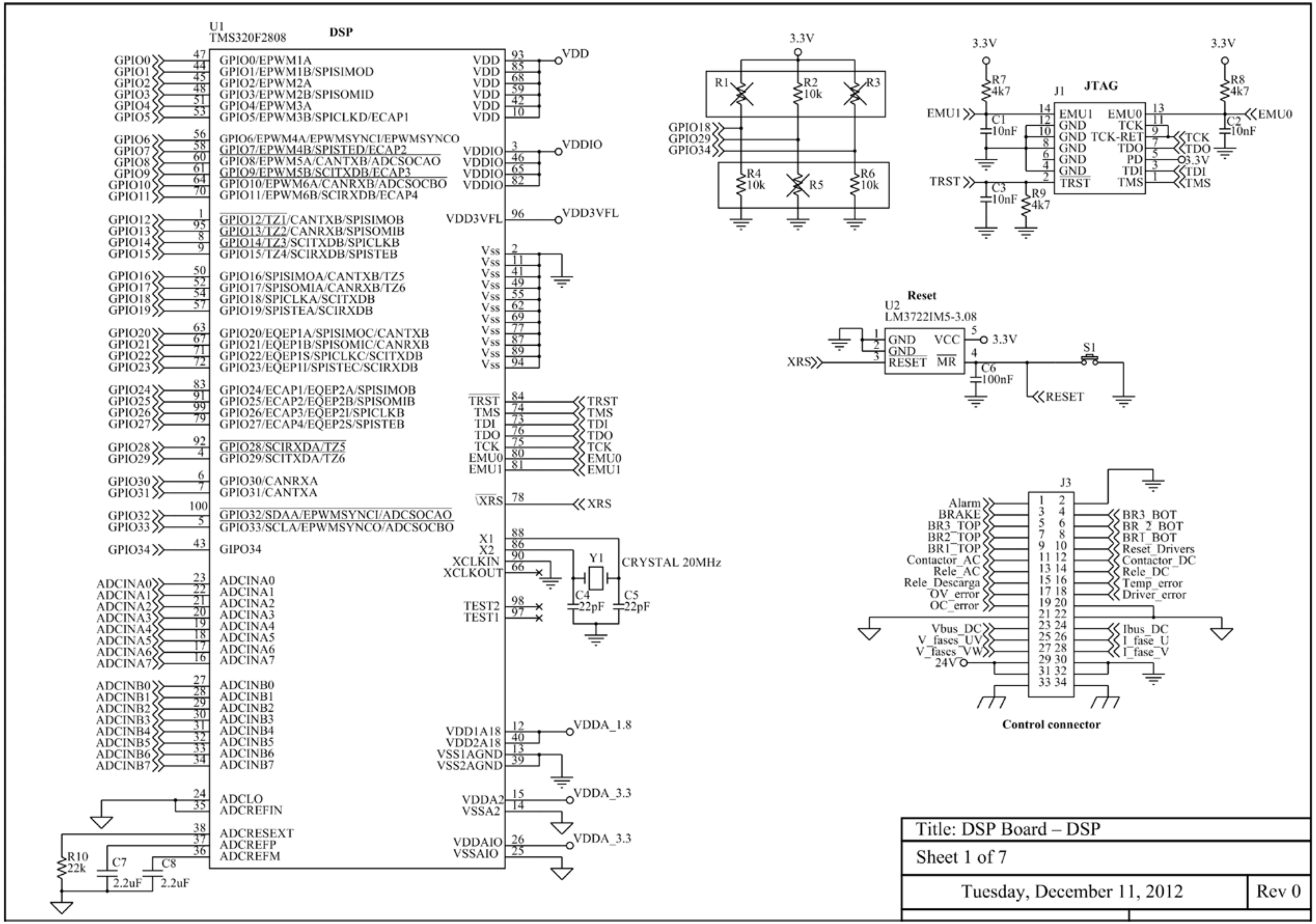
U1
TMS320F2808
DSP
GPIO0/EPWM1A
GPIO1/EPWM1B/SPISIMOD
GPIO2/EPWM2A
GPIO3/EPWM2B/SPISOMID
GPIO4/EPWM3A
GPIO5/EPWM3B/SPICLKD/ECAP1
GPIO6/EPWM4A/EPWMSYNCI/EPWMSYNCO
GPIO7/EPWM4B/SPISTED/ECAP2
GPIO8/EPWM5A/CANTXB/ADCSOCAO
GPIO9/EPWM5B/SCITXDB/ECAP3
GPIO10/EPWM6A/CANRXB/ADCSOCBO
GPIO11/EPWM6B/SCIRXDB/ECAP4
GPIO12/TZ1/CANTXB/SPISIMOB
GPIO13/TZ2/CANRXB/SPISOMIB
GPIO14/TZ3/SCITXDB/SPICLKB
GPIO15/TZ4/SCIRXDB/SPISTEB
GPIO16/SPISIMOA/CANTXB/TZ5
GPIO17/SPISOMIA/CANRXB/TZ6
GPIO18/SPICLKA/SCITXDB
GPIO19/SPISTEA/SCIRXDB
GPIO20/EQEP1A/SPISIMOC/CANTXB
GPIO21/EQEP1B/SPISOMIC/CANRXB
GPIO22/EQEP1S/SPICLKC/SCITXDB
GPIO23/EQEP1I/SPISTEC/SCIRXDB
GPIO24/ECAP1/EQEP2A/SPISIMOB
GPIO25/ECAP2/EQEP2B/SPISOMIB
GPIO26/ECAP3/EQEP2I/SPICLKB
GPIO27/ECAP4/EQEP2S/SPISTEB
GPIO28/SCIRXDA/TZ5
GPIO29/SCITXDA/TZ6
GPIO30/CANRXA
GPIO31/CANTXA
GPIO32/SDAA/EPWMSYNCI/ADCSOCAO
GPIO33/SCLA/EPWMSYNCO/ADCSOCBO
GIPO34
ADCINA0 ADCINA1 ADCINA2 ADCINA3 ADCINA4 ADCINA5 ADCINA6 ADCINA7
ADCINB0 ADCINB1 ADCINB2 ADCINB3 ADCINB4 ADCINB5 ADCINB6 ADCINB7
ADCLO
ADCREFIN
ADCRESEXT
ADCREFP
ADCREFM
R10 22k
C7 2.2uF
C8 2.2uF
VDD
VDDIO
VDD3VFL
Vss
TRST TMS TDI TDO TCK EMU0 EMU1
XRS
X1 X2 XCLKIN XCLKOUT
Y1 CRYSTAL 20MHz
C4 22pF
C5 22pF
TEST2 TEST1
VDD1A18 VDD2A18 VSS1AGND VSS2AGND
VDDA_1.8
VDDA2 VSSA2
VDDA_3.3
VDDAIO VSSAIO
VDDA_3.3
3.3V
R1 R2 10k R3
R4 10k R5 R6 10k
GPIO18 GPIO29 GPIO34
3.3V
R7 4k7
C1 10nF
EMU1
TRST
C3 10nF
R9 4k7
J1 JTAG
EMU1 GND GND GND GND GND TRST
EMU0 TCK TCK-RET TDO PD TDI TMS
3.3V
R8 4k7
C2 10nF
EMU0 TCK TDO 3.3V TDI TMS
Reset
U2
LM3722IM5-3.08
GND GND RESET VCC MR
3.3V
C6 100nF
S1
RESET
XRS
J3
Alarm BRAKE BR3_TOP BR2_TOP BR1_TOP Contactor_AC Rele_AC Rele_Descarga OV_error OC_error
BR3_BOT BR_2_BOT BR1_BOT Reset_Drivers Contactor_DC Rele_DC Temp_error Driver_error
Vbus_DC V_fases_UV V_fases_VW 24V
Ibus_DC I_fase_U I_fase_V
Control connector
Title: DSP Board – DSP
Sheet 1 of 7
Tuesday, December 11, 2012
Rev 0

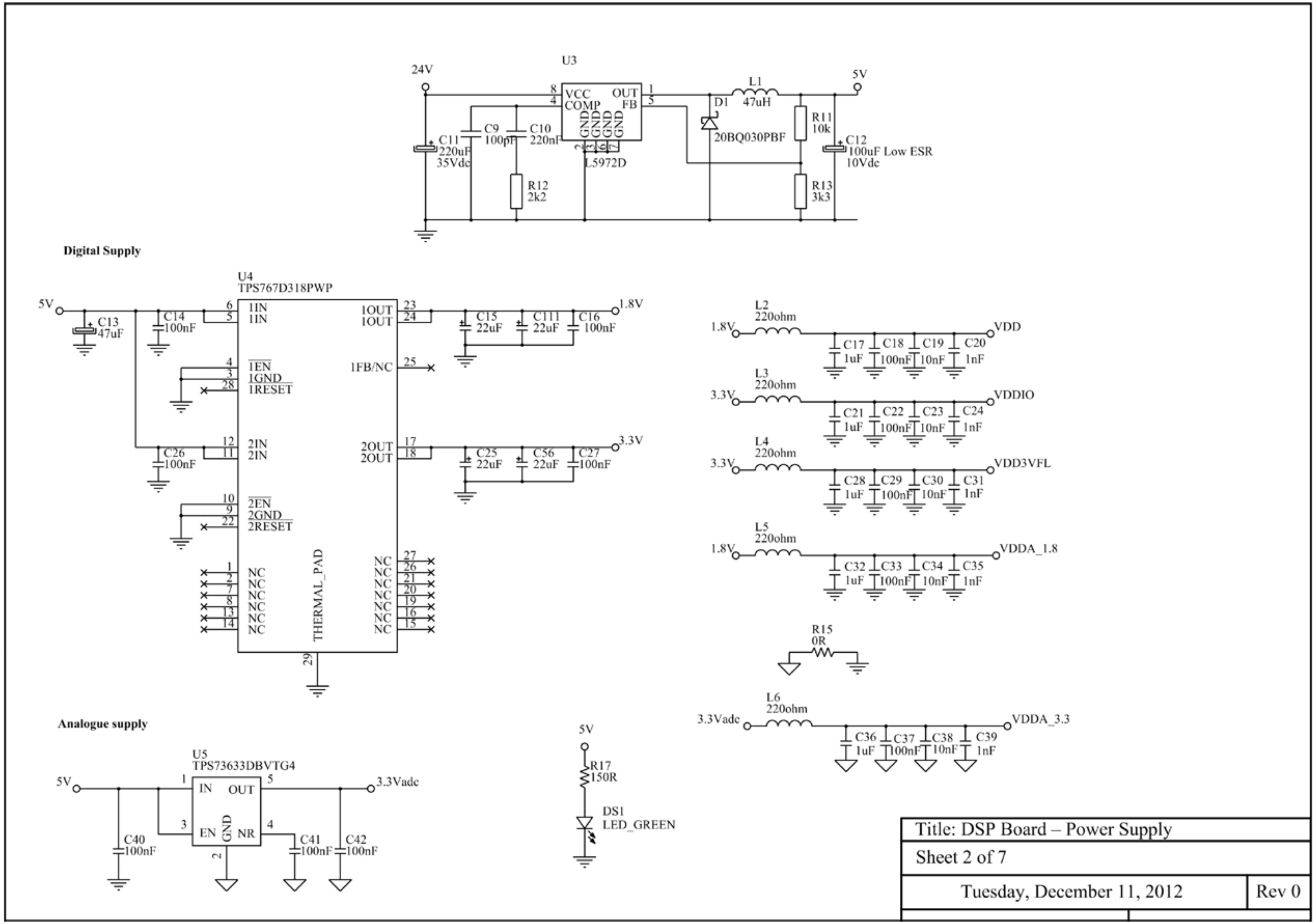
U3
24V
8 VCC
4 COMP
OUT 1
FB 5
GND GND GND GND
2 3 6 7
L5972D
C11 220uF 35Vdc
C9 100pF
C10 220nF
R12 2k2
L1 47uH
D1 20BQ030PBF
R11 10k
R13 3k3
5V
C12 100uF Low ESR 10Vdc
Digital Supply
U4 TPS767D318PWP
5V
C13 47uF
C14 100nF
6 1IN
5 1IN
4 1EN
3 1GND
28 1RESET
12 2IN
11 2IN
C26 100nF
10 2EN
9 2GND
22 2RESET
1 NC
2 NC
7 NC
8 NC
13 NC
14 NC
THERMAL_PAD
29
1OUT 23
1OUT 24
1FB/NC 25
2OUT 17
2OUT 18
NC 27
NC 26
NC 21
NC 20
NC 19
NC 16
NC 15
C15 22uF
C111 22uF
C16 100nF
1.8V
C25 22uF
C56 22uF
C27 100nF
3.3V
L2 220ohm
1.8V
VDD
C17 1uF
C18 100nF
C19 10nF
C20 1nF
L3 220ohm
3.3V
VDDIO
C21 1uF
C22 100nF
C23 10nF
C24 1nF
L4 220ohm
3.3V
VDD3VFL
C28 1uF
C29 100nF
C30 10nF
C31 1nF
L5 220ohm
1.8V
VDDA_1.8
C32 1uF
C33 100nF
C34 10nF
C35 1nF
R15 0R
L6 220ohm
3.3Vadc
VDDA_3.3
C36 1uF
C37 100nF
C38 10nF
C39 1nF
Analogue supply
U5 TPS73633DBVTG4
5V
1 IN
OUT 5
3 EN
GND 2
NR 4
3.3Vadc
C40 100nF
C41 100nF
C42 100nF
5V
R17 150R
DS1 LED_GREEN
Title: DSP Board – Power Supply
Sheet 2 of 7
Tuesday, December 11, 2012
Rev 0

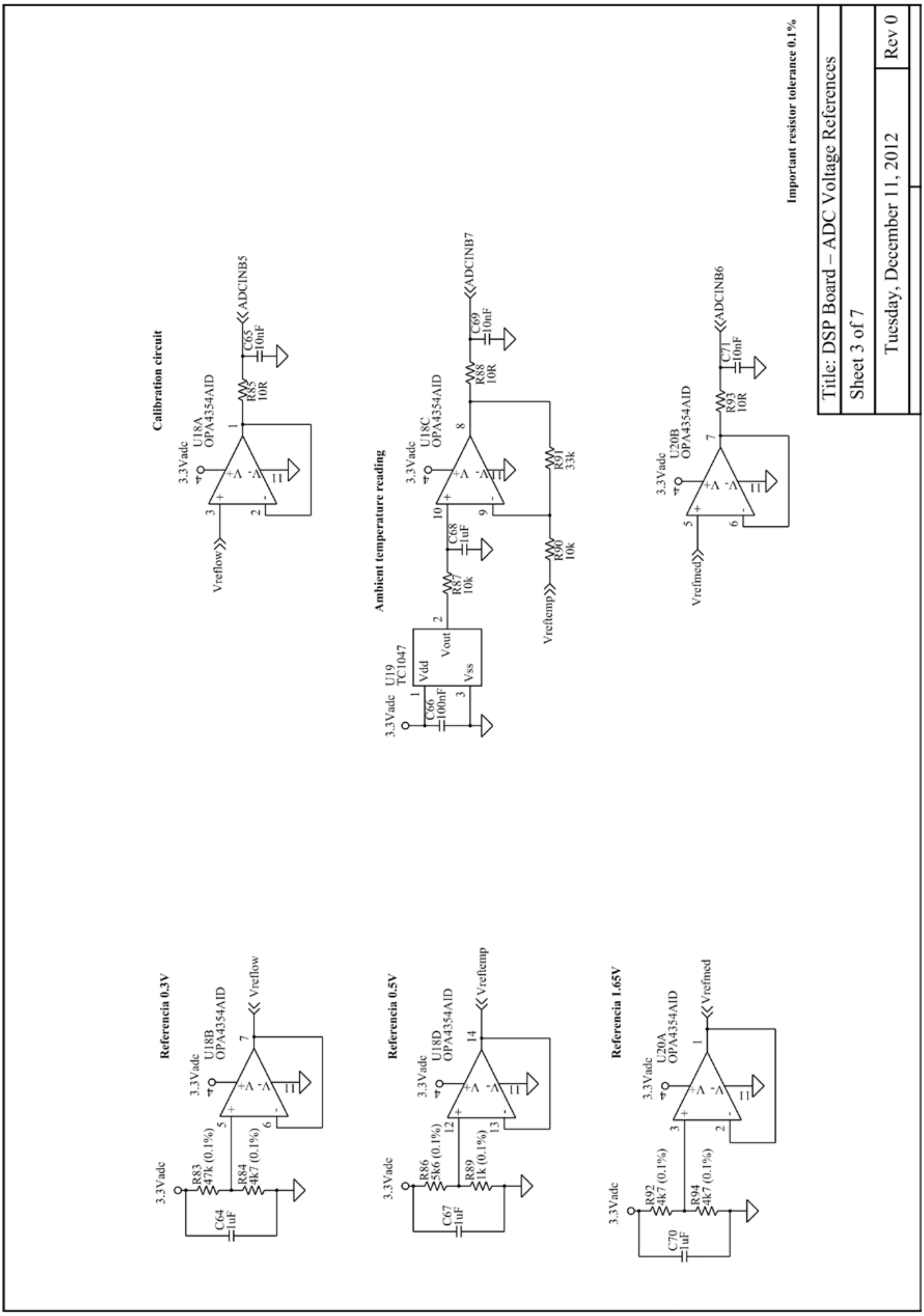
Important resistor tolerance 0.1%
Title: DSP Board – ADC Voltage References
Sheet 3 of 7
Tuesday, December 11, 2012
Rev 0
Calibration circuit
U18A
OPA4354AID
3.3Vadc
Vreflow
R85
10R
C65
10nF
ADCINB5
Ambient temperature reading
U19
TC1047
Vdd
Vout
Vss
C66
100nF
R87
10k
C68
1uF
U18C
OPA4354AID
R88
10R
C69
10nF
ADCINB7
R90
10k
R91
33k
Vreftemp
U20B
OPA4354AID
R93
10R
C71
10nF
ADCINB6
Vrefmed
Referencia 0.3V
R83
47k (0.1%)
R84
4k7 (0.1%)
C64
1uF
U18B
OPA4354AID
Vreflow
Referencia 0.5V
R86
5k6 (0.1%)
R89
1k (0.1%)
C67
1uF
U18D
OPA4354AID
Vreftemp
Referencia 1.65V
R92
4k7 (0.1%)
R94
4k7 (0.1%)
C70
1uF
U20A
OPA4354AID
Vrefmed

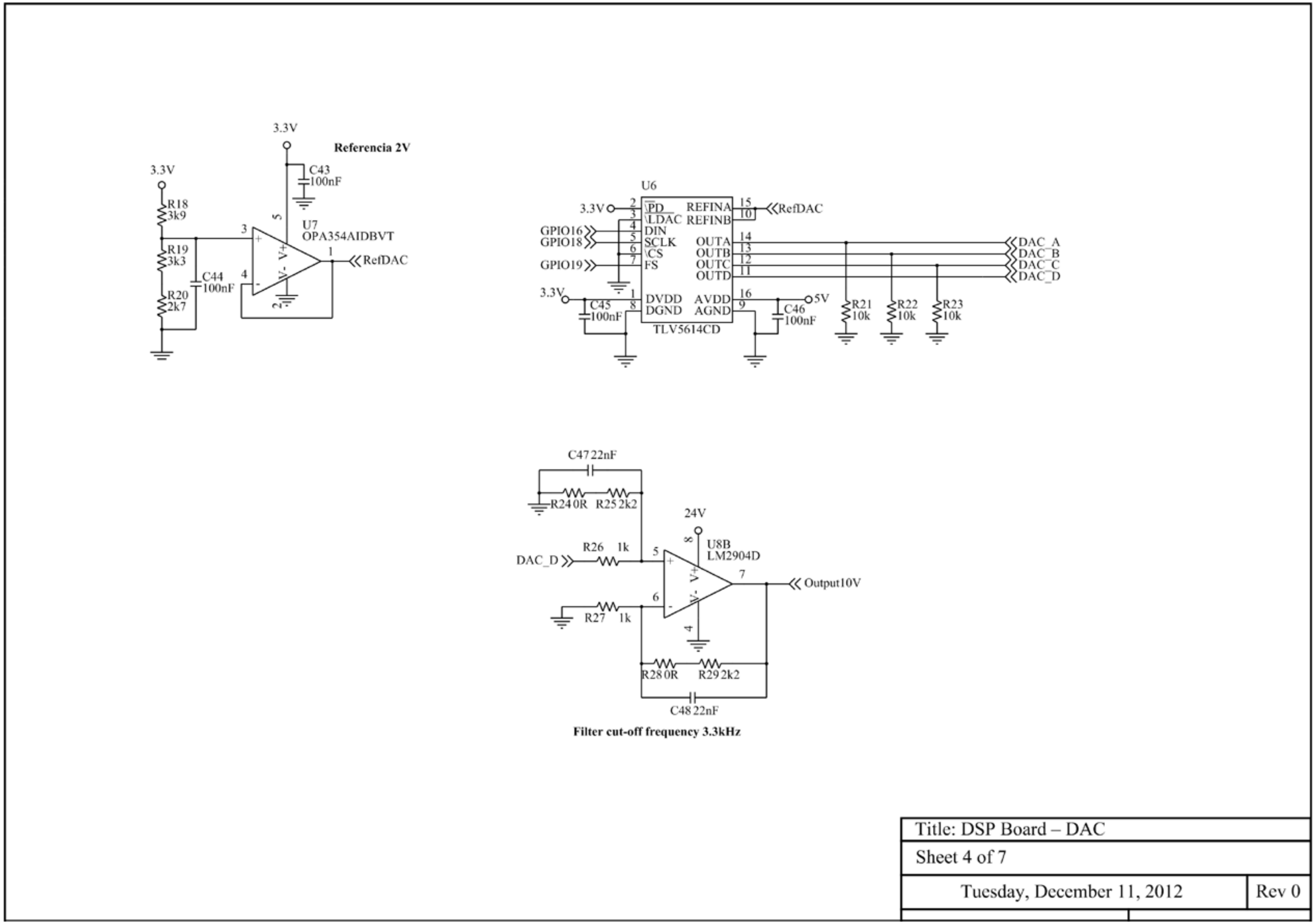

Title: DSP Board – DAC

Sheet 4 of 7

Tuesday, December 11, 2012

Rev 0

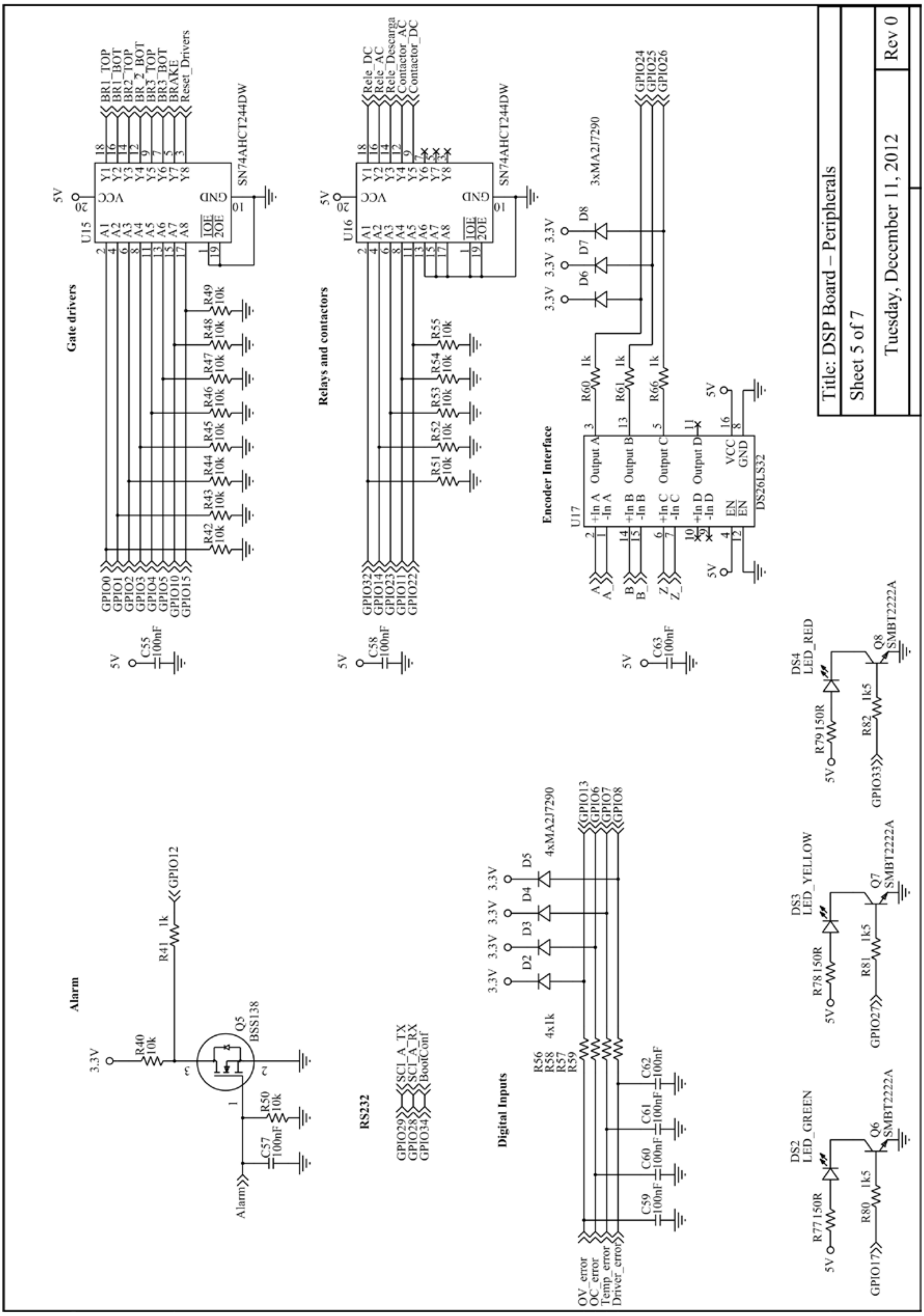
Gate drivers
U15
SN74AHCT244DW
BR1_TOP
BR1_BOT
BR2_TOP
BR_2_BOT
BR3_TOP
BR3_BOT
BRAKE
Reset_Drivers
GPIO0
GPIO1
GPIO2
GPIO3
GPIO4
GPIO5
GPIO10
GPIO15
R42 10k
R43 10k
R44 10k
R45 10k
R46 10k
R47 10k
R48 10k
R49 10k
C55 100nF
Relays and contactors
U16
SN74AHCT244DW
Rele_DC
Rele_AC
Rele_Descarga
Contactor_AC
Contactor_DC
GPIO32
GPIO14
GPIO23
GPIO11
GPIO22
R51 10k
R52 10k
R53 10k
R54 10k
R55 10k
C58 100nF
Encoder Interface
U17
DS26LS32
R60 1k
R61 1k
R66 1k
D6
D7
D8
3xMA2J7290
GPIO24
GPIO25
GPIO26
A
A_
B
B_
Z
Z_
C63 100nF
Alarm
R40 10k
R41 1k
GPIO12
Q5
BSS138
R50 10k
C57 100nF
Alarm
RS232
GPIO29
GPIO28
GPIO34
SCI_A_TX
SCI_A_RX
BootConf
Digital Inputs
R56
R58
R57
R59
4x1k
D2
D3
D4
D5
4xMA2J7290
GPIO13
GPIO6
GPIO7
GPIO8
C59 100nF
C60 100nF
C61 100nF
C62 100nF
OV_error
OC_error
Temp_error
Driver_error
DS2 LED_GREEN
R77 150R
R80 1k5
Q6 SMBT2222A
GPIO17
DS3 LED_YELLOW
R78 150R
R81 1k5
Q7 SMBT2222A
GPIO27
DS4 LED_RED
R79 150R
R82 1k5
Q8 SMBT2222A
GPIO33
5V
3.3V
Title: DSP Board – Peripherals
Sheet 5 of 7
Tuesday, December 11, 2012
Rev 0

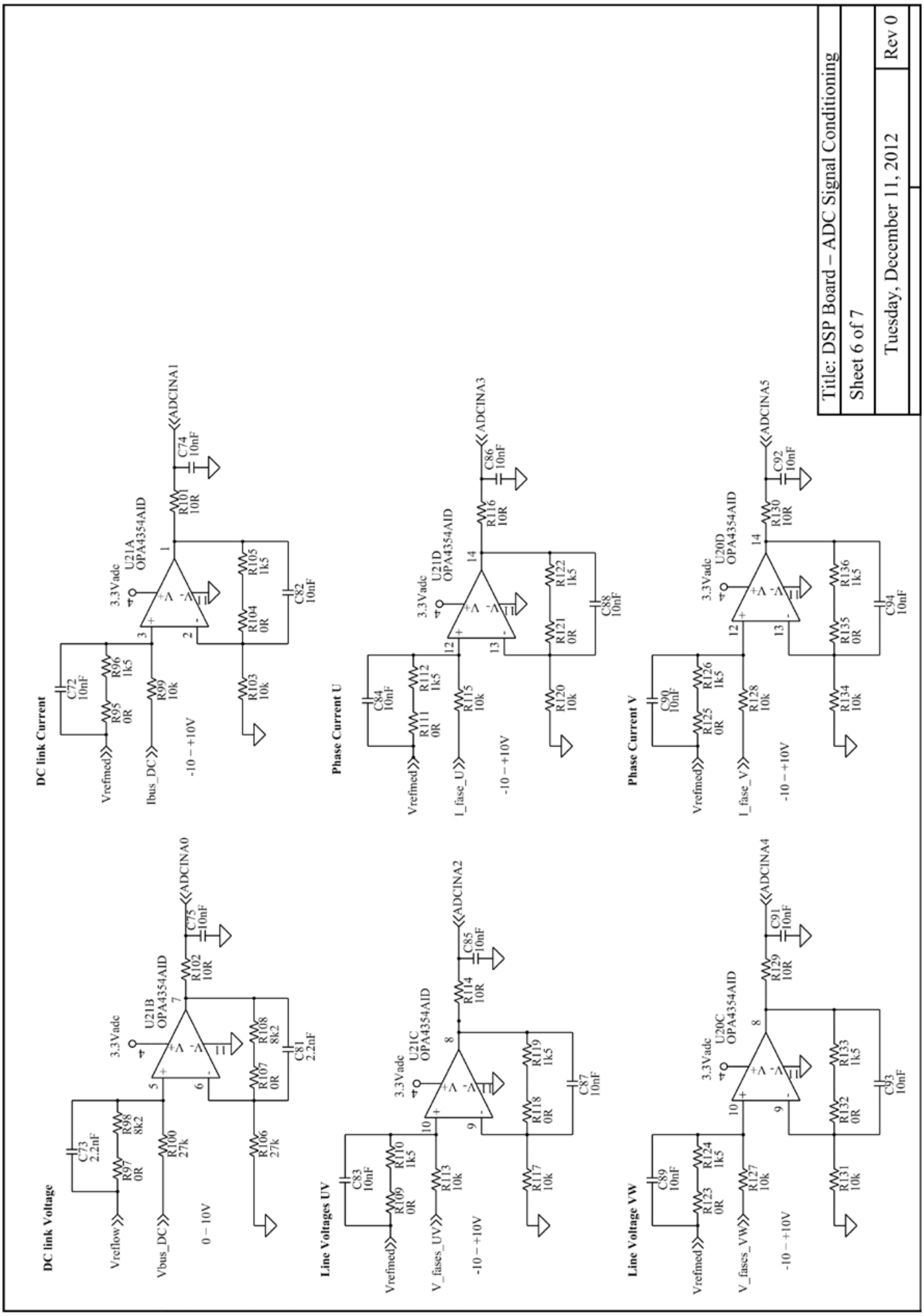
Title: DSP Board – ADC Signal Conditioning
Sheet 6 of 7
Tuesday, December 11, 2012
Rev 0
DC link Voltage
Vreflow
Vbus_DC
0 – 10V
R97 0R
C73 2.2nF
R98 8k2
R100 27k
R106 27k
R107 0R
R108 8k2
C81 2.2nF
3.3Vadc
U21B OPA4354AID
R102 10R
C75 10nF
ADCINA0
DC link Current
Vrefmed
Ibus_DC
-10 – +10V
R95 0R
C72 10nF
R96 1k5
R99 10k
R103 10k
R104 0R
R105 1k5
C82 10nF
U21A OPA4354AID
R101 10R
C74 10nF
ADCINA1
Line Voltages UV
V_fases_UV
R109 0R
C83 10nF
R110 1k5
R113 10k
R117 10k
R118 0R
R119 1k5
C87 10nF
U21C OPA4354AID
R114 10R
C85 10nF
ADCINA2
Phase Current U
I_fase_U
R111 0R
C84 10nF
R112 1k5
R115 10k
R120 10k
R121 0R
R122 1k5
C88 10nF
U21D OPA4354AID
R116 10R
C86 10nF
ADCINA3
Line Voltage VW
V_fases_VW
R123 0R
C89 10nF
R124 1k5
R127 10k
R131 10k
R132 0R
R133 1k5
C93 10nF
U20C OPA4354AID
R129 10R
C91 10nF
ADCINA4
Phase Current V
I_fase_V
R125 0R
C90 10nF
R126 1k5
R128 10k
R134 10k
R135 0R
R136 1k5
C94 10nF
U20D OPA4354AID
R130 10R
C92 10nF
ADCINA5

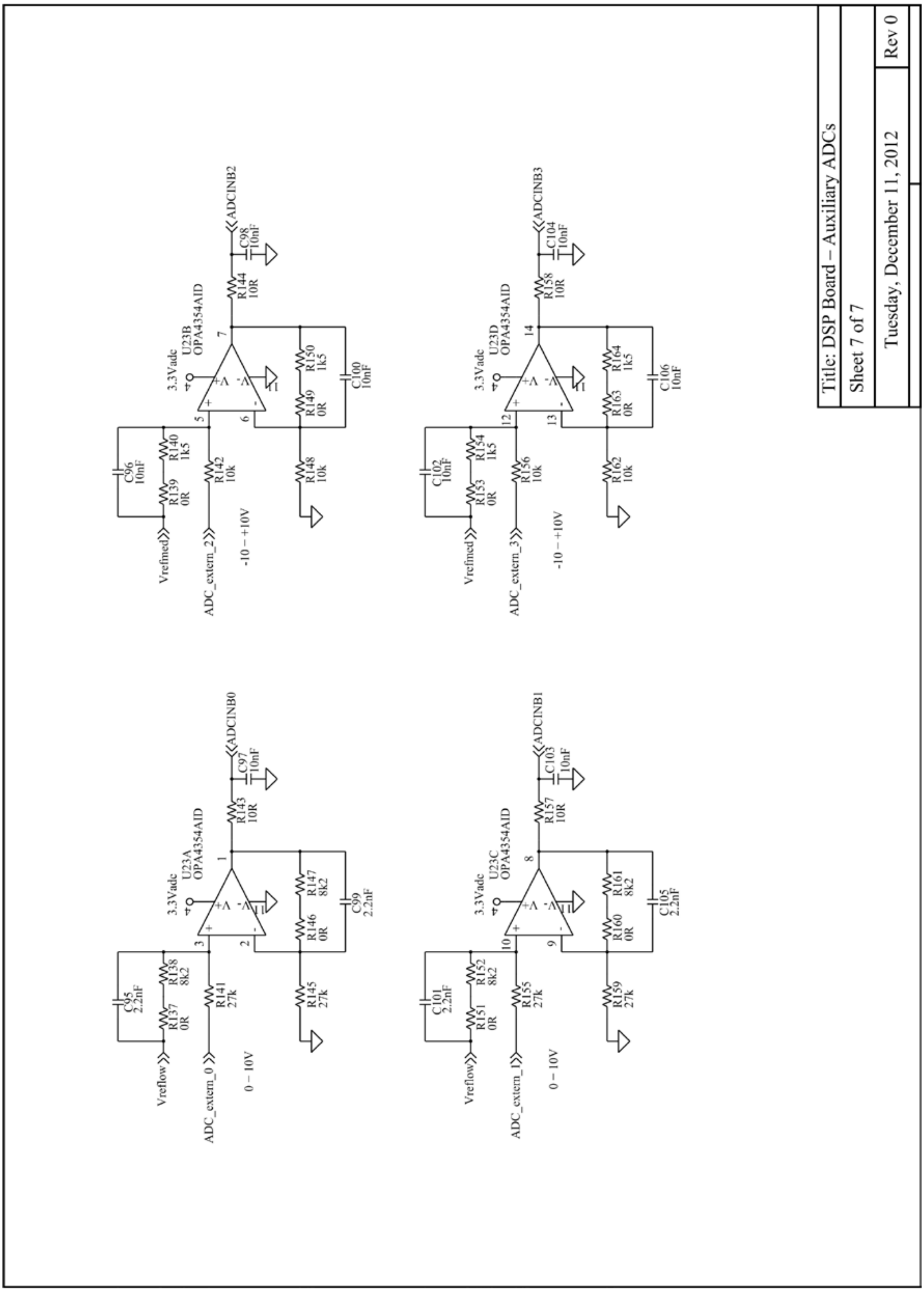
Title: DSP Board – Auxiliary ADCs
Sheet 7 of 7
Tuesday, December 11, 2012
Rev 0
U23A OPA4354AID
U23B OPA4354AID
U23C OPA4354AID
U23D OPA4354AID
3.3Vadc
ADCINB0
ADCINB1
ADCINB2
ADCINB3
Vreflow
Vrefmed
ADC_extern_0
ADC_extern_1
ADC_extern_2
ADC_extern_3
0 – 10V
-10 – +10V
C95 2.2nF
R137 0R
R138 8k2
R141 27k
R145 27k
R146 0R
R147 8k2
C99 2.2nF
R143 10R
C97 10nF
C96 10nF
R139 0R
R140 1k5
R142 10k
R148 10k
R149 0R
R150 1k5
C100 10nF
R144 10R
C98 10nF
C101 2.2nF
R151 0R
R152 8k2
R155 27k
R159 27k
R160 0R
R161 8k2
C105 2.2nF
R157 10R
C103 10nF
C102 10nF
R153 0R
R154 1k5
R156 10k
R162 10k
R163 0R
R164 1k5
C106 10nF
R158 10R
C104 10nF

Appendix F

Publications

As a result of the work carried out in this research, 6 journal papers and 1 conference paper have been published or submitted for publication.

<u>Journal papers</u>

- J. Licari, C. E. Ugalde-Loo, J. Liang, J. Ekanayake, and N. Jenkins, "Torsional Damping considering both Shaft and Blade Flexibilities," *Wind Engineering*, vol. 36, pp. 181-196, 2012. DOI: 10.1260/0309-524X.36.2.181
- J. Licari, C. E. Ugalde-Loo, J. Ekanayake, and N. Jenkins, "Damping of Torsional Vibrations in a Variable-Speed Wind Turbine " *IEEE Transactions on Energy Conversion*, vol. 28, p. 172-180, 2013. DOI: 10.1109/TEC.2012.2224868
- J. Licari, J. Ekanayake, and N. Jenkins, "Investigation of a speed exclusion zone to prevent tower resonance in variable-speed wind turbines" *IEEE Transactions on Sustainable Energy*. DOI: 10.1109/TSTE.2013.2257899 – **Accepted**
- J. Licari, J. Ekanayake, and I. Moore, "Inertia Response from Full-power converter based permanent magnet wind generators " *Automation of Electric Power Systems - Special Issue on Wind Power Technologies*. – **Accepted**
- J. Licari, C. E. Ugalde-Loo, J. Ekanayake, and N. Jenkins, "Performance and stability analysis of two torsional vibration dampers for variable-speed wind turbines in the presence of model uncertainties," *Wind Energy*. – **Submitted**
- J. Licari, J. Ekanayake, and N. Jenkins, "Coordinated inertia response from wind farms," *IET Renewable Power Generation*. – **Submitted**

<u>Conference papers</u>

- J. Licari, C. E. Ugalde-Loo, J. Ekanayake, and N. Jenkins, "Comparison of the performance of two torsional vibration dampers considering model uncertainties and parameter variation," in *EWEA*, Copenhagen 2012.